



Universitat d'Alacant
Universidad de Alicante

Ni-based catalysts supported on CeO₂
for CO₂ valorisation

Andrea Cárdenas Arenas



Tesis Doctorales

UNIVERSIDAD de ALICANTE

Unitat de Digitalització UA

Unidad de Digitalización UA

Departamento de Química Inorgánica
Instituto Universitario de Materiales
Grupo de Materiales Carbonosos y Medio Ambiente

Ni-based catalysts supported on CeO₂ for CO₂ valorisation

Andrea Cárdenas Arenas

Doctorado en Ciencia de Materiales

Tesis presentada para aspirar al grado de

DOCTORA POR LA UNIVERSIDAD DE ALICANTE
MENCIÓN DE DOCTORA INTERNACIONAL

Dirigida por:

Dra. Dolores Lozano Castelló

Catedrática de Química Inorgánica
Universidad de Alicante

Dr. Agustín Bueno López

Catedrático de Química Inorgánica
Universidad de Alicante

Alicante, noviembre de 2020

*“Si escuchas una voz dentro de ti que dice
“no puedes pintar”, entonces, por supuesto, pinta y
esa voz se silenciará.”*

-Vincent van Gogh

Universitat d'Alacant
Universidad de Alicante
A mis padres y hermana.

Agradecimientos

La realización de esta Tesis Doctoral no habría sido posible sin los conocimientos, el soporte, la ayuda y el cariño de todas las personas que de una u otra manera han sido parte de este proceso tan importante en mi vida.

En primer lugar, quiero agradecer a mis directores de Tesis, Lola y Agustín, por la confianza depositada en mí, por su dedicación e interés en mi formación como científica y por darme la oportunidad de hacer parte de este equipo tan maravilloso. Soy muy afortunada de trabajar de la mano de los mejores. Les aprecio y admiro inmensamente.

Quiero aprovechar la oportunidad para agradecer también a quien fue mi primer maestro en la investigación, a Ángel Meléndez. A veces, que alguien confíe en nosotros es ese empujón que necesitamos para atrevernos a sacar lo mejor que tenemos. Su amor por la enseñanza y la ciencia me hizo llegar aquí, donde nunca imaginé llegar.

Quiero dar las gracias a mis compañeros y amigos del doctorado, con quienes he compartido más allá de un laboratorio. En especial, quiero destacar a Vero, Ana, Cristian, Sergio, Zayra, Laurita, Javi, JuanCa, Jessica, Álex, Sonia y al mítico Mauro. Gracias por hacer mejores mis días, por sus invalables charlas científicas y no científicas. Gracias también a Esther por su gran aporte a esta Tesis. Ha sido un placer haber tenido la oportunidad de trabajar juntas. Definitivamente, los lugares los hacen las personas.

Como una Tesis Doctoral no se escribe todos los días, quiero dar gracias a esas personas que, fuera del ámbito académico, han sido parte fundamental de mi vida, que por años han estado a mi lado y, a pesar de la distancia, las circunstancias y el tiempo, han permanecido. De manera especial, me gustaría agradecer a la familia Pinzón Vega y a la tía Nelcy por abrirme las puertas de su casa y de sus vidas y acogerme como un miembro más de su familia. A mis mejores amigos, Fabi y Stefy, su cariño y apoyo incondicional es de los tesoros más valiosos que me ha dado la vida. Espero poder seguir llenando mis recuerdos de momentos con ustedes y que esos lazos de amistad no tengan fecha de caducidad.

Por supuesto, me gustaría dar las gracias a mi familia, a mis padres, Edilia y Óscar, a mi hermana Alby, a mis nonos, Helí y Lilia y, a la más brillante de las estrellas, mi nona Rosa. Ustedes son el motor de mi vida, son mi ejemplo de fortaleza y mi motivación más grande para buscar un mejor futuro. No podría sentirme más orgullosa

y afortunada de la familia que me ha tocado. Este logro también es de ustedes. Finalmente, quiero darle las gracias a Miguel, por tomar mi mano y caminar a mi lado, por ser mi confidente y apoyo en los días difíciles, por ser mi compañero de risas, de copas y de sueños. Gracias por abrazar mis defectos con la misma fuerza que has abrazado mis virtudes. Gracias por estar, simplemente gracias.

A todos ustedes, ¡infinitas gracias!



Universitat d'Alacant
Universidad de Alicante

Resumen

La tala descontrolada de bosques y la quema de combustibles fósiles como el petróleo y el carbón han provocado un aumento de la cantidad de CO₂ en la atmósfera, potenciando el efecto invernadero y contribuyendo al calentamiento global. Debido a esto, ha aumentado el interés de los investigadores por desarrollar tecnologías de producción de energía a partir de fuentes renovables que sean sostenibles y amigables con el medio ambiente. Dada la alta demanda energética del mundo actual, la captura y utilización de CO₂ como fuente de carbono es una opción prometedora que ofrece la posibilidad de capturar el CO₂ para luego utilizarlo como materia prima en la síntesis de productos químicos y combustibles. Esta Tesis Doctoral se centra en la utilización de CO₂ en el sector energético y de combustibles, específicamente en la producción de metano a partir de la reacción de metanación de CO₂ y en la producción de gas de síntesis por medio del reformado seco de metano.

La reacción de metanación de CO₂ permite utilizar la energía excedente para producir metano a partir de hidrógeno y CO₂. Una vez obtenido el metano, es almacenado y transportado a través de la red de gas natural ya existente para ser utilizado como una opción de almacenamiento de energía renovable, así como para la generación de calor de los hogares, para el transporte, para estabilizar la red eléctrica en plantas de energía a gas y como materia prima para la fabricación de otros productos químicos. Por su parte, el reformado seco de metano permite utilizar dos gases de efecto invernadero, el CO₂ y el CH₄, para la producción de gas de síntesis (CO + H₂), siendo así un proceso atractivo desde el punto de vista medioambiental y económico que contribuye a disminuir las emisiones de gases de efecto invernadero para transformarlos en un producto de valor. El gas de síntesis es ampliamente utilizado como fuente de hidrógeno renovable que se usa en la tecnología de pilas de combustibles y como reactivo base para producir productos químicos importantes como alcanos superiores y oxigenados a través de la síntesis de Fischer-Tropsch.

Debido a las condiciones de reacción de la metanación de CO₂ y del reformado seco de metano es necesario el uso de catalizadores que aceleren la reacción hasta valores con relevancia práctica para su uso a nivel industrial. En el caso de la metanación de CO₂, aunque es exotérmica, tiene limitaciones cinéticas generadas por la alta estabilidad de los gases de reacción y, dependiendo del catalizador utilizado y las condiciones de reacción, su producto principal puede ser CH₄ o CO. Por su parte, el reformado seco de metano requiere de temperaturas muy altas, que pueden alcanzar los 900 °C para obtener un alto rendimiento en la producción de gas de síntesis. Debido a

esto se hace necesario el desarrollo de catalizadores con alta actividad catalítica, que sean térmicamente estables y que resistan la desactivación por deposición de carbono.

Los catalizadores basados en metales nobles son los más eficientes para la reacción de metanación de CO₂ y reformado seco de metano, pero su alto precio limita su aplicación práctica y a gran escala. Entre los catalizadores más adecuados, los catalizadores basados en Ni son la mejor opción desde un punto de vista comercial debido a su actividad catalítica aceptable, su abundancia en la naturaleza y su precio más bajo que los metales nobles. Por esta razón, se han utilizado catalizadores de Ni en esta investigación. El soporte sobre el cual se deposita la fase activa tiene una gran influencia en el comportamiento catalítico de estos catalizadores. En esta tesis se utiliza CeO₂ como soporte debido a sus propiedades redox donde coexisten especies de Ce⁴⁺/Ce³⁺ y su capacidad para el almacenamiento de oxígeno, lo cual puede ser beneficioso para la actividad catalítica, además la buena interacción entre los óxidos de Ni y CeO₂ puede inhibir la sinterización del Ni. Aunque se ha avanzado en el estudio de los procesos de metanación de CO₂ y reformado seco de metano como alternativas viables para la valorización del CO₂ aún queda camino por recorrer en el estudio de los mecanismos de reacción, la optimización de los sitios activos y en la síntesis de catalizadores que sean altamente activos, selectivos y estables en condiciones de reacción.

La actividad catalítica de un catalizador depende en gran medida del tipo de metal utilizado, la naturaleza y área superficial del soporte, el tamaño de partícula y la interacción metal-soporte. En esta investigación se estudia la influencia de la morfología de los catalizadores en sus propiedades catalíticas mediante el uso de soportes 3DOM, soportes de xerogeles de carbón y catalizadores basados en nanopartículas. La selección de un soporte adecuado es fundamental para la obtención de catalizadores eficientes. Utilizar soportes con estructura 3DOM permite un transporte eficiente de reactivos y productos a través de los macroporos combinados con la selectividad y los beneficios catalíticos de los mesoporos y microporos. Además, ofrecen áreas superficiales más altas que permiten una mejor dispersión de la fase activa. Por su parte, las nanopartículas son materiales que se caracterizan por tener un tamaño muy reducido y propiedades físico-químicas muy diferentes a los materiales a granel. Sus características estructurales frecuentemente están relacionadas con actividades y selectividades muy mejoradas, pero en condiciones de reacción pueden sufrir cambios morfológicos, estructurales y químicos, lo cual hace que obtener un catalizador de nanopartículas altamente estable sea todo un reto. Por otra parte, la poca distribución de los minerales de cerio en el planeta hace interesante optimizar su uso mezclándola con un soporte de mayor superficie y menor precio como el carbón. Los xerogeles de carbón son un excelente soporte catalítico debido a propiedades como su elevada porosidad y

superficie específica que permite una buena dispersión de la fase activa, su ajustable textura porosa y química superficial y su alta estabilidad térmica y química.

En esta Tesis Doctoral se ha hecho un avance significativo en el estudio del mecanismo de reacción de la metanación de CO₂ sobre catalizadores de NiO/CeO₂ y NiO/Al₂O₃. Los resultados indican que la alta actividad catalítica y selectividad del catalizador NiO/CeO₂ se debe a que combina dos tipos de sitios activos eficientes para la disociación del CO₂ en la interfase NiO-CeO₂ y para la disociación del H₂ en las partículas Ni⁰. Además, aunque la desorción del agua es el paso más lento del mecanismo, la alta movilidad del oxígeno a lo largo de la red de la ceria hace que el agua no se forme necesariamente en los mismos sitios activos donde se quimisorbe el CO₂, es decir, los sitios activos necesarios para la quimisorción de CO₂ no están bloqueados por las moléculas de agua. También se vio que la superficie de este catalizador no acumula especies de carbono durante la reacción, lo que permite una quimisorción y disociación más rápida del CO₂. Por su parte, el catalizador NiO/Al₂O₃ tiene la desventaja que todos los pasos del mecanismo ocurren en los mismos sitios activos, además la liberación lenta del agua y la acumulación de formiatos que se generan en la superficie del catalizador retrasan la quimisorción de más moléculas de CO₂.

Con base en los resultados obtenidos anteriormente se ha estudiado el papel de los sitios activos Ni⁰ y NiO/CeO₂ en catalizadores NiO/CeO₂, y se ha optimizado la proporción de estos sitios activos para maximizar la actividad en la reacción de metanación de CO₂. Para este propósito, se varió la proporción de cada centro activo mediante la modificación de la interacción NiO-CeO₂ utilizando diferentes métodos de incorporar el Ni y controlando la estructura del soporte de CeO₂ usando estructuras 3DOM. Los resultados indican que la proporción óptima requerida para lograr una máxima conversión de estos catalizadores en la reacción de metanación de CO₂ es de 25% de Ni⁰ para la disociación del H₂ y 75% de NiO-CeO₂ para la disociación de CO₂. Un desequilibrio de los sitios activos tiene como consecuencia la formación de especies de carbono en la superficie del catalizador durante la reacción y, por tanto, la actividad catalítica se ve afectada. En este sentido, el catalizador con la proporción óptima de sitios activos mantiene su superficie limpia de intermedios de carbono, mientras que en un catalizador con exceso de sitios activos para la disociación de CO₂ acumula bicarbonatos en su superficie.

Con el fin de avanzar en el diseño y síntesis de nuevos catalizadores para la reacción de metanación de CO₂ se ha preparado, caracterizado y probado un catalizador basado en nanopartículas de óxido mixto NiO-CeO₂. El comportamiento catalítico de este material ha sido comparado con otros catalizadores NiO-CeO₂ de referencia. Los

resultados obtenidos evidencian que el catalizador de nanopartículas de NiO-CeO₂ es mucho más activo que los catalizadores de referencia con los que se ha comparado y sus propiedades catalíticas están relacionadas con su alta área superficial específica y con la presencia de especies Ni-O-Ce altamente reducibles sobre la superficie del catalizador. Además, presentó una alta estabilidad, manteniendo la misma actividad en condiciones de reacción durante 25 horas.

Por otra parte, con el fin de reducir y/o optimizar del uso de la ceria se ha mezclado con xerogeles de carbón. Para ello, se han preparado, caracterizado y probado en la reacción de metanación de CO₂ catalizadores basados en una mezcla física de NiO/CeO₂ y NiO/C y se ha analizado el efecto del carbón tanto en la naturaleza de los sitios activos de níquel como el comportamiento de las fases NiO/CeO₂. Los resultados ponen en manifiesto que la presencia de carbón favorece la reducibilidad de los catalizadores y aumenta la proporción de especies NiO en superficie. En este sentido, se ha obtenido un catalizador con buenas propiedades catalíticas compuesto de 25%NiO/CeO₂ y 75%NiO/C. Su alta actividad catalítica podría estar relacionada con la alta superficie específica del soporte de carbón, la cual favorece la dispersión de las partículas de níquel, y/o al efecto químico del carbón en la interacción NiO/CeO₂.

Finalmente, debido a la alta estabilidad presentada por el catalizador basado en nanopartículas de óxido mixto NiO-CeO₂ bajo condiciones de reacción en la metanación de CO₂, se consideró como una opción prometedora para ser usado en la reacción de reformado seco de metano. Estas nanopartículas mostraron estabilidad catalítica bajo las severas condiciones de reacción del reformado seco de metano (700 °C), y una mejor resistencia a la formación de carbón con respecto a un catalizador de óxido mixto NiO-CeO₂ de referencia preparado sin control del tamaño de partícula. La resistencia a la formación de carbón de este catalizador está relacionada con que presenta una mejor interacción y cooperación entre las fases NiO y CeO₂. Además, en estas nanopartículas, la participación de cationes de cerio en los procesos redox que ocurren durante la reacción de reformado seco de metano parece estabilizar las especies catiónicas de níquel. Por el contrario, el catalizador preparado sin control de la estructura presenta una segregación de Ni la cual sería responsable de una mayor formación de carbón.

Summary

The uncontrolled felling of forests and the burning of fossil fuels such as oil and coal have caused an increase in the amount of atmospheric CO₂, enhancing the greenhouse effect and contribution to the global warming. This has led to an increase in the interest of researchers to develop energy production technologies from renewable sources that are sustainable and environmental friendly. In a world with high energy demand, the capture and use of CO₂ as a carbon source is a promising path that offers the possibility of using it as a raw material in the synthesis of chemicals and fuels. This doctoral thesis is focused on the use of CO₂ in the energy and fuel sector, specifically on the production of methane from the CO₂ methanation reaction and on the syngas production by dry reforming of methane reaction.

The CO₂ methanation reaction allows the use of excess energy to produce methane from hydrogen and CO₂. The methane produced can be directly injected into the existing network of natural gas pipelines and used as a renewable energy storage option, as well as fuel or feedstock for the manufacture of other chemical products. In the case of dry reforming of methane (DRM), it has been proposed to diminish emission of two greenhouse gases, CO₂ and CH₄, to yield a mixture of H₂ and CO (syngas). DRM is an environmental friendly pathway alternative to conventional production of syngas through steam reforming, which contributes to decrease greenhouse gases emissions producing products with practical interest. The syngas obtained by DRM can be used in fuel cell technology as a renewable source of hydrogen, and for Fischer-Tropsch synthesis of hydrocarbons of different nature.

Due to the sluggish kinetics of CO₂ methanation and dry methane reforming, it is necessary to use catalysts to accelerate the reaction to more practical values for the industrial use. From a thermodynamic point of view, the CO₂ methanation reaction is exothermic, but the great stability of the CO₂ and H₂ molecules make it necessary to use a suitable catalyst to reach acceptable reaction rate and selectivity. In the case of dry reforming of methane, high temperatures are required to obtain a high yield in the production of syngas. For this reason, it is necessary to develop catalysts with high catalytic activity, thermally stable and resistant to deactivation by carbon deposition.

The most efficient catalysts for these reactions are supported noble metals, but its high price limits their practical and big scale application. Among the suitable catalysts, Ni-based catalysts are the most interesting at industrial level because combine an acceptable catalytic activity, high availability in nature and lower price than noble

metals. For this reason, Ni catalysts are used in this research. The support of the active phase strongly influences the catalytic behavior of these catalysts. In this thesis, ceria is used as a support due to its redox properties where $\text{Ce}^{4+}/\text{Ce}^{3+}$ species coexist and its capacity to give oxygen, which can be beneficial for catalytic activity, in addition to the good interaction between NiO and CeO_2 oxides can inhibit Ni sintering. Although progress has been made in the study of CO_2 methanation processes and dry methane reforming as viable alternatives for the recovery of CO_2 , there is still a long way to go in the study of reaction mechanisms, the optimization of active sites and the synthesis of highly active, selective and stable catalysts under reaction conditions.

The catalytic activity of a catalyst is strongly affected by the material used, the nature and surface of the support, the particle size and the metal-support interaction. In this Doctoral Thesis, the influence of catalyst morphology on their catalytic properties is studied by using three dimensionally ordered macroporous supports (3DOM), carbon xerogel supports and nanoparticle-based catalysts. The selection of a suitable support is essential to obtain efficient catalysts. 3DOM structured supports combine efficient transport of reactants and products through macropores with the selectivity and catalytic benefits of mesopores and micropores. Also, their higher surface areas allow better dispersion of the active phase. On the other hand, nanoparticles are materials that are characterized by having high area/mass ratio and by having different physico-chemical properties than bulk materials. The structural characteristics of nanoparticles are frequently related to improvements in catalytic activity, but they can have morphological, structural and chemical changes under reaction conditions, which makes developing a highly stable nanoparticle catalyst a great challenge. Moreover, due to the poor distribution of cerium minerals on the planet, optimizing its use by mixing it with a support of greater surface area and lower price such as carbon can be interesting. Carbon xerogels are an excellent catalytic support due to its high porosity and specific surface that allow a good dispersion of the active phase, adjustable porous morphology and surface chemical texture and high thermal and chemical stability.

In this doctoral thesis, an important advance in the study of the reaction mechanism of CO_2 methanation on NiO/CeO_2 and $\text{NiO}/\text{Al}_2\text{O}_3$ catalysts has been reported. The results show that the high catalytic activity and selectivity of the NiO/CeO_2 catalyst is because it combines two types of efficient active sites for the dissociation of CO_2 at the $\text{NiO}-\text{CeO}_2$ interface and for the dissociation of H_2 on Ni^0 particles. In addition, it has been proven that H_2O desorption, which is the slowest step in the reaction mechanism due to the high oxygen mobility throughout the ceria lattice, is not necessarily taken place on the same active sites of CO_2 chemisorption. Also, the surface of this catalyst does not accumulate carbon-containing species under reaction conditions, which allows faster chemisorption and dissociation of CO_2 . On the contrary,

it has been reported that the NiO/Al₂O₃ catalyst has the disadvantage that all the steps of the mechanism take place on the same active sites, and the slow release of water and the accumulation of surface on these sites delay the chemisorption of further CO₂ molecules.

Based on the results obtained, the role of Ni⁰ and NiO/CeO₂ active sites on NiO/CeO₂ catalysts has been studied, and the proportion of these active sites has been optimized to maximize the catalytic activity for CO₂ methanation. For this purpose, the proportion of each active site was varied by the modification of the NiO-CeO₂ interaction using different methods for Ni incorporation to the structure and by controlling the surface of the CeO₂ support using 3DOM structures. The results show that the optimal ratio required to achieve maximum conversion in the CO₂ methanation reaction is 25% Ni⁰ for H₂ dissociation and 75% NiO-CeO₂ for CO₂ dissociation. An imbalance of the active sites results in the formation of carbon species on the catalyst surface during the reaction and therefore the catalytic activity is affected. The catalyst with the optimal proportion of active sites keeps its surface clean of carbon intermediates under reaction conditions, while bicarbonates are accumulated on the catalyst surface when an excess of active sites for CO₂ dissociation is reported.

In order to advance in the design and synthesis of new catalysts for the CO₂ methanation reaction, a catalyst consisting in NiO-CeO₂ mixed nanoparticles has been prepared, characterized and tested for CO₂ methanation. The catalytic behavior of this material has been compared with other reference NiO-CeO₂ catalysts. The results obtained show that the NiO-CeO₂ nanoparticle catalyst is much more active than the reference catalysts and its catalytic properties are related with its high specific surface area (122 m²/g; 6 nm particle diameter) and with the presence of highly reducible Ni-O-Ce species on the catalyst surface. This catalyst presented high stability, maintaining the same activity under reaction conditions for 25 hours.

The role of a carbon support in NiO-CeO₂ catalysts for CO₂ methanation reaction has been studied to reduce and/or optimize the use of ceria. Catalysts consisting of a physical mixture of NiO/CeO₂ and NiO/C have been prepared, characterized and tested to CO₂ methanation and the effect of carbon both in the nature of the Nickel species and in the behavior of the NiO/CeO₂ phase has been analyzed. The results show that the presence of carbon enhances the reducibility of the catalysts and increases the proportion of the surface NiO species. In this sense, the most effective utilization of ceria is obtained in a catalyst with 25%NiO/CeO₂ and 75%NiO/C. Its high catalytic activity can be related to the high specific surface area of the carbon support, which favors the dispersion of the nickel particles, and/or the chemical effect of carbon on the NiO/CeO₂ interaction.

Finally, due to the high stability shown by the NiO-CeO₂ mixed oxide nanoparticle based catalyst under reaction conditions in CO₂ methanation, it was considered as a promising option to be used in the dry reforming reaction of methane. These nanoparticles showed catalytic stability under the severe reaction conditions of dry methane reforming (700 ° C), and better resistance to carbon formation than the reference NiO-CeO₂ mixed oxide catalyst prepared without particle size control. The improved carbon resistance of this catalyst can be related to the better interaction and cooperation between NiO and CeO₂ mixed phases. Furthermore, in these nanoparticles, participation of Ce cations in the redox processes taking place during the DRM seems to stabilize cationic Ni species. On the contrary, the catalyst prepared without control of the structure suffered a segregation of Ni which can be responsible of the catalytic formation of carbon.



Index

0.	Thesis structure	1
1.	Introducción y objetivos	5
1.1.	Problemática ambiental	6
1.2.	Valorización de CO₂	9
1.2.1.	Proceso Power-to-Gas	11
1.2.2.	Producción de gas de síntesis	14
1.3.	Metanación de CO₂	16
1.3.1.	Mecanismo de reacción de la metanación de CO ₂	18
1.3.1.1.	Mecanismo por formación de CO como intermedio principal	18
1.3.1.2.	Mecanismo por formación de formiato como intermedio principal	20
1.3.2.	Desarrollo de catalizadores para la reacción de metanación de CO ₂	21
1.4.	Reformado seco de metano	23
1.4.1.	Mecanismo de reacción para el reformado seco de metano	25
1.4.2.	Desarrollo de catalizadores para el reformado seco de metano	27
1.5.	Influencia de la morfología de los catalizadores en sus propiedades catalíticas	29
1.5.1.	Sólidos macroporosos con orden tridimensional (3DOM; Three Dimensionally Ordered Macroporous Solids)	30
1.5.2.	Nanopartículas	32
1.6.	Objetivos	34
1.7.	Referencias	35
2.	Metodología y técnicas experimentales	51
2.1.	Muestras y metodología de síntesis	52

2.1.1. Catalizadores sin control de la estructura	53
2.1.2. Catalizadores macroporosos con orden tridimensional 3DOM	54
2.1.3. Catalizadores basados en nanopartículas	55
2.1.4. Catalizadores NiO/CeO ₂ -NiO/C	56
2.2. Técnicas de caracterización físico-química	57
2.2.1. Adsorción física de gases	57
2.2.2. Porosimetría de mercurio	60
2.2.3. Difracción de rayos X (DRX)	61
2.2.4. Espectroscopía de emisión por plasma de acoplamiento inductivo (ICP-OES)	63
2.2.5. Microscopía electrónica de barrido (SEM)	64
2.2.6. Microscopía electrónica de transmisión (TEM)	65
2.2.7. Reacciones a temperatura programada: H ₂ -TPR y He-TPD	66
2.2.8. Espectroscopía fotoelectrónica de rayos X (XPS)	68
2.2.9. Termogravimetría (TG)	70
2.3. Ensayos de actividad catalítica	71
2.3.1. Reacción de metanación de CO ₂ (MCMA-UA)	71
2.3.2. Reacción de metanación de CO ₂ (TQSA-UPV)	72
2.3.3. Reacción de reformado seco de metano (CEPT-US)	72
2.4. Técnicas de caracterización avanzadas utilizadas en el estudio del mecanismo de reacción de la metanación de CO₂	73
2.4.1. Ensayos isotópicos con pulsos de ¹³ C ¹⁸ O ₂	73
2.4.2. Ensayos DRIFTS in-situ	74
2.5. Referencias	75

3. Study of the CO₂ methanation mechanism using NiO/CeO₂ and NiO/Al₂O₃ catalysts	79
3.1. Introduction	80
3.2. Experimental section	81
3.2.1. Catalysts preparation and characterization	81
3.2.2. Catalytic tests and mechanistic studies	81
3.3. Results and discussion	82
3.3.1. Catalysts characterization by N ₂ adsorption, XDR and H ₂ -TPR	82
3.3.2. Catalytic tests	85

3.3.3.	Fresh and used catalysts characterization by XPS	86
3.3.4.	Isotopic experiments	89
3.3.5.	In-situ DRIFTS experiments	94
3.3.6.	$\text{CO}_2 + \text{H}_2$ reaction mechanism on NiO/CeO_2 and $\text{NiO}/\text{Al}_2\text{O}_3$ catalysts	96
3.4.	Conclusions	98
3.5.	References	99
4.	Design of active sites in NiO/CeO_2 catalysts for the CO_2 methanation: tailoring the $\text{NiO}-\text{CeO}_2$ contact	105
4.1.	Introduction	106
4.2.	Experimental section	107
4.2.1.	Supports preparation	107
4.2.2.	Catalysts preparation	107
4.2.3.	Catalysts characterization	108
4.2.4.	Catalytic tests	109
4.2.5.	Mechanistic studies	109
4.3.	Results and discussion	110
4.3.1.	Catalysts characterization	110
4.3.2.	CO_2 methanation tests	121
4.3.3.	In-situ DRIFTS experiments	124
4.3.4.	Pulse experiments with isotopic CO_2	125
4.4.	Conclusions	129
4.5.	References	131
5.	Highly active, selective and stable $\text{NiO}-\text{CeO}_2$ nanoparticles for CO_2 methanation	135
5.1.	Introduction	136
5.2.	Experimental details	137
5.2.1.	Catalysts preparation	137
5.2.2.	CO_2 methanation tests	138
5.2.3.	Catalysts characterization	138
5.3.	Results and discussion	138
5.3.1.	CO_2 methanation tests	138

5.3.2. Catalysts characterization	141
5.4. Conclusions	150
5.5. References	150
6. Effect of carbon content in the NiO/CeO₂ catalysts for the CO₂ methanation	157
6.1. Introduction	158
6.2. Experimental details	159
6.2.1. Catalysts preparation	159
6.2.2. Catalysts characterization	159
6.2.3. CO ₂ methanation tests	160
6.3. Results and discussion	160
6.3.1. Catalysts characterization	160
6.3.2. CO ₂ methanation tests	169
6.4. Conclusions	171
6.5. References	172
7. Stable NiO-CeO₂ nanoparticles with improved carbon resistance for methane dry reforming. The size matters	177
7.1. Introduction	178
7.2. Experimental details	179
7.2.1. Catalysts preparation	179
7.2.2. Catalytic tests	180
7.2.3. Catalysts characterization	180
7.3. Results and discussion	180
7.3.1. Catalysts characterization	180
7.3.2. Catalytic tests	184
7.3.3. XPS analysis of the catalysts before and after the DRM tests	187
7.4. Conclusions	190
7.5. References	191
8. General conclusions/ Conclusiones generales	195

8.1. General conclusions	196
8.2. Conclusiones generales	198
Curriculum Vitae	203



Universitat d'Alacant
Universidad de Alicante



Thesis structure

This Doctoral Thesis has been structured in 8 chapters.

Chapter 1 presents a literature review about environmental problem generated by high CO₂ emissions into the atmosphere, as well as mitigation strategies, specifically the use of CO₂ in the energy and fuel sector, through the Power to Gas processes and the production of synthesis gas. In this sense, the catalytic conversion of CO₂ to methane using renewable H₂ through the CO₂ methanation reaction and the dry reforming of methane for the production of synthesis gas are exposed, describing in detail the fundamental principles of these reactions, the reaction mechanisms as well as the different catalysts that have been developed. Finally, the objectives of the doctoral thesis have been also exposed in this chapter.

Chapter 2 compiles the materials and the synthesis methods used in the catalysts preparation. The fundamental principles, devices and operating conditions of the experimental techniques used in the physicochemical characterization have also been described. Finally, the experimental conditions of the catalytic tests and the advanced characterization techniques used in mechanistic studies have also been presented.

Chapter 3 reports the study of the CO₂ methanation mechanism over NiO/CeO₂ and NiO/Al₂O₃ catalysts, tested and characterized through diverse techniques: X-ray diffraction, N₂ adsorption-desorption isotherms, H₂-TPR and X-ray photoelectron spectroscopy (XPS), which showed that the higher methanation activity and selectivity of NiO/CeO₂ catalyst is attributed to the cooperation of two types of active sites efficient

Chapter 0

for CO₂ dissociation at the NiO-ceria interface and for H₂ dissociation on Ni⁰ particles. Additionally, isotopic ¹³C¹⁸O₂ pulse experiments demonstrated that water desorption is the slowest mechanism step and, due to the high oxygen mobility throughout the ceria lattice, water is not necessarily formed on the same active sites that chemisorb CO₂ in NiO/CeO₂ catalyst. Finally, in-situ DRIFTS experiments reveal that the NiO/CeO₂ surface does not accumulate carbon-containing species under reaction conditions, which allows faster chemisorption and dissociation of CO₂. On the contrary, the NiO/Al₂O₃ catalyst handicaps are that all the steps of the mechanism take place on the same active sites, and the slow release of water and the accumulation of surface formates on these sites delay the chemisorption of further CO₂ molecules.

The results of this chapter have been published in:

A. Cárdenas-Arenas, A. Quindimil, A. Davó-Quiñonero, E. Bailón-García, D. Lozano-Castelló, U. De-La-Torre, B. Pereda-Ayo, J. A. González-Marcos, J. R. González-Velasco, A. Bueno-López. *Isotopic and in situ DRIFTS study of the CO₂ methanation mechanism using Ni/CeO₂ and Ni/Al₂O₃ catalysts*. Appl. Catal. B Environ. 265 (2020) 118538.

In Chapter 4 the role of the CO₂ chemisorption and dissociation sites at the NiO-ceria interface and H₂ dissociation sites on Ni⁰ entities over NiO/CeO₂ catalysts in the CO₂ methanation has been studied. Additionally, the proportion of these active sites has been optimized to maximize the activity. For these purposes, NiO/CeO₂ catalysts with different proportion of active sites were prepared varying the Ni-incorporation method and controlling the structure of the ceria support in order to modify the NiO-ceria interaction. According to XPS, the optimal proportion of both sites required to achieve the maximum conversion was 25% Ni⁰ and 75% NiO-CeO₂ for H₂ and CO₂ dissociation, respectively. In-situ DRIFTS and isotopic experiments with ¹³C¹⁸O₂ showed that this optimum catalyst keeps the catalyst surface clean of carbon intermediates under reaction conditions, while surface bicarbonates are accumulated on a catalyst with an excess of active sites for CO₂ chemisorption/dissociation.

The results of this chapter have been published in:

A. Cárdenas-Arenas, A. Quindimil, A. Davó-Quiñonero, E. Bailón-García, D. Lozano-Castelló, U. De-La-Torre, B. Pereda-Ayo, J. A. González-Marcos, J. R. González-Velasco, A. Bueno-López. *Design of active sites in Ni/CeO₂ catalysts for the methanation of CO₂: tailoring the Ni-CeO₂ contact*. Appl. Mater. Today 19 (2020) 100591.

In Chapter 5 a novel catalyst consisting in NiO-CeO₂ mixed oxide nanoparticles has been prepared, characterized and tested for CO₂ methanation. The behaviour of this

novel material has been compared with other reference NiO-CeO₂ catalysts, including a mixed oxide with the same composition but prepared without control of the size, a counterpart NiO-CeO₂ mixed oxide with three dimensionally ordered macroporous (3DOM) structure and an inverse catalyst consisting of bulk NiO-supported CeO₂ nanoparticles among others. The novel NiO-CeO₂ nanoparticles catalyst is much more active than all reference catalysts with the same composition, and the high catalytic properties are related with its high specific surface area (122 m²/g; ~ 6 nm) and with the presence of highly-reducible Ni-O-Ce species on the nanoparticles surface. The selectivity towards CH₄ formation of the novel NiO-CeO₂ nanoparticles catalyst is ~100% in the whole range of temperature studied, and is also highly stable, keeping the same activity during a 25 hours catalytic experiments.

The results of this chapter have been published in:

A. Cárdenas Arenas, H. Cortés Soriano, E. Bailón García, A. Davó Quiñonero, D. Lozano Castelló, A. Bueno López. *Active, selective and stable NiO-CeO₂ nanoparticles for CO₂ methanation*, Fuel Process. Technol. 212 (2021) 106637.

In [Chapter 6](#), the role of a carbon support in NiO-CeO₂ catalysts for CO₂ methanation reaction has been studied in order to reduce and/or optimize the use of ceria. Catalysts based on physical mixture of NiO/CeO₂-NiO/C in proportion of 0, 25, 50, 75 and 100% NiO/C have been prepared, characterized and tested in CO₂ methanation. H₂-TPR and XPS showed that the reducibility of the NiO species is better in the carbon-containing catalysts than in carbon-free one. This can be attributed to the high surface area of the carbon support, which favours the dispersion of the nickel active phase, and/or to the chemical effect of carbon in the NiO-CeO₂ interaction. The selectivity towards CH₄ formation of all catalysts is very high (~98% at 300 °C). The most effective utilization of ceria is obtained in the 25%NiO/CeO₂-75%NiO/C catalyst. In this sense, a promising catalyst with a high catalytic activity for the CO₂ methanation has been obtained incorporating carbon as part of the support and using only 25% of the NiO/CeO₂ component.

[Chapter 7](#) presents the successful utilization of the novel NiO-CeO₂ catalyst consisting of high surface area mixed oxide nanoparticles as a promising material for the dry reforming of methane (DRM) reaction. These nanoparticles showed catalytic stability during 5 hours under the severe conditions of the reaction (700 °C), and improved carbon resistance with regard to a counterpart NiO-CeO₂ mixed oxide prepared without control of the size. Both the novel nanoparticles and the reference catalyst present high activity and selectivity for DRM, almost reaching the conversion and ratio of products predicted by thermodynamics for the experimental conditions used. Nevertheless, the novel nanoparticles reduced by 63% the accumulation of carbon

Chapter 0

during the DRM tests. XPS and H₂-TPR suggest that the improved carbon resistance of the nanoparticles is related to the better interaction and cooperation between NiO and CeO₂ mixed phases. In the novel nanoparticles, the participation of cerium cations in the redox processes taking place during DRM seems to stabilize cationic species of nickel. On the contrary, the catalyst prepared without control of the size suffered certain segregation of Ni during DRM reaction (while not the novel nanoparticles), and the presence of segregated Ni would be responsible of the higher catalytic formation of carbon.

The results of this chapter have been published in:

A. Cárdenas-Arenas, E. Bailón-García, D. Lozano-Castelló, P. Da Costa, A. Bueno-López. *Stable NiO-CeO₂ nanoparticles with improved carbon resistance for methane dry reforming*, J. Rare Earths (in press).

Finally, [Chapter 8](#), compiles the most relevant conclusions of this Doctoral Thesis.



Universitat d'Alacant
Universidad de Alicante

Introducción y objetivos

- 1.1. Problemática ambiental**
- 1.2. Valorización de CO₂**
 - 1.2.1. Proceso Power-to-Gas
 - 1.2.2. Producción de gas de síntesis
- 1.3. Metanación de CO₂**
 - 1.3.1. Mecanismo de reacción de la metanación de CO₂
 - 1.3.2. Desarrollo de catalizadores para la reacción de metanación de CO₂
- 1.4. Reformado seco de metano**
 - 1.4.1. Mecanismo de reacción para el reformado seco de metano
 - 1.4.2. Desarrollo de catalizadores para el reformado seco de metano
- 1.5. Influencia de la morfología de los catalizadores en sus propiedades catalíticas**
 - 1.5.1. Sólidos Macroporosos con orden tridimensional (3DOM; Three Dimensionally Ordered Macroporous Solids)
 - 1.5.2. Nanopartículas
- 1.6. Objetivos**
- 1.7. Referencias**

1.1. Problemática ambiental

El cambio climático hace referencia a una variación de los patrones del clima durante un periodo prolongado. El cambio climático puede producirse por procesos internos naturales de la Tierra y el Sistema Solar o por factores externos como la actividad humana [1]. La comunidad científica afirma que el planeta se está calentando, y los factores climáticos naturales no pueden explicar por si solos esta tendencia. Las actividades humanas, especialmente el uso de combustibles fósiles como fuente de energía dominante, ha producido un incremento de la concentración de gases de efecto invernadero en la atmósfera. La Figura 1.1. muestra la contribución porcentual de las emisiones de gases de efecto invernadero en la UE por sectores en el año 2017, donde destaca la contribución de los procesos de obtención y utilización de la energía [2].

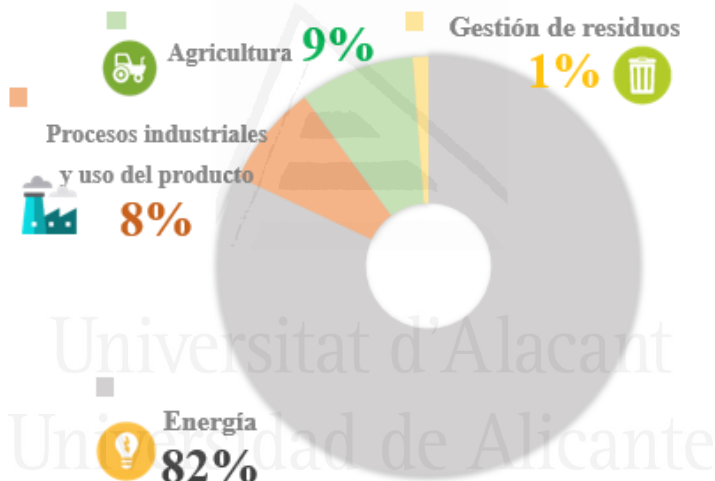


Figura 1.1. Emisiones de gases de efecto invernadero en la UE por sector en 2017 [3].

Los gases de efecto invernadero son aquellos que absorben la radiación infrarroja en la atmósfera, atrapando el calor y calentando la superficie de la tierra. Sin el efecto invernadero natural, la temperatura global promedio de la tierra sería mucho más fría y la vida en la Tierra sería imposible [3]. Las actividades humanas están cambiando el efecto invernadero natural de la Tierra. La acumulación de estos gases en la atmósfera y, por tanto, el aumento de la temperatura del planeta, ya se evidencia en el aumento de la temperatura del aire y los océanos, el aumento de los niveles de mar producido por el

derretimiento de hielos y glaciares de todo el mundo, los eventos climáticos extremos como las inundaciones, sequías, tormentas y olas de calor [2–6].

Los principales gases implicados en el efecto invernadero son el dióxido de carbono (CO_2), metano (CH_4), óxido nitroso (N_2O) y gases fluorados, de los cuales el CO_2 aporta aproximadamente el 81% del total de gases efecto invernadero emitidos en el mundo (Figura 1.2.) [4]. El CO_2 está presente naturalmente en la atmósfera como parte del ciclo de carbono de la Tierra (la circulación natural del carbono entre la atmósfera, los océanos, el suelo, las plantas y los animales) [6]. Las actividades humanas están alterando el ciclo del carbono, debido al aumento de las emisiones de CO_2 que se ha presentado desde la revolución industrial. En la Figura 1.3. se evidencia el aumento de los niveles de CO_2 atmosférico basado en la comparación de muestras atmosféricas contenidas en núcleos de hielo y mediciones directas más recientes. En el 2013, por primera vez en la historia de la humanidad, el nivel diario de dióxido de carbono en la atmósfera superó las 400 partes por millón y, a pesar de la creciente concienciación acerca del cambio climático, las emisiones de gases de efecto invernadero siguen aumentando [5].

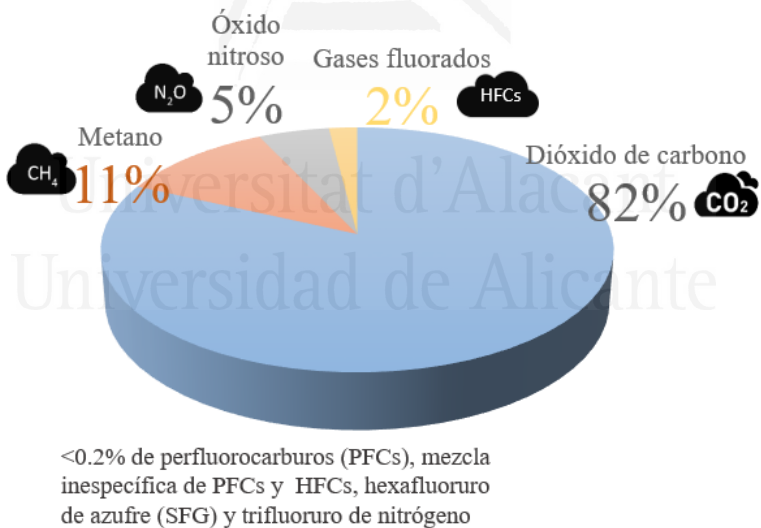


Figura 1.2. Emisiones atmosféricas mundiales de gases de efecto invernadero por contaminante en 2017 [4].

La problemática del cambio climático se debe abordar desde dos perspectivas, las cuales implican una adaptación al cambio climático ya existente y la realización de procesos de mitigación que reduzcan las emisiones, con el fin de estabilizar los niveles

de gases de efecto invernadero presentes en la atmósfera. En la 21^a Conferencia de las Naciones Unidas Sobre el Cambio Climático en París en 2015, acuerdo COP21 [7], se establece una ruta para disminuir las emisiones de CO₂ lo suficiente como para limitar el aumento de la temperatura global por debajo de los 2 °C. En este sentido, la ciencia juega un papel muy importante debido a que tiene la ardua tarea de renovar y optimizar los procesos industriales, ahora contaminantes, transformándolos en procesos respetuosos con el medio ambiente. Los desafíos ambientales de las emisiones de CO₂ se enfocan en las tecnologías de captura y utilización de CO₂ tanto para la producción de combustibles como para la producción combinada de calor y energía.



Figura 1.3. Concentraciones globales de CO₂ en la atmósfera en partes por millón (ppm) durante los últimos 800.000 años [8]. Gráfico de NOAA Climate.gov basado en datos del Programa de Paleoclimatología de NOAA NCEI.

La captura y secuestro de CO₂ (CCS) es un conjunto de tecnologías que pueden reducir en gran medida las emisiones de CO₂ producidas por el uso de combustibles fósiles en procesos como generación de electricidad y procesos industriales, evitando que el CO₂ sea emitido a la atmósfera [9,10]. El CO₂ puede capturarse de diversas fuentes dependiendo de su presión parcial, las condiciones de funcionamiento y la

composición de la mezcla de gases, utilizando aplicaciones de captura previa o posterior a la combustión, así como la captura directa desde el aire [11]. El dióxido de carbono puede estar disponible en todos los procesos de combustión, siendo el producto principal. Una vez ocurrida la combustión, la captura de los gases de combustión puede realizarse mediante distintas tecnologías que se basan en métodos biológicos, físicos, químicos y combinaciones de estos. Sin embargo, las tecnologías CCS aún enfrentan varios desafíos técnicos y económicos.

Se están estudiando muchos otros enfoques para utilizar el CO₂, y ya se usa en una variedad de sectores y procesos, en los que se incluyen la producción de hidrógeno, la producción de gas natural sintético y la producción de metanol entre otros [12–15]. El gran número de tecnologías implicadas en el uso del CO₂ ofrece una gran variedad de oportunidades para la innovación industrial permitiendo a las empresas que aumenten el uso de prácticas sostenibles. Se espera que los proyectos de captura y utilización de CO₂, junto con los de captura y almacenamiento de CO₂, produzcan ingresos favorables en las economías en desarrollo, liberando parte de la presión sobre los costos y la reducción de la energía, apuntando a productos de valor agregado que crean empleos y beneficios económicos [16]. En 2018, la Iniciativa Global de CO₂ presentó un mercado anual de productos a base de CO₂ de 0,8 a 1,1 billones de dólares a través del uso de más del 10% de las emisiones globales anuales de CO₂.

Además, es importante tener en cuenta que los gobiernos están impulsando las investigaciones sobre el uso de CO₂. Por ejemplo, en Europa, en el marco del programa Horizonte 2020, la comisión europea ha abierto varias convocatorias en donde se apoya la investigación sobre la utilización de CO₂ como un enfoque viable para la producción sostenible de combustibles, productos químicos e intermedios [17]. Teniendo en cuenta lo anterior, en este trabajo de investigación se ha explorado la utilización de CO₂ para convertirlo en productos de alto valor a la vez que reduce las emisiones de CO₂ a la atmósfera.

1.2. Valorización del CO₂

Hoy en día, la problemática asociada al cambio climático es posiblemente el tema en materia de política ambiental más desafiante que enfrentan los gobiernos y los investigadores de todo el mundo. Para disminuir las emisiones de CO₂ a la atmósfera se han planteado varias opciones, como lo son mejorar la eficiencia de los procesos de conversión de energía y así disminuir el consumo energético y utilizar fuentes de energías renovables o combustibles con menos carga de carbono. Sin embargo, estas opciones pueden no ser suficientes para mitigar el calentamiento global, por lo que se

han propuesto las tecnologías de captura, almacenamiento y utilización de CO₂ como soluciones a medio plazo para mitigar los impactos ambientales a la vez que permite seguir haciendo uso de los combustibles fósiles hasta que las tecnologías de energía renovable estén listas para su aplicación [18].

El CO₂ capturado puede almacenarse en formaciones geológicas, también conocidas como almacenamiento geológico, o en los océanos. La primera representa una opción más viable, ya que se tiene un conocimiento más amplio acerca de las propiedades de los yacimientos agotados de petróleo y gas, mientras que, por el contrario, no está claro cómo el almacenamiento de CO₂ en los océanos afectaría la acidez y las especies marinas. Por otra parte, el CO₂ se puede usar directamente en diferentes sectores industriales, incluidos los alimentos y bebidas así como la industria farmacéutica, o se puede convertir en productos de alta demanda comercial como urea, metanol y biocombustibles [19].

En el mundo actual, con alta demanda energética, un enfoque que es muy prometedor para reducir las emisiones de gases de efecto invernadero es la captura y utilización del CO₂ (CCU). Bajo este concepto, el CO₂ se capturaría de grandes fuentes puntuales como plantas de energía, y luego se utilizaría como materia prima en la síntesis de productos químicos y combustibles, al tiempo que contribuye a mitigar el cambio climático [12,13,20,21]. Una de las ventajas que tiene la tecnología CCU es que la utilización del CO₂ es una actividad donde los productos se pueden vender. Además, el CO₂ tiene la ventaja de ser un recurso “renovable” si se cierra el ciclo de emisión-recuperación-reutilización.

El CO₂ se utiliza en diversos sectores como el sector químico, petrolero y energético, así como en el sector alimentario, farmacéutico y en la industria del acero, entre otros. Se puede utilizar de manera directa como, por ejemplo, en la industria de alimentos y bebidas donde se usa comúnmente como agente carbonatante, conservante, como gas de envasado y como disolvente para la extracción de sabores y en el proceso de descafeinado [22,23]. De manera directa, también es utilizado en la extracción de petróleo crudo de campos petroleros (EOR) [24] y en la extracción de gas natural de depósitos de carbón (ECBM) [25]. El mayor potencial en el uso de CO₂ se centra en la industria química y petrolera, en la producción de urea, el procesamiento de polímeros, así como la síntesis de combustibles y químicos como el metanol y el ácido fórmico [26–32].

Este trabajo de investigación se centra en la utilización del CO₂ en el sector energético y de combustibles, específicamente en el proceso Power-to-Gas y en la producción de *gas de síntesis*. El proceso Power-to-Gas es una posibilidad prometedora que permite utilizar la energía excedente para producir metano a partir de hidrógeno y

CO_2 acoplando la hidrólisis del agua con la reacción de metanación de CO o de CO_2 . El metano producido puede almacenarse y transportarse a través de la infraestructura de gas natural ya existente, y es una opción viable para el almacenamiento de energía renovable. Por su parte, la producción de gas de síntesis ($\text{CO} + \text{H}_2$), como materia prima, es un objetivo futuro valioso dada la inminente disminución de los recursos de petróleo. La producción de gas de síntesis mediante el reformado seco de metano permite utilizar dos gases de efecto invernadero, el CO_2 y el CH_4 , para producir una mezcla de $\text{CO} + \text{H}_2$ que puede usarse en la síntesis de Fischer-Tropsch o en sistemas de transmisión de energía química.

En resumen, el aprovechamiento del CO_2 y la posibilidad de disponer de hidrógeno como vector energético abrirán nuevas vías a la gestión de los combustibles del futuro permitiendo cerrar un ciclo virtuoso producido en la combustión de los combustibles fósiles. El hidrógeno permite completar el proceso para generar combustibles sintéticos y los combustibles sintéticos producen el CO_2 necesario para volverlos a generar utilizando el hidrógeno como portador. Si la única fuente de energía del proceso la aportan fuentes renovables se trataría de un proceso limpio, pudiendo ser una forma de utilización de energía en el futuro: renovables + gas natural sintético.

1.2.1. Proceso Power-to-Gas

El desarrollo de las tecnologías de producción de energía a partir de fuentes renovables está aumentando. En un escenario de utilización masiva de estas energías renovables podría haber momentos de exceso de producción de energía que no puede volcarse a la red eléctrica si la demanda es menor. Esto da como resultado la necesidad de soluciones de almacenamiento de energía a largo plazo y a grandes escalas [33]. Para lograr esto, la unión de la electricidad renovable producida y el reciclaje de CO_2 como materia prima para la producción de combustibles y productos químicos es un enfoque prometedor que conduce a una economía circular neutra de CO_2 y al almacenamiento exitoso de energía renovable [34–36].

El uso de CO_2 como fuente de carbono ofrece la posibilidad de reemplazar el gas natural o los compuestos de la refinación de petróleo, evitando así las emisiones de CO_2 procedente de fuentes fósiles. Las fuentes potenciales de CO_2 concentrado son las instalaciones de biogás, la combustión de biomasa o la gasificación y los gases de escape de los altos hornos [37]. Como se ve, la disponibilidad de CO_2 es alta y el CO_2 puede separarse directamente después de su formación en los diferentes procesos industriales.

La Figura 1.4. muestra diversas aplicaciones de conversión de CO_2 combinada con hidrógeno producido en un proceso Power-to-Gas. El metano es el hidrocarburo

gaseoso más común y el componente principal del Gas Natural Sintético (SNG), pero además del metano, el CO₂ puede convertirse en otros hidrocarburos como metanol, etanol, dimetiléter o ácido fórmico. Los productos de la hidrogenación de CO₂, tales como metanol y dimetiléter son combustibles extraordinarios para motores de combustión interna, y además fáciles de almacenar y transportar. Aunque la producción de metanol y DME desde CO₂ son procesos prometedores, necesitan realizarse a elevadas presiones (~5 MPa) [27,28,38,39]. Como ejemplo avanzado de este tipo de tecnologías, la empresa canadiense Carbon Engineering ha ejecutado un proyecto a nivel de planta piloto en el que se ha estudiado un proceso de captura directa de aire para la extracción de CO₂ del aire para ser utilizado en la producción de combustible sintético. El costo del proceso se ha estimado por debajo de \$100 USD por tonelada [40].

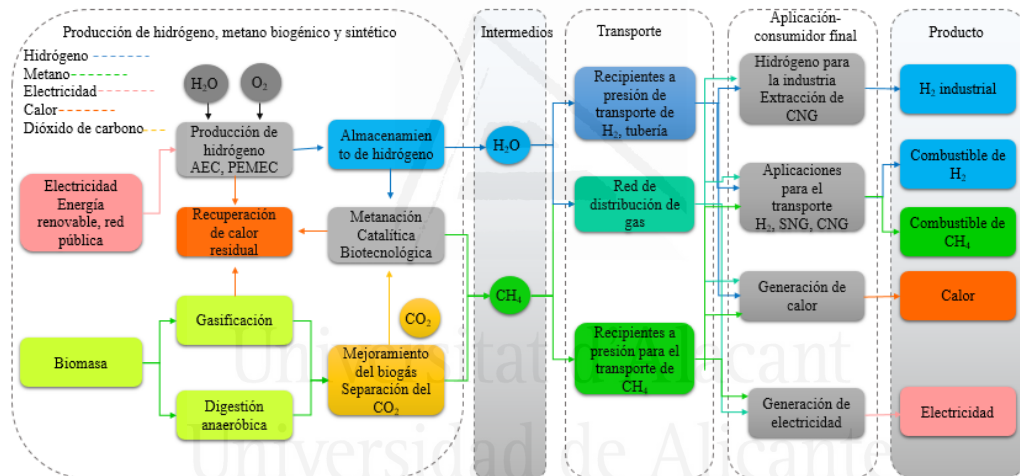


Figura 1.4. Vías de aplicación para la producción de hidrógeno, metano biogénico y sintético mediante el proceso Power-to-Gas.

El proceso Power-to-Gas es un proceso que implica tres pasos, la generación de electricidad a partir de fuentes renovables, la producción de H₂ a partir de un exceso de energía eléctrica renovable mediante la electrólisis del agua y el uso del H₂ renovable producido en la conversión del CO₂ a metano mediante la reacción de metanación de CO₂, también llamada reacción de Sabatier. Una vez producido el metano es introducido a la red de gas natural ya existente (Figura 1.5.) [41]. De esta manera se puede utilizar de manera fácil en todas las instalaciones de gas natural establecidas para la generación de calor en los hogares, para el transporte y para estabilizar la red eléctrica en plantas

de energía a gas, o como materia prima para la fabricación de otros productos químicos. En el futuro, la conversión fotocatalítica de CO_2 y H_2O podría ser una alternativa interesante a la cadena del proceso Power-to-Gas [42–44].

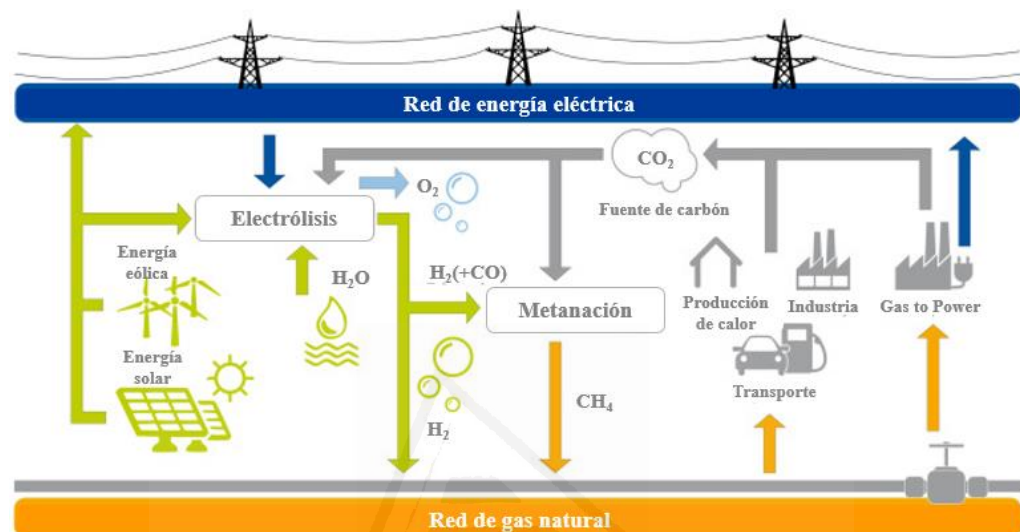


Figura 1.5. Proceso Power-to-Gas donde se une la red de energía eléctrica con la red de gas natural y permite el almacenamiento de energía renovable en forma de metano, formando el ciclo cerrado del carbono mediante el uso de CO_2 como materia prima.

Actualmente, la tecnología de electrólisis comercial se basa en electrolizadores alcalinos, los cuales tienen una eficiencia que varía del 48 al 83% [45]. Además, se están desarrollando otras dos tecnologías para la electrólisis, los electrolizadores de membrana polimérica de intercambio de protones (PEM) y las células de electrolizadores de óxido sólido (SOEC). Los electrolizadores SOEC parecen tener el mayor potencial de eficiencia (más del 73% de potencia a hidrógeno), mejores costos de inversión y capacidad de producción, así como la capacidad potencial de mantener la eficiencia a cargas más bajas [46]. SOEC es un electrolizador de alta temperatura y, por lo tanto, necesita vapor, pero esta demanda de calor puede integrarse en la mayoría de los procesos utilizando calor excedente de, por ejemplo, la metanación. El proceso Sabatier es exotérmico y produce un exceso de calor que, por ejemplo, puede usarse para calentar el electrolizador utilizado para producir el hidrógeno [47].

La integración de procesos y la coproducción son importantes para la eficiencia energética y de recursos. Por lo tanto, dado estos desarrollos, el impulso de la economía

del H₂, y la urgencia de mitigar las emisiones de gases de efecto invernadero, parece necesario abordar más a fondo la aplicación del reciclaje del CO₂ de las diferentes fuentes emisoras. Es por eso que este trabajo de investigación ha sido enfocado en la metanación catalítica de CO₂, la cual será explicada detalladamente más adelante.

1.2.2. Producción de gas de síntesis

Gas de síntesis o Syngas, es una mezcla de gases que consiste principalmente en hidrógeno, monóxido de carbono y muy a menudo algo de dióxido de carbono. El gas de síntesis se puede producir a partir de varias materias primas como el gas natural, el carbón, hidrocarburos de diferente naturaleza o biomasa, mediante un proceso de gasificación por reacción habitualmente con vapor de agua o con oxígeno (Figura 1.6.) [48–50]. El Syngas es una materia prima de gran valor para la industria petroquímica, dado a que es muy importante en los procesos de producción de combustibles líquidos a gran escala. Además, el gas de síntesis puede ser convertido en metanol y dimetiléter a través de procesos catalíticos, transformarlo en etanol o alcoholes superiores por medio de la fermentación, o usarlo en la síntesis Fischer Tropsch (FTS) para la producción de gasolina y diésel [51].

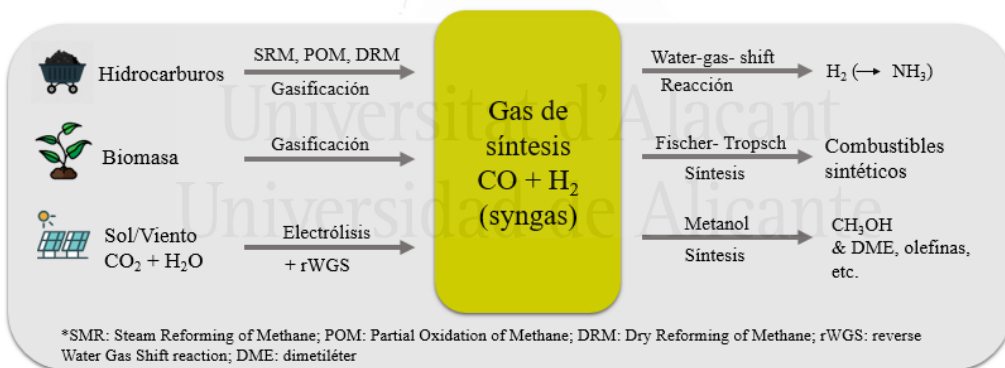


Figura 1.6. Productos obtenidos a partir del gas de síntesis.

El método que se elija depende de la economía de la materia prima y su disponibilidad [52]. Al manipular el proceso de reformado, se puede optimizar la proporción de H₂/CO presente en el gas de síntesis y en este sentido se puede producir, por ejemplo, H₂ de alta pureza para ser utilizado como combustible limpio para el transporte. Debido a su alto valor de calentamiento y bajo impacto ambiental, el hidrógeno ha recibido un gran interés por las aplicaciones de combustible. Puede

reaccionar con oxígeno para generar electricidad en una celda de combustible o quemarse en un motor de combustión interna para proporcionar energía a los vehículos [53]. A continuación, se explicarán los principales métodos utilizados para producir hidrógeno a partir de metano.

❖ *Reformado de metano con vapor de agua:*

El reformado de metano con vapor de agua (SRM; del inglés, Steam Reforming of Methane) es ampliamente usado en el mundo en la producción de H₂. El SRM es una reacción endotérmica, que se da a temperaturas muy altas (700-1000 °C) y utiliza metano y vapor de agua para producir hidrógeno y monóxido de carbono:



El CO formado puede reaccionar aún más con el vapor de agua mediante la reacción de Water-Gas shift (WGS)



para producir hidrógeno adicional y dióxido de carbono.

Para obtener una alta conversión de H₂ mediante SRM se puede reducir la temperatura de WGS (ésta ocurre entre 150-400 °C) o se puede agregar un exceso de vapor [54].

❖ *Reformado por oxidación parcial de metano:*

El reformado por oxidación parcial de metano (POM; del inglés, Partial Oxidation of Methane) se produce mediante la oxidación parcial del metano usando oxígeno o aire para producir hidrógeno y monóxido de carbono



POM es una reacción exotérmica y puede ser combinada con el reformado en seco o el reformado a vapor para proporcionar calor. La combinación de SRM y POM se conoce como reformado autotérmico (ATR; del inglés, Auto-Thermal Reforming), el cual también es usado para la producción de hidrógeno [55].

❖ *Reformado seco de metano:*

El reformado seco de metano (DRM; del inglés, Dry Reforming of Methane) se produce por la reacción de dos moléculas estables, el CH₄ y el CO₂, para producir gas de síntesis:



El DRM se da a temperaturas altas, entre 700 – 900 °C y es una reacción altamente endotérmica, por lo que es necesario el uso de catalizadores. El gas de síntesis producido por DRM tiene una relación teórica de H₂/CO = 1, que se prefiere para la producción de hidrocarburos por medio de la síntesis de Fischer-Tropsch. El DRM suele ir acompañado de varias reacciones secundarias, especialmente el craqueo de CH₄, la reacción de Boudouard y la reacción inversa de Water-Gas shift [55,56].

Hasta ahora, el reformado de hidrocarburos con vapor, en especial, el reformado de metano con vapor de agua ha sido la forma más utilizada y económica de producir hidrógeno y gas de síntesis. Sin embargo, produce gas de síntesis con una relación alta de H₂/CO, lo cual no es adecuado para la producción de metanol y la síntesis de Fischer-Tropsch. El sistema de reformado autotérmico apunta a la oxidación exotérmica de metano con oxígeno. Sin embargo, el uso de oxígeno puro supone una serie de inconvenientes técnicos y económicos que hace que el proceso sea inviable a nivel industrial. La oxidación parcial o total de metano usando O₂ es en todos los casos exotérmica. Sin embargo, el impacto económico de utilizar sólo oxígeno puede conducir a utilizar CO₂ o H₂O en el proceso lo cual afectaría la relación H₂/CO del gas de salida. Por su parte, el reformado seco de metano, aunque es una reacción más endotérmica que el reformado de metano con vapor de agua produce una relación baja de H₂/CO, lo que permite su aplicación en la síntesis de Fischer-Tropsch [56,57].

En resumen, el reformado de metano con vapor de agua y el reformado autotérmico se usan ampliamente para la producción de hidrógeno, mientras que el reformado seco y el reformado oxidativo parcial proporcionan materiales de partida para la síntesis de Fischer-Tropsch. En este trabajo de tesis se ha estudiado el DRM como una alternativa interesante para revalorizar dos gases de efecto invernadero, el CH₄ y el CO₂, y de esta forma contribuir a los esfuerzos que se vienen adelantando en la lucha contra el cambio climático, por lo que se explicará ampliamente más adelante.

1.3. Metanación de CO₂

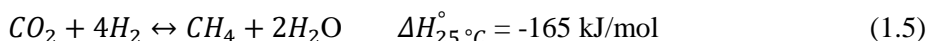
Tal y como se ha comentado en las secciones anteriores, la creciente crisis ambiental, los recursos limitados del petróleo y el gas natural, así como la creciente demanda de energía, nos obligan a buscar energías alternativas cada vez más eficientes y más amigables con el medio ambiente. El hidrógeno se considera un portador de energía prometedor [53]. Sin embargo, existen varios problemas inherentes a la utilización de H₂, desde su transporte hasta su distribución. La transformación de la

molécula de H₂ en un compuesto que contiene carbono ofrecerá la posibilidad de utilizar la infraestructura de la red de transporte de gas natural. La hidrogenación del CO₂ puede producir metanol, ácido fórmico o metano, dependiendo de las condiciones de operación [58].

La reacción de hidrogenación de CO₂ para producir CH₄ recibe el nombre de reacción de metanación o reacción de Sabatier y fue descubierta hace aproximadamente un siglo. En sus inicios se utilizó para eliminar rastros de óxidos de carbono del gas de alimentación en la síntesis de amoniaco [59]. Recientemente, los científicos han mostrado un renovado interés por su utilización como una ruta potencial para producir gas natural sintético a partir de las emisiones de CO₂ mediante el proceso Power-to-Gas [35] y en la valorización del biogás [60]. La metanación no sólo se utiliza en el proceso Power-to-Gas, sino que también se utiliza en otras aplicaciones comunes que incluyen la eliminación de CO y CO₂ de las corrientes de H₂ utilizadas en las pilas de combustible [61], purificación de H₂ utilizado en la fabricación de amoniaco [62], en la eliminación de CO₂ de espacios confinados como submarinos y naves espaciales, en la síntesis de propulsores para naves espaciales [63] y en detectores de cromatografía de gases (GC) que convierten el CO y el CO₂ en metano para mejorar la sensibilidad, entre otras.

Una de las aplicaciones interesantes de esta reacción es su uso en la NASA como una forma complementaria para intentar resolver los problemas de abastecimiento de agua en las estaciones espaciales, y su desarrollo se considera un elemento clave para el éxito de las futuras misiones espaciales a Marte [64]. A partir del CO₂ generado en la respiración y haciéndolo reaccionar con hidrógeno podrían producir agua y metano. El agua tiene un doble uso en las estaciones espaciales, como bebida de los astronautas y como elemento primario de un ciclo de electrólisis para producir oxígeno para la respiración. Es más fácil enviar hidrógeno comprimido al espacio que agua, que no es compresible, y en la cadena de reacciones, el oxígeno se convertiría en un portador que pasaría del agua al dióxido de carbono y de éste al agua, creando un ciclo cerrado. Adicionalmente, la agencia espacial está analizando el ciclo Bosch que mediante pirolisis convierte el metano en carbono e hidrógeno con lo que este último podría cerrar, como el oxígeno, un ciclo por completo. Sin duda, los avances de la NASA en la mejora de estas reacciones tendrán repercusiones inmediatas también en sus aplicaciones con fines energéticos.

La metanación de CO₂ es una reacción exotérmica en la cual el H₂ reacciona con el CO₂ para producir CH₄ y H₂O.



Teóricamente, la reacción de metanación de CO₂ ocurre a bajas temperaturas, donde la conversión del CO₂ y la selectividad a CH₄ alcanzan valores cerca del 100%. El aumento de la temperatura aumenta la velocidad de reacción haciendo favorable la reacción WGS inversa (RWGS) cuando se superan los 500 °C por lo que la reacción de metanación de CO₂ suele estudiarse por debajo de esta temperatura [65–67]. Por lo tanto, el control de la temperatura es muy importante ya que al ser una reacción exotérmica se producirá un aumento de la temperatura, que puede generar sinterización, y aumento en la deposición de carbono en el catalizador y, por tanto, su desactivación. Aunque la reacción de Sabatier es exotérmica, tiene limitaciones cinéticas generadas por la alta estabilidad de los gases reactivos, lo que hace necesario un catalizador para acelerar la reacción hasta valores con relevancia práctica para la aplicación industrial [68].

1.3.1. Mecanismo de reacción de la metanación de CO₂

La metanación de CO₂ se lleva a cabo de forma catalítica y, dependiendo del catalizador utilizado y las condiciones generales de reacción, el producto principal de la reacción puede ser CO o CH₄. Aunque es una reacción simple, su mecanismo de reacción ha sido difícil de establecer y se han propuesto algunas opiniones controvertidas al respecto. Las vías de reacción de la metanación de CO₂ se dividen en dos categorías principales, la metanación de CO₂ a metano mediante la formación de CO como principal intermedio o la metanación de CO₂ por reacción directa de CO₂ a metano. Una primera propuesta es un mecanismo en el cual se produce la conversión de CO₂ a CO mediante la reacción inversa de Water-Gas shift y su posterior reacción a CH₄ a través de la metanación de CO. Alternativamente, se puede formar CO mediante la adsorción dissociativa de CO₂ sobre el catalizador. La segunda propuesta es la metanación de CO₂ directa, en la cual el CO₂ se quimisorbe molecularmente con el H₂ para producir formiatos como los principales intermedios de reacción, que posteriormente se hidrogenan a CH₄. Generalmente, se acepta que en la mayoría de catalizadores utilizados en la metanación de CO₂ producen CO como principal intermedio.

1.3.1.1. Mecanismo por formación de CO como intermedio principal

El mecanismo más ampliamente aceptado en la reacción de metanación de CO₂ es la combinación de la reacción exotérmica de metanación de CO (Ecuación 1.1), y la reacción WGS (Ecuación 1.2), la cual es endotérmica.

Esto significa que después de la adsorción y disociación de CO₂ en la superficie del catalizador, la metanación de CO₂ continúa por la misma ruta que la metanación de

CO. Cabe señalar que el agua como producto secundario puede tener un efecto negativo en la reacción de metanación. La eliminación de agua de los centros de reacción es crítica para aumentar el rendimiento de reacción de CH₄ y minimizar la liberación de CO como producto secundario.

Este mecanismo puede implicar dos rutas, que el CO₂ se disocie directamente en carbonilo CO_{ad} y O_{ad} y posteriormente se hidrogene, o que una vez disociado se disocie aún más para formar C_{ad} y O_{ad} (Ecuación 1.6) [65,69].



Los siguientes pasos corresponderían a la hidrogenación a metano del carbono adsorbido y de los intermedios de carbono (Ecuaciones 1.7 – 1.11) y la hidrogenación a agua del oxígeno adsorbido (Ecuaciones 1.12 – 1.14).



Este mecanismo fue modificado posteriormente por Coenen y colaboradores, quien había planteado inicialmente un mecanismo que implicaba la adsorción disociativa de H₂ y CO y la hidrogenación gradual de H_{2,ad} y CO_{ad} descrito por las ecuaciones anteriores. En el nuevo estudio [70], realizado con gases marcados isotópicamente plantearon un nuevo mecanismo el cual relaciona la disociación asistida por hidrógeno del CO_{ad} con la formación de C_{ad} teniendo COH_{ad} como un intermedio de reacción. Así mismo se propuso que el paso determinante de la velocidad puede ser la disociación de CO mediante la Ecuación 1.6 o la disociación del COH_{ad}. Esta última hipótesis plantea dos nuevas reacciones (Ecuación 1.15 y 1.16).



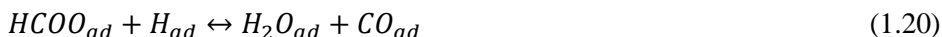
Cabe señalar que incluso cuando la metanación de CO₂ ocurre a través de la formación de CO, no significa necesariamente que la formación de CO deba proceder a través de la reacción inversa de Water-Gas shift. El estudio realizado por Jacquemin y col. [71] sobre catalizadores de Rh/γ-Al₂O₃ determinó que el primer paso en la metanación de CO₂ es la adsorción disociativa del CO₂ para formar CO_{ad} y O_{ad} en la superficie del catalizador, mediante la Ecuación 1.17.



Cabe señalar que todavía hay opiniones diferentes sobre la naturaleza del proceso intermedio y el proceso de formación de metano, donde tanto el metal como el soporte juegan un papel importante en el mecanismo de reacción de metanación. Además de lo expuesto anteriormente, se propone un mecanismo de reacción que incluye la formación del formiato mediante una especie de carbonato. Aziz y col. [72] llevaron a cabo la metanación sobre una variedad de metales (incluidos Ni, Cu, Rh y Ru) soportados en nanopartículas de sílice mesoestructurada (MSN) y determinaron que cuando se depositaba el metal en el soporte MSN la metanación de CO₂ procedía mediante la formación del intermedio CO. Así, el CO₂ y el H₂ se adsorben y disocian en los sitios activos metálicos que forman CO_{ad}, O_{ad} y H_{ad}, y las especies formadas luego migran a la superficie de MSN, donde CO_{ad} interactúa con las superficies de óxido del soporte para formar especies carbonilo, mientras que la presencia de H facilita la formación de formiato bidentado. Tanto las especies de carbonilo como las de formiato podrían ser las responsables de la formación del metano. Sin embargo, estas últimas podrían ser la ruta principal las cuales en presencia del átomo de H_{ad} forman metano.

1.3.1.2. Mecanismo por formación de formiato como intermedio principal

En este mecanismo se sugiere la formación de especies de formiato como intermedio principal mediante las Ecuaciones 1.18 y 1.19 y se justifica la presencia de CO mediante la Ecuación 1.20.



Como ejemplo de este mecanismo de reacción, Pan y col. [73] estudiaron la metanación de CO₂ en catalizadores de níquel soportado en ceria y zirconia (Ni/Ce_{0.5}Zr_{0.5}O₂) donde observaron que los principales intermedios de reacción de la

metanación fueron las especies de formiato. Se cree que estas especies de formiatos podrían derivar de la hidrogenación de carbonatos formados en sitios activos del soporte, oxígeno en la superficie y vacantes de oxígeno en superficie de la ceria o la zirconia, así como de los sitios superficiales de hidroxilo. Se detectaron cantidades menores de CO el cual se consideró solo como un subproducto de la reacción y de ninguna manera como un intermedio.

1.3.2. Desarrollo de catalizadores para la reacción de metanación de CO₂

A lo largo del tiempo se han desarrollado catalizadores para la reacción de metanación de CO₂, fundamentalmente de níquel o rutenio sobre alúmina, relativamente activos en condiciones sencillas de proceso. Sin embargo, se ha renovado el interés de desarrollar catalizadores activos a temperaturas más bajas, así como de mejorar las condiciones de operación de la reacción (presión y temperatura) y los reactores en los que se realiza. También se están abordando otros aspectos como la necesidad de arranques y paradas rápidos, la mejora de la resistencia a la desactivación de los catalizadores debido a estos modos rápidos de ciclado, la reversibilidad y exotermicidad de la reacción, y la necesidad de su integración en microrreactores [58,67].

Los sistemas catalíticos para la metanación de CO₂ consisten en metales preciosos como Ru [74], Rh [75] y Pd [76] y metales de transición como el Ni [77–79] soportados en diversos óxidos (Al₂O₃, TiO₂, SiO₂, ZrO₂ y CeO₂). El Ru es más activo que el Ni, lo que resulta de utilidad cuando se desea llevar a cabo la reacción a baja temperatura (aprox. 200 °C) [80]. Sin embargo, el Ni tiene una buena relación entre la alta actividad catalítica y el bajo precio, por los que suele ser la opción preferida para acelerar la reacción, trabajándose a temperaturas algo superiores (> 300 °C) [67,77,81], además de tener una alta selectividad a metano.

Teniendo en cuenta que los catalizadores basados en Ni son la mejor opción desde un punto de vista comercial y que la actividad de estos catalizadores dependen en gran medida de varios parámetros como el soporte sobre el cual se deposita, el método de síntesis, el tamaño de partícula, entre otros [82], en esta tesis se ha querido estudiar la influencia del soporte en el mecanismo de reacción de la metanación de CO₂ en catalizadores basados en Ni. Además, se ha investigado sobre cómo afecta el método de incorporación del Ni a la estructura del soporte a las propiedades físico-químicas y catalíticas, y el comportamiento catalítico y estabilidad de nanopartículas basadas en Ni en condiciones de reacción en la metanación de CO₂.

Se han estudiado diversos soportes para depositar tanto Ni como Ru con el fin de catalizar la hidrogenación de CO₂ en CH₄, como por ejemplo TiO₂ [80,83], SiO₂ [84],

Al_2O_3 [31,85], La_2O_3 [86], CeO_2 [87–89], ZrO_2 [90], $\text{Ce}_x\text{Zr}_{1-x}\text{O}_2$ [91]. En general, lo que se espera de un soporte para el caso de esta reacción es que permita dispersar bien las partículas metálicas depositadas, que evite que estas sintericen durante la reacción, que no forme compuestos estables con los metales depositados que lleven a su desactivación y que favorezcan la quimisorción de CO_2 , así como la desorción de los productos de reacción (principalmente del H_2O). El soporte de CeO_2 es prometedor para la reacción de metanación debido a sus propiedades redox donde coexisten especies de $\text{Ce}^{4+}/\text{Ce}^{3+}$ y su capacidad de almacenar oxígeno, lo cual puede mejorar la actividad catalítica [88,89,92]. Además, la interacción entre los óxidos basados en Ni y ceria puede inhibir la sinterización del Ni [88].

En nuestro grupo de investigación se ha estudiado ampliamente y empleado satisfactoriamente el CeO_2 como catalizador para la combustión de hollín y la oxidación de CO [93–97] entre otras reacciones. Además, previamente se realizó un estudio aplicado a la metanación de CO_2 utilizando catalizadores de Ni soportados en LnO_x ($\text{Ln}=\text{La, Ce y Pr}$) donde el catalizador Ni/ CeO_2 fue el catalizador que tuvo un mejor comportamiento catalítico. Debido a estos resultados y a los conocimientos previos sobre las propiedades físico-químicas del CeO_2 que han servido como soporte y punto de partida en este trabajo de tesis se ha profundizado en el estudio de catalizadores basados en Ni- CeO_2 para su aplicación en la reacción de metanación de CO_2 .

El enfoque en el desarrollo de catalizadores óptimos para la reacción de metanación de CO_2 está orientado hacia la modificación del soporte, la adición de promotores y la utilización de nuevos materiales. Dada la poca disponibilidad de los minerales de cerio en el planeta sería interesante optimizar su uso, por ejemplo, mezclándola con un soporte que tenga una alta superficie, como lo es el carbón. [98]. Los catalizadores metálicos con soportes de carbón se usan ampliamente para diversas reacciones como la hidrogenación selectiva [99,100], la deshidrogenación [100], la producción de oxidación de urea [101], entre otras.

Los materiales de carbón presentan varias ventajas como soportes de catalizadores, tales como: i) facilita la reducción de la fase activa, ii), se pueden preparar con una amplia textura porosa y química superficial, iii) tienen alta estabilidad térmica y química, iv) se pueden preparar con diferentes estructuras y morfologías, como nanotubos, fibras, xerogelos, etc., v) la fase activa se puede recuperar fácilmente, y vi) su precio suele ser menor que el de otros soportes convencionales [102]. El carbón como soporte de sistemas Ni- CeO_2 se ha empleado en otras reacciones. Se ha estudiado el efecto del soporte en la reacción de WGS utilizando catalizadores de Ni- CeO_2 soportados en nanotubos de carbón, donde se vio que el incorporar carbón como parte

del soporte del catalizador mejoraba la dispersión de la ceria y había un mejor contacto con la fase activa [98].

El carbón puede usarse como soporte de catalizador en reacciones que se necesiten temperaturas y presiones moderadas, de tal manera que se pueda mantener estable bajo las condiciones de reacción, como lo es la metanación de CO₂. En este trabajo de investigación se ha estudiado la posibilidad de utilizar carbón como parte del soporte como una alternativa para optimizar la cantidad de CeO₂ empleada en los catalizadores utilizados en la metanación de CO₂, teniendo en cuenta que el carbón es un excelente soporte catalítico dada su elevada porosidad y superficie específica que permite una buena dispersión de la fase activa, a su ajustable textura porosa y química superficial y a su alta estabilidad térmica y química.

1.4. Reformado seco de metano

El metano y el dióxido de carbono son los principales compuestos químicos que constituyen los gases de efecto invernadero, responsables del calentamiento global y del cambio climático [4]. En vista de los aumentos proyectados en CH₄ y CO₂, es importante encontrar formas de utilizar eficientemente estos dos gases de efecto invernadero. Entre los procesos de reformado, el proceso catalítico de reformado seco de metano (DRM) (Ecuación 1.4) es un proceso atractivo desde el punto de vista medioambiental y económico que permite la revalorización del CO₂, así como la disminución de la huella de carbono producida por el uso de metano procedente de combustibles fósiles, ya que utiliza CO₂ como agente oxidante que se combina con el metano para transformarlos en productos de alto valor como el gas de síntesis [103,104].

El gas de síntesis (H₂ + CO) es útil no sólo como fuente de hidrógeno, considerada una energía limpia cuando se usa en la tecnología de pilas de combustible [105,106] sino también como reactivo base para producir otros productos químicos importantes como alkanos superiores y oxigenados mediante la síntesis de Fischer-Tropsch [49,56,107,108]. Como se mencionó en el apartado 1.2.2. hay diferentes métodos disponibles para producir gas de síntesis (reformado con vapor de metano, oxidación parcial, reformado autotérmico y reformado seco de metano) y aunque el reformado con vapor de metano (SRM) y el reformado autotérmico (ATR) son actualmente los métodos más utilizados, el DRM ofrece varias ventajas. Específicamente, el DRM produce gas de síntesis con una relación favorable de H₂/CO, y ofrece la posibilidad de usar eficientemente metano de depósitos naturales que son ricos en CO₂. Los enfoques actuales para abordar este último problema utilizan procesos con elevado coste de energía para separar el CO₂ del producto de metano deseado, pero

por medio del DRM se podrían reducir significativamente estos costos y permitir que los procesos de transformación de gas de síntesis de combustibles líquidos se implementen de manera eficiente en el sitio cerca del pozo de producción, lo que permite la producción económica de combustibles de campos de gas previamente ignorados, que no han sido explotados debido a su alto contenido de CO₂ [109,110].

A pesar de estas ventajas, el DRM no se ha adoptado ampliamente debido a que es una reacción altamente endotérmica, por lo que, para alcanzar los niveles de conversión deseables, requiere altas temperaturas de funcionamiento de entre 800 – 1000 °C. Esto promueve la sinterización de las partículas y/o la formación de carbono que eventualmente conduce a la desactivación del catalizador. El DRM suele ir acompañado de varias reacciones secundarias, especialmente del craqueo de metano (Ecuación 1.21), la reacción de Boudouard (Ecuación 1.22) y la reacción inversa de Water-Gas shift [108].

❖ *Craqueo de metano*

El craqueo de metano ocurre a altas temperaturas de 600 – 800 °C. Este proceso contribuye a la formación de carbono, el cual se deposita sobre la superficie del catalizador disminuyendo su actividad catalítica.



❖ *Reacción de Boudouard*

La reacción de Boudouard (Ecuación 1.22) también produce depósitos de carbono. A diferencia del craqueo de metano, la reacción de Boudouard es exotérmica, tiene lugar a una temperatura mucho más baja de 250 – 350 °C y no se produce a temperaturas superiores a 700 °C. La combinación del craqueo de metano y la reacción de Boudouard hace que sea difícil evitar la formación y el depósito de carbono en la reacción de reformado en seco. El uso de CO₂ en exceso en la alimentación puede evitar la formación de carbono a temperaturas más bajas.



❖ *Reacción inversa de Water-Gas shift*

La reacción inversa de Water-Gas shift es endotérmica y se prefiere en entornos ricos en CO₂. Esta reacción secundaria produce H₂O y disminuye la relación H₂/CO a un valor inferior a 1 a temperaturas entre 400 – 800 °C.

La estabilidad de un catalizador y, por tanto, su longevidad se convierte en un parámetro crucial y uno de los puntos de comparación más importantes. Las reacciones del DRM, si se completan de manera eficiente, generan una relación equimolar de monóxido de carbono e hidrógeno, es decir que una señal de que la reacción es eficaz debe combinar alta conversión de metano, así como una relación H₂/CO de 1. Si la relación es de alguna manera más alta que 1, significa que hay proporcionalmente más hidrógeno producido con respecto al monóxido de carbono. Esta pérdida de CO está esencialmente relacionada con la formación de coque, la cual puede ocurrir, como se dijo anteriormente, a través de dos reacciones diferentes; craqueo de metano y la reacción de Boudouard. Si la relación H₂/CO es inferior a 1 indicaría que se ha producido más monóxido de carbono con respecto al hidrógeno. Dicha observación también podría estar vinculada a la formación de carbono [56].

1.4.1. Mecanismo de reacción para el reformado seco de metano

La actividad catalítica, la cinética de reacción, así como los diferentes pasos en el mecanismo de reacción han sido estudiados con el fin de minimizar la desactivación de los catalizadores por sinterización y deposición de coque. De acuerdo con la literatura se han propuesto dos tipos de mecanismos, el mecanismo monofuncional y el mecanismo bifuncional [104,111], pero hasta la fecha no hay un consenso general acerca del mecanismo de reacción del reformado seco debido a que éste depende de muchos factores, como la naturaleza y composición del catalizador, la acidez del soporte y la presencia de promotores, y las condiciones de reacción, especialmente la temperatura de reacción [111,112].

En el mecanismo monofuncional el CH₄ y el CO₂ se activan en los sitios metálicos de la siguiente manera: el CH₄ se adsorbe y disocia en los sitios metálicos produciendo especies de hidrógeno y CH_x. Al igual que el CH₄, el CO₂ se adsorbe en los sitios metálicos y se disocia en CO y O adsorbidos. Seguidamente, el hidrógeno y el oxígeno adsorbidos reaccionan para formar grupos hidroxilo que pueden movilizarse a los sitios metálicos y/o a los sitios metal/soporte para, finalmente, reaccionar con otro hidrógeno adsorbido para producir agua. Así mismo, las especies de CH_x reaccionan con el oxígeno adsorbido para producir CO.

En general, la mayoría de los investigadores concuerdan en que el mecanismo más aceptado en DRM es el mecanismo bifuncional. En el mecanismo bifuncional el CH₄ se activa en la fase metálica y el CO₂ se activa en los soportes ácidos/básicos (Figura 1.7.). En general, la mayoría de investigaciones concuerdan en que el mecanismo bifuncional de DRM se puede resumir en los siguientes cuatro pasos [104,108,111]:

❖ Adsorción y activación del metano:

Generalmente, se acepta que la disociación del metano en el catalizador es disociativa y es el paso limitante en la velocidad, aunque la energía de disociación de los enlaces CH_x-H dependa de las propiedades superficiales. Una vez disociadas las especies CH_x se adsorben, preferiblemente, en sitios que completen su tetravalencia. De esta manera, las especies ·CH₃ se adsorben en la parte superior de las partículas metálicas, mientras que las especies :CH₂ se adsorben entre dos átomos metálicos (Figura 1.7a.).

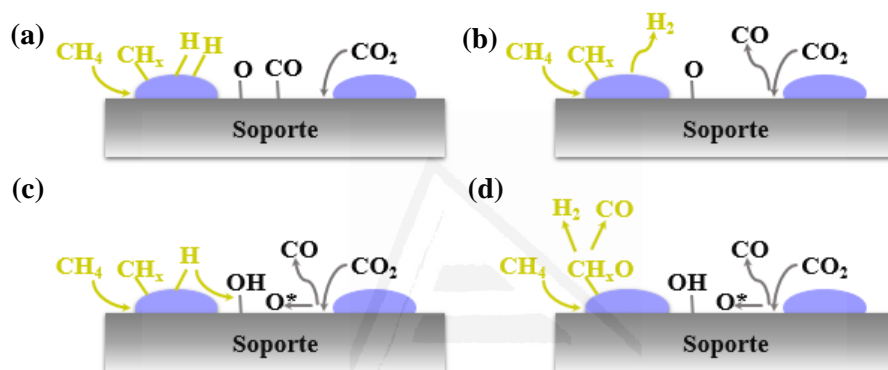


Figura 1.7. Mecanismo bifuncional de reacción para el reformado seco de metano: **(a)** Adsorción disociativa del CH₄ en la fase metálica y adsorción disociativa del CO₂ en la interfase metal-soporte. **(b)** Desorción rápida del CO e H₂. **(c)** Formación de hidroxilos en la superficie y liberación de oxígeno. **(d)** Los hidroxilos superficiales y los óxigenos oxidan las especies CH_x pobres en hidrógeno formando H₂ y CO.

❖ Adsorción y activación del dióxido de carbono:

El CO₂ tiende a adsorberse en la interfase metal-soporte y es un paso, generalmente, rápido. Al igual que el metano, la disociación y reducción del CO₂ es sensible a la estructura, dándose en sitios con defectos, como los átomos de las esquinas de los cristales. La adsorción puede ocurrir a través de tres geometrías de coordinación diferentes: coordinación de carbono puro, coordinación de oxígeno puro, y coordinación mixta de oxígeno y carbono, siendo las dos últimas las más favorables para el reformado seco (Figura 1.7b.).

❖ *Formación de hidroxilos superficiales y agua:*

Una vez que el metano y el dióxido de carbono se adsorben, se producen diversas reacciones en la superficie, que conducen a los productos deseados y a los no deseados. La mayoría de los modelos cinéticos predicen que el hidrógeno migra desde la superficie del metal hacia el soporte donde reacciona con especies de oxígeno formando grupos hidroxilo (Figura 1.7c.).

❖ *Oxidación de CH_x, formación y desorción de H₂ y CO:*

El oxígeno superficial reacciona con las especies CH_x pobres en hidrógeno ($0 \leq x \leq 3$) formando especies CH_xO o CO. Algunos investigadores consideran la formación de CH_xO como una especie intermedia a la formación de CO, mientras otros autores plantean que el CO se forma directamente sin la formación previa de los formiatos CH_xO (Figura 1.7d.).

1.4.2. Desarrollo de catalizadores para el reformado seco de metano

En la mayoría de investigaciones se ha podido demostrar que la utilización de catalizadores en el DRM reduce la demanda de energía para activar la reacción con respecto a los valores de equilibrio. La termodinámica dice que el DRM requiere temperaturas que pueden alcanzar los 900 °C para obtener altos rendimientos en la formación del gas de síntesis. Por lo tanto, existe la necesidad de desarrollar un catalizador con alta actividad catalítica que a la vez sea térmicamente estable y que resista la desactivación debido a la deposición y sinterización de carbono [56,113].

La actividad catalítica de un catalizador depende en gran medida del tipo de metal utilizado, la naturaleza y área superficial del soporte, el tamaño de partícula y la interacción metal-soporte [114,115].

Los catalizadores basados en metales nobles como el Pt, el Rh y el Ru son altamente activos para la reacción de DRM, además que presentan una baja deposición de carbono, pero son caros [103,116]. Los catalizadores basados en rutenio han emergido como candidatos ideales para la reacción de DRM por su baja disposición para la formación de coque, pero la disponibilidad de rutenio es demasiado baja lo cual lo hace inviable a nivel económico [111,117]. Hasta ahora, los catalizadores basados en níquel han sido los más estudiados para esta reacción debido a su actividad catalítica aceptable, además es abundante en la naturaleza y, tiene un precio más bajo que los metales nobles, lo que lo hace más adecuado para un proceso comercial rentable [118–120]. Se han integrado diferentes estrategias de las mencionadas anteriormente para mejorar los catalizadores basados en níquel. En este sentido, se han desarrollado

catalizadores estructurados de película delgada [121], catalizadores bimetálicos en los que se han combinado el níquel con metales nobles [107,117]. También, se ha hecho uso de reactores de plasma en los que se han utilizado catalizadores basados en perovskitas y Ni con estructura espinela [56,122,123].

Desde un punto de vista económico, los catalizadores basados en Ni son más adecuados para aplicaciones comerciales que los de metales nobles. Por lo tanto, un desafío actual es encontrar un catalizador de Ni que presente una buena actividad catalítica y tenga una nula o baja deposición de coque. Para ello se están investigando diferentes técnicas de síntesis que permitan producir materiales con distintas propiedades morfológicas y fisicoquímicas que conduzcan a diferentes resultados catalíticos para el DRM. En esta Tesis Doctoral se ha estudiado el uso de catalizadores basados en nanopartículas con el fin de determinar su rendimiento catalítico y la deposición de coque bajo condiciones de reacción de DRM.

También se han hecho avances en el estudio de varios óxidos como soportes para la fase activa [107,118,120,124]. Al estudiar el mecanismo de reacción del RDM podemos ver que el papel del soporte en esta reacción, especialmente en los catalizadores de níquel, va más allá de proporcionar un área superficial. El soporte debe ofrecer la máxima dispersión del metal, asegurando la estabilidad del catalizador en condiciones de reacción y evitando la sinterización. Además, teniendo en cuenta el mecanismo bifuncional planteado anteriormente, el soporte debe proporcionar sitios activos para la adsorción y disociación del CO₂.

Se han estudiado soportes como SiO₂ [119], Al₂O₃ [107,125], ZrO₂ [125,126], TiO₂ [127], CeO₂ [119,120,128], La₂O₃ [129] y MgO [130]. Los óxidos con baja acidez de Lewis y/o sitios básicos como el MgO, el ZrO₂ y el La₂O₃ presentan una mejora en su rendimiento catalítico, y óxidos como el CeO₂, además, aumentan la dispersión del níquel, mejorando así la resistencia a la desactivación por sinterización y formación de coque [131]. El Al₂O₃ es uno de los soportes más utilizados, ya que es económico y tiene una buena estabilidad térmica y mecánica, pero su acidez-basicidad depende del método de preparación y de las impurezas que contiene [107]. Mediante los métodos de preparación convencionales, generalmente, las partículas de níquel depositadas sobre alúmina presentan un tamaño por encima de los 10 nm y tienden a sinterizar y formar carbono filamentoso, además que puede formarse aluminato de níquel, que es difícil de reducir y, por tanto, es inactivo para la descomposición del CH₄. Como la oxidación de las especies CH_x es uno de los pasos limitantes en la reacción de reformado, es importante la disponibilidad de oxígeno en superficie [56,132]. La ceria es conocida por su alta capacidad de almacenar y transportar oxígeno, es decir, que tienen la capacidad

de ceder oxígenos en un ambiente pobre en oxígeno y reoxidarse rápidamente en un ambiente rico en oxígeno.

En el reformado seco de metano, la ceria puede reducirse por el H₂ y el CO, luego la adsorción y activación del CO₂ puede llevarse a cabo en los sitios de Ce³⁺ formando CO a la vez que oxida el Ce³⁺ a Ce⁴⁺. Además, mejora la dispersión y estabilidad de las partículas metálicas, ya que interactúa fuertemente con estas [81,120]. En este trabajo de Tesis Doctoral se ha utilizado CeO₂ como soporte catalítico para el DRM debido a que en nuestro grupo de investigación se ha estudiado ampliamente y se ha empleado en reacciones como la oxidación de CO y la combustión de hollín obteniendo resultados satisfactorios dado en gran parte a sus notables propiedades redox [93,96,97], que, entre otras cosas, tiene un impacto beneficioso en el control y/o eliminación de depósitos de carbono, uno de los principales inconvenientes de los catalizadores utilizados en DRM [133].

1.5. Influencia de la morfología de los catalizadores en sus propiedades catalíticas

Generalmente, los parámetros más importantes que influyen en la actividad, selectividad y estabilidad de un catalizar son la naturaleza y tamaño de partícula de la fase activa, la naturaleza, textura y estructura del soporte y las condiciones de reacción. La interacción metal-soporte puede influir en el rendimiento catalítico de diferentes maneras, las cuales pueden estar asociadas a factores como i) efectos geométricos (cambio en el tamaño de partícula, morfología determinada debido a la presencia de un soporte), ii) efectos electrónicos (transferencia de carga entre metales y efecto del soporte debido a la coordinación del metal por el soporte), iii) actividad en la interfase, donde sitios específicos de la interfase metal-soporte proporcionan una actividad dada, y iv) participación directa del soporte en la catálisis [102].

En los últimos años se han publicado diversos estudios acerca de los procesos de metanación de CO₂ y reformado seco de metano como alternativas para la valorización del CO₂, pero aún falta camino por recorrer en el estudio de los mecanismos de reacción, la optimización de los sitios activos y en la síntesis de catalizadores que sean altamente activos y selectivos a la vez que se mantengan estables en condiciones de reacción. En esta Tesis Doctoral se estudia la influencia de la morfología de los catalizadores en sus propiedades fisicoquímicas y catalíticas mediante el uso de soportes 3DOM y catalizadores basados en nanopartículas.

1.5.1. Sólidos macroporosos con orden tridimensional (3DOM, Three Dimensionally Ordered Macroporous Solids)

Con el desarrollo de una amplia gama de técnicas de síntesis química blanda, ahora es posible diseñar estructuras tridimensionales (3D) en escalas de longitud múltiple, que van desde unos pocos Angstroms hasta dimensiones macroscópicas. Se pueden introducir características porosas regulares durante la síntesis empleando agentes de dirección de estructura, plantillas o rellenos de espacio. Por ejemplo, se han utilizado moléculas orgánicas individuales para controlar la estructura porosa de los materiales microporosos cristalinos, por medio de agentes tensioactivos o copolímeros se han podido obtener matrices sólidas ordenadas de mesoporos. Incluso los macroporos han sido moldeados utilizando emulsiones y una variedad de métodos de plantillas de esferas [134]. Esta investigación se centrará en la síntesis y uso de plantillas de esferas poliméricas para la formación de sólidos macroporosos con orden tridimensional (3DOM).

Los sólidos con estructura 3DOM están captando un interés creciente en diversas áreas de la química y la física debido a sus propiedades características [135–137]. La estructura bien definida contiene grandes cantidades de macroporos que se conectan entre sí a través de los poros, lo cual puede proporcionar canales de transferencia de masa para el reactivo gaseoso a los sitios activos internos. Además, los materiales 3DOM tienen una superficie específica más alta que los gránulos no porosos [95]. En general, se acepta que el área de superficie ampliada podría proporcionar centros más reactivos.

El proceso de preparación de este tipo de sólidos con estructura 3DOM consta de las siguientes etapas (Figura 1.8.): i) pretratamiento del sólido plantilla para facilitar la impregnación con la disolución precursora; ii) infiltración de los sólidos plantilla con la disolución precursora del ion metálico; iii) precipitación de oxalatos o citratos de los correspondientes precursores; iv) calcinación para eliminar el sólido plantilla y obtener el correspondiente óxido metálico macroporoso [134,138].

Para obtener óxidos de metales con estructuras 3DOM bien ordenada, el disolvente y el precursor del metal utilizados deben cumplir los siguientes requisitos:

- ❖ el disolvente debe mojar bien las esferas del polímero de PMMA, de forma que el fluido pueda penetrar completamente en la matriz de la plantilla, y así evitar defectos en la estructura final producida por regiones que no habían sido mojadas;
- ❖ el precursor tiene que tener una elevada solubilidad en el disolvente para maximizar la carga del precursor, y así obtener paredes lo suficientemente fuertes, para evitar colapsos en el sólido calcinado;

- ❖ el punto de fusión del precursor debe ser mayor que la temperatura a la que las esferas se gasifican o se queman.

Es bien sabido que el rendimiento catalítico de los catalizadores soportados depende de la naturaleza y la propiedad del soporte empleado. El soporte influye en las propiedades del catalizador principalmente porque mejora la dispersión de la fase activa y modifica la reducibilidad de los precursores de óxido mediante la manipulación de la interacción entre la fase activa y el soporte [68,81,139]. Por lo tanto, la selección de un soporte adecuado es crucial para la preparación de catalizadores más eficientes. Se están haciendo avances en ciertas reacciones de catálisis heterogénea modificando los soportes, controlando su estructura a nivel nanométrico para mejorar sus propiedades.



Figura 1.8. Esquema del método de preparación de óxidos metálicos con estructura 3DOM.

Utilizar soportes con estructura 3DOM permite un transporte eficiente de reactivos y productos a través de los macroporos combinados con la selectividad y los beneficios catalíticos de los mesoporos y microporos. En este sentido, los materiales con porosidad diseñada han permitido hacer avances en diversas reacciones catalíticas y fotocatalíticas. Se han estudiado numerosos catalizadores con estructura 3DOM, como por ejemplo catalizadores AuPd/3DOM-TiO₂ para la reducción fotocatalítica de CO₂, donde la estructura 3DOM ayudaba a mejorar la eficiencia en la captación de luz [140], catalizadores 3DOM para estudiar el mecanismo de combustión del hollín [95], catalizadores basados en cobalto 3DOM M_xCO_{3-x}O₄ para la oxidación de hollín asistida por NO_x, donde la estructura macroporosa 3DOM facilita el paso de las partículas de hollín al interior del catalizador [141], catalizadores 3DOM-LaSrCoFeO_{6-δ} para la reducción térmica y fototérmica de CO₂ a CH₄, donde la estructura 3DOM proporciona una mejora en la absorción de la radiación solar [142]. También se han empleado perovskitas 3DOM de LaFeO₃ como soporte de nanopartículas de oro para la

combustión de carbonilla [143], ceria 3DOM como soporte de oro para la oxidación de formaldehido [144] y alúmina 3DOM como soporte de Co y Mo para reacciones de desulfuración [145], entre otros ejemplos [137,146–148].

En términos generales, los catalizadores con estructura 3DOM comparados con los catalizadores no porosos exhiben un mejor rendimiento catalítico debido a sus áreas superficiales más altas que permiten una mejor dispersión de la fase activa y a sus propiedades de difusión fáciles. Anteriormente, nuestro grupo de investigación optimizó la síntesis de una plantilla consistente en cristales coloidales de esferas monodispersas de polimetilmetacrilato (PMMA) para generar una serie de materiales catalíticos con estructura 3DOM [93,94,96,97,149], y observó que la mayoría de ellos funcionó bien en la oxidación preferencial de CO y en la combustión de hollín. Sin embargo, hasta la fecha, no se ha reportado el uso de este tipo de estructuras 3DOM para acelerar la reacción de metanación de CO₂. Por lo cual, en esta Tesis Doctoral se ha investigado el diseño y síntesis de catalizadores basados en sistemas níquel-ceria con estructura 3DOM, que presentan un comportamiento óptimo en la reacción de metanación de CO₂.

1.5.2. Nanopartículas

Las nanopartículas (NP), son materiales que tiene un tamaño entre 1 y 100 nm. La importancia de estos materiales aumentó cuando se descubrió que el tamaño puede influir en las propiedades físico-químicas de una sustancia. Debido a sus propiedades ópticas, electrónicas, magnéticas, mecánicas y térmicas, las NP pueden usarse en una variedad de aplicaciones como, por ejemplo, aplicaciones médicas [150–152], aplicaciones en ciencia de los materiales [153,154], aplicaciones medioambientales [155,156], energéticas [157,158], en la industria mecánica [159,160], entre otras. En catálisis, gracias a la llegada de la nanotecnología, se han dado pasos importantes hacia el diseño y síntesis de nuevos catalizadores. En consecuencia, se han realizado diversos estudios para entender la influencia del tamaño, la forma, la interacción con el soporte y el estado de oxidación con sus propiedades catalíticas.

En catálisis, las nanopartículas metálicas se caracterizan por tener un tamaño muy reducido, entre 1 – 10 nm, y una mejora significativa en sus propiedades catalíticas en muchas ocasiones. Sin embargo, debido a las interacciones químicas con los gases reactivos y a las temperaturas de reacción, están sujetas a cambios estructurales y químicos. Los catalizadores metálicos que se usan en procesos industriales consisten, generalmente, en nanopartículas metálicas que están ancladas a un soporte, que, en su mayoría, son óxidos metálicos con alta superficie y estabilidad térmica [81,161–163]. Debido a que la reacción química ocurre en la superficie de las nanopartículas metálicas y/o en la interfase metal-soporte, se reconoce que el rendimiento catalítico de las

nanopartículas metálicas está estrechamente relacionado con el tamaño, la forma y la estructura en la interfase [81]. Estas características estructurales frecuentemente están relacionadas con la actividad, selectividad y estabilidad obtenidas durante la reacción [164].

Se pueden emplear diversos métodos para la síntesis de NP, los cuales se dividen en dos tipos principales, de enfoque ascendente y de enfoque descendente. En el método de enfoque ascendente, las NP se forman a partir de sustancias más simples que, por ejemplo, nuclean y hacen crecer partículas de distribuciones finas en fase líquida o vapor, por lo que se le conoce también como enfoque constructivo (Figura 1.9a.). Entre este método se encuentran las técnicas de sedimentación y reducción. El método de enfoque descendente emplea un enfoque destructivo, es decir, las NP se obtienen a partir de la descomposición de una partícula más grande en partículas más pequeñas (Figura 1.9b.) [165,166]. En esta Tesis Doctoral se utilizó una técnica de tipo ascendente denominada método de microemulsión inversa, el cual es muy utilizado para la síntesis de nanopartículas de óxidos metálicos. Este método permite controlar el tamaño de las partículas, la geometría, la homogeneidad y el área superficial [165,167,168].

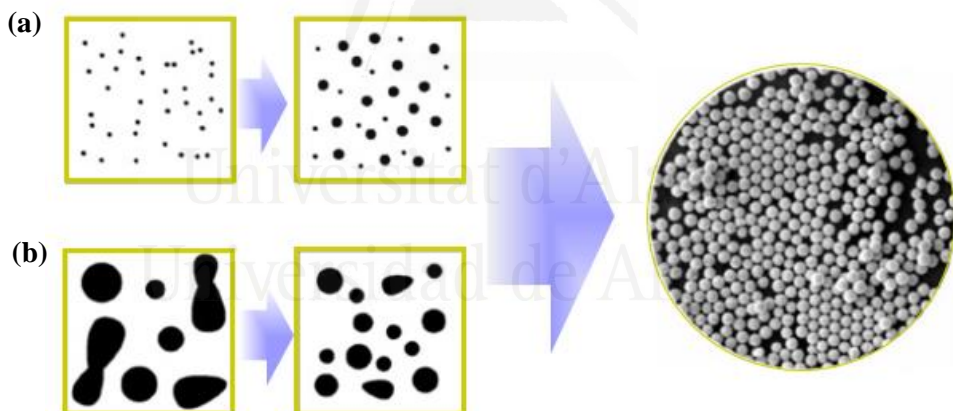


Figura 1.9. Métodos para la síntesis de nanopartículas. **(a)** Método ascendente: un precursor molecular se desgrega en átomos/iones metálicos que se convierten en coloides. **(b)** Método descendente: grandes gotas/partículas de un metal se reducen en estructuras más pequeñas [163].

Las nanopartículas metálicas dispersas sobre soportes metálicos se han empleado en catálisis heterogénea en diversas aplicaciones industriales como la fabricación de productos químicos y en aplicaciones relacionadas con la energía y la remediación

ambiental [163,169–171]. Generalmente, el alta área superficial y la promoción de sitios más activos promueven reacciones más rápidas, aumentando el rendimiento catalítico [101,164,172,173]. Entre las múltiples aplicaciones se encuentran electrooxidación de ácido fórmico [174], degradación catalítica del azul de metileno a través de la activación de bisulfito con nanopartículas de CoO [175], sinergia de nanopartículas de metales de transición (Co, Ni, Fe, Mn) para la reducción catalítica de 4-nitrofenol [176], composites de nanopartículas de paladio y óxido de grafeno como catalizador altamente activo y reutilizable para la hidrogenación de nitroareos [177]. En metanación de CO₂ y reformado seco de metano también se han utilizado las nanopartículas como catalizadores para acelerar la reacción, pero se siguen haciendo esfuerzos por conseguir catalizadores que sean estables bajo condiciones de reacción [83,127,178–182].

Se sabe que las NP tienen propiedades físicas y químicas drásticamente diferentes en comparación con sus homólogos a granel, y en muchos casos se han informado actividades y selectividades muy mejoradas para los nanocatalizadores. Pero, a pesar de tener estructuras iniciales bien definidas, en muchas aplicaciones estos catalizadores se comportan como entidades dinámicas sujetas a cambios morfológicos, estructurales y químicos en condiciones de reacción. En otras palabras, la forma y el tamaño cuidadosamente logrados de las NP pueden perderse en condiciones de reacción [183]. Debido a esto y a, como se dijo anteriormente, los esfuerzos que se siguen haciendo por conseguir catalizadores estables en la metanación de CO₂ y el reformado seco de metano, en esta Tesis Doctoral se ha sintetizado un catalizador basado en nanopartículas de NiO-CeO₂ para estudiar su comportamiento catalítico y estabilidad en condiciones de reacción en la metanación de CO₂ y en el reformado seco de metano, así como la evolución de su morfología y estado químico después de reacción.

1.6. Objetivos

Considerando lo expuesto anteriormente, el objetivo principal de esta Tesis Doctoral es el estudio de los sistemas catalíticos de NiO-CeO₂ para la metanación de CO₂ y el reformado seco de metano como alternativas para la revalorización del CO₂.

Más precisamente, los objetivos específicos de esta tesis son:

- ❖ Sintetizar y caracterizar química y estructuralmente catalizadores de NiO-CeO₂ y NiO-Al₂O₃ para su uso en el estudio de los mecanismos de la reacción de metanación de CO₂.

- ❖ Diseñar y sintetizar catalizadores de NiO-CeO₂ con un comportamiento excelente en la reacción de metanación de CO₂ basados en estructuras macroporosas (3DOM), en los que se ha optimizado los sitios activos implicados en dicha reacción.
- ❖ Optimizar la morfología de los catalizadores NiO-CeO₂ para la reacción de metanación de CO₂, mediante la síntesis y posterior caracterización química, física y catalítica de catalizadores basados en nanopartículas, nanopartículas soportadas, catalizadores macroporosos 3DOM y catalizadores macroporosos convencionales.
- ❖ Estudiar la influencia de la incorporación de carbón como parte del soporte en catalizadores NiO/CeO₂ utilizados en la reacción de metanación de CO₂ mediante la síntesis y caracterización química, estructural y catalítica de catalizadores NiO/CeO₂-NiO/C.
- ❖ Diseñar y sintetizar un catalizador basado en nanopartículas de NiO-CeO₂ con un comportamiento catalítico óptimo en la reacción de reformado seco de metano y con elevada estabilidad.

1.7. Referencias

- [1] P. Nema, S. Nema, P. Roy, An overview of global climate changing in current scenario and mitigation action, Renew. Sustain. Energy Rev. 16 (2012) 2329–2336.
- [2] S. Planton, M. Déqué, F. Chauvin, L. Terray, Expected impacts of climate change on extreme climate events, Comptes Rendus Geosci. 340 (2008) 564–574.
- [3] Sources of greenhouse gas emissions. <https://www.epa.gov/ghgemissions/sources-greenhouse-gas-emissions>. Access in March 2020.
- [4] Global greenhouse gas emission data. <https://www.epa.gov/ghgemissions/overview-greenhouse-gases>. Access in March 2020
- [5] CO₂ and greenhouse gas emissions. <https://ourworldindata.org/co2-and-other-greenhouse-gas-emissions>. Access in March 2020.
- [6] The Carbon Cycle. <https://www.earthobservatory.nasa.gov/features/CarbonCycle>. Access in March 2020.
- [7] Sustainable innovation forum 2015. <http://www.cop21paris.org/>. Access in March 2020.
- [8] R. Lindsey, Climate Change: Atmospheric Carbon Dioxide.

<https://www.climate.gov/news-features/understanding-climate/climate-change-atmospheric-carbon-dioxide>. Access in March 2020.

- [9] C. Hepburn, E. Adlen, J. Beddington, E.A. Carter, S. Fuss, N. Mac Dowell, J.C. Minx, P. Smith, C.K. Williams, The technological and economic prospects for CO₂ utilization and removal, *Nature*. 575 (2019) 87–97.
- [10] M.N. Anwar, A. Fayyaz, N.F. Sohail, M.F. Khokhar, M. Baqar, A. Yasar, K. Rasool, A. Nazir, M.U.F. Raja, M. Rehan, M. Aghbashlo, M. Tabatabaei, A.S. Nizami, CO₂ utilization: Turning greenhouse gas into fuels and valuable products, *J. Environ. Manage.* 260 (2020) 110059.
- [11] A. Rafiee, K.R. Khalilpour, D. Milani, M. Panahi, Trends in CO₂ conversion and utilization: A review from process systems Perspective, *J. Environ. Chem. Eng.* 6 (2018) 5771-5794.
- [12] O.Y. Abdelaziz, W.M. Hosny, M.A. Gadalla, F.H. Ashour, I.A. Ashour, C.P. Hulteberg, Novel process technologies for conversion of carbon dioxide from industrial flue gas streams into methanol, *J. CO₂ Util.* 21 (2017) 52–63.
- [13] Y. Hao, A. Steinfeld, Fuels from Water, CO₂ and solar energy, *Sci. Bull.* 62 (2017) 1099–1101.
- [14] A. Delparish, A.K. Avci, Intensified catalytic reactors for Fischer-Tropsch synthesis and for reforming of renewable fuels to hydrogen and synthesis gas, *Fuel Process. Technol.* 151 (2016) 72–100.
- [15] H. Arakawa, M. Aresta, J.N. Armor, M.A. Bartea, E.J. Beckman, A.T. Bell, J.E. Bercaw, C. Creutz, E. Dinjus, D.A. Dixon, K. Domen, D.L. DuBois, J. Eckert, E. Fujita, D.H. Gibson, W.A. Goddard, D.W. Goodman, J. Keller, G.J. Kubas, H.H. Kung, J.E. Lyons, L.E. Manzer, T.J. Marks, K. Morokuma, K.M. Nicholas, R. Periana, L. Que, J. Rostrup-Nielson, W.M.H. Sachtler, L.D. Schmidt, A. Sen, G.A. Somorjai, P.C. Stair, B. Ray Stults, W. Tumas, Catalysis research of relevance to carbon management: Progress, challenges, and opportunities, *Chem. Rev.* 101 (2001) 953–996.
- [16] E.I. Koitsoumpa, C. Bergins, E. Kakaras, The CO₂ economy: Review of CO₂ capture and reuse technologies, *J. Supercrit. Fluids.* 132 (2018) 3–16.
- [17] Commission activities to enable CO₂ transformation and utilisation. <https://setis.ec.europa.eu/publications/setis-magazine/carbon-capture-utilisation-and-storage/commission-activities-enable-co2>. Access in March 2020.
- [18] A. Azapagic, R.M. Cue, Carbon capture, storage and utilisation technologies: A critical analysis and comparison of their life cycle environmental impacts, *J. CO₂ Util.* 9 (2015) 82–102.
- [19] L. Li, N. Zhao, W. Wei, Y. Sun, A review of research progress on CO₂ capture, storage, and utilization in Chinese Academy of Sciences, *Fuel.* 108 (2013) 112–

130.

- [20] E.F. J. Ralston, Catalytic CO₂ recycle (CCRTM) Technology, in: Proc. 7th Power Plant Air Pollut. Control “Mega” Symp. 2008, Baltimore, US: pp. 1–12.
- [21] Y. Jiang, H.D. May, L. Lu, P. Liang, X. Huang, Z.J. Ren, Carbon dioxide and organic waste valorization by microbial electrosynthesis and electro-fermentation, *Water Res.* 149 (2019) 42–55.
- [22] A. Pietsch, Decaffeination-Process and Quality, in: *Cr. Sci. Coffee*, 2017: pp. 225–243.
- [23] IPCC, 2005: IPCC Special Report on Carbon Dioxide Capture and Storage. Prepared by Working Group III of the Intergovernmental Panel on Climate Change [Metz, B., O. Davidson, H. C. de Coninck, M. Loos, and L. A. Meyer (eds.)]. Cambridge University Press, Cambridge, United Kingdom and New York, NY, USA, 442 pp.
- [24] N.A. Azzolina, D. V Nakles, C.D. Gorecki, W.D. Peck, S.C. Ayash, L.S. Melzer, S. Chatterjee, CO₂ storage associated with CO₂ enhanced oil recovery: A statistical analysis of historical operations, *Int. J. Greenh. Gas Control.* 37 (2015) 384–397.
- [25] M. Godec, G. Koperna, J. Gale, CO₂-ECBM: A review of its status and global potential, *Energy Procedia.* 63 (2014) 5858–5869.
- [26] L.R. Thippeswamy, A. Kumar Yadav, Heat transfer enhancement using CO₂ in a natural circulation loop, *Sci. Rep.* 10 (2020) 1507.
- [27] K. Ploner, L. Schlicker, A. Gili, A. Gurlo, A. Doran, L. Zhang, M. Armbrüster, D. Obendorf, J. Bernardi, B. Klötzer, S. Penner, Reactive metal-support interaction in the Cu-In₂O₃ system: intermetallic compound formation and its consequences for CO₂-selective methanol steam reforming, *Sci. Technol. Adv. Mater.* 20 (2019) 356–366.
- [28] M. Ramdin, A.R.T. Morrison, M. De Groen, R. Van Haperen, R. De Kler, E. Irtem, A.T. Laitinen, L.J.P. Van Den Broeke, T. Breugelmans, J.P.M. Trusler, W. De Jong, T.J.H. Vlugt, High-pressure electrochemical reduction of CO₂ to formic acid/formate: Effect of pH on the downstream separation process and economics, *Ind. Eng. Chem. Res.* 58 (2019) 22718–22740.
- [29] M. Gazda-Grzywacz, D. Burchart-Korol, A. Smoliński, K. Zarębska, Environmental protection - Greenhouse gas emissions from electricity production in Poland, *J. Phys. Conf. Ser.* 1398 (2019) 012004.
- [30] H. Wu, W. Chen, J. Wu, Z. Zheng, L. Duan, Synergistic removal of SO_x and NO_x in CO₂ compression and purification in oxy-fuel combustion power plant, *Energy and Fuels.* 33 (2019) 12621–12627.
- [31] S. Rahmani, M. Rezaei, F. Meshkani, Preparation of highly active nickel catalysts supported on mesoporous nanocrystalline γ-Al₂O₃ for CO₂

- Universitat d'Alacant
Campus de Sant Joan
Avda. la Pintor Ros 12
03007 Alacant
- methanation, *J. Ind. Eng. Chem.* 20 (2014) 1346–1352.
- [32] J. Calles, A. Carrero, A. Vizcaíno, M. Lindo, Effect of Ce and Zr addition to Ni/SiO₂ catalysts for hydrogen production through ethanol steam reforming, *catalysts*. 5 (2015) 58–76.
- [33] C. Mebrahtu, F. Krebs, S. Abate, S. Perathoner, G. Centi, R. Palkovits, CO₂ methanation: Principles and challenges, in: *Stud. Surf. Sci. Catal.*, 1st ed., Elsevier B.V., 2019: pp. 85–103.
- [34] D. Katla, Ł. Bartela, A. Skorek-Osikowska, Evaluation of electricity generation subsystem of Power-to-Gas-to-Power unit using gas expander and heat recovery steam generator, *E3S Web Conf.* 137 (2019) 01017.
- [35] M. Götz, J. Lefebvre, F. Mörs, A. McDaniel Koch, F. Graf, S. Bajohr, R. Reimert, T. Kolb, Renewable Power-to-Gas: A technological and economic review, *Renew. Energy*. 85 (2016) 1371–1390.
- [36] J. Gorre, F. Ortloff, C. van Leeuwen, Production costs for synthetic methane in 2030 and 2050 of an optimized Power-to-Gas plant with intermediate hydrogen storage, *Appl. Energy*. 253 (2019) 113594.
- [37] M.G. Iglesias, C. De Vries, M. Claeys, G. Schaub, Chemical energy storage in gaseous hydrocarbons via iron Fischer-Tropsch synthesis from H₂/CO₂. Kinetics, selectivity and process considerations, *Catal. Today*. 242 (2015) 184–192.
- [38] W.J. Shen, K.W. Jun, H.S. Choi, K.W. Lee, Thermodynamic investigation of methanol and dimethyl ether synthesis from CO₂ hydrogenation, *Korean J. Chem. Eng.* 17 (2000) 210–216.
- [39] O.I. Awad, R. Mamat, O.M. Ali, N.A.C. Sidik, T. Yusaf, K. Kadrigama, M. Kettner, Alcohol and ether as alternative fuels in spark ignition engine: A review, *Renew. Sustain. Energy Rev.* 82 (2018) 2586–2605.
- [40] Pilot plant demonstrates low-cost conversion of CO₂ into fuel. <https://newatlas.com/direct-air-carbon-capture-cost-effective/54964/>. Access in March 2020.
- [41] H. Blanco, A. Faaij, A review at the role of storage in energy systems with a focus on Power to Gas and long-term storage, *Renew. Sustain. Energy Rev.* 81 (2018) 1049–1086.
- [42] T. Bacquart, K. Arrhenius, S. Persijn, A. Rojo, F. Auprêtre, B. Gozlan, N. Moore, A. Morris, A. Fischer, A. Murugan, S. Bartlett, G. Doucet, F. Laridant, E. Gernot, T.E. Fernández, C. Gómez, M. Carré, G. De Reals, F. Haloua, Hydrogen fuel quality from two main production processes: Steam methane reforming and proton exchange membrane water electrolysis, *J. Power Sources*. 444 (2019) 227170.
- [43] I. Staffell, D. Scamman, A. Velazquez Abad, P. Balcombe, P.E. Dodds, P. Ekins,

- N. Shah, K.R. Ward, The role of hydrogen and fuel cells in the global energy system, *Energy Environ. Sci.* 12 (2019) 463–491.
- [44] L. de Santoli, R. Paiolo, G. Lo Basso, Energy-environmental experimental campaign on a commercial CHP fueled with H₂NG blends and oxygen enriched air hailing from on-site electrolysis, *Energy*. 195 (2020) 116820.
 - [45] A. Ursua, L.M. Gandia, P. Sanchis, Hydrogen production from water electrolysis: Current status and future trends, *Proc. IEEE*. 100 (2012) 410–426.
 - [46] I. Ridjan, B.V. Mathiesen, D. Connolly, Synthetic fuel production costs by means of solid oxide electrolysis cells, *Energy*. 76 (2014) 104–113.
 - [47] J. Pawel, M. Ni, Q. Sun, S. Hwa, Production of sustainable methane from renewable energy and captured carbon dioxide with the use of Solid Oxide Electrolyzer: A thermodynamic assessment, *Energy*. 82 (2015) 714–721.
 - [48] A. Grimalt-Alemany, I. V. Skiadas, H.N. Gavala, Syngas biomethanation: state of the art review and perspectives, *Biofuels, Bioprod. Biorefining*. 12 (2018) 139–158.
 - [49] A. Scarabello, D. Dalle Nogare, P. Canu, R. Lanza, Partial oxidation of methane on Rh/ZrO₂ and Rh/Ce–ZrO₂ on monoliths: Catalyst restructuring at reaction conditions, *Appl. Catal. B Environ.* 174–175 (2015) 308–322.
 - [50] P. Moretti, J. Morais de Araujo, A. Borges de Castilhos, P. Buffière, R. Gourdon, R. Bayard, Characterization of municipal biowaste categories for their capacity to be converted into a feedstock aqueous slurry to produce methane by anaerobic digestion, *Sci. Total Environ.* 716 (2020) 137084.
 - [51] L. Yang, X. Ge, Biogas and Syngas Upgrading, *Adv. Bioenergy*. 1 (2016) 125–188.
 - [52] M.M. Mariano, Syngas, in: *Ind. Chem. Process Anal. Des.* (2016) 199–297.
 - [53] S.G. Sørensen Bent, Hydrogen, *Hydrog. Fuels Cells* (2018) 5–105.
 - [54] J.R. Rostrup-nielsen, New aspects of syngas production and use, *Catal. Today*. 63 (2000) 159–164.
 - [55] N. Kumar, M. Shojaee, J.J. Spivey, Catalytic bi-reforming of methane: from greenhouse gases to syngas, *Curr. Opin. Chem. Eng.* 9 (2015) 8–15.
 - [56] J.M. Lavoie, Review on dry reforming of methane, a potentially more environmentally-friendly approach to the increasing natural gas exploitation, *Front. Chem.* 2 (2014) 1–17.
 - [57] D. Pham Minh, T.J. Siang, D.-V.N. Vo, T.S. Phan, C. Ridart, A. Nzihou, D. Grouset, Hydrogen Production From Biogas Reforming: An Overview of Steam Reforming, Dry Reforming, Dual Reforming, and Tri-Reforming of Methane, in: *Hydrog. Supply Chain.*, Elsevier Ltd., 2018: pp. 111–166.

- [58] F.D. Meylan, V. Moreau, S. Erkman, Material constraints related to storage of future European renewable electricity surpluses with CO₂ methanation, *Energy Policy*. 94 (2016) 366–376.
- [59] W.B.M. Vogt Charlotte, Monai Matteo, Jan Kramer Gert, The renaissance of the Sabatier reaction and its applications on Earth and in space, *Nat. Catal.* 2 (2019) 188–197.
- [60] L. Jürgensen, E. Augustine, J. Born, J.B. Holm-nielsen, Dynamic biogas upgrading based on the Sabatier process: Thermodynamic and dynamic process simulation, *Bioresour. Technol.* 178 (2015) 323–329.
- [61] S. Takenaka, T. Shimizu, K. Otsuka, Complete removal of carbon monoxide in hydrogen-rich gas stream through methanation over supported metal catalysts, *Int. J. Hydrogen Energy*. 29 (2004) 1065–1073.
- [62] A.S. Abdullah, A.A. Abdulabbas, A.A. Al Asadi, Modeling and simulation of methanation catalytic reactor in ammonia plant, *Int. J. Adv. Res. Chem. Sci.* 2 (2015) 80–84.
- [63] J. Hu, K.P. Brooks, J.D. Holladay, D.T. Howe, T.M. Simon, Catalyst development for microchannel reactors for martian in situ propellant production, *Catal. Today*. 125 (2007) 103–110.
- [64] The Sabatier System: Producing Water on the Space Station. https://www.nasa.gov/mission_pages/station/research/news/sabatier.html. Access in March 2020.
- [65] S. Rönsch, J. Schneider, S. Matthischke, M. Schlüter, M. Götz, J. Lefebvre, P. Prabhakaran, S. Bajohr, Review on methanation - From fundamentals to current projects, *Fuel*. 166 (2016) 276–296.
- [66] R. Maatman, A kinetic study of the methanation of CO₂ over nickel-alumina, *J. Catal.* 62 (1980) 349–356.
- [67] W. Wang, J. Gong, Methanation of carbon dioxide: An overview, *Front. Chem. Eng. China*. 5 (2011) 2–10.
- [68] K. Stangeland, D. Kalai, H. Li, Z. Yu, CO₂ methanation: The effect of catalysts and reaction conditions, *Energy Procedia*. 105 (2017) 2022–2027.
- [69] B. Miao, S.S.K. Ma, X. Wang, H. Su, S.H. Chan, Catalysis mechanisms of CO₂ and CO methanation, *Catal. Sci. Technol.* 6 (2016) 4048–4058.
- [70] J.W.E. Coenen, P.F.M.T. van Nisselrooy, M.H.J.M. de Croon, P.F.H.A. van Dooren, R.Z.C. van Meerten, The dynamics of methanation of carbon monoxide on nickel catalysts, *Appl. Catal.* 25 (1986) 1–8.
- [71] M. Jacquemin, A. Beuls, P. Ruiz, Catalytic production of methane from CO₂ and H₂ at low temperature: Insight on the reaction mechanism, *Catal. Today*. 157 (2010) 462–466.

- [72] M.A.A. Aziz, A.A. Jalil, S. Triwahyono, S.M. Sidik, Methanation of carbon dioxide on metal-promoted mesostructured silica nanoparticles, *Appl. Catal. A*, Gen. 486 (2014) 115–122.
- [73] Q. Pan, J. Peng, T. Sun, D. Gao, S. Wang, S. Wang, CO₂ methanation on Ni/Ce_{0.5}Zr_{0.5}O₂ catalysts for the production of synthetic natural gas, *Fuel Process. Technol.* 123 (2014) 166–171.
- [74] L. Falbo, C.G. Visconti, L. Lietti, J. Szanyi, The effect of CO on CO₂ methanation over Ru/Al₂O₃ catalysts: a combined steady-state reactivity and transient DRIFT spectroscopy study, *Appl. Catal. B Environ.* 256 (2019) 117791.
- [75] A. Karelovic, P. Ruiz, Mechanistic study of low temperature CO₂ methanation over Rh/TiO₂ catalysts, *J. Catal.* 301 (2013) 141–153.
- [76] P. Panagiotopoulou, Hydrogenation of CO₂ over supported noble metal catalysts, *Appl. Catal. A*, Gen. 542 (2017) 63–70.
- [77] T. Van Herwijnen, H. Van Doesburg, W.A. De Jong, Kinetics of the methanation of CO and CO₂ on a nickel catalyst, *J. Catal.* 28 (1973) 391–402.
- [78] P.A.U. Aldana, F. Ocampo, K. Kobl, B. Louis, F. Thibault-Starzyk, M. Daturi, P. Bazin, S. Thomas, A.C. Roger, Catalytic CO₂ valorization into CH₄ on Ni-based ceria-zirconia. Reaction mechanism by operando IR spectroscopy, *Catal. Today.* 215 (2013) 201–207.
- [79] M. V. Konishcheva, D.I. Potemkin, S.D. Badmaev, P. V. Snytnikov, E.A. Paukshtis, V.A. Sobyanin, V.N. Parmon, On the Mechanism of CO and CO₂ Methanation Over Ni/CeO₂ Catalysts, *Top. Catal.* 59 (2016) 1424–1430.
- [80] K.P. Brooks, J. Hu, H. Zhu, R.J. Kee, Methanation of carbon dioxide by hydrogen reduction using the Sabatier process in microchannel reactors, *Chem. Eng. Sci.* 62 (2007) 1161–1170.
- [81] R.K. Singha, A. Shukla, A. Yadav, L.N. Sivakumar Konathala, R. Bal, Effect of metal-support interaction on activity and stability of Ni-CeO₂ catalyst for partial oxidation of methane, *Appl. Catal. B Environ.* 202 (2017) 473–488.
- [82] C. Italiano, J. Llorca, L. Pino, M. Ferraro, V. Antonucci, A. Vita, A. Energy, T. Nicola, V.S. Lucia, CO and CO₂ methanation over Ni catalysts supported on CeO₂, Al₂O₃ and Y₂O₃ oxides, *Appl. Catal. B Environ.* 264 (2020) 118494.
- [83] J. Liu, C. Li, F. Wang, S. He, H. Chen, Y. Zhao, M. Wei, D.G. Evans, X. Duan, Enhanced low-temperature activity of CO₂ methanation over highly-dispersed Ni/TiO₂ catalyst, *Catal. Sci. Technol.* 3 (2013) 2627–2633.
- [84] R.P. Ye, W. Gong, Z. Sun, Q. Sheng, X. Shi, T. Wang, Y. Yao, J.J. Razink, L. Lin, Z. Zhou, H. Adidharma, J. Tang, M. Fan, Y.G. Yao, Enhanced stability of Ni/SiO₂ catalyst for CO₂ methanation: Derived from nickel phyllosilicate with strong metal-support interactions, *Energy.* 188 (2019) 116059.

- [85] A. Beuls, C. Swalus, M. Jacquemin, G. Heyen, A. Karelovic, P. Ruiz, Methanation of CO₂: Further insight into the mechanism over Rh/γ-Al₂O₃ catalyst, *Appl. Catal. B Environ.* 113–114 (2012) 2–10.
- [86] G. Tang, D. Gong, H. Liu, L. Wang, Highly loaded mesoporous Ni–La₂O₃ catalyst prepared by colloidal solution combustion method for CO₂ methanation, *Catalysts*. 9 (2019) 442.
- [87] Z. Wu, M. Li, S.H. Overbury, On the structure dependence of CO oxidation over CeO₂ nanocrystals with well-defined surface planes, *J. Catal.* 285 (2012) 61–73.
- [88] R.P. Ye, Q. Li, W. Gong, T. Wang, J.J. Razink, L. Lin, Y.Y. Qin, Z. Zhou, H. Adidharma, J. Tang, A.G. Russell, M. Fan, Y.G. Yao, High-performance of nanostructured Ni/CeO₂ catalyst on CO₂ methanation, *Appl. Catal. B Environ.* 268 (2019) 118474.
- [89] A. Cárdenas-Arenas, A. Quindimil, A. Davó-Quiñonero, E. Bailón-García, D. Lozano-Castelló, U. De-La-Torre, B. Pereda-Ayo, J.A. González-Marcos, J.R. González-Velasco, A. Bueno-López, Isotopic and in situ DRIFTS study of the CO₂ methanation mechanism using Ni/CeO₂ and Ni/Al₂O₃ catalysts, *Appl. Catal. B Environ.* 265 (2020) 118538.
- [90] X. Jia, X. Zhang, N. Rui, X. Hu, C. jun Liu, Structural effect of Ni/ZrO₂ catalyst on CO₂ methanation with enhanced activity, *Appl. Catal. B Environ.* 244 (2019) 159–169.
- [91] F. Ocampo, B. Louis, A.C. Roger, Methanation of carbon dioxide over nickel-based Ce_{0.72}Zr_{0.28}O₂ mixed oxide catalysts prepared by sol-gel method, *Appl. Catal. A Gen.* 369 (2009) 90–96.
- [92] F. Ocampo, B. Louis, L. Kiwi-Minsker, A.C. Roger, Effect of Ce/Zr composition and noble metal promotion on nickel based Ce_xZr_{1-x}O₂ catalysts for carbon dioxide methanation, *Appl. Catal. A Gen.* 392 (2011) 36–44.
- [93] B. Sellers-antón, E. Bailon-garcía, A. Cárdenas-arenas, A. Davó-quiñonero, D. Lozano-castello, A. Bueno-lópez, Enhancement of the generation and transfer of active oxygen in Ni/CeO₂ catalysts for soot combustion by controlling the Ni-ceria contact and the three-dimensional structure, *Environ. Sci. Technol.* 54 (2020) 2439–2447.
- [94] V. Alcalde-santiago, E. Bailón-garcía, A. Davó-quiñonero, D. Lozano-castelló, A. Bueno-lópez, Three-dimensionally ordered macroporous PrOx: An improved alternative to ceria catalysts for soot combustion, *Appl. Catal. B Environ.* 248 (2019) 567–572.
- [95] V. Alcalde-Santiago, A. Davó-Quiñonero, D. Lozano-Castelló, A. Bueno-López, On the soot combustion mechanism using 3DOM ceria catalysts, *Appl. Catal. B Environ.* 234 (2018) 187–197.
- [96] A. Davó-Quiñonero, A.; González-Mira, J.; Such-Basañez, I.; Juan-Juan, J.;

- Lozano-Castelló, D.; Bueno-López, Improved CO Oxidation Activity of 3DOM Pr-Doped Ceria Catalysts: Something Other Than an Ordered Macroporous Structure, *Catalysts.* 7 (2017) 67.
- [97] V. Alcalde-santiago, A. Davó-quijonero, D. Lozano-castelló, On the soot combustion mechanism using 3DOM ceria catalysts, *Appl. Catal. B Environ.* 234 (2018) 187–197.
- [98] A.B. Dongil, L. Pastor-Pérez, N. Escalona, A. Sepúlveda-Escribano, Carbon nanotube-supported Ni-CeO₂ catalysts. Effect of the support on the catalytic performance in the low-temperature WGS reaction, *Carbon.* 101 (2016) 296–304.
- [99] L. Ning, S. Liao, H. Li, R. Tong, C. Dong, M. Zhang, W. Gu, X. Liu, Carbon-based materials with tunable morphology confined Ni (0) and Ni-N_x active sites: Highly efficient selective hydrogenation catalysts, *Carbon.* 154 (2019) 48–57.
- [100] S. Cattaneo, F.J.S. Trujillo, N. Dimitratos, A. Villa, The effect of carbon nanofibers surface properties in hydrogenation and dehydrogenation reactions, *Appl. Sci.* 9 (2019) 5061.
- [101] N.A.M. Barakat, M.T. Amen, F.S. Al-Mubaddel, M.R. Karim, M. Alrashed, NiSn nanoparticle-incorporated carbon nanofibers as efficient electrocatalysts for urea oxidation and working anodes in direct urea fuel cells, *J. Adv. Res.* 16 (2019) 43–53.
- [102] I.C. Gerber, P. Serp, A theory/experience description of support effects in carbon-supported catalysts, *Chem. Rev.* 120 (2019) 1250–1349.
- [103] R. Singh Rattanvir, A. Dhir, S.K. Mohapatra, Dry reforming of methane using various catalysts in the process: review, *Biomass Convers. Biorefinery.* 10 (2019) 567–587.
- [104] M.A.A. Aziz, H.D. Setiabudi, L.P. Teh, N.H.R. Annar, A.A. Jalil, A review of heterogeneous catalysts for syngas production via dry reforming, *J. Taiwan Inst. Chem. Eng.* 101 (2019) 139–158.
- [105] Y. Wang, K.S. Chen, J. Mishler, S. Chan, X. Cordobes, A review of polymer electrolyte membrane fuel cells: Technology, applications, and needs on fundamental research, *Appl. Energy.* 88 (2011) 981–1007.
- [106] A. Midilli, I. Dincer, Hydrogen as a renewable and sustainable solution in reducing global fossil fuel consumption, *Int. J. Hydrogen Energy.* 33 (2008) 4209–4222.
- [107] R. Chein, Z. Yang, Experimental study on dry reforming of biogas for syngas production over Ni-Based Catalysts, *ACS Omega.* 4 (2019) 20911–20922.
- [108] J. Gao, Z. Hou, H. Lou, X. Zheng, Dry (CO₂) reforming, in: *Fuel Cells Technol. Fuel Process.*, First Edit, Elsevier, Hangzhou, 2011: pp. 191–221.

- [109] L.S. Tan, K.K. Lau, M.A. Bustam, A.M. Shariff, Removal of high concentration CO₂ from natural gas at elevated pressure via absorption process in packed column, *J. Nat. Gas Chem.* 21 (2012) 7–10.
- [110] F. Polo-Garzon, J.K. Scott, D.A. Bruce, Microkinetic model for the dry reforming of methane on Rh doped pyrochlore catalysts, *J. Catal.* 340 (2016) 196–204.
- [111] P. Ferreira-Aparicio, I. Rodriguez-Ramos, J.A. Anderson, A. Guerrero-Ruiz, Mechanistic aspects of the dry reforming of methane over ruthenium catalysts, *Appl. Catal. A, Gen.* 202 (2000) 183–196.
- [112] G. Xanthopoulou, K. Karanasios, S. Tungatarova, T. Baizhumanova, M. Zhumabek, G. Kaumenova, B. Massalimova, K. Shorayeva, Catalytic methane reforming into synthesis gas over developed composite materials prepared by combustion synthesis, *React. Kinet. Mech. Catal.* 126 (2019) 645–661.
- [113] D. Pakhare, J. Spivey, A review of dry (CO₂) reforming of methane over noble metal catalysts, *Chem. Soc. Rev.* 43 (2014) 7813–7837.
- [114] M. Usman, W.M.A. Wan Daud, H.F. Abbas, Dry reforming of methane: Influence of process parameters — A review, *Renew. Sustain. Energy Rev.* 45 (2015) 710–744.
- [115] A. Abdulrasheed, A. Abdul, Y. Gambo, M. Ibrahim, H. Umar, M. Yusuf, S. Hamid, A review on catalyst development for dry reforming of methane to syngas: Recent advances, *Renew. Sustain. Energy Rev.* 108 (2019) 175–193.
- [116] B. De Caprariis, P. De Filippis, V. Palma, A. Petrullo, A. Ricca, C. Ruocco, M. Scarsella, Rh, Ru and Pt ternary perovskites type oxides BaZr_(1-x)Me_xO₃ for methane dry reforming, *Appl. Catal. A, Gen.* 517 (2016) 47–55.
- [117] H. Zhou, T. Zhang, Z. Sui, Y. Zhu, C. Han, K. Zhu, X. Zhou, A single source method to generate Ru-Ni-MgO catalysts for methane dry reforming and the kinetic effect of Ru on carbon deposition and gasification, *Appl. Catal. B Environ.* 233 (2018) 143–159.
- [118] A. Movasati, S. Mehdi, G. Mazloom, Dry reforming of methane over CeO₂-ZnAl₂O₄ supported Ni and Ni-Co nano- catalysts, *Fuel.* 236 (2019) 1254–1262.
- [119] X. Yan, T. Hu, P. Liu, S. Li, B. Zhao, Q. Zhang, W. Jiao, S. Chen, P. Wang, J. Lu, L. Fan, X. Deng, Y. Pan, Highly efficient and stable Ni/CeO₂-SiO₂ catalyst for dry reforming of methane: Effect of interfacial structure of Ni/CeO₂ on SiO₂, *Appl. Catal. B Environ.* 246 (2019) 221–231.
- [120] I. Luisetto, S. Tuti, C. Romano, M. Boaro, E. Di, J. Kopula, S. Senthil, K. Selvakumar, Dry reforming of methane over Ni supported on doped CeO₂: New insight on the role of dopants for CO₂ activation, *J. CO₂ Util.* 30 (2019) 63–78.
- [121] A. Fontana Dalla, B. Faroldi, L.M. Cornaglia, A.M. Tarditi, Development of catalytic membranes over PdAu selective films for hydrogen production through

- the dry reforming of methane, Mol. Catal. 481 (2020) 100643.
- [122] R. Vakili, R. Gholami, C.E. Stere, S. Chansai, H. Chen, S.M. Holmes, Y. Jiao, C. Hardacre, X. Fan, Plasma-assisted catalytic dry reforming of methane (DRM) over metal- organic frameworks (MOFs)-based catalysts, Appl. Catal. B Environ. 260 (2020) 118195.
 - [123] X. Tu, J.C. Whitehead, Plasma-catalytic dry reforming of methane in an atmospheric dielectric barrier discharge: Understanding the synergistic effect at low temperature, Appl. Catal. B Environ. 125 (2012) 439–448.
 - [124] Q. Zhang, T. Tang, J. Wang, M. Sun, H. Wang, H. Sun, P. Ning, Facile template-free synthesis of Ni-SiO₂ catalyst with excellent sintering- and coking-resistance for dry reforming of methane, Catal. Commun. 131 (2019) 105782.
 - [125] A.S. Al-fatesh, J.K. Abu-dahrieh, H. Atia, U. Armbruster, A.A. Ibrahim, W.U. Khan, A. Elhag, A.H. Fakeeha, Effect of pre-treatment and calcination temperature on Al₂O₃-ZrO₂ supported Ni-Co catalysts for dry reforming of methane, Int. J. Hydrogen Energy. 44 (2019) 21546–21558.
 - [126] X. Hu, X. Jia, X. Zhang, Y. Liu, C. Liu, Improvement in the activity of Ni/ZrO₂ by cold plasma decomposition for dry reforming of methane, Catal. Commun. 128 (2019) 105720.
 - [127] M. Shah, A. Bordoloi, A. Kumar, P. Mondal, Effect of Ti/Al ratio on the performance of Ni/TiO₂-Al₂O₃ catalyst for methane reforming with CO₂, Fuel Process. Technol. 192 (2019) 21–35.
 - [128] R.O. da Fonseca, R.C. Rabelo-Neto, R.C.C. Simoes, L. V. Mattos, F.B. Noronha, Pt supported on doped CeO₂/Al₂O₃ as catalyst for dry reforming of methane, Int. J. Hydrogen Energy. 45 (2020) 5182–5191.
 - [129] J. Lv, D. Wang, M. Wang, Y. Li, L. Jin, H. Hu, Integrated coal pyrolysis with dry reforming of low carbon alkane over Ni/La₂O₃ to improve tar yield, Fuel. 266 (2020) 117092.
 - [130] S. Devasahayam, Catalytic actions of MgCO₃/MgO system for efficient carbon reforming processes, Sustain. Mater. Technol. 22 (2019) e00122.
 - [131] A. Kambolis, H. Matralis, A. Trovarelli, C. Papadopoulou, Ni/CeO₂-ZrO₂ catalysts for the dry reforming of methane, Appl. Catal. A Gen. 377 (2010) 16–26.
 - [132] N. Abdel, K. Aramouni, J.G. Touma, B.A. Tarboush, J. Zeaiter, M.N. Ahmad, Catalyst design for dry reforming of methane: Analysis review, Renew. Sustain. Energy Rev. 82 (2018) 2570–2585.
 - [133] D.G. Araiza, D.G. Arcos, A. Gómez-cortés, G. Díaz, Dry reforming of methane over Pt-Ni/CeO₂ catalysts: Effect of the metal composition on the stability, Catal. Today. (2019).

- [134] A. Stein, Sphere templating methods for periodic porous solids, *Microporous Mesoporous Mater.* 45 (2001) 227–239.
- [135] Y. Liu, H. Dai, Y. Du, J. Deng, L. Zhang, Z. Zhao, C.T. Au, Controlled preparation and high catalytic performance of three-dimensionally ordered macroporous LaMnO₃ with nanovoid skeletons for the combustion of toluene, *J. Catal.* 287 (2012) 149–160.
- [136] H. Arandiyan, H. Dai, J. Deng, Y. Liu, B. Bai, Y. Wang, X. Li, S. Xie, J. Li, Three-dimensionally ordered macroporous La_{0.6}Sr_{0.4}MnO₃ with high surface areas: Active catalysts for the combustion of methane, *J. Catal.* 307 (2013) 327–339.
- [137] H. Liu, Y. Wu, L. Liu, B. Chu, Z. Qin, G. Jin, Z. Tong, L. Dong, B. Li, Three-dimensionally ordered macroporous Fe-doped ceria catalyst with enhanced activity at a wide operating temperature window for selective catalytic reduction of NO_x, *Appl. Surf. Sci.* 498 (2019) 143780.
- [138] A. Stein, R.C. Schroden, Colloidal crystal templating of three-dimensionally ordered macroporous solids: Materials for photonics and beyond, *Curr. Opin. Solid State Mater. Sci.* 5 (2001) 553–564.
- [139] A. Ricca, L. Truda, V. Palma, Study of the role of chemical support and structured carrier on the CO₂ methanation reaction, *Chem. Eng. J.* 377 (2019) 120461.
- [140] J. Jiao, Y. Wei, Y. Zhao, Z. Zhao, A. Duan, J. Liu, Y. Pang, J. Li, G. Jiang, Y. Wang, AuPd/3DOM-TiO₂ catalysts for photocatalytic reduction of CO₂: High efficient separation of photogenerated charge carriers, *Appl. Catal. B, Environ.* 209 (2017) 228–239.
- [141] Y.S. Minjie Zhao, Jianlin Deng, Jian Liu, Yongheng Li, Jixing Liu, Zhichen Duan, Jing Xiong, Zhen Zhao, Yuechang Wei, Weiyu Song, Roles of Surface-Active Oxygen Species on 3DOM Cobalt-Based Spinel Catalysts M_xCo_{3-x}O₄ (M = Zn and Ni) for NO_x-Assisted Soot Oxidation, *ACS Catal.* 9 (2019) 7548–7567.
- [142] M.N. Ha, G. Lu, Z. Liu, L. Wang, Z. Zhao, 3DOM-LaSrCoFeO_{6-δ} as a highly active catalyst for thermal and photothermal reduction of CO₂ with H₂O to CH₄, *J. Mater. Chem. A.* 4 (2016) 13155–13165.
- [143] H. Li, L. Zhang, H. Dai, H. He, Facile synthesis and unique physicochemical properties of three-dimensionally ordered macroporous magnesium oxide, gamma-alumina, and ceria-zirconia solid solutions with crystalline mesoporous walls, *Inorg. Chem.* 48 (2009) 4421–4434.
- [144] J. Zhang, Y. Jin, C. Li, Y. Shen, L. Han, Z. Hu, X. Di, Z. Liu, Creation of three-dimensionally ordered macroporous Au/CeO₂ catalysts with controlled pore sizes and their enhanced catalytic performance for formaldehyde oxidation, *Appl. Catal. B Environ.* 91 (2009) 11–20.

- [145] D. Han, X. Li, L. Zhang, Y. Wang, Z. Yan, S. Liu, Hierarchically ordered meso/macroporous γ -alumina for enhanced hydrodesulfurization performance, *Microporous Mesoporous Mater.* 158 (2012) 1–6.
- [146] X. Zhang, Y. Liu, J. Deng, X. Yu, Z. Han, K. Zhang, H. Dai, Alloying of gold with palladium: An effective strategy to improve catalytic stability and chlorine-tolerance of the 3DOM CeO₂-supported catalysts in trichloroethylene combustion, *Appl. Catal. B Environ.* 257 (2019) 117879.
- [147] W. Pei, Y. Liu, J. Deng, K. Zhang, Z. Hou, X. Zhao, H. Dai, Partially embedding Pt nanoparticles in the skeleton of 3DOM Mn₂O₃: An effective strategy for enhancing catalytic stability in toluene combustion, *Appl. Catal. B Environ.* 256 (2019) 117814.
- [148] X. Zhao, R. Zhang, Y. Liu, J. Deng, P. Xu, J. Yang, Z. Han, In-situ reduction-derived Pd/3DOM La_{0.6}Sr_{0.4}MnO₃: Good catalytic stabilityin methane combustion, *Appl. Catal. A, Gen.* 568 (2018) 202–212.
- [149] V. Alcalde-Santiago, A. Davó-Quiñonero, I. Such-Basáñez, D. Lozano-Castelló, A. Bueno-López, Macroporous carrier-free Sr-Ti catalyst for NO_x storage and reduction, *Appl. Catal. B Environ.* 220 (2018) 524–532.
- [150] A.I. Journal, L. Li, W. Zhang, V. Devanatha, D. Seshadri, Synthesis and characterization of gold nanoparticles from Marsdenia tenacissima and its anticancer activity of liver cancer HepG2 cells and its anticancer activity of liver cancer HepG2 cells, *Artif. Cells, Nanomedicine, Biotechnol.* 47 (2019) 3029–3036.
- [151] J.-M. Nam, C.S. Thaxton, C.A. Mirkin, Nanoparticle-based bio-bar codes for the ultrasensitive detection of proteins, *Science.* 301 (2003) 1884–1886.
- [152] L. Pot, F. Franko, M. Bambousková, P. Dráber, Rapid and sensitive detection of cytokines using functionalized gold nanoparticle-based immuno-PCR , comparison with immuno-PCR and ELISA, *J. Immunol. Methods.* 371 (2011) 38–47.
- [153] M. Streckova, J. Szabo, I. Batko, M. Batkova, Z. Bircakova, J. Fuzer, P. Kollar, A. Kovalcikova, R. Bures, L. Medvecky, Design of Permalloy – ferrite – polymer soft magnetic composites doped by ferrite nanoparticles and visualization of magnetic, *Bull. Mater. Sci.* 43 (2020) 37.
- [154] M. Wojtalik, Z. Bojarska, Ł. Makowski, Experimental studies on the chemical wet synthesis for obtaining high-quality MoS₂ nanoparticles using impinging jet reactor, *J. Solid State Chem.* 285 (2020) 121254.
- [155] X. Cui, T. Wei, M. Hao, Q. Qi, H. Wang, Z. Dai, Highly sensitive and selective colorimetric sensor for thiocyanate based on electrochemical oxidation-assisted complexation reaction with Gold nanostars etching, *J. Hazard. Mater.* 391 (2020) 122217.

- [156] J. Liu, J. Jiang, Y. Meng, A. Aihemaiti, Y. Xu, H. Xiang, Y. Gao, X. Chen, Preparation, environmental application and prospect of biochar-supported metal nanoparticles: A review, *J. Hazard. Mater.* 388 (2020) 122026.
- [157] Z. Cheng, X. Chu, W. Zhao, J. Yin, B. Dai, H. Zhong, J. Xu, Controllable synthesis of Cu/Al energetic nanocomposites with excellent heat release and combustion performance, *Appl. Surf. Sci.* 513 (2020) 145704.
- [158] D. Xu, Y. Yang, H. Cheng, Y. Yang, K. Zhang, Integration of nano-Al with Co₃O₄ nanorods to realize high-exothermic core – shell nanoenergetic materials on a silicon substrate, *Combust. Flame*. 159 (2012) 2202–2209.
- [159] M. Fattahi, A. Ghaheri, N. Arabian, F. Amirkhanlu, H. Moayedi, Applying the ultrasonic vibration during TIG welding as a promising approach for the development of nanoparticle dispersion strengthened aluminum weldments, *J. Mater. Process. Tech.* 282 (2020) 116672.
- [160] E. Guo, S. Shuai, D. Kazantsev, S. Karagadde, A.B. Phillion, T. Jing, W. Li, P.D. Lee, The influence of nanoparticles on dendritic grain growth in Mg alloys, *Acta Mater.* 152 (2019) 127–137.
- [161] T.H. Pham, H. An, Q. Than, H.M. Bui, The catalytic oxidation of toluene at low temperature over palladium nanoparticles supported on alumina sphere catalysts: effects of palladium precursors and preparation method, *Polish J. Chem. Technol.* 21 (2019) 48–50.
- [162] H. Zhou, Y. Zhao, J. Xu, H. Sun, Z. Li, W. Liu, T. Yuan, W. Liu, X. Wang, W. Cheong, Z. Wang, X. Wang, C. Zhao, Y. Yao, W. Wang, F. Zhou, M. Chen, B. Jin, R. Sun, J. Liu, X. Hong, T. Yao, S. Wei, J. Luo, Y. Wu, Recover the activity of sintered supported catalysts by nitrogen-doped carbon atomization, *Nat. Commun.* 11 (2020) 335.
- [163] I. Khan, K. Saeed, I. Khan, Nanoparticles: Properties, applications and toxicities, *Arab. J. Chem.* 12 (2019) 908–931.
- [164] Y. Zhou, C. Jin, Y. Li, W. Shen, Dynamic behavior of metal nanoparticles for catalysis, *Nano Today*. 20 (2018) 101–120.
- [165] A.V. Rane, K. Kanny, V.K. Abitha, S. Thomas, Methods for synthesis of nanoparticles and fabrication of nanocomposites, in: *Synth. Inorg. Nanomater.*, Elsevier Ltd., 2018: pp. 121–139.
- [166] P. Govindrao, N.W. Ghule, A. Haque, M.G. Kalaskar, Metal nanoparticles synthesis: An overview on methods of preparation, advantages and disadvantages, and applications, *J. Drug Deliv. Sci. Technol.* 53 (2019) 101174.
- [167] M.A. Malik, M. Younus, M.A. Hashim, Microemulsion method: A novel route to synthesize organic and inorganic nanomaterials, *Arab. J. Chem.* 5 (2012) 397–417.
- [168] R. Kosydar, I. Szewczyk, P. Natkański, D. Duraczyńska, J. Gurgul, P.

- Kuśtrowski, A. Drelinkiewicz, New insight into the effect of surface oxidized groups of nanostructured carbon supported Pd catalysts on the furfural hydrogenation, *Surfaces and Interfaces*. 17 (2019) 100379.
- [169] M. Duan, L. Jiang, G. Zeng, D. Wang, W. Tang, J. Liang, H. Wang, D. He, Z. Liu, L. Tang, Bimetallic nanoparticles/metal-organic frameworks: Synthesis, applications and challenges, *Appl. Mater. Today*. 19 (2020) 100564.
 - [170] E. Bagheri, L. Ansari, E. Sameiyan, K. Abnous, S. Mohammad, M. Ramezani, M. Alibolandi, Biosensors and bioelectronics sensors design based on hybrid gold-silica nanostructures, *Biosens. Bioelectron.* 153 (2020) 112054.
 - [171] D. Li, B. Kumari, X. Zhang, C. Wang, X. Mei, V.M. Rotello, Purification and separation of ultra-small metal nanoclusters, *Adv. Colloid Interface Sci.* 276 (2020) 102090.
 - [172] Y. Zhang, J. Zhang, B. Zhang, R. Si, B. Han, F. Hong, L. Sun, L. Li, B. Qiao, K. Sun, J. Huang, M. Haruta, Boosting the catalysis of gold by O₂ activation at Au-SiO₂ interface, *Nat. Commun.* 11 (2020) 558.
 - [173] N.K. Reddy Bogireddy, P. Sahare, U. Pal, S.F. Olive Méndez, L. Martinez Gomez, V. Agarwal, Platinum nanoparticle-assembled porous biogenic silica 3D hybrid structures with outstanding 4-nitrophenol degradation performance, *Chem. Eng. J.* 388 (2020) 124237.
 - [174] Z. Guo, X. Kang, X. Zheng, J. Huang, S. Chen, PdCu alloy nanoparticles supported on CeO₂ nanorods: Enhanced electrocatalytic activity by synergy of compressive strain, PdO and oxygen vacancy, *J. Catal.* 374 (2019) 101–109.
 - [175] R. Dou, H. Cheng, J. Ma, Y. Qin, Y. Kong, S. Komarneni, Catalytic degradation of methylene blue through activation of bisulfite with CoO nanoparticles, *Sep. Purif. Technol.* 239 (2020) 116561.
 - [176] A.F. Baye, R. Appiah-ntiamoah, H. Kim, Synergism of transition metal (Co, Ni, Fe, Mn) nanoparticles and “active support” Fe₃O₄@C for catalytic reduction of 4-nitrophenol Fe₃O₄ for efficient hydride formation towards 4-nitrophenol reduction ., *Sci. Total Environ.* 712 (2020) 135492.
 - [177] H. Genc, H. Burhan, F. Diler, K. Cellat, E. Kuyuldar, M. Zengin, F. Sen, Composites of palladium nanoparticles and graphene oxide as a highly active and reusable catalyst for the hydrogenation of nitroarenes, *Microporous Mesoporous Mater.* 296 (2020) 110014.
 - [178] T. Liang, H. Chen, D. Tsai, Nickel hybrid nanoparticle decorating on alumina nanoparticle cluster for synergistic catalysis of methane dry reforming, *Fuel Process. Technol.* 201 (2020) 106335.
 - [179] I. V. Yentekakis, G. Goula, M. Hatzisymeon, I. Betsi-argyropoulou, G. Botzolaki, K. Kousi, D.I. Kondarides, M.J. Taylor, C.M.A. Parlett, A. Osatiashvili, G. Kyriakou, J. Pedro, R.M. Lambert, Effect of support oxygen

- storage capacity on the catalytic performance of Rh nanoparticles for CO₂ reforming of methane, *Appl. Catal. B Environ.* 243 (2019) 490–501.
- [180] S. Ali, M.M. Khader, M.J. Almarri, A.G. Abdelmoneim, Ni-based nanocatalysts for the dry reforming of methane, *Catal. Today.* 343 (2020) 26–37.
- [181] D. Zhong, L. Ouyang, J. Liu, H. Wang, Metallic Ni nanocatalyst in situ formed from LaNi₅H₅ toward efficient CO₂ methanation, *Int. J. Hydrogen Energy.* 44 (2019) 29068–29074.
- [182] P. Riani, G. Garbarino, T. Cavattoni, F. Canepa, G. Busca, Unsupported cobalt nanoparticles as catalysts: Effect of preparation method on catalytic activity in CO₂ methanation and ethanol steam reforming, *Int. J. Hydrogen Energy.* 44 (2019) 27319–27328.
- [183] B. Roldan, F. Behafarid, Nanocatalysis: size and shape-dependent chemisorption and catalytic reactivity, *Surf. Sci. Rep.* 70 (2015) 135–187.



Universitat d'Alacant
Universidad de Alicante

2

Metodología y técnicas experimentales

2.1. Muestras y metodología de síntesis

- 2.1.1. Catalizadores sin control de la estructura
- 2.1.2. Catalizadores macroporosos con orden tridimensional 3DOM
- 2.1.3. Catalizadores basados en nanopartículas
- 2.1.4. Catalizadores NiO/CeO₂-NiO/C

2.2. Técnicas de caracterización físico-química

- 2.2.1. Adsorción física de gases
- 2.2.2. Porosimetría de mercurio
- 2.2.3. Difracción de rayos X (DRX)
- 2.2.4. Espectroscopía de emisión por plasma de acoplamiento inductivo (ICP-OES)
- 2.2.5. Microscopía electrónica de barrido (SEM)
- 2.2.6. Microscopía electrónica de transmisión (TEM)
- 2.2.7. Reacciones a temperatura programada: H₂-TPR y He-TPD
- 2.2.8. Espectroscopía fotoelectrónica de rayos X (XPS)
- 2.2.9. Termogravimetría (TG)

2.3. Ensayos de actividad catalítica

- 2.3.1. Reacción de metanación de CO₂ (MCMA-UA)
- 2.3.2. Reacción de metanación de CO₂ (TQSA-UPV)
- 2.3.3. Reacción de reformado seco de metano (CEPT-US)

2.4. Técnicas de caracterización avanzadas utilizadas en el estudio del mecanismo de reacción de la metanación de CO₂

- 2.4.1. Ensayos isotópicos con pulsos de ¹³C¹⁸O₂
- 2.4.2. Ensayos DRIFTS in-situ

2.5. Referencias

2.1. Muestras y metodología de síntesis

En esta tesis doctoral se han preparado catalizadores basados en níquel-ceria, los cuales han sido preparados con diferentes estructuras morfológicas: catalizadores sin modificación de su estructura, catalizadores macroporosos con orden tridimensional (3DOM), nanopartículas y sistemas Ni/ceria-Ni/carbón. El contenido teórico de Ni en todos los catalizadores fue de 8.5 %p/p. Como precursor de níquel se utilizó $\text{Ni}(\text{NO}_3)_2 \cdot 6\text{H}_2\text{O}$ (Sigma-Aldrich) y como precursor de cerio se utilizó $\text{Ce}(\text{NO}_3)_3 \cdot 6\text{H}_2\text{O}$ (99.5%, Alfa Aesar). Los detalles de todos los métodos de preparación son descritos a continuación. En cada capítulo se indicará, específicamente, los catalizadores que han sido utilizados.

La Tabla 2.1. muestra los catalizadores utilizados en el desarrollo del presente trabajo de investigación, indicando su respectiva nomenclatura y estructura.

Tabla 2.1. Muestras sintetizadas

Muestra	Estructura
NiO/Al ₂ O ₃ -US (I)	No definida
CeO ₂ -US	No definida
NiO/CeO ₂ -US (I)	No definida
NiO-CeO ₂ -US (CI)	No definida
CeO ₂ -3DOM	3DOM
NiO/CeO ₂ -3DOM (I)	3DOM
NiO-CeO ₂ -3DOM (CI)	3DOM
NiO/CeO ₂ -3DOM (SI)	3DOM
NiO-CeO ₂ -np	Nanopartículas
NiO-CeO ₂ -np/NiO-CeO ₂ -3DOM (CI)	Nanopartículas/3DOM
CeO ₂ -np/NiO	Nanopartículas/No definida
NiO/CeO ₂	No definida
NiO/C	Xerogel de carbón
75%NiO/CeO ₂ -25%NiO/C	Xerogel de carbón
50%NiO/CeO ₂ -50%NiO/C	Xerogel de carbón
25%NiO/CeO ₂ -75%NiO/C	Xerogel de carbón

2.1.1. Catalizadores sin control de la estructura:

En este estudio se han preparado catalizadores convencionales, sin control de su estructura. Estos catalizadores han sido referenciados como NiO/Al₂O₃-US (I), NiO/CeO₂-US (I), NiO-CeO₂-US (CI) y NiO/CeO₂y el método de síntesis utilizado para su obtención se describe a continuación:

- ❖ *NiO/Al₂O₃-US (I):*

Se preparó mediante impregnación húmeda incipiente del soporte de alúmina (γ -Alúmina comercial, Alfa Aesar, Stock nº 43855) con Ni(NO₃)₂·6H₂O disuelto en etanol. Se secó a 80 °C durante 24 horas y, seguidamente, se calcinó a 600 °C en aire durante 6 horas, usando una velocidad de calentamiento de 5 °C/min.

- ❖ *CeO₂-US y NiO/CeO₂-US (I):*

El soporte de óxido de cerio (CeO₂-US) fue preparado disolviendo en etanol Ce(NO₃)₃·6H₂O y ácido cítrico en proporciones estequiométricas. Posteriormente, se secó a 80 °C durante 24 horas y se calcinó a 600 °C en aire durante 6 horas, usando una velocidad de calentamiento de 5 °C/min. El catalizador NiO/CeO₂-US (I) fue preparado por medio del método de impregnación húmeda incipiente del soporte CeO₂-US con una disolución etanólica de Ni(NO₃)₂·6H₂O. Seguidamente, se realizó el mismo tratamiento térmico utilizado para la obtención del soporte CeO₂-US, descrito anteriormente.

- ❖ *NiO-CeO₂-US (CI):*

Se preparó disolviendo los precursores Ni(NO₃)₂·6H₂O y Ce(NO₃)₃·6H₂O en etanol. Se agregó ácido cítrico para formar los respectivos citratos (Ni/ácido cítrico relación molar 1:4, Ce/ácido cítrico relación molar 1:1). Se secó a 80 °C durante 24 horas y, seguidamente, se calcinó a 600 °C en aire durante 6 horas, usando una velocidad de calentamiento de 5 °C/min.

- ❖ *NiO/CeO₂:*

El soporte de CeO₂ se preparó mediante calcinación del nitrato de cerio (Ce(NO₃)₃·6H₂O) a 600 °C en aire durante 6 horas, usando una velocidad de calentamiento de 5 °C/min y posterior impregnación con Ni(NO₃)₂·6H₂O disuelto en etanol. Finalmente, se secó a 80 °C durante 24 horas y se realizó el mismo tratamiento térmico descrito anteriormente.

2.1.2. *Catalizadores macroporosos con orden tridimensional 3DOM:*

Se han preparado catalizadores avanzados, basados en un sólido plantilla tridimensional, los cuales han sido referenciados como NiO/CeO₂-3DOM (I), NiO-CeO₂-3DOM (CI) y NiO/CeO₂-3DOM (SI). Para la preparación de la estructura 3DOM, se sintetizó una plantilla consistente en cristales coloidales de esferas monodispersas de polimetilmacrilato (PMMA). La síntesis del PMMA fue realizada siguiendo un procedimiento descrito en otra investigación [1]. Esta plantilla fue preparada por polimerización de metilmacrilato, ácido metacrílico y divinilbenceno. Se utilizó K₂S₂O₈ como iniciador para la reacción de polimerización. Después de completarse la síntesis, los cristales coloidales de PMMA son obtenidos mediante centrifugación. Una vez obtenidas las esferas de PMMA se incorporó el níquel y la ceria mediante diferentes métodos de síntesis (impregnación, co-impregnación e impregnación sucesiva) los cuales son descritos a continuación:

❖ *Soporte CeO₂-3DOM*

Se obtuvo mediante impregnación húmeda incipiente del PMMA con una disolución etanólica de Ce(NO₃)₃·6H₂O y ácido cítrico en una proporción equimolar. El exceso se eliminó bajo vacío suave. Después de secar a 80 °C durante 24 horas, se calcinó a 600 °C en aire durante 6 horas, para eliminar la plantilla del PMMA y formar el respectivo óxido de cerio.

❖ *NiO/CeO₂-3DOM (I)*

Se obtuvo mediante el método de impregnación. La fase activa se incorporó al soporte CeO₂-3DOM mediante impregnación húmeda incipiente de una disolución etanólica de Ni(NO₃)₂·6H₂O. Seguidamente, se secó a 80 °C durante 24 horas y se calcinó en aire a 600 °C durante 6 horas a una velocidad de calentamiento de 5 °C/min.

❖ *NiO-CeO₂-3DOM (CI):*

Se obtuvo por el método de coimpregnación. La plantilla de PMMA fue impregnada con una disolución etanólica que contenía los precursores de NiO y CeO₂ y la correspondiente cantidad de ácido cítrico necesaria para formar los respectivos citratos (Ni/ácido cítrico relación molar 1:4, Ce/ácido cítrico relación molar 1:1). Después de secar a 80 °C durante 24 horas se calcinó a 600 °C durante 6 horas para eliminar la plantilla polimérica y formar los respectivos óxidos.

❖ *NiO/CeO₂-3DOM (SI):*

Se obtuvo mediante impregnación sucesiva. El Ni(NO₃)₂·6H₂O se disolvió en etanol y se añadió ácido cítrico en una relación molar de 1:4. La solución se agregó al PMMA mediante impregnación húmeda incipiente y el exceso se eliminó bajo vacío. Despues de secar a 80 °C se agregó una disolución etanólica de Ce(NO₃)₃·6H₂O y ácido cítrico en una relación equimolar. Finalmente se realizó el mismo tratamiento térmico descrito anteriormente para eliminar la plantilla de PMMA y formar los respectivos óxidos.

2.1.3. Catalizadores basados en nanopartículas:

En este estudio fueron preparados tres catalizadores basados en nanopartículas, los cuales han sido referenciados como NiO-CeO₂-np, NiO-CeO₂-np/NiO-CeO₂-3DOM (CI) y CeO₂-np/NiO. Las nanopartículas fueron obtenidas mediante el método de microemulsión inversa, modificando una síntesis reportada previamente [2,3]. La síntesis de estos catalizadores es descrita a continuación:

❖ *NiO-CeO₂-np:*

Inicialmente, se preparó una disolución acuosa con los precursores metálicos Ni(NO₃)₂·6H₂O y Ce(NO₃)₃·6H₂O. Luego, se preparó una primera microemulsión en n-heptano con Tritón X-100 como surfactante y hexanol como cosurfactante. Una segunda microemulsión fue preparada en forma similar a la primera, pero en lugar de los precursores metálicos, se agregó hidróxido de tetrametilamonio. Se mezclaron las dos microemulsiones y se agitó durante 24 horas. Seguidamente, se centrifugó a 3000 rev/min durante 6 minutos y se decantó la fase líquida. Finalmente, el sólido obtenido se lavó con agua desionizada, se secó a 110 °C y se calcinó a 500 °C durante 1 hora.

❖ *NiO-CeO₂-np/NiO-CeO₂-3DOM (CI):*

El catalizador NiO-CeO₂-3DOM (CI) fue utilizado como soporte de las nanopartículas NiO-CeO₂-np. Las nanopartículas de óxido mixto NiO-CeO₂-np fueron dispersas en etanol utilizando ultrasonido durante 3 horas. Seguidamente, el NiO-CeO₂-3DOM (CI) fue agregado a la suspensión. Se utilizó una proporción NiO-CeO₂-np y NiO-CeO₂-3DOM (CI) de 1:1. La mezcla se mantuvo en agitación durante 24 horas. Posteriormente, el catalizador se secó utilizando agitación con burbujeo de nitrógeno y finalmente, se calcinó a 500 °C durante 1 hora.

❖ *CeO₂-np/NiO*

Las nanopartículas de CeO₂ fueron preparadas siguiendo el mismo método de síntesis de las nanopartículas mixtas NiO-CeO₂-np, pero sin agregar el precursor metálico Ni(NO₃)₂·6H₂O. El bulk de NiO fue sintetizado mediante calcinación del precursor de níquel a 600 °C durante 6 horas. Seguidamente, fue impregnado con una suspensión etanólica de CeO₂-np. Finalmente, se secó a 80 °C para obtener el sólido.

2.1.4. Catalizadores NiO/CeO₂-NiO/C:

Se han preparado catalizadores basados en una mezcla física de NiO/CeO₂ y NiO/C. Los catalizadores de este estudio han sido referenciados como 25%NiO/CeO₂-75%NiO/C, 50%NiO/CeO₂-50%NiO/C, 75%NiO/CeO₂-25%NiO/C. El componente Ni/CeO₂ ha sido obtenido por el método de síntesis descrito en el apartado 2.1.1. La síntesis del componente NiO/C se describen a continuación. Una vez obtenidos el NiO/CeO₂ nitrato y el NiO/C se mezclaron con la ayuda de un mortero en proporciones de 25, 50 y 75% de NiO/C hasta tener un aspecto homogéneo.

❖ *NiO/C:*

El xerogel de carbón fue obtenido por el método de emulsión inversa usando resorcinol - formaldehido como precursor del carbón y Teepol como surfactante aniónico. La síntesis del xerogel de carbón ha sido realizada modificando un trabajo previo [4]. Una primera disolución fue preparada con 10 mL de Teepol disuelto en 700 mL de n-heptano. Seguidamente, se calentó hasta 65 °C bajo reflujo y se agitó a 450 rev/min. Una segunda disolución fue preparada mezclando resorcinol, formaldehido y agua, se agregó gota a gota a la primera disolución y se dejó envejecer a 70 °C durante 24 horas en agitación. El gel formado se filtró para obtener el sólido y, para intercambiar el agua que queda dentro de los poros, fue dejado en acetona durante 5 días, haciendo un cambio de acetona 2 veces al día. Finalmente, se filtró y se secó en microondas hasta tener un peso constante. Para obtener el xerogel de carbón se carbonizó a 900 °C durante 2 horas en un horno tubular usando un flujo de N₂ de 300 mL/min, con una velocidad de calentamiento de 5 °C/min. Luego de impregnar la fase activa de níquel por impregnación húmeda incipiente se trató en un flujo de 100 mL/min de N₂ a 350 °C durante 2 horas, con una velocidad de calentamiento de 5 °C/min.

2.2. Técnicas de caracterización físico-química

La actividad catalítica, la selectividad y la estabilidad de un material se ve influenciado por propiedades físico-químicas como la porosidad, la estructura cristalina y la química superficial. Con el objetivo de entender el comportamiento catalítico de los distintos catalizadores empleados en esta investigación se emplearon distintas técnicas de caracterización.

Los equipos utilizados para la caracterización físico-química de los catalizadores se encuentran en las instalaciones de los Servicios Técnicos de Investigación de la universidad de Alicante (SSTI-UA) y en los laboratorios del grupo de investigación en Materiales Carbonosos y Medio Ambiente de la universidad de Alicante (MCMA-UA). A continuación, se realiza una descripción de los principios físico-químicos de cada técnica empleada en esta tesis indicando, además, las condiciones de operación utilizadas en los ensayos de caracterización.

2.2.1. Adsorción física de gases

La adsorción de gases es una de las técnicas más importantes para la caracterización textural de sólidos porosos. Esta técnica permite conocer el tipo de porosidad, cuantificar el volumen de poros de un material y su área superficial específica aparente (m^2/g). Cuando un gas (adsorbato) se pone en contacto con un sólido poroso (adsorbente) en un espacio cerrado a una determinada presión y temperatura, el sólido adsorbe el gas incrementando su peso y disminuyendo la presión del gas en el recipiente. Una vez alcanzado el equilibrio, la presión se hace constante, lo que permite establecer una relación entre las moléculas adsorbidas y la presión a temperatura constante que se representa por medio de una isoterma de adsorción [5]. Estos parámetros tienen una gran trascendencia en catálisis heterogénea, donde el proceso químico transcurre en la interfase sólido-gas (o líquido), que depende muy fuertemente de la superficie activa del catalizador y de su porosidad.

Las isothermas de adsorción proporcionan información sobre el volumen adsorbido a una determinada presión y el análisis de estas curvas permite determinar diferentes parámetros que definen las propiedades texturales de los sólidos mediante diferentes cálculos matemáticos y modelos teóricos [5,6]. De todos los gases que se pueden utilizar como adsorbato, la adsorción de N_2 a -196 °C es la más utilizada, sin embargo, presenta problemas de difusión en la porosidad más estrecha (tamaño de poros por debajo de los 0.4 nm) [6,7], por lo que, dependiendo del material, es necesario complementarla con adsorción de CO_2 a 0 °C. El CO_2 adsorbido a 0 °C presenta una

cinética de adsorción más rápida que el N₂ cuya temperatura de adsorción es -196 °C, evitando así los problemas de difusión [8].

❖ *Área superficial específica BET:*

A partir de los datos obtenidos de las isotermas de adsorción de N₂, se puede calcular la superficie específica BET aplicando la teoría de Brunauer, Emmett y Teller (BET) (Ecuación 2.1), la cual usualmente se cumple en el rango de presiones relativas (P/P₀) entre 0.05 y 0.30 [9].

$$\frac{\frac{P}{P_0}}{n\left(1-\frac{P}{P_0}\right)} = \frac{1}{n_m C} + \frac{C-1}{n_m C} \left(\frac{P}{P_0}\right) \quad (2.1)$$

Siendo “n” el número de moles adsorbidos a una presión relativa P/P₀ (P es la presión relativa del gas y P₀ es la presión de vapor de saturación), “n_m” la capacidad de la monocapa (mol/g) y “C” una constante relacionada con el calor de adsorción. Al graficar [P/P₀]/[n(1-P/P₀)] frente a P/P₀ se obtiene una recta cuya ordenada en el origen y pendiente correspondientes a los parámetros de la ecuación BET n_m y C, respectivamente. A partir de n_m se determina el valor de la superficie aparente del sólido “S_{BET}” (Ecuación 2.2), así:

$$S_{BET} = n_m a_m N_A 10^{-21} \quad (2.2)$$

Donde, “a_m” el área que ocupa una sola molécula de adsorbato (nm²/molécula), que en el caso del N₂ a -196 °C es 0,162 nm², y “N_A” el número de Avogadro (6,022·10²³ moléculas/mol).

A partir de las isotermas de adsorción-desorción de N₂ a -196 °C también se puede calcular el volumen de la porosidad dependiendo del tamaño de la porosidad, así:

❖ *Volumen de la microporosidad (diámetro de poro $\phi < 2 \text{ nm}$):*

Se puede calcular el volumen de microporo a partir de los datos de la isoterma de adsorción de N₂ a -196 °C aplicando la ecuación de Dubinin-Radushkevich (Ecuación 2.3) [10,11]. Esta se basa en la teoría de Polanyi, la cual dice que en los microporos la condensación del gas se da en forma de capas equipotenciales [9].

$$\frac{V}{V_0} = \exp\left(\left(\frac{-1}{(E_0\beta)^2}\right)\left(RT \ln\left(\frac{P_0}{P}\right)\right)^2\right) \quad (2.3)$$

Donde, “V” es el volumen adsorbido a una presión “P”, “ V_0 ” es el volumen total de microporos, E_0 es la energía característica dependiente de cada poro, “ β ” es el coeficiente de afinidad característico del adsortivo y P_0 es la presión de saturación del adsortivo a la temperatura de trabajo. El volumen total de microporos se obtiene al representar $\log(V)$ frente al $\log(P_0/P)^2$.

❖ *Volumen de la mesoporosidad (diámetro de poro: 2 nm < ϕ < 50 nm):*

El volumen de mesoporoso se calcula por diferencia entre el volumen de N_2 adsorbido a $P/P_0 = 0.9$ y el volumen de N_2 adsorbido a $P/P_0 = 0.2$ [12,13]. El volumen se expresa como líquido. Debido a una limitación práctica de esta técnica se recomienda usar porosimetría de mercurio para $\phi > 20$ nm.

❖ *Volumen total de la porosidad:*

En términos generales, se puede calcular a partir de la cantidad de N_2 adsorbido a $P/P_0 = 0.99$. Las isotermas tipo IV, que tienen un límite de adsorción, se puede tomar como el correspondiente al volumen total de poros [13].

Los ensayos de adsorción-desorción de N_2 a -196 °C de los catalizadores sin modificación de su estructura, catalizadores 3DOM y nanopartículas se realizaron en los laboratorios del MCMA de la Universidad de Alicante. Para ello, se utilizó un equipo automático de determinación volumétrica Quantachrome, modelo Autosorb-6B (Figura 2.1a.). Este equipo consta de dos unidades, una de desgasificación y otra de adsorción. La unidad de desgasificación consiste en un sistema de vacío y seis hornos independientes cuya temperatura es regulable. Las muestras caracterizadas en este trabajo se desgasificaron durante 4 horas a 150 °C. Una vez que la muestra está desgasificada, se traslada a la unidad de adsorción física donde todas las operaciones realizadas durante el proceso experimental están controladas por ordenador. Estas operaciones incluyen un proceso de vacío y posterior llenado con el gas adsorbato a distintas presiones relativas ($0 < P/P_0 < 1$, para las isotermas de N_2 a -196 °C). El sistema, mediante detectores de presión, registra la presión una vez alcanzado el equilibrio, y por diferencia respecto a la presión introducida, es capaz de calcular el volumen de gas adsorbido a esa presión relativa.

Los ensayos de adsorción-desorción de N_2 a -196 °C y CO_2 a 0 °C de las muestras $NiO/CeO_2-NiO/C$ se realizaron en los Servicios Técnicos de Investigación de la Universidad de Alicante. Para ello, se utilizó un equipo volumétrico automático de adsorción física de gases AUTOSORB-6 (Figura 2.1b.) y un desgasificador AUTOSORB DESGASSER, ambos de la marca QUANTACHROME INSTRUMENT. Estas muestras fueron desgasificadas durante 8 horas a 150 °C.



Figura 2.1. Equipos de adsorción física de gases: (a) AUTOSORB-6B disponible en los laboratorios del grupo MCMA-UA y (b) AUTOSORB-6 disponible en los SSTI-UA.

2.2.2. Porosimetría de mercurio

La porosimetría por intrusión de Hg es una técnica para la caracterización del sistema poroso de los materiales, obteniéndose fundamentalmente a partir de ella la distribución de la porosidad en función del tamaño aparente de acceso a los poros. El ensayo porosímétrico consiste en introducir mercurio, un material que “no moja”, mediante presión isostática y registrar el volumen de mercurio que penetra en la muestra. Para cada intervalo de presión considerado, el volumen de mercurio que penetra nos indica el volumen de poros de la muestra que tienen un determinado intervalo de tamaño de acceso. La porosimetría de mercurio aporta información de la porosidad de un material desde 900 μm a prácticamente 4 nm [14,15].

Esta técnica se basa en la ley de Washburn (Ecuación 2.4) [16], que relaciona la presión aplicada con el diámetro de poro en el que se introduce el mercurio. La expresión matemática de esta ley es:

$$D = \frac{-4\gamma \cos \theta}{P} \quad (2.4)$$

Donde, “D” es el diámetro de poro, “P” la presión necesaria para introducir el líquido dentro del poro de diámetro D, “ γ ” corresponde a la tensión superficial del líquido y “ θ ” es el ángulo de contacto entre el líquido y la superficie del sólido.

Esta técnica se utilizó para complementar el estudio de la porosidad de los catalizadores. Para ello, se utilizó un equipo POREMASTER-60 GT de la marca QUANTACHROME INSTRUMENTS, disponible en los SSTI-UA (Figura 2.2.).



Figura 2.2. Equipo POREMASTER-60 GT, marca QUANTACHROME INSTRUMENTS, disponible en los SSTI-UA.

2.2.3. Difracción de rayos X (DRX)

Los rayos X son una radiación electromagnética de elevada energía y longitud de onda corta entre los 0.01 nm y 10 nm aproximadamente. La espectroscopía de Rayos X convencional se limita, en su mayor parte, a la región de 0.1 Å a 25 Å. Esta técnica se basa en el fenómeno físico de la difracción de un haz monocromático de rayos X al incidir sobre la superficie de un cristal. Cuando un haz de rayos X incide sobre un material sólido, parte del haz se dispersa en todas las direcciones por la interacción con los electrones asociados a los átomos o iones que se encuentra en el trayecto, pero el resto del haz puede dar lugar al fenómeno de difracción de rayos X, si existe una disposición ordenada de átomos o iones. La radiación difractada será detectada cuando los haces emitidos emergan en fase, de tal manera que la interferencia sea constructiva. Para ello, la diferencia de caminos ópticos debe ser un múltiplo de la longitud de onda del haz, lo que se define matemáticamente con la ley de Bragg (ecuación 2.5) [17].

$$\lambda = 2d_{hkl} \operatorname{sen}\theta \quad (2.5)$$

Donde, “ d_{hkl} ” es la distancia entre planos atómicos, “ λ ” la longitud de onda y “ θ ” el ángulo de difracción. La representación de la intensidad de la radiación tras

interaccionar con la muestra en función del ángulo de incidencia (generalmente 2θ) se denomina difractograma y es característico de cada cristal. Por medio de esta técnica se puede obtener información tanto cualitativa como cuantitativa de sólidos cristalinos que permite conocer la estructura de cristales y la posición de los átomos en la red. Cuando se tiene muestras policristalinas, se observará un difractograma con picos a ángulos de difracción característicos, lo que permite identificar la muestra [18].

A partir de la posición de las reflexiones que se recogen en el difractograma de Rayos X y la ley de Bragg, se puede calcular el valor del espaciado cristalino. El parámetro d_{hkl} depende del sistema cristalino y está relacionado a su vez con los parámetros de red a través de diversas fórmulas. Para el cálculo del parámetro de red, en el caso del CeO₂, que cristaliza en un sistema cúbico tipo fluorita, se suele emplear el pico de difracción correspondiente al plano (111), debido a que es la reflexión más intensa. Primeramente, se debe calcular el espaciado cristalino d_{111} por medio de la siguiente fórmula (Ecuación 2.6) [19]:

$$d_{111} = \frac{\lambda}{2\sin\theta_{111}} \quad (2.6)$$

Una vez obtenido este valor, se puede calcular el tamaño experimental de la arista de la celdilla cúbica “a” mediante la siguiente relación cristalográfica (Ecuación 2.7) [17].

$$a = \sqrt{d_{hkl}^2(h^2 + k^2 + l^2)} \quad (2.7)$$

Donde, “a” el tamaño de arista en la celdilla cúbica y “h,k,l” los índices de Miller del plano cristalográfico determinado. Mediante esta técnica también puede determinarse el tamaño de los cristales, utilizando la anchura de los picos de difracción a mitad de altura, la cual disminuye al aumentar el tamaño de cristal. La ecuación de Scherrer permite hallar el diámetro medio de los cristales “D” de un sólido cristalino a partir de la anchura del pico de difracción a mitad de altura (Ecuación 2.8) [20,21].

$$D = \frac{k\lambda}{B\cos\theta} \quad (2.8)$$

Siendo, “λ” la longitud de onda de la radiación empleada para obtener el difractograma, “k” la constante de Scherrer o factor de forma, “B” la anchura a mitad de altura expresada en radianes, y “θ” el ángulo de difracción. Para el CeO₂, el parámetro “k” tiene un valor propuesto de 0.94.

En esta tesis doctoral, los difractogramas de Rayos X fueron realizados con un difractómetro Bruker D8-Advance, (Figura 2.3.), equipado con un espejo Göebel con un generador de rayos-X Kristalloflex K 760-80F, usando radiación de Cu K α ($\lambda = 1.540598 \text{ \AA}$). Los difractogramas se registraron en un intervalo de 2θ , con tamaño de paso de 0.05° y un tiempo de paso de 3 segundos.

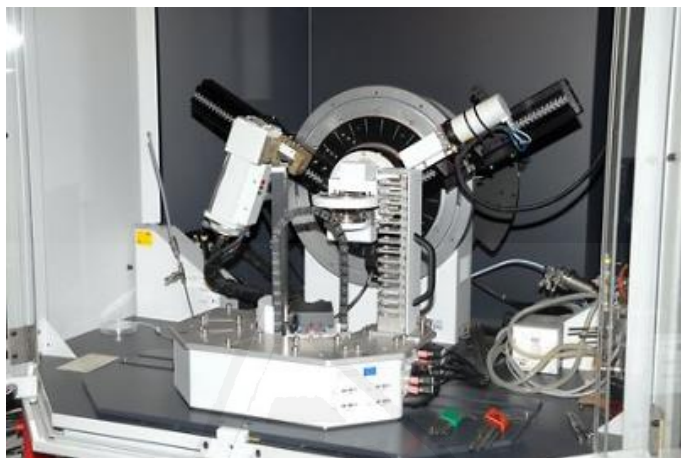


Figura 2.3. Difractómetro Bruker D8-Advance, disponible en los SSTI-UA.

2.2.4. Espectroscopia de emisión por plasma de acoplamiento inductivo (ICP-OES)

La técnica ICP-OES permite determinar de forma cuantitativa la mayoría de los elementos de la tabla periódica a niveles de traza y ultratraza, partiendo de muestras en disolución acuosa. La técnica se basa en la vaporización, disociación, ionización y excitación de los elementos químicos presentes en la muestra líquida, por acción de un plasma [22].

La muestra, en forma líquida, es transportada por medio de una bomba peristáltica hasta el sistema nebulizador donde es transformada en aerosol gracias a la acción de gas argón. Dicho aerosol es conducido a la zona de ionización que consiste en un plasma generado al someter un flujo de gas argón a la acción de un campo magnético oscilante inducido por una corriente de alta frecuencia. En el interior del plasma se pueden llegar a alcanzar temperaturas de hasta 8000°C . En estas condiciones, los átomos presentes en la muestra son ionizados/excitados. Al volver a su estado fundamental, estos iones o átomos excitados emiten radiaciones de una longitud de onda que es característica de cada elemento. Esta radiación pasa a través de un sistema óptico que separa la radiación según su longitud onda. A continuación, un detector mide la

intensidad de cada una de las radiaciones relacionando esta con la concentración de cada elemento en la muestra [23,24].

La caracterización mediante ICP-OES se utilizó para determinar la cantidad real de níquel presente en los catalizadores. Los ensayos se realizaron en un espectrofotómetro de emisión con plasma de acoplamiento inductivo marca Perkin Elmer modelo optima 4300 DV (Figura 2.4.). Las muestras fueron tratadas previamente en una disolución acuosa, aciduladas con HNO_3 2% y filtradas a 0.45 μm .



Figura 2.4. Espectrofotómetro de emisión con plasma de acoplamiento inductivo Perkin Elmer, disponible en los SSTI-UA.

2.2.5. Microscopía electrónica de barrido (SEM)

La microscopía SEM proporciona información morfológica y topológica de la superficie del sólido. Las imágenes que se obtienen en el microscopio electrónico de barrido corresponden a electrones secundarios o electrones retrodispersados emitidos tras la interacción con la muestra de un haz incidente de entre 5 y 30 KeV. El haz de electrones se desplaza sobre la muestra realizando un barrido en las direcciones X e Y de tal modo que la posición en la que se encuentra el haz en cada momento coincide con la aparición de brillo, proporcionalmente a la señal emitida, en un determinado punto de la pantalla [25,26].

La señal de electrones secundarios se forma en una delgada capa superficial, del orden de 50 a 100 Å. Son electrones de baja energía, menos de 50 eV, que pueden ser desviados fácilmente de su trayectoria emergente inicial y permiten obtener información

de zonas que no están a la vista del detector. Esta particularidad otorga a esta señal la posibilidad de aportar información “en relieve” [27].

La emisión de electrones retrodispersados depende fuertemente del número atómico de la muestra. Esto implica que dos partes de la muestra que tengan distinta composición se revelan con distinta intensidad, aunque no exista ninguna diferencia de topografía entre ellas. Los rayos X que se generan en una muestra sometida a bombardeo electrónico permiten identificar los elementos presentes y establecer su concentración [26,28].

Las imágenes SEM fueron obtenidas en un microscopio electrónico de barrido de emisión de campo (FESEM) marca Zeiss modelo Merlin VP Compact equipado con un sistema de microanálisis por EDX marca BRUKER modelo Quantax 400 (Figura 2.5.).



Figura 2.5. Microscopio Zeiss modelo Merlin VP Compact disponible en los SSTI-UA.

2.2.6. *Microscopia electrónica de transmisión (TEM)*

Al igual que la microscopía SEM, la microscopía TEM proporciona información acerca de la morfología de la muestra. A través de microscopía TEM se puede determinar forma, dimensiones y posición de los microcristales o partículas del sólido, así como información cristalográfica y composición química del material. La técnica consiste en irradiar una muestra delgada (se recomienda utilizar muestras con un grosor máximo de 100 nm) con un haz de electrones de 200 keV [28,29]. A diferencia de la microscopía SEM, el análisis de la muestra se realiza a partir de electrones que atraviesan la muestra. Parte de esos electrones son transmitidos, otra parte son

dispersados y otra parte da lugar a interacciones que producen distintos fenómenos como emisión de luz, electrones secundarios y Auger, rayos X, etc [30,31]. A partir de la transmisión/dispersión de los electrones el microscopio electrónico de transmisión forma las imágenes, la difracción de los electrones brinda información acerca de la estructura cristalina y la emisión de rayos X permite conocer la composición elemental de la muestra [28].

En este trabajo se utilizó un microscopio electrónico de transmisión marca JEOL modelo JEM-2010 (Figura 2.6.), para estudiar la morfología de los catalizadores que contienen nanopartículas.



Figura 2.6. Microscopio JEOL modelo FEM-2010 disponible en los SSTI-UA.

2.2.7. Reacciones a temperatura programada: H₂-TPR y He-TPD

Las reacciones a temperatura programada permiten estudiar la evolución del comportamiento de un material sometido a una temperatura controlada en presencia de una determinada atmósfera gaseosa. En esta tesis se han empleados las técnicas de reducción a temperatura programada en hidrógeno (H₂-TPR) y desorción a temperatura programada en argón (He-TPD).

La técnica de reducción a temperatura programada es un procedimiento que se incluye dentro del grupo de técnicas de reacción a temperatura programada. En general, estas técnicas permiten adquirir información a través de una reacción sólido-gas simultánea con un aumento de la temperatura. La respuesta térmica del sustrato a analizar ante una atmósfera seleccionada se registra en perfiles señal-temperatura, con

picos característicos relacionados con la cinética de la transformación y la naturaleza del sistema de estudio [28,32].

En concreto, la reducción a temperatura programada permite analizar la reducibilidad de un catalizador ante la presencia de gas reductor en función de la temperatura. El gas empleado para estos ensayos es H₂ diluido en un gas inerte (los más habituales son Ar y N₂), y la detección de la transformación química se efectúa mediante un detector de conductividad térmica (por sus siglas en inglés, TCD), que controla los cambios de conductividad que se producen en el gas a la salida del reactor, consecuencia del consumo de H₂ [28,33].

Los ensayos de H₂-TPR se realizaron utilizando dos equipos diferentes por factores de disponibilidad. Un equipo Micromeritics Pulse Chemisorb 2705 (Figura 2.7a.) fue utilizado en la caracterización de los materiales estudiados en los Capítulos 3, 4, 5 y 7, usando un reactor de cuarzo de lecho fijo con 40 mg de muestra y una trampa fría a -80 °C entre el reactor y el detector TCD. Se utilizó 40 ml/min de flujo de 5% H₂/Ar con una velocidad de calentamiento de 10 °C/min hasta 900 °C. Para la cuantificación del H₂ consumido, se empleó un patrón de CuO. Por otra parte, la caracterización de los materiales utilizados en el Capítulo 6 fue llevada a cabo en espectrómetro de masas, el cual ha sido empleado para la identificación y cuantificación del H₂O generada durante los procesos de reducción. Para ello, se ha utilizado un equipo DSC-TGA (TA Instruments, SDT 2960 Simultenaous) acoplado a un espectrómetro de masas (ThermoStar, modelo GSD 300 T3, Balzers) (Figura 2.7b.). En los experimentos, se utilizaron 20 mg de catalizador y un flujo de 50 ml/min de 5%H₂/Ar, con una velocidad de calentamiento de 10 °C/min hasta 900 °C. Se empleó un patrón de CuO para cuantificar el H₂ consumido.

Otra de las técnicas de reacciones a temperatura programada es la desorción a temperatura programada. Esta técnica es muy empleada en la caracterización de la química superficial de materiales carbonos. La técnica permite analizar los gases producidos durante la descomposición de los grupos superficiales que emite la muestra al ser sometida un programa de temperaturas controlado en una atmósfera de gas inerte. El análisis de los gases de salida aporta información acerca de la composición química y la estabilidad de los grupos funcionales superficiales.

Los gases procedentes de los carbonos son, principalmente, H₂O, CO y CO₂, los cuales pueden producirse de la desorción del agua adsorbida por el material y durante la descomposición de los grupos funcionales oxigenados superficiales y/o la descomposición de compuestos inorgánicos presentes [34,35]. Los gases son desorbidos a diferentes temperaturas dependiendo de la energía de descomposición de cada grupo oxigenado. A temperaturas bajas suele producirse CO₂ procedente de la descomposición

de los grupos carboxílicos, lactonas y anhíbridos, mientras que a temperaturas elevadas suele emitirse CO como producto de la descomposición de los grupos carbonilos, quinona, fenoles o éter [35].

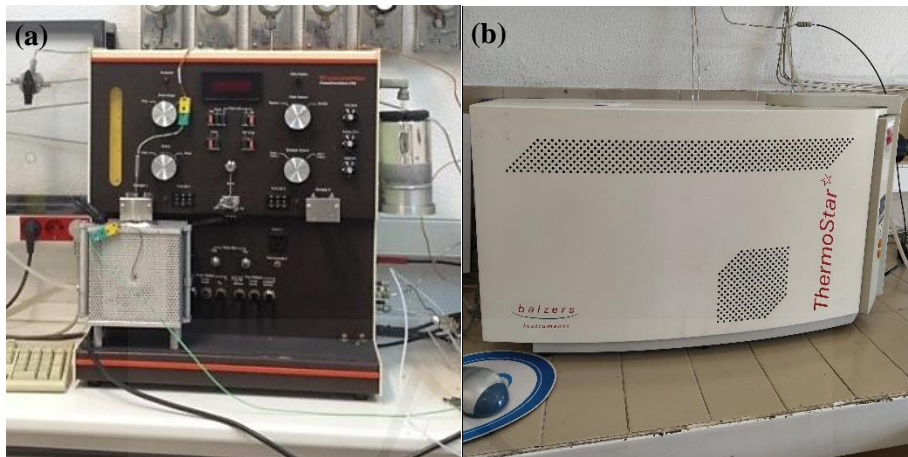


Figura 2.7. Equipos utilizados en reacciones a temperatura programada: (a) Micromeritics Pulse Chemisorb 2705 y (b) espectrómetro de masas OmniStar, ambos disponibles en los laboratorios del grupo MCMA-UA.

La técnica TPD fue empleada en esta tesis para la caracterización de la química superficial del xerogel de carbón utilizado en el Capítulo 6. El experimento fue llevado a cabo en el equipo DSC-TGA acoplado a un espectrómetro de masas, descrito anteriormente (Figura 2.7b). Para ello, se utilizaron 20 mg de muestra y 40 ml/min de Helio como gas de arrastre. La velocidad de calentamiento fue 10 °C/min desde temperatura ambiente hasta 900 °C.

2.2.8. Espectroscopía fotoelectrónica de rayos X (XPS)

La técnica XPS es una técnica de caracterización ampliamente utilizada que permite obtener la composición química de la superficie de materiales. La espectroscopía fotoelectrónica da información tanto del estado de oxidación del elemento químico, así como del entorno químico en el que se encuentra el átomo ionizado [36,37]. Aunque la ionización se puede producir a distintas profundidades, sólo los electrones procedentes de regiones muy cercanas a la superficie pueden escapar del sólido manteniendo la información, lo cual limita la sensibilidad de la técnica a la

superficie de los materiales a aproximadamente 1-2 nm de profundidad. Se pueden detectar todos los elementos, excepto el hidrógeno [38,39].

Esta técnica consiste en la excitación mediante un haz monocromático de Rayos X de los electrones más internos de los átomos, provocando la emisión de fotoelectrones que nos proporcionan información sobre la energía de cada nivel y, por tanto, sobre la naturaleza de cada átomo emisor. Al incidir la muestra con un haz de rayos X esta liberará fotoelectrones con una energía cinética característica de los elementos que la componen. La velocidad de los electrones emitidos es cuantificada por un espectrómetro y el valor de la energía cinética permite hallar la composición elemental de la muestra y la concentración de cada elemento [40].

Los análisis XPS han sido realizados en un espectrómetro K-Alpha de Thermo-Scientific (Figura 2.8.) totalmente automatizado equipado con un monocromador de alta resolución y una fuente de electrones e iones para compensación de carga automatizada, así como una fuente de iones de argón para decapado de alta precisión, con un tamaño de haz de menos de 300 μ m. Antes de la adquisición de los espectros, las muestras fueron mantenidas en la cámara de análisis hasta tener una presión residual de $5 \cdot 10^{-10}$ mbar y se utilizó el detector en modo de energía constante con una energía de paso de 50 eV. La energía de ligadura se ajustó teniendo como referencia la transición 1s del C a 284,6 eV. Los valores de energías de ligadura fueron obtenidos mediante el software Peak-Fit incorporado en el programa informático de control del espectrómetro, con una precisión de $\pm 0,2$ eV [41].



Figura 2.8. Espectrómetro K-Alpha de Thermo-Scientific disponible en los SSTI-UA.

Los elementos de los catalizadores analizados mediante XPS fueron Ce (línea 3d), O (línea 1s), C (línea 1s) y Ni (línea 2p). La intensidad de las contribuciones de cada especie química de un elemento en el espectro de XPS se ha estimado calculando la integral de cada pico, previa substracción de la línea base y ajuste de la curva experimental a una combinación de curvas con forma Lorentziana y Gaussiana.

2.2.9. *Termogravimetría (TG)*

La termogravimetría es una técnica de análisis térmico que se emplea para estudiar materiales que sufren cambios en su masa cuando son sometidos a un tratamiento térmico de pérdida de masa. Permite analizar la estabilidad térmica, la descomposición y la cinética en una muestra al ser sometida a unas condiciones de temperatura y atmósfera determinadas [40]. Los resultados obtenidos, así como las curvas termogravimétricas, son influenciados por factores como la velocidad de calentamiento, el tamaño de partícula de la muestra, la cantidad de muestra, la atmósfera y el caudal del gas empleado [41].

En términos generales, un equipo de análisis térmico está compuesto por un horno, una balanza, un controlador de gases y un sistema que adquiere y registra los datos. Los ensayos se pueden realizar a temperatura ambiente, enfriando o calentando la muestra a una velocidad constante o en un programa de temperatura que combine cualquiera de ellos. Los experimentos pueden realizarse en una atmósfera estática o dinámica, utilizando gas inerte o mezcla de gases reactiva. Esta técnica permite llevar a cabo un sinnúmero de procesos que llevan asociados una variación de masa como lo son procesos de reducción, oxidación, descomposición, absorción y desorción, entre otros [28,40].

En este trabajo de tesis, la termogravimetría se ha empleado para determinar la cantidad de carbón presente en los catalizadores NiO/CeO₂-NiO/C y la cantidad de carbón depositado en los catalizadores empleados en los ensayos catalíticos de reformado seco de metano después de reacción. Para ello, se empleó una termobalanza SDT 2960 Simultaneous DSC-TGA marca TA Instruments (Figura 2.9.), donde se calentó 10 mg de muestra hasta 800 °C usando una velocidad de calentamiento de 10 °C/min, en un flujo de 100 mL/min de aire.



Figura 2.9. Termobalanza SDT 2960 Simultaneous DSC-TGA de la marca TA Instruments disponible en los laboratorios del grupo MCMA-UA.

2.3. Ensayos de actividad catalítica

El comportamiento catalítico de los catalizadores estudiados en este trabajo de investigación fue determinado mediante dos reacciones de interés medioambiental, la metanación de dióxido de carbono y el reformado seco de metano. Los ensayos catalíticos de metanación de dióxido de carbono (Figura 2.10.) fueron realizados en las instalaciones del grupo de Materiales Carbonosos y Medio Ambiente de la Universidad de Alicante (MCMA-UA) y en los laboratorios del grupo Tecnologías Químicas para la Sostenibilidad Ambiental de la Universidad del País Vasco (TQSA-UPV), y los ensayos catalíticos de reformado seco de metano (Figura 2.11.) fueron realizados en el grupo *Combustion, Energies Propres and Turbulence* de la Universidad de la Sorbona, Francia (CEPT-US). En cada capítulo de resultados se indicará el laboratorio donde se realizaron los respectivos ensayos catalíticos y a continuación se especificará las condiciones de cada uno de ellos.

2.3.1. Reacción de metanación de CO₂ (MCMA-UA)

Las pruebas catalíticas de metanación de dióxido de carbono que se realizaron en el grupo MCMA-UA fueron llevadas a cabo en reactor tubular de 9.3 mm de diámetro interno utilizando 200 mg de catalizador mezclado con partículas de cuarzo. Se utilizó un volumen de lecho de 1 cm³ y GHSV de 12000 h⁻¹. El catalizador se trató previamente a 500 °C durante 1 hora en un flujo de 200 mL/min de 50% H₂/Ar. Después de enfriar a 200 °C en gas inerte, se alimentó el reactor con 200 mL/min de una mezcla de reacción

compuesta por 16% CO₂ + 64% H₂ en balance de He. La temperatura de reacción se elevó hasta 450 °C con una velocidad de calentamiento de 5 °C/min, en pasos de 25 °C. Una vez alcanzado el equilibrio en cada paso de temperatura, se determinó la concentración de los gases de salida compuesto por CH₄, CO, H₂ y O₂, para lo que se utilizaron dos equipos diferentes: un cromatógrafo de gases (Agilent 8860 GC System) y un equipo con detectores de CH₄, CO, H₂ y O₂ (AwifLEX). En los capítulos donde se presentan los resultados obtenidos se indicará el equipo específico utilizado.

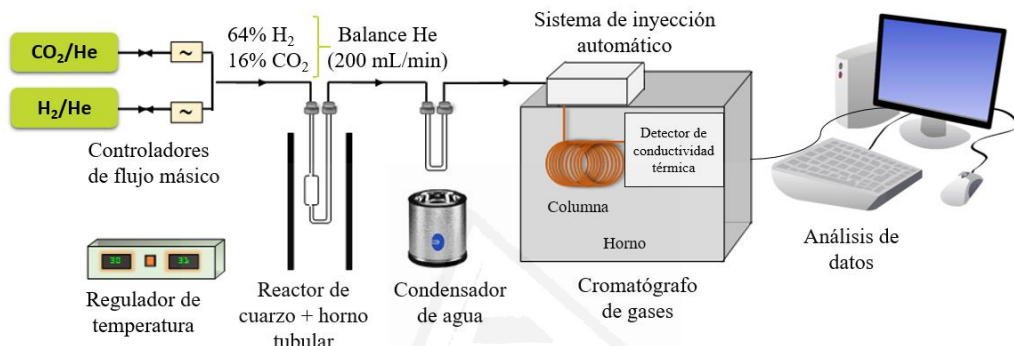


Figura 2.10. Esquema del equipo utilizado en los ensayos de actividad catalítica de la reacción de metanación de dióxido de carbono.

2.3.2. Reacción de metanación de CO₂ (TQSA-UPV)

Las pruebas catalíticas se realizaron en un reactor cilíndrico de lecho fijo de 9 mm de diámetro interno utilizando 400 mg de catalizador mezclado con partículas de cuarzo. El volumen del lecho fue de 1 cm³ y el GHSV fue de 12000 h⁻¹. La composición del gas se controló con un cromatógrafo de gases (Agilent HP7890B). El catalizador se trató previamente a 500 °C durante 1 hora en un flujo de 200 mL/min de 20% H₂/He. Despues de enfriar a 200 °C en gas inerte, se alimentó el reactor con 200 mL/min de la mezcla de reacción (16% CO₂ + 64% H₂, en balance con He). La temperatura se elevó a 450 °C en etapas de 25 °C, con una velocidad de calentamiento de 5 °C/min entre etapas, y la composición del gas se midió en cada etapa en condiciones de estado estacionario.

2.3.3. Reacción de reformado seco de metano (CEPT-US)

Los ensayos catalíticos de la reacción de reformado seco de metano fueron realizados en un reactor de lecho fijo de 12 mm de diámetro interno acoplado a un

cromatógrafo de gases (Agilent Varian GC490, Agilent). Los catalizadores fueron tratados previamente a 500 °C durante 1 hora en un flujo de 100 mL/min de 5% H₂/Ar. La reacción fue llevada a cabo a 700 °C alimentando el reactor con un flujo de 100 mL/min de la mezcla de gases de reacción compuesta por 10% CH₄ + 10% CO₂ en balance de Ar. Se utilizó una GHSV de 24000 h⁻¹.

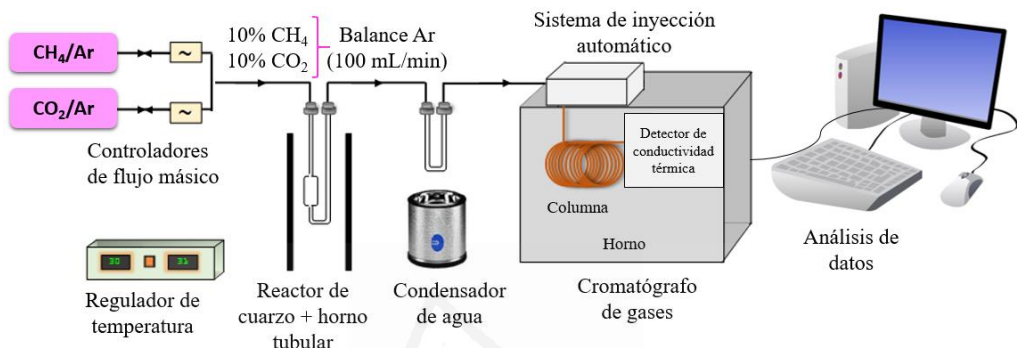


Figura 2.11. Esquema del equipo utilizado en los ensayos de actividad catalítica de la reacción de reformado seco de metano.

2.4. Técnicas de caracterización avanzadas utilizadas en el estudio del mecanismo de reacción de la metanación de CO₂

2.4.1. Ensayos isotópicos con pulsos de ¹³C¹⁸O₂

Los experimentos isotópicos se llevaron a cabo con pulsos de ¹³C¹⁸O₂ (Aldrich; 99% ¹³C, 95% ¹⁸O), en un reactor cilíndrico de diámetro interno de 4 mm acoplado a un espectrómetro de masas Pfeiffer Vacuum (modelo OmniStar) que funciona a una frecuencia de 1 segundo. Los ensayos se realizaron utilizando 50 mg de muestra. El catalizador se trató previamente a 500 °C durante 1 hora en 50% H₂/He (20 ml/min). Una vez pretratada la muestra, la temperatura se estabilizó a 350 °C bajo el mismo flujo de gas, que se mantuvo durante todo el experimento. Se usó una válvula de seis vías con un loop de 100 µL, que se llenó a 9 psi con el gas a pulsar. Este volumen de gas es arrastrado por la corriente de gas principal una vez que se cambia la posición de la válvula. Primero se alimentaron tres pulsos de Ar, y luego, tres pulsos de ¹²C¹⁶O₂ seguidos por tres pulsos de ¹³C¹⁸O₂. Los pulsos se alimentaron en intervalos de 7 minutos, lo que permite la estabilización de todas las señales m/z después del pulso.

anterior. La Figura 2.12. muestra un esquema general de la configuración experimental utilizada.

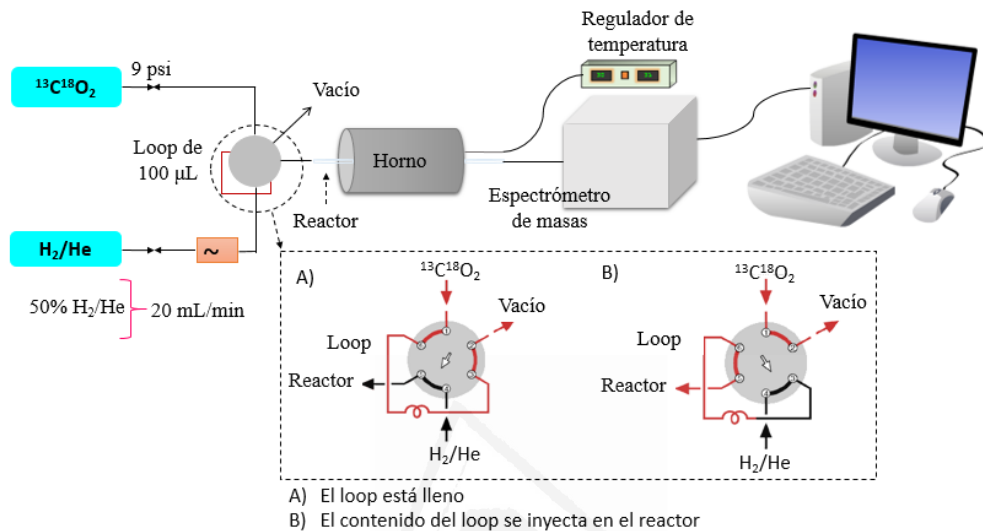


Figura 2.12. Esquema experimental de los ensayos isotómicos con pulsos de $^{13}\text{C}^{18}\text{O}_2$.

2.4.2. Ensayos DRIFTS *in-situ*

Se realizaron experimentos DRIFTS *in situ* en un espectrómetro de infrarrojos Jasco, modelo FT/IR-4100 usando una celda de reacción para controlar la temperatura y el gas de reacción. La celda se diseñó para permitir que el gas fluya a través del lecho catalítico. Se utilizó 70 mg de muestra. El catalizador se pretrató en 50% H_2/He a 450 °C durante 60 minutos, y luego se enfrió a temperatura ambiente en la misma mezcla de gas. El espectro de fondo se registró en He a 150 °C, y luego, la temperatura se elevó hasta 450 °C / min en pasos de 150 °C alimentando con la mezcla de gases de reacción para metanación de CO_2 (16% CO_2 + 64% H_2 en balance de He). Los espectros se registraron después de 60 minutos en condiciones isotérmicas a cada temperatura de 4000 a 1000 cm^{-1} con un paso de 1 cm^{-1} . La Figura 2.13 muestra el esquema experimental utilizado en la realización de los ensayos DRIFTS *in situ*.

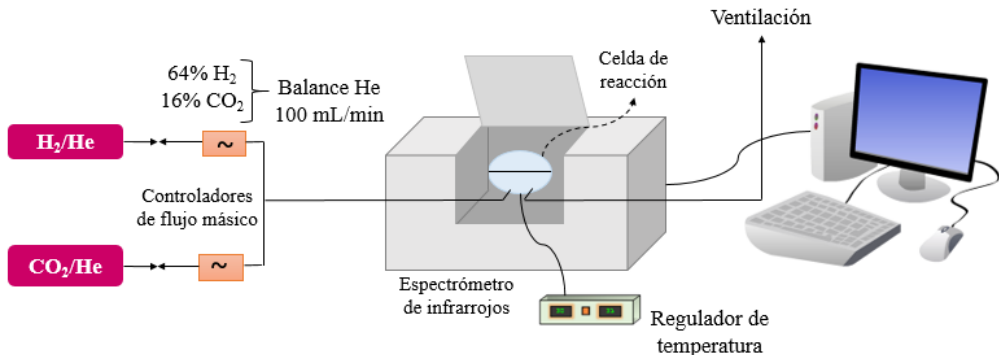


Figura 2.13. Esquema experimental de los ensayos DRIFTS in situ.

2.5. Referencias

- [1] V. Alcalde-Santiago, A. Davó-Quiñonero, D. Lozano-Castelló, A. Bueno-López, On the soot combustion mechanism using 3DOM ceria catalysts, *Appl. Catal. B Environ.* 234 (2018) 187–197.
- [2] J.G. Mira, V.R. Pérez, A. Bueno-López, Effect of the CeZrNd mixed oxide synthesis method in the catalytic combustion of soot, *Catal. Today.* 253 (2015) 77–82.
- [3] N. Guillén-Hurtado, A. García-García, A. Bueno-López, Active oxygen by Ce-Pr mixed oxide nanoparticles outperform diesel soot combustion Pt catalysts, *Appl. Catal. B Environ.* 174–175 (2015) 60–66.
- [4] E. Bailón-García, F. Carrasco-Marín, A.F. Pérez-Cadenas, F.J. Maldonado-Hódar, Microspheres of carbon xerogel: An alternative Pt-support for the selective hydrogenation of citral, *Appl. Catal. A Gen.* 482 (2014) 318–326.
- [5] K.D. Hammond, W.C. Conner Jr., Analysis of Catalyst Surface Structure by Physical Sorption, in: *Adv. Catal.*, 2013: pp. 1–101.
- [6] M. Thommes, K. Kaneko, A. V. Neimark, J.P. Olivier, F. Rodriguez-Reinoso, J. Rouquerol, K.S.W. Sing, Physisorption of gases, with special reference to the evaluation of surface area and pore size distribution (IUPAC Technical Report), *Pure Appl. Chem.* 87 (2015) 1051–1069.
- [7] K. Sing, The use of nitrogen adsorption for the characterisation of porous materials, *Colloids Surfaces A Physicochem. Eng. Asp.* 187–188 (2001) 3–9.
- [8] M.A. Bagherinia, M. Shadman, Investigations of CO₂, CH₄ and N₂ physisorption in single-walled silicon carbon nanotubes using GCMC simulation, *Int. Nano Lett.* 4 (2014) 95.

- [9] K.S.W. Sing, F. Rouquerol, J. Rouquerol, Classical interpretation of physisorption isotherms at the gas-solid interface, in: *Adsorpt. by Powders Porous Solids Princ. Methodol. Appl.* Second Ed., 2013: pp. 159–189.
- [10] K.S.W. Sing, F. Rouquerol, P. Llewellyn, J. Rouquerol, Assessment of microporosity, in: *Adsorpt. by Powders Porous Solids Princ. Methodol. Appl.* Second Ed., 2013: pp. 303–320.
- [11] C. Nguyen, D.D. Do, The Dubinin-Radushkevich equation and the underlying microscopic adsorption description, *Carbon*, 39 (2001) 1327–1336.
- [12] B. Huang, C.H. Bartholomew, B.F. Woodfield, Improved calculations of pore size distribution for relatively large, irregular slit-shaped mesopore structure, *Microporous Mesoporous Mater.* 184 (2014) 112–121.
- [13] H.-Y. Zhu, E.F. Vansant, Determination of porosity in pillared clays by N₂ adsorption isotherms, *J. Porous Mater.* 2 (1995) 107–113.
- [14] F.Fu, L.Lin, E.Xu, Functional pretreatments of natural raw materials, in: *Adv. High Strength Nat. Fibre Compos. Constr.*, 2017: pp. 87–114.
- [15] I. M.Hutten, Testing of Nonwoven Filter Media, in: *Handb. Nonwoven Filter Media.* Second Ed., 2016: pp. 343–408.
- [16] M.T. Lowell, J.E. Shields, M.A. Thomas, Characterization of porous solids and powders: surface area, pore size and density. *Choice Reviews Online*. 42 (2005) 5288
- [17] M. Sardela, X-Ray diffraction and reflectivity, in: *Pract. Mater. Charact.*, 2014: pp. 1–41.
- [18] P. Gergaud, Analysis through X-ray diffraction of polycrystalline thin films, in: *Ferroelectr. Dielectr. Integr. Silicon*, 2011: pp. 111–158.
- [19] A. Trovarelli, Catalytic Properties of Ceria and CeO₂-Containing Materials, *Catal. Rev.* 38 (1996) 439–520.
- [20] S.. Misturea, R.. Snyderb, X-ray diffraction, in: *Encycl. Mater. Sci. Technol.* Second Ed., 2001: pp. 9799–9808.
- [21] Difracción de Rayos X. <https://ssti.ua.es/es/instrumentacion-cientifica/unidad-de-rayos-x/difraccion-de-rayos-x.html>. Access in April 2020.
- [22] V.A. Fassel, R.N. Kniseley, Inductively coupled plasma. Optical emission spectroscopy, *Anal. Chem.* 46 (1975) 1110–1120.
- [23] G.L. Donati, R.S. Amais, C.B. Williams, Recent advances in inductively coupled plasma optical emission spectrometry, *J. Anal. At. Spectrom.* 32 (2017) 1283–1296.

- [24] Espectroscopía de emisión por plasma de acoplamiento inductivo. <https://ssti.ua.es/es/instrumentacion-cientifica/unidad-de-analisis/espectroscopia-de-emision-por-plasma-de-acoplamiento-inductivo.html>. Access in April 2020.
- [25] W. Zhou, R. Apkarian, Z.L. Wang, D. Joy, Fundamentals of Scanning Electron Microscopy (SEM), in: Scanning Microsc. Nanotechnol., Springer, New York, NY, 2006: pp. 1–40.
- [26] L. Reimer, Scanning electron microscopy. Physics of imagen formation and microanalysis, Second Edition. Measurement Science and Technology. 11 (2000) 1826–1826.
- [27] Microscopía Electrónica de Barrido. <https://ssti.ua.es/es/instrumentacion-cientifica/unidad-de-microscopia/microscopia-electronica-de-barrido.html>. Access in April 2020.
- [28] S. Ebnesajjad, Surface and material characterization techniques, in: Surf. Treat. Mater. Adhes. Bond. Second Ed., 2014: pp. 39–75.
- [29] Microscopia Electrónica de Transmisión. <https://ssti.ua.es/es/instrumentacion-cientifica/unidad-de-microscopia/microscopia-electronica-de-transmision.html>. Access in April 2020.
- [30] D.J. Barber, Transmission electron microscopy. Physics of imagen formation and microanalysis. Optica Acta: International Journal of Optics. 31 (1984) 848–848.
- [31] B. Fultz, J.M. Howe, Transmission electron microscopy and diffractometry of materials (Springer Berlin Heidelberg, 2008).
- [32] Textural characterisation of catalysts, in: Physico-Chemical Anal. Ind. Mater. A Pract. Guid. to Characterisation, 2003: p. 26.
- [33] J.. Moulijn, P.. van Leeuwen, R.. van Santen, Temperature programmed reduction and sulphiding, in: Catal. An Integr. Approach to Homog. Heterog. Ind. Catal., 1993: pp. 400–417.
- [34] M.C. Román Martínez, D. Cazorla Amorós, A. Linares Solano, C. Salinas Martinez de Lecea, TPD and TPR characterization of carbonaceous support and Pt/C catalysts, Carbon, 31 (1993) 895–902.
- [35] J.L. Figueiredo, M.F.R. Pereira, M.M.A. Freitas, J.J.M. Órfão, Modification of the surface chemistry of activated carbons, Carbon, 37 (1999) 1379–1389.
- [36] P. van der Heide, X-Ray Photoelectron Spectroscopy. An Introduction to Principles and Practices (John Wiley and Sons, 2011).
- [37] D. M. Mattox, Substrate (“Real”) Surfaces and Surface Modification, in: Handb.

- Phys. Vap. Depos. Process. Second Ed., 2010: pp. 25–72.
- [38] J.F. Moulder, W.F. Stickle, P.E. Sobol, K.D. Bomben, Handbook of X-ray photoelectron spectroscopy: A reference book of standard spectra for identification and interpretation of XPS data (Perkin-Elmer Corporation, 1992).
- [39] M.C. Burrell, Chemical analysis, Electron spectroscopy, in: Encycl. Mater. Sci. Technol. Second Ed., 2001: pp. 1142–1149.
- [40] H. Konno, X-ray photoelectron spectroscopy, in: Mater. Sci. Eng. Carbon, 2016: pp. 153–171.
- [41] Espectroscopía Fotoelectrónica de Rayos X. <https://ssti.ua.es/es/instrumentacion-cientifica/unidad-de-rayos-x/espectroscopia-fotoelectronica-de-rayos-x.html>. Access in April 2020.



3

Study of the CO₂ methanation mechanism using NiO/CeO₂ and NiO/Al₂O₃ catalysts

3.1. Introduction

3.2. Experimental section

3.2.1. Catalysts preparation and characterization

3.2.2. Catalytic tests and mechanistic studies

3.3. Results and discussion

3.3.1. Catalysts characterization by N₂ adsorption, XRD and H₂-TPR

3.3.2. Catalytic tests

3.3.3. Fresh and used catalysts characterization by XPS

3.3.4. Isotopic experiments

3.3.5. In-situ DRIFTS experiments

3.3.6. CO₂ + H₂ reaction mechanism on NiO/CeO₂ and NiO/Al₂O₃ catalysts

3.4. Conclusions

3.5. References

3.1. Introduction

Substitution of fossil fuels by clean energy sources is one of the main worldwide challenges to face the problem of global warming. H₂ obtained by renewable energies will be probably be an important energy vector in the future and for that reason, suitable H₂ storage and transportation technologies are being developed.

As mentioned in Chapter 1, one of the options is CO₂ hydrogenation to yield CH₄, which is known as Sabatier's reaction or CO₂ methanation reaction [1,2]. CH₄ can be stored and transported more easily than H₂ using the already available infrastructures used for natural gas. In addition, this process contributes to mitigate the emission of CO₂ to the atmosphere if the energy used both for H₂ production and for acceleration of the Sabatier's reaction comes from renewable sources [3].

From a thermodynamic point of view, the methanation reaction is exothermic, but kinetics at low temperature are not favourable because both CO₂ and H₂ molecules are quite stable and an important energy barrier must be overcome to break their bonds. In addition, the CO₂-H₂ reaction can yield different reaction products, such as CO, different hydrocarbons, alcohols, etc., and selectivity towards CH₄ is necessary in this case. Several catalysts have demonstrated to accelerate CO₂ and H₂ dissociation, and to favour the formation of methane as main reaction product. These catalysts include nickel [4–11] and novel metals (ruthenium [1,12–19], palladium [20–22] and rhodium [23–26], the former being a promising option for practical use due to the lower prize.

As it has been explained in detail in Chapter 1, two reaction mechanisms have been proposed to describe the catalytic hydrogenation of CO₂ [27], the so-called associative mechanism and the dissociative mechanism. They mainly differ on the pathway for chemisorption and dissociation of the CO₂ molecules. In the associative mechanism, CO₂ is molecularly chemisorbed, and CO₂ oxygens are removed by H₂ afterwards in two consecutive steps. On the contrary, in the dissociative mechanism the CO₂ molecules dissociate upon chemisorption, yielding a surface carbonyl and an oxygen atom that reacts with H₂ afterwards.

The type of CO₂ methanation mechanism depends on the catalyst, and understanding the reaction pathways taking place is necessary for further design better catalysts. It has been reported [28] that CeO₂-supported Ni catalysts are more active and selective towards CH₄ formation than Ni catalysts supported on Al₂O₃, TiO₂ and MgO, but the mechanisms responsible of these differences have not been studied in detail. Also, Ni/Ce_{0.5}Zr_{0.5}O₂ has been reported [7] to be more active than Ni/γ-Al₂O₃, and differences in the type of surface CO₂ species were detected upon CO₂ chemisorption in the absence of H₂.

The goal of this chapter is to study differences in the role of the CeO₂ and Al₂O₃ supports in the Ni-catalyzed CO₂ methanation reaction, and isotopic ¹³C¹⁸O₂ experiments and in situ DRIFTS reactions have been carried out for this purpose.

3.2. Experimental section

3.2.1. Catalysts preparation and characterization

Two catalysts have been prepared and used in this study, which are referred as NiO/CeO₂-US (I) and NiO/Al₂O₃-US (I). CeO₂ support was prepared by calcination of cerium citrate and commercial γ -Al₂O₃ was used as support. Nickel (8.5 wt. %) was loaded by incipient wetness impregnation, as detailed in *Section 2.1.1.* from *Chapter 2*. The catalysts were characterized by means of complementary techniques. The nickel content was determined by ICP-OES. Textural properties have been characterized by N₂ adsorption-desorption at -196 °C, after outgassing the catalysts under vacuum at 150 °C for 4 hours. Crystalline properties of the catalysts were studied by XRD and the reduction of the catalysts was studied by H₂-TPR. XPS spectra were obtained to study the electronic state of the added metal species. Description of the techniques and of the experimental conditions and procedures has been detailed in *Chapter 2*.

3.2.2. Catalytic tests and mechanistic studies

Catalytic activity measurements were performed at the university of the Basque Country and the experimental conditions has been detailed in *Section 2.3.2* from *Chapter 2*. Briefly, catalytic tests were performed using 400 mg of catalysts. The sample was pre-treated at 500 °C during 1 h under 20 % H₂/He. The reaction mixture (16 % CO₂ + 64 % H₂ and He balance) was fed with a total flowrate of 200 mL/min. The temperature was raised to 450 °C in steps of 25 °C, with a heating rate of 5 °C/min between steps, and the gas composition was measured in each step under steady state conditions. The gas composition was monitored with a gas chromatograph.

Isotopic experiments were carried out at 350 °C with ¹³C¹⁸O₂ pulses, using 50 mg of catalyst and a flowing mixture of 50 % H₂/He (20 mL/min). Three Ar pulses were first fed, and afterwards, three pulses of ¹²C¹⁶O₂ followed by three pulses of ¹³C¹⁸O₂. The exhaust gases were monitored with a mass spectrometer. The experimental procedures can be found in *Section 2.4.1*.

In-situ DRIFTS experiments were performed in an infrared spectrometer using a reaction cell with 70 mg of catalyst and the CO₂ methanation mixture (16 % CO₂ + 64 % H₂ and He balance). The temperature was raised up from 150 to 450 °C in steps of 150 °C. Spectra were recorded after 60 min in isothermal conditions at each temperature. All the experimental aspects are detailed in *Section 2.4.2*.

3.3. Results and discussion

3.3.1. Catalysts characterization by N₂ adsorption, XRD and H₂-TPR

Figure 3.1. shows the N₂ adsorption-desorption isotherms recorded at -196 °C, and the BET specific surface areas determined from these isotherms are included in Table 3.1.

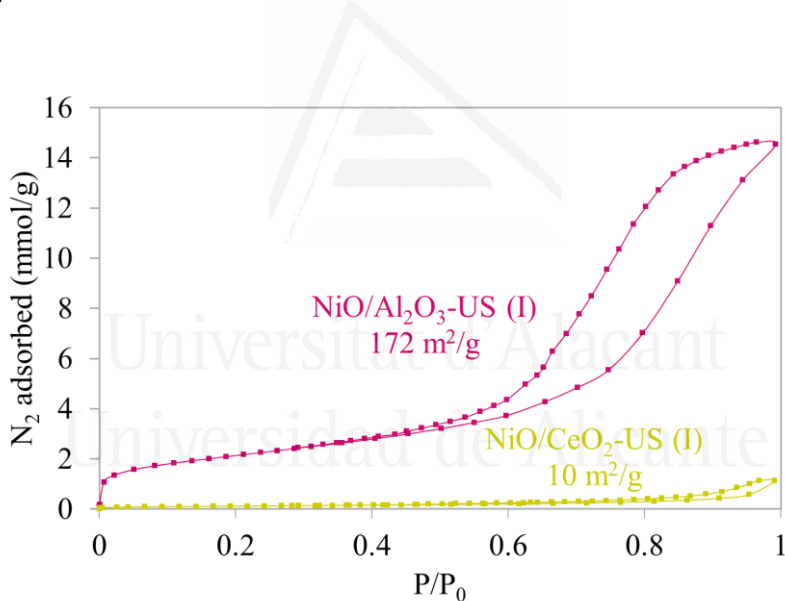


Figure 3.1. N₂ adsorption-desorption isotherms at -196 °C.

N₂ uptake is significantly higher for NiO/Al₂O₃-US (I) than for NiO/CeO₂-US (I), which is consistent with the BET values (172 vs 10 m²/g, respectively). The shape of the NiO/Al₂O₃-US (I) isotherm combines rapid N₂ uptake at very low relative pressure, which could be related with the presence of micropores, with smooth uptake at intermediate pressures and a hysteresis loop above P/P₀ = 0.5 that evidences the

presence of mesopores. This type of porosity is characteristic of the commercial γ -Al₂O₃ support used in the preparation of this catalyst. The low porosity of the NiO/CeO₂-US (I) catalyst is also expected for a CeO₂ support prepared by calcination of citrates.

The Ni content is 9.4 wt.% for NiO/Al₂O₃-US (I) and 8.2 wt.% for NiO/CeO₂-US (I).

Table 3.1. Results of the catalysts characterization by ICP-OES and N₂ adsorption-desorption isotherms at -196 °C

Sample	Ni (wt. %)	B.E.T. specific surface area (m ² /g)
NiO/Al ₂ O ₃ -US (I)	9.4	172
NiO/CeO ₂ -US (I)	8.2	10

The crystalline phases were studied by XRD, and the diffractograms of the two catalysts are included in Figure 3.2.

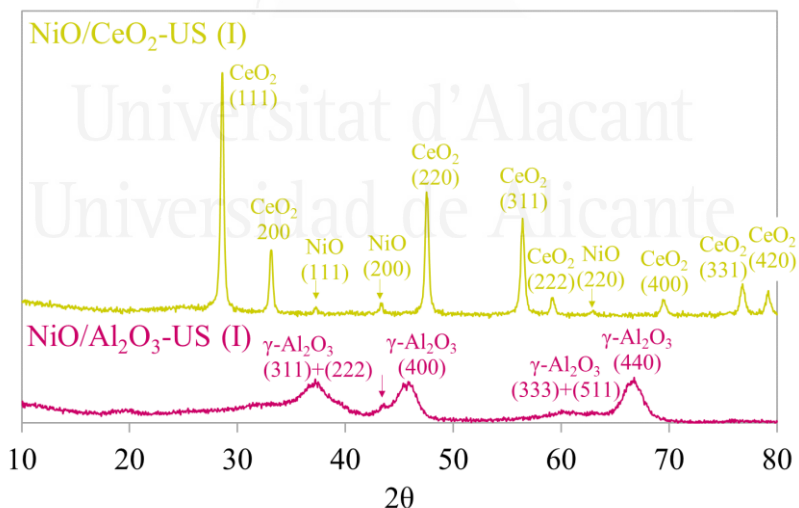


Figure 3.2. X-Ray diffractogram of the catalysts.

The NiO/CeO₂-US (I) catalyst shows peaks attributed to CeO₂ (JCPDS 00-034-0394) and NiO (JCPDS 01-075-0269) [29,30], and the NiO/Al₂O₃-US (I) catalyst shows

peaks of the $\gamma\text{-Al}_2\text{O}_3$ phase [31]. CeO_2 crystallizes in fluorite structure, with main peaks at 28.5, 33.1, 47.6, and 56.5°, and these peaks are sharper than those of the $\gamma\text{-Al}_2\text{O}_3$ phase. The broad peaks of $\gamma\text{-Al}_2\text{O}_3$ are consistent with the low crystallinity of this phase. The tiny peaks of the cubic structure of NiO at 37.5, 43.4 and 63.0° are properly identified in the $\text{NiO}/\text{CeO}_2\text{-US}$ (I) diffractogram, but are not so obvious in that of $\text{NiO}/\text{Al}_2\text{O}_3\text{-US}$ (I). This is, in part, because some NiO and $\gamma\text{-Al}_2\text{O}_3$ peaks appear at similar angles, and the broad $\gamma\text{-Al}_2\text{O}_3$ peaks mask the tiny peaks of NiO . However, the intensity of the (200) NiO peak at 43.4°, which is observed in both diffractograms, is much better defined in that of $\text{NiO}/\text{CeO}_2\text{-US}$ (I), and this suggests that NiO crystals are smaller on $\text{NiO}/\text{Al}_2\text{O}_3\text{-US}$ (I) than on $\text{NiO}/\text{CeO}_2\text{-US}$ (I). Quantitative comparison of the NiO crystallite sizes is not possible because the crystallite size cannot be obtained for $\text{NiO}/\text{Al}_2\text{O}_3\text{-US}$ (I). The smaller crystals of NiO on $\gamma\text{-Al}_2\text{O}_3$ can be attributed to the better dispersion due to higher surface area of the $\gamma\text{-Al}_2\text{O}_3$ support with regard to CeO_2 .

The reduction of the catalysts was studied by $\text{H}_2\text{-TPR}$ experiments, and the reduction profiles are shown in Figure 3.3. Reduction of the $\text{NiO}/\text{CeO}_2\text{-US}$ (I) catalyst takes place at much lower temperature than $\text{NiO}/\text{Al}_2\text{O}_3\text{-US}$ (I) reduction, as expected, showing several reduction events. On the one hand, a small sharp peak is observed at 250 °C, with small shoulders at lower temperature that can be assigned to NiO reduction [28]. The amount of H_2 consumed has been calculated and it is estimated that only 1.6 % of the total amount of NiO loaded on the catalyst has been reduced in this event. On the other hand, a large peak appears at 345 °C with a shoulder at higher temperature. The amount of H_2 consumed in this event is 122% of the NiO available, i.e., not only NiO is being reduced in this event but also part of surface CeO_2 . Moreover, a third peak is observed at 810 °C related to the reduction of bulk ceria.

In the case of $\text{NiO}/\text{Al}_2\text{O}_3\text{-US}$ (I) catalyst, the reduction starts at 500 °C and a main peak is observed at 825 °C with two shoulders at 725 and 600 °C. The total amount of H_2 consumed is that required for 100 % NiO reduction to Ni^0 . Al_2O_3 -supported NiO has been reported to be reduced in three events [32,33], which is consistent with the shape of the $\text{Ni}/\text{Al}_2\text{O}_3\text{-US}$ (I) reduction curve shown in Figure 3.3. The low temperature shoulders are attributed to reduction of NiO species with different interaction with alumina, the interaction being weaker for 600 °C reduced species and stronger for those reduced at 725 °C [34,35]. Finally, the highest temperature peak at 825 °C is assigned to well dispersed NiAl_2O_4 spinel reduction.

In conclusion, characterization results evidence that the $\gamma\text{-Al}_2\text{O}_3$ support has much higher surface area than ceria, and NiO seems to be better dispersed on the alumina support than on ceria. However, NiO reduction is improved in the $\text{NiO}/\text{CeO}_2\text{-}$

US (I) catalyst with regard to NiO/Al₂O₃-US (I), with evidences a simultaneous reduction of NiO and surface CeO₂.

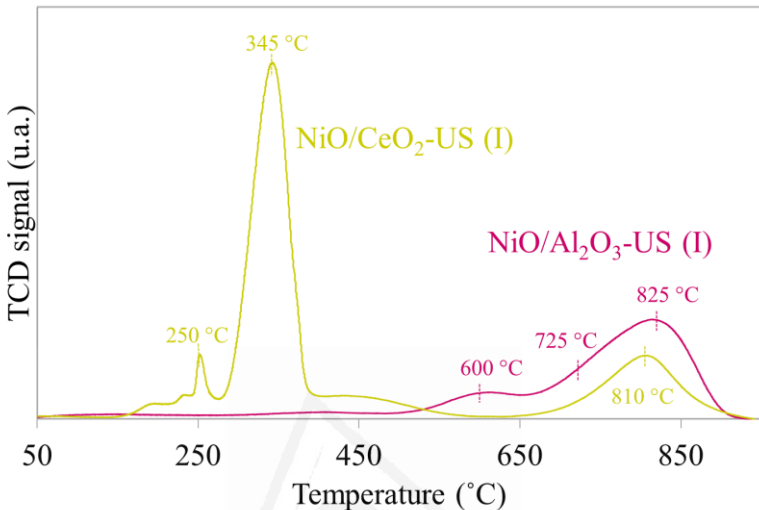


Figure 3.3. H₂-TPR characterization of the catalysts.

3.3.2. Catalytic tests

The catalytic methanation of CO₂ has been studied, and the CO₂ conversion curves are shown in Figure 3.4a. together with CH₄ selectivity profiles in Figure 3.4b.

The NiO/CeO₂-US (I) catalyst is much more active than NiO/Al₂O₃-US (I), with onset CO₂ conversion at 250 °C and a progressive increase until reaching the equilibrium curve at 375 °C. CH₄ is the only reaction product, with 100 % selectivity in the whole range of temperatures screened.

The catalytic activity of NiO/Al₂O₃-US (I) is much lower, with a slow increase in CO₂ conversion above 250 °C and without reaching thermodynamic equilibrium conversions in the range of temperatures studied. The CH₄ selectivity is not 100 % in this case and CO is also produced together with CH₄, the CH₄ selectivity increasing with temperature from 65 to 90%.

These differences in catalytic activity have been already reported by other authors [7,28], and the higher activity and selectivity of ceria supported nickel catalysts with regard to NiO/Al₂O₃-US (I) has been tentatively attributed to differences in the reaction intermediates created upon CO₂ chemisorption and to the reducibility of ceria.

XPS characterization, isotopic experiments and catalytic reactions followed by in situ DRIFTS have been carried out in this study, and results are discussed in the coming section providing further insights about the role of the support in the Ni-catalysed CO₂ methanation.

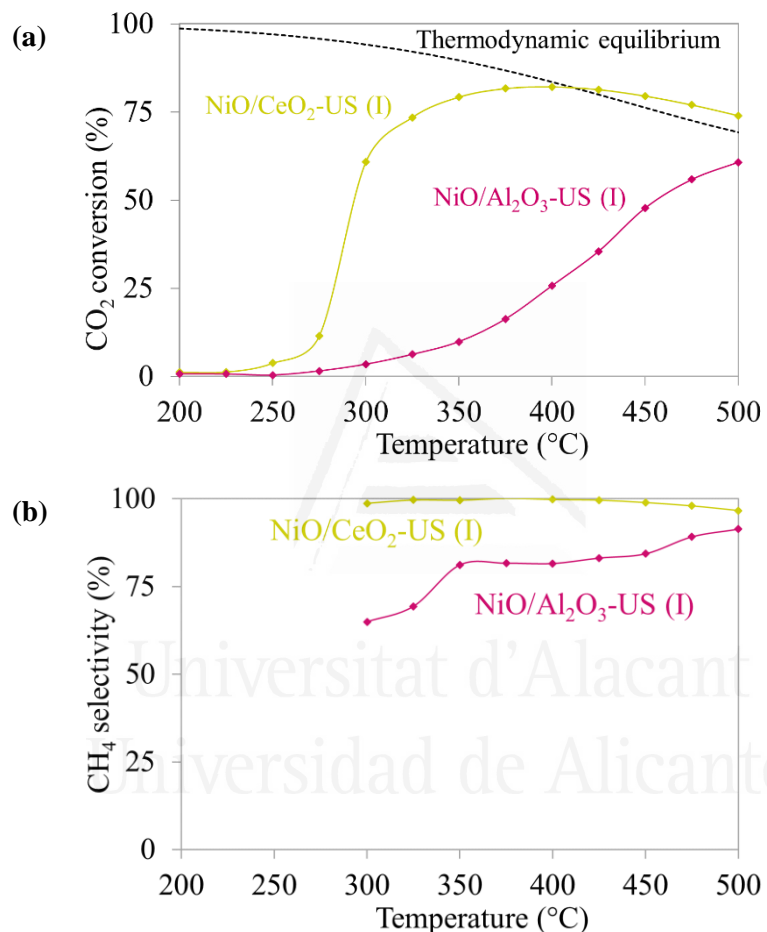


Figure 3.4. CO₂ methanation catalytic test. **(a)** CO₂ conversion and **(b)** CH₄ selectivity.

3.3.3. Fresh and used catalysts characterization by XPS

Changes in the oxidation state of nickel during the catalytic tests were studied by XPS by analysing the Ni_{2p} energy region for both catalysts before and after the catalytic experiments. Figure 3.5a. compiles the spectra, where important differences are noticed depending on the catalyst support.

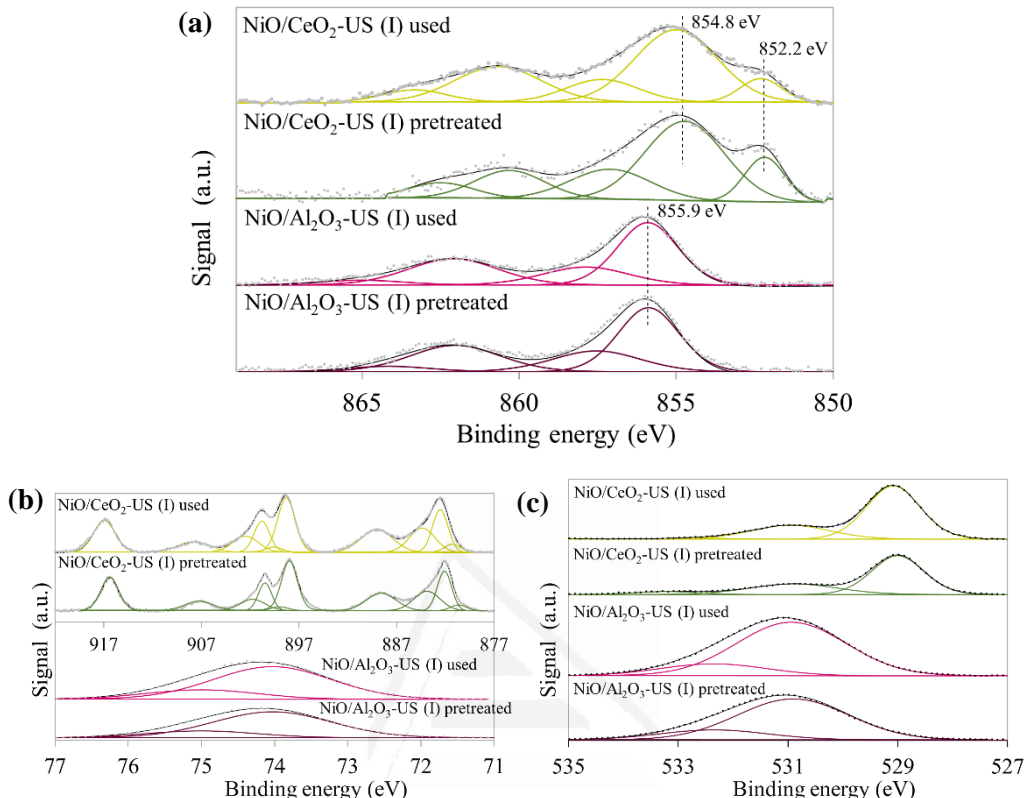


Figure 3.5. (a) Ni_{2p} (b) Ce_{3d} and Al_{2p} and (c) O_{1s} spectra of the catalysts before and after the catalytic tests.

Ni_{2p} spectra can be deconvoluted in several contributions, but there is not a general consensus about the assignation of these bands. It has been suggested that the position of the most intense peak can be used to determine the oxidation state of nickel and to obtain information about the charge density of its cations [36–39]. According to literature, the main peaks centered at 852.3, 853.4 and 856.7 eV can be assigned to metallic Ni, NiO, and Ni₂O₃, respectively [40–43]. The peak at 856.0 eV can be also attributed to surface Ni³⁺ species associated to the presence of Ni²⁺ vacancies in NiO crystal lattices [34], which is close to the binding energy of Ni₂O₃ and Ni(OH)₂ [44].

The main peak for the NiO/Al₂O₃-US (I) catalyst is centered at 855.9 eV, and this energy is consistent with the presence of Ni²⁺ cations, either forming NiO or partially hydrated oxides [37,38,45]. The Ni_{2p} spectrum of NiO/Al₂O₃-US (I) does not change during the catalytic tests, suggesting that the charge density of the Ni²⁺ cations is the same before and after methanation.

However, the main Ni_{2p} peak for the NiO/CeO₂-US (I) catalyst is centered at 854.8 eV, that is, there is a shift of more than 1 eV in the binding energy of this main peak with regard to NiO/Al₂O₃-US (I), and this is an evidence of the different NiO-support interaction. The main peak in the Ni_{2p} spectra of NiO/CeO₂-US (I) also shows a shoulder at low binding energy (852.2 eV), which indicates the presence of Ni⁰. Differences in the interaction between Ni²⁺ species and CeO₂ support affect the Ni species formed during reduction treatment. When the NiO-CeO₂ interaction is poor large, NiO particles are formed on the CeO₂ surface, which facilitates its reduction to Ni⁰ under reducing conditions. On the contrary, when there is a very close NiO-CeO₂ interaction, Ni²⁺ species strongly interacts with the crystal lattice of ceria behaving as a single entity, therefore, under reduction conditions, nickel will not necessarily be reduced and oxygen vacancies are formed. The coexistence of these two nickel species is very positive for the CO₂ methanation reaction, because nickel oxide species in close contact with ceria are active sites for CO₂ chemisorption and dissociation, and Ni⁰ species are effective sites for H₂ dissociation [46]. This distribution of nickel species, combining Ni²⁺ and Ni⁰, is maintained after the catalytic tests, and this is consistent with the stability of this catalyst as previously demonstrated in a 24 h stability test [47].

Ce_{3d} and Al_{2p} regions are depicted in Figure 3.5b. The Ce_{3d} spectrum consists of 5 doubles (3d_{5/2} and 3d_{3/2} components), three of which correspond to Ce⁴⁺ (882.1-900.8 eV, 888.6-906.9 eV and 898.0-916.3 eV), while the remaining two are attributed to Ce³⁺ (880.6-898.9 eV and 883.9-902.0 eV). The peaks at 74.0 and 75.0 eV in Al_{2p} region of NiO/Al₂O₃-US (I) catalyst indicates the presence of Al-O and AlO-H bonds, respectively [48]. The distribution of Ce_{3d} and Al_{2p} species is maintained after the catalytic tests.

O_{1s} region was also analyzed and results are collected in Figure 3.5c. Three peaks were required to fit this region for CeO₂-based catalysts centered at 529.0, 531.0 and 533.0 eV, which can be assigned to lattice oxygen, surface-adsorbed oxygen, hydroxyl groups and carbonates, and molecular water, respectively [49,50], whereas two peaks localized at 531.0 and 532.3 eV are required for Al₂O₃-based catalysts, which corresponds to Al-O and AlO-H, respectively [51,52]. This distribution of species, is maintained after the catalytic test for NiO/Al₂O₃-US (I) catalyst, however for NiO/CeO₂-US (I) catalyst the relative concentration of surface-adsorbed oxygen, hydroxyl groups, and carbonates, and molecular water decreases from 35.5 to 28.7 %, which can indicate a removal of surface groups during the catalytic tests. To corroborate this, C_{1s} region (region not shown) was also analyzed. It is observed that carbon content decreases from 12.0 to 6.9 % after the reaction in NiO/CeO₂-US (I) sample whereas from 7.5 to 8.4 %. This seems to indicate that whereas in NiO/Al₂O₃-US (I) catalyst

carbon species are formed on the catalyst surface during the catalyst tests, in NiO/CeO₂-US (I) catalyst carbon species are removed from the catalyst surface.

3.3.4. Isotopic experiments

The CO₂ methanation mechanisms have been studied for NiO/Al₂O₃-UA (I) and NiO/CeO₂-US (I), and isotopic experiments have been performed with ¹³C¹⁸O₂ pulses in order to understand the role of catalyst oxygen during the reaction. Figure 3.6. shows results of the first ¹³C¹⁸O₂ pulse performed together with reference Ar pulse for NiO/Al₂O₃-US (I) (Figure 3.6a.) and NiO/CeO₂-US (I) (Figure 3.6b.). For proper interpretation of the results, note that not all *m/z* signals monitored during the experiments are plotted in these figures, i.e., those signals with negligible values are not included in Figure 3.6. for the sake of simplicity.

The shape of Ar profiles is characteristic of an inert gas pulse. Most signals detected once ¹³C¹⁸O₂ is pulsed appear at the same relative time than Ar, considering time = 0 s the injection of the gas. These signals include CO₂, CO and CH₄ species, which indicates that exchange of oxygens between CO₂ molecules and catalysts, all reaction steps required to hydrogenate CO₂, and the desorption of CH₄ and CO occur in a time frame much lower than the seconds scale of the measurements. The main difference between the Ar peaks and peaks of CO₂, CO and CH₄ species is the area, which is lower for reactants and products than for Ar. On the contrary, the H₂O profiles appear delay by 40 seconds with regard to the Ar reference, and this evidences that the H₂O desorption is significantly slower than the remaining steps of the mechanism. Note that CO is detected in the isotopic experiments but not in the catalytic tests performed with NiO/CeO₂-US (I), because the experimental conditions of both types of experiments are very different with much higher concentration of CO₂ in the catalytic tests than in the isotopic experiments.

¹³C¹⁸O₂ is not detected in the pulse experiments shown in Figure 3.6., and all oxygen-containing species measured come with ¹⁶O of the catalysts. The detection of a high ¹³C¹⁶O₂ signal indicates that the double exchange of oxygen atoms between the ¹³C¹⁸O₂ pulsed and the catalysts takes place in a significant extent. ¹³C¹⁶O is also detected, probably because the catalysts are partially reduced by H₂ before the pulse, and part of the oxygens of ¹³C¹⁸O₂ reoxidize the catalysts. The release of ¹²C¹⁶O and ¹²CH₄, with ¹²C, evidences that surface carbon species chemisorbed on the catalysts before the ¹³C¹⁸O₂ pulse are also desorbed and participate in the hydrogenation processes.

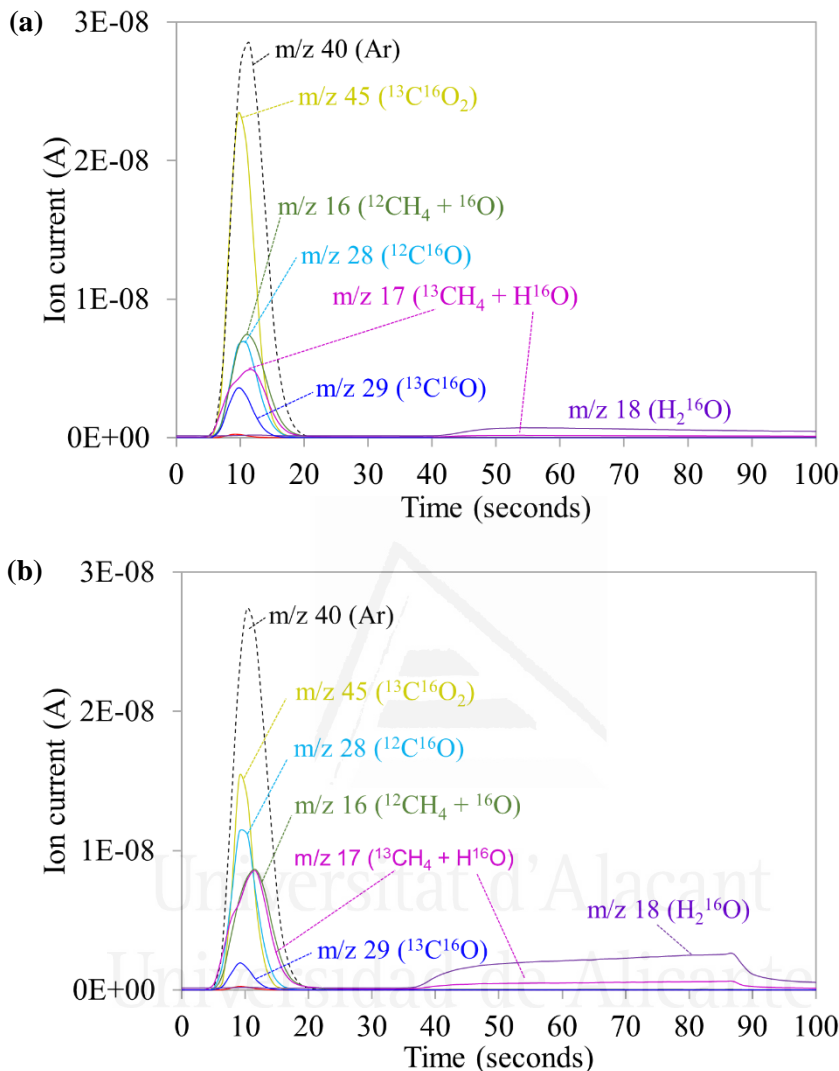


Figure 3.6. First pulse of Ar and ¹³C¹⁸O₂ into a continuous flow of H₂ (50% H₂/He) at 350 °C, over (a) NiO/Al₂O₃-US (I) and (b) NiO/CeO₂-US (I).

For a quantitative analysis of the pulse experiments, the area of the different peaks has been calculated and has been expressed as mass balance. Figure 3.7. compiles the mass balances of carbon species, including CO₂, CO and CH₄ species, both with ¹²C and ¹³C, for the three consecutive ¹³C¹⁸O₂ pulses performed to each catalyst.

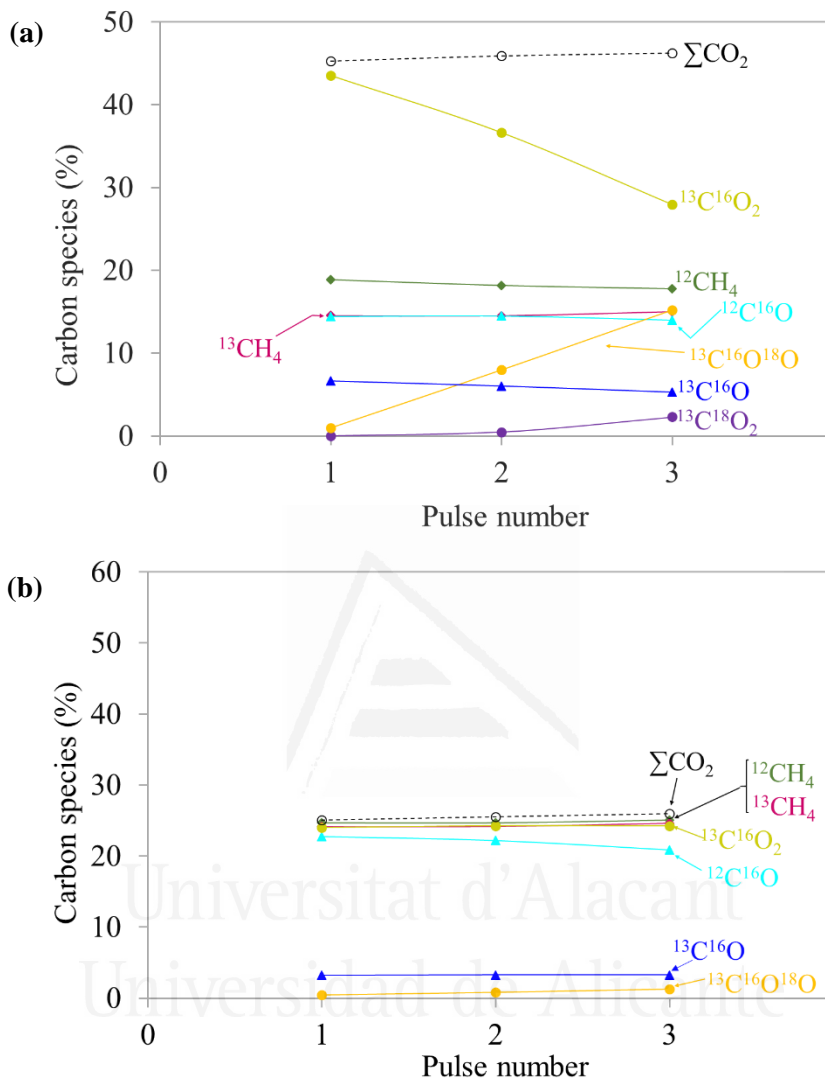


Figure 3.7. Percentage of carbon species in three consecutive pulses of $^{13}\text{C}^{18}\text{O}_2$ into a continuous flow of H₂ (50% H₂/He) at 350 °C, over (a) NiO/Al₂O₃-US (I) and (b) NiO/CeO₂-US (I).

The carbon species distribution keeps constant for the three pulses fed to NiO/CeO₂-US (I), but not for those fed to NiO/Al₂O₃-US (I). The release of ¹⁸O-containing species is almost negligible for NiO/CeO₂-US (I) (only few $^{13}\text{C}^{16}\text{O}^{18}\text{O}$ is detected), while for NiO/Al₂O₃-US (I), the $^{13}\text{C}^{16}\text{O}^{18}\text{O}$ signal increases progressively at expense of the $^{13}\text{C}^{16}\text{O}_2$ decrease. This means that both catalysts exchange oxygen with the CO₂ molecules, but the exchange capacity of ceria is much higher than that of

alumina, as expected. This effect is also observed in the H₂O yielded as reaction product, as observed in the mass balances of H₂O plotted in Figure 3.8. Only H₂¹⁶O (98 %) is detected for the three pulses carried out with NiO/CeO₂-US (I), while some H₂¹⁸O (11 %) is observed in the third pulse to NiO/Al₂O₃-US (I).

As shown in Figure 3.7., the value of the sum of all CO₂ species is constant in progressive pulses for both catalysts, indicating that the conversions are always the same, and NiO/CeO₂-US (I) reaches higher conversions (lower \sum CO₂ values) than NiO/Al₂O₃-US (I) in agreement with the catalytic tests.

The total amount of CH₄ (¹²CH₄ + ¹³CH₄) yielded as hydrogenation product is higher for NiO/CeO₂-US (I) than for NiO/Al₂O₃-US (I), which is also in accordance with the higher catalytic activity observed in the catalytic test results. Note that the percentages of ¹²CH₄ and ¹³CH₄ released are equal for NiO/CeO₂-US (I) and almost equal for NiO/Al₂O₃-US (I), and this evidences the hydrogenation of carbon species (with ¹²C) present on the catalysts before the ¹³C¹⁸O₂ pulses together with those created upon ¹³C¹⁸O₂ chemisorption.

¹³C¹⁶O and ¹²C¹⁶O signals are also observed for both catalysts. This was expected for NiO/Al₂O₃-US (I), because CO was also detected in the catalytic tests, but not for NiO/CeO₂-US (I). This apparent discrepancy between the catalytic tests and the isotopic experiments is attributed to the different experimental conditions used, CO₂ and H₂ being in stoichiometric conditions in the catalytic experiments but not in the pulse experiments with isotopic gas.

The isotopic experiments provide valuable information about the CO₂ methanation mechanism. It can be concluded that, in a first step, the CO₂ molecules are chemisorbed on the catalysts and, in most cases the double C=O bonds are broken. This involves reduced sites of the catalysts that gets oxidized by CO₂. Then, different reaction pathways can be followed. Part of the oxygens removed upon the double bonds breaking are replaced by catalyst oxygen and are released as CO or CO₂, leaving reduced sites on the catalyst again. Simultaneously, part of the carbon species adsorbed on the catalysts surface are hydrogenated and released as CH₄. NiO/CeO₂-US (I) is get involved very efficiently in these processes, and isotopic experiments suggest that the energy demanding dissociation of the CO₂ double bonds is significantly improved by this catalyst. As observed by XPS, the NiO/CeO₂-US (I) catalyst combines reduced nickel with cationic nickel species, and it is postulated that the cationic species are probably stabilized at the NiO-CeO₂ interface while nickel with poor contact with ceria is reduced more easily. This combines partially reduced nickel oxide actives sites for CO₂ dissociation in an oxidized environment located at the NiO-CeO₂ interface, with highly reduced nickel sites suitable for H₂ dissociation. Once ¹²O¹⁸O₂ is chemisorbed and

dissociated at the NiO-CeO₂ interface, the adsorbed ¹⁸O is not necessarily removed by H₂ in this particular active site. Probably, these oxygens are transferred to ceria using the oxygen vacancies created on this support through ceria oxygen removal by H₂ (yielding H₂¹⁶O₂) somewhere else on the ceria surface. That is why ¹⁸O is not detected in the isotopic experiments with NiO/CeO₂-US (I), because the ¹⁸O atoms left by ¹³C¹⁸O₂ are sent and get lost into the ceria support. This is possible due to the high oxygen and vacants mobility of ceria, while other metal oxides, such as alumina, do not have this option.

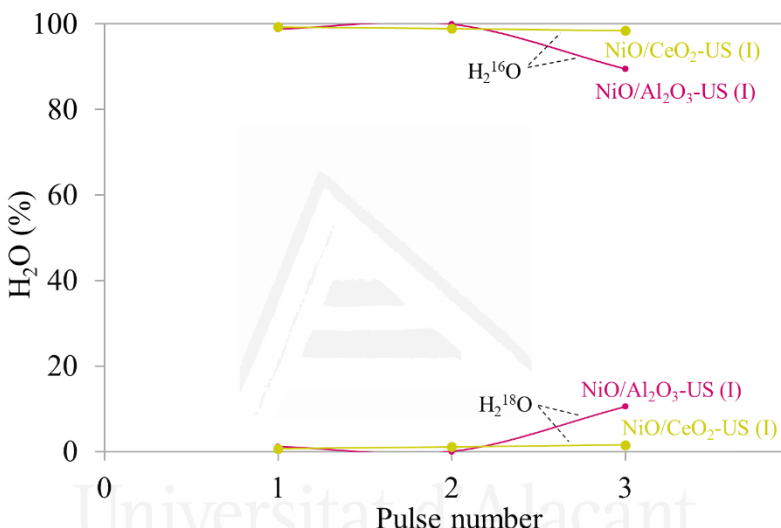


Figure 3.8. Percentage of H₂O species in three consecutive pulses of ¹³C¹⁸O₂ at 350 °C, over NiO/Al₂O₃-US (I) and NiO/CeO₂-US (I).

NiO/Al₂O₃-US (I) is also able to promote the dissociation of CO₂, which is evidenced by the detection of ¹³C¹⁶O₂ molecules (with catalyst oxygen), but NiO/Al₂O₃-US (I) is not as efficient as NiO/CeO₂-US (I). The detection of gas products with ¹⁸O after the first pulse of ¹³C¹⁸O₂ indicates that a high proportion of catalyst sites available for the dissociation of ¹³C¹⁸O₂ are used in the first pulse. These results also show that the ¹⁸O adsorbed in the first pulse is either removed by H₂, yielding H₂¹⁸O, or used in a further pulse to be exchanged with other ¹³C¹⁸O₂ molecule. One of the reasons of the lower activity of NiO/Al₂O₃-US (I) with regard to NiO/CeO₂-US (I) is that CO₂ dissociation and H₂O formation takes place in the same active sites. As deduced from the shape of the H₂O peaks in the pulse experiments, H₂O desorption is much slower than CO₂ chemisorption and dissociation, and therefore, the slow desorption of H₂O

limits further chemisorption and dissociation of other CO₂ molecules. On the contrary, the high oxygen mobility of oxygen into the ceria support allows dissociate CO₂ in certain active sites (probably at the NiO-CeO₂ interface) while H₂O is being formed and released somewhere else of the ceria surface.

3.3.5. *In-situ DRIFTS experiments*

In-situ DRIFTS experiments were carried out to monitor the nature of the surface species present on the catalysts under reaction conditions at different temperatures, and Figure 3.9. compiles the recorded spectra.

Gas phase CO₂ provides an intense double band at 2350 cm⁻¹ together with two double bands localized between 3500 – 3750 cm⁻¹. For easy identification of the surface species on the spectra, Figure 3.10. shows a scheme of the main surface carbon species together with the ranges of wavenumbers active in infrared [21,46,53–57].

Important information about the methanation mechanism is obtained from bands below 1700 cm⁻¹, and the behaviour of these bands with temperature is different for NiO/Al₂O₃-US (I) (Figure 3.9a.) and NiO/CeO₂-US (I) (Figure 3.9b.).

The methanation reaction does not occur at 150 °C (see Figure 3.4.), and the positive bands in the spectra of both catalysts evidence accumulation of surface species at this temperature. NiO/Al₂O₃-US (I) spectrum at 150 °C shows bands at 1652, 1430 and 1225 cm⁻¹ that can be assigned to bicarbonates, which are created by CO₂ chemisorption on hydroxyl groups. The O-H stretching of these bicarbonates is also observed at 3625 cm⁻¹. The role of the alumina support in the chemisorption of CO₂ was already described by other authors, this step playing an important role in the methanation reaction [5].

According to the catalytic tests (Figure 3.4.), the onset reaction temperature is around 250 °C, and the NiO/Al₂O₃-US (I) spectra at this and higher temperatures evidence the depletion of bicarbonates and the formation of formates as one of the possible reaction intermediates. We cannot rule out the presence of other intermediates which present a high kinetic rate of formation and decomposition and, thus, cannot be observed by DRIFT. The tiny bands at 3000 and 2900 cm⁻¹ are related to the CH-stretching mode of formates, and the bands at 1588 and 1375 cm⁻¹ correspond to their symmetric and asymmetric vOCO modes. The formation of formates upon CO₂ chemisorption, probably on hydroxyl groups of alumina, is consistent with kinetic studies reported by other authors [8,58] predicting that CO₂ chemisorption on NiO/Al₂O₃-US (I) takes place with dissociation of one of the oxygens. The presence of formates under reaction conditions explains the production of CO during the catalytic

tests. Formates are created once CO₂ is chemisorbed and could be partially hydrogenated, yielding CH₄ or desorbed yielding CO + H₂O.

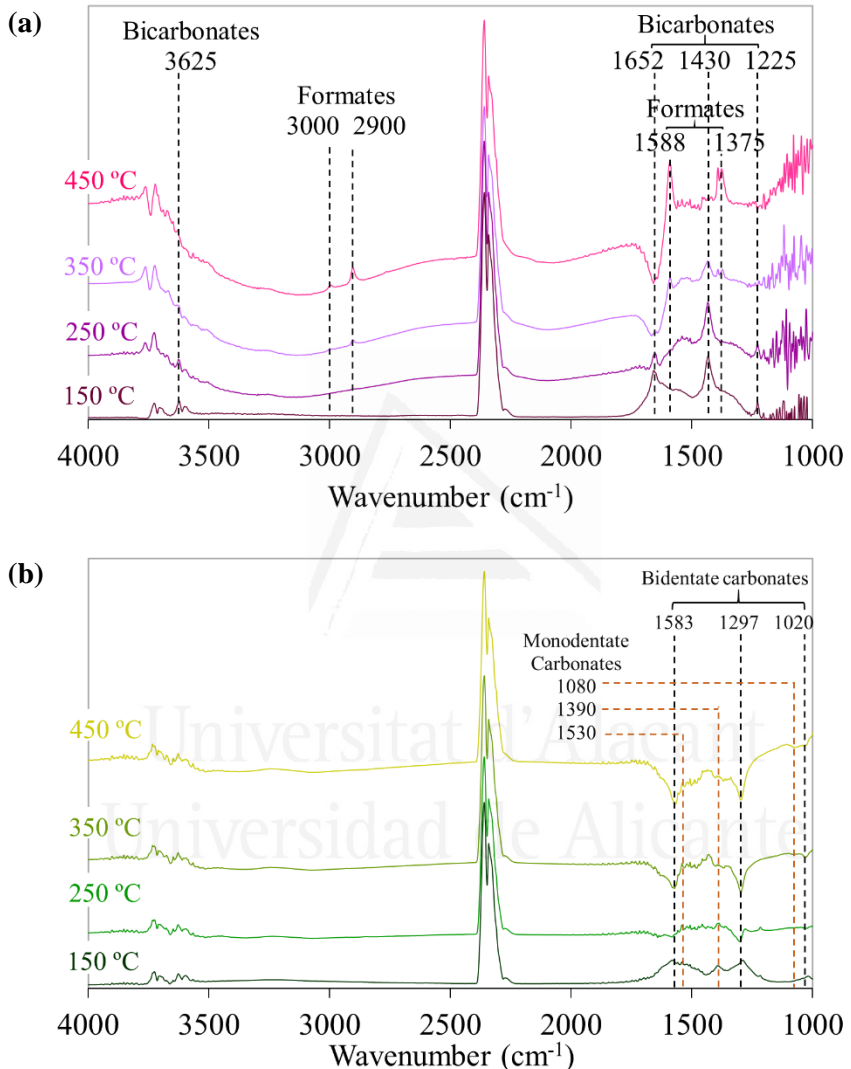


Figure 3.9. In situ DRIFTS experiments under H₂/CO₂/He at different temperatures. **(a)** NiO/Al₂O₃-US (I) and **(b)** NiO/CeO₂-US (I). Spectra were recorded after 60 minutes under reaction conditions at each temperature and the background spectrum recorded at room temperature under He was subtracted in all cases.

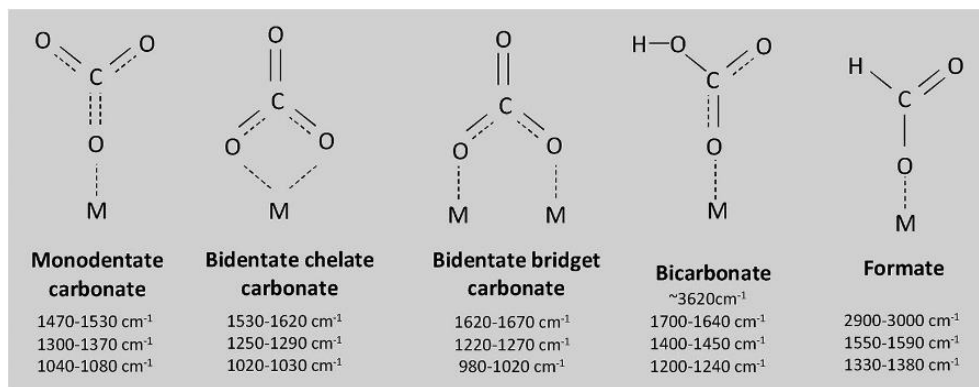


Figure 3.10. Scheme of surface carbon species and adsorption regions in infrared spectra.

On the contrary, the behaviour of NiO/CeO₂-US (I) is different. The spectrum of this catalyst at 150 °C shows bands at 1583 and 1297 cm⁻¹, which are consistent with the presence of bidentate carbonates in chelate configuration, and these bands disappear under reaction conditions. There two bands are negative at 250 °C and higher temperatures, which evidences the depletion of carbonates that were present on the samples when the background spectrum was recorded in He at 150 °C. A small band is also observed at 1390 cm⁻¹ at 150 °C, and also disappears at higher temperatures. This band can be assigned to monodentate carbonates, and these species should additionally present bands around 1300 – 1370 cm⁻¹ and 1040 – 1080 cm⁻¹ which are hardly observed in Figure 3.10b. The absence of surface carbon species on the NiO/CeO₂-US (I) catalyst under methanation reaction conditions is consistent with the conclusions of the isotopic exchange experiments and XPS, that is, CO₂ is chemisorbed and dissociated on reduced sites of the catalyst and carbon intermediates are not observed by infrared because the carbon left is either desorbed as CO₂ taking oxygens from the catalyst or is hydrogenated yielding CH₄.

3.3.6. CO₂ + H₂ reaction mechanism on NiO/CeO₂ and NiO/Al₂O₃ catalysts

As a summary of the conclusions obtained by the different techniques used in this study, Figure 3.11. shows schemes with the main steps of the CO₂ + H₂ reaction mechanisms taking place on NiO/Al₂O₃-US (I) and NiO/CeO₂-US (I).

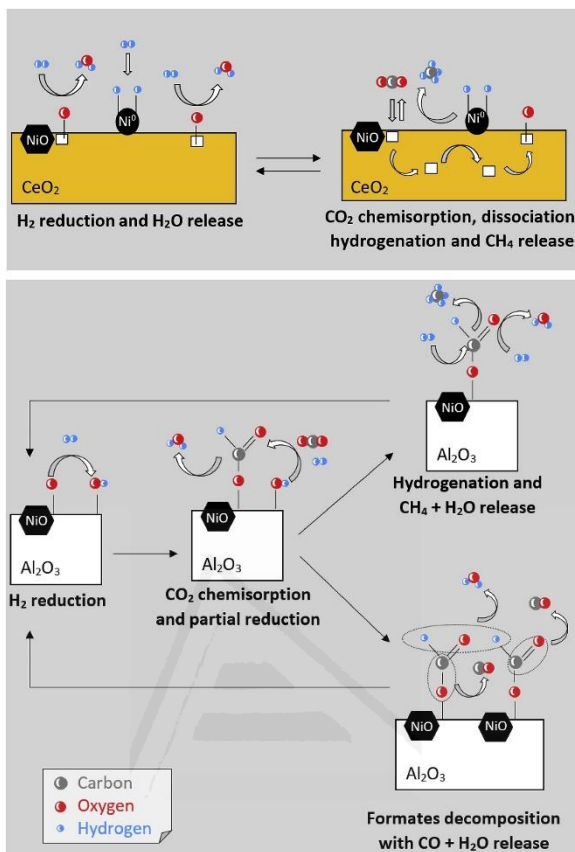


Figure 3.11. Scheme of the CO₂ + H₂ reaction mechanisms on NiO/CeO₂-US (I) and NiO/Al₂O₃-US (I) catalysts.

The NiO/CeO₂-US (I)-catalysed CO₂ methanation reaction starts with the reduction of the catalyst. This reduction takes place both at the NiO-CeO₂ interface, creating reduced sites on an oxidized NiO-rich environment, and on the ceria support creating oxygen vacancies. Among these sites, the NiO-CeO₂ interface is reduced more easily, but the ceria support is much more abundant, and therefore is statistically more accessible to H₂. Additionally, XPS results evidence that part of the NiO particles, those with poor interaction with the ceria support, are reduced to metal nickel where H₂ molecules are efficiently dissociated. CO₂ chemisorption takes place on the partially reduced NiO-CeO₂ interface, where CO₂ is dissociated, and oxygens are transferred to the ceria support to restore the oxygen balance. These oxygens move throughout the ceria lattice using the previously created vacancies. This transfer of oxygen from the NiO-CeO₂ interface to somewhere else into the ceria support leaves the active sites at

the NiO-CeO₂ interface available for further CO₂ chemisorption. Hence, the H₂ reduction of the NiO-CeO₂ interface is not necessary after the chemisorption of every CO₂ molecule since the high oxygen mobility on this catalyst allows the reduction to take place somewhere else on the ceria surface. Isotopic experiments indicate that, upon CO₂ dissociation, the carbon atom either can accept ceria oxygens to yield CO₂ again or dissociated hydrogens to yield methane.

This mechanism is very effective for several reasons: i) the NiO/CeO₂-US (I) catalyst combine two types of active sites efficient for CO₂ and H₂ dissociation, respectively; ii) water desorption is the slowest step of the mechanism, as observed in the isotopic experiments and this product is not necessarily formed on the same active sites over which CO₂ is chemisorbed, i.e., the CO₂ chemisorption sites at the NiO-CeO₂ interface are not blocked by water molecules; iii) the catalyst surface does not accumulate carbon-containing species under reaction conditions, which allows faster chemisorption of CO₂.

The NiO/Al₂O₃-US (I)-catalysed CO₂-H₂ reaction follows a different mechanism, and in this case, the participation of the alumina support is not so relevant. Hydroxyl groups are created by H₂ reduction of the NiO-Al₂O₃ interface, where CO₂ is chemisorbed afterwards. The isotopic experiments indicate that part of the chemisorbed CO₂ molecules are desorbed after the CO₂ oxygens are exchanged by catalyst oxygens. In this case, unlike NiO/CeO₂-US (I), CO₂ oxygens cannot migrate throughout the alumina surface and remain wherever CO₂ has been dissociated. These chemisorbed CO₂ molecules block the active sites and hinder further CO₂ molecules chemisorption and dissociation. The CO₂ molecules that are not desorbed yield formates and water upon H₂ reduction. Part of these formates could be further hydrogenated yielding CH₄ + H₂O and part decompose yielding CO + H₂O, which explains the lower selectivity of NiO/Al₂O₃-US (I) observed in the catalytic tests. The handicaps of this reaction mechanism, in comparison to that taking place on NiO/CeO₂-US (I) are: i) There are not specific active sites for H₂ dissociation, and molecular H₂ must reduce surface species; ii) all the steps of the mechanism take place on the same active sites, and the slow release of water and the accumulation of surface formates on these sites delay the dissociation and chemisorption of further CO₂ molecules.

3.4. Conclusions

The CO₂ methanation reaction mechanism has been studied for NiO/CeO₂-US (I) and NiO/Al₂O₃-US (I) catalysts, and the following conclusions can be summarized:

- ❖ For both catalysts, isotopic experiments evidence a dynamic equilibrium between gas phase CO₂ and catalyst oxygen, consisting of CO₂ chemisorption, exchange of CO₂ oxygens with the catalysts, and CO₂ desorption. In the presence of H₂, part of the chemisorbed CO₂ is desorbed after oxygens exchange and part is hydrogenated.
- ❖ The higher methanation activity and 100% CH₄ selectivity of NiO/CeO₂-US (I) is attributed to the following mechanistic aspects: i) the presence of two different actives sites for the CO₂ dissociation (NiO-Ceria interface) and for H₂ dissociation (reduced Ni⁰ particles) which was pointed out by XPS; ii) pulse experiments indicate that the slowest step of the mechanism is the water desorption, however, in NiO/CeO₂-US (I) catalysts due to the presence of two type of actives sites and the high oxygen mobility throughout the ceria lattice, the formation of water not necessarily occurs in the CO₂ chemisorption sites and thus the NiO-CeO₂ interface are not blocked by water molecules; iii)faster chemisorption and dissociation of CO₂ is allowed in Ni/CeO₂ surface due to the not accumulation of carbon-containing species under reaction conditions as was observed by in situ DRIFTS experiments.
- ❖ The handicaps of the NiO/Al₂O₃-US (I) catalyst, in comparison to NiO/CeO₂-US (I), are: i) There are not specific active sites for H₂ dissociation, and molecular H₂ must reduce surface species; ii) all the steps of the mechanism take place on the same active sites, and the slow release of water and the accumulation of surface formates on these sites delay the chemisorption of further CO₂ molecules. iii) The formation of formates as reaction intermediates results in the production of CO as undesired by-product.

3.5. References

- [1] L. Falbo, C.G. Visconti, L. Lietti, J. Szanyi, The effect of CO on CO₂ methanation over Ru/Al₂O₃ catalysts: a combined steady-state reactivity and transient DRIFT spectroscopy study, *Appl. Catal. B Environ.* 256 (2019) 117791.
- [2] G. Garbarino, C. Wang, T. Cavattoni, E. Finocchio, P. Riani, M. Flytzani-stephanopoulos, G. Busca, A study of Ni/La-Al₂O₃ catalysts: A competitive system for CO₂ methanation, *Appl. Catal. B Environ.* 248 (2019) 286–297.
- [3] J. Lin, C. Ma, Q. Wang, Y. Xu, G. Ma, J. Wang, H. Wang, C. Dong, C. Zhang, M. Ding, Enhanced low-temperature performance of CO₂ methanation over mesoporous Ni/Al₂O₃-ZrO₂ catalysts, *Appl. Catal. B Environ.* 243 (2019) 262–272.
- [4] N.T. S. ichiro Fujita, H. Terunuma, M. Nakamura, Mechanisms of methanation

- of CO and CO₂ over Ni, *Ind. Eng. Chem. Res.* 30 (1991) 1146–1151.
- [5] A.E. Aksoylu, A.N. Akin, Z.I. Önsan, D.L. Trimm, Structure/activity relationships in coprecipitated nickel-alumina catalysts using CO₂ adsorption and methanation, *Appl. Catal. A Gen.* 145 (1996) 185–193.
 - [6] M. Yamasaki, H. Habazaki, T. Yoshida, E. Akiyama, A. Kawashima, K. Asami, K. Hashimoto, M. Komori, K. Shimamura, Compositional dependence of the CO₂ methanation activity of Ni/ZrO₂ catalysts prepared from amorphous Ni-Zr alloy precursors, *Appl. Catal. A Gen.* 163 (1997) 187–197.
 - [7] Q. Pan, J. Peng, T. Sun, S. Wang, S. Wang, Insight into the reaction route of CO₂ methanation: Promotion effect of medium basic sites, *Catal. Commun.* 45 (2014) 74–78.
 - [8] R.A. Hubble, J.Y. Lim, J.S. Dennis, Kinetic studies of CO₂ methanation over a Ni/ γ -Al₂O₃ catalyst, *Faraday Discuss.* 192 (2016) 529–544.
 - [9] L. Xu, F. Wang, M. Chen, J. Zhang, K. Yuan, L. Wang, K. Wu, G. Xu, W. Chen, CO₂ methanation over a Ni based ordered mesoporous catalyst for the production of synthetic natural gas, *Roya Soc. Chem. Adv.* 6 (2016) 28489–28499.
 - [10] L. Xu, F. Wang, M. Chen, D. Nie, X. Lian, Z. Lu, H. Chen, K. Zhang, P. Ge, CO₂ methanation over rare earth doped Ni based mesoporous catalysts with intensified low-temperature activity, *Int. J. Hydrogen Energy.* 42 (2017) 15523–15539.
 - [11] M. Li, H. Amari, A.C. Van Veen, Metal-oxide interaction enhanced CO₂ activation in methanation over ceria supported nickel nanocrystallites, *Appl. Catal. B Environ.* 239 (2018) 27–35.
 - [12] N.M. Gupta, V.S. Kamble, A. Rao, R.M. Iyer, On the mechanism of CO and CO₂ methanation over Ru/molecular-sieve catalyst, *J. Catal.* 60 (1979) 57–67.
 - [13] F. Solymosi, A. Erdöhelyi, M. Kocsis, Methanation of CO₂ on supported Ru catalysts, *J. Chem. Soc. Faraday Trans. 1 Phys. Chem. Condens. Phases.* 77 (1981) 1003–1012.
 - [14] S. Scirè, C. Crisafulli, R. Maggiore, S. Minicò, S. Galvagno, Influence of the support on CO₂ methanation over Ru catalysts: an FT-IR study, *Catal. Letters.* 51 (1998) 41–45.
 - [15] T. Abe, M. Tanizawa, K. Watanabe, A. Taguchi, CO₂ methanation property of Ru nanoparticle-loaded TiO₂ prepared by a polygonal barrel-sputtering method, *Energy Environ. Sci.* 2 (2009) 315–321.
 - [16] Q. Lin, X.Y. Liu, Y. Jiang, Y. Wang, Y. Huang, T. Zhang, Crystal phase effects on the structure and performance of ruthenium nanoparticles for CO₂ hydrogenation, *Catal. Sci. Technol.* 4 (2014) 2058–2063.

- [17] C. Janke, M.S. Duyar, M. Hoskins, R. Farrauto, Catalytic and adsorption studies for the hydrogenation of CO₂ to methane, *Appl. Catal. B, Environ.* 152–153 (2014) 184–191.
- [18] D.C. Upham, A.R. Derk, S. Sharma, CO₂ methanation by Ru-doped ceria: the role of the oxidation state of the surface, *Catal. Sci. Technol.* 5 (2015) 1783–1791.
- [19] J.A.H. Dreyer, P. Li, L. Zhang, G. Khai, R. Zhang, P.H. Sit, W. Yang, Influence of the oxide support reducibility on the CO₂ methanation over Ru-based catalysts, *Appl. Catal. B Environ. Environ.* 219 (2017) 715–726.
- [20] A. Erdöhelyi, M. Pásztor, F. Solymosi, Catalytic hydrogenation of CO₂ over supported palladium, *J. Catal.* 98 (1986) 166–177.
- [21] A. Karelovic, P. Ruiz, Improving the hydrogenation function of Pd/γ-Al₂O₃ catalyst by Rh/γ-Al₂O₃ Addition in CO₂ methanation at low temperature, *ACS Catal.* 3 (2013) 2799–2812.
- [22] X. Wang, H. Shi, J.H. Kwak, J. Szanyi, Mechanism of CO₂ hydrogenation on Pd/Al₂O₃ catalysts: kinetics and transient DRIFTS-MS studies, *ACS Catal.* 5 (2015) 63337–6349.
- [23] Z. Zhang, A. Kladi, X.E. Verykios, Effects of carrier doping on kinetic parameters of CO₂ hydrogenation on supported rhodium catalysts, *J. Catal.* 148 (1994) 737–747.
- [24] C. De Leitenburg, A. Trovarelli, J. Kaspar, A temperature-programmed and transient kinetic study of CO₂ activation and methanation over CeO₂ supported noble metals, *J. Catal.* 166 (1997) 98–107.
- [25] M. Jacquemin, A. Beuls, P. Ruiz, Catalytic production of methane from CO₂ and H₂ at low temperature: Insight on the reaction mechanism, *Catal. Today.* 157 (2010) 462–466.
- [26] A. Karelovic, P. Ruiz, Mechanistic study of low temperature CO₂ methanation over Rh/TiO₂ catalysts, *J. Catal.* 301 (2013) 141–153.
- [27] B. Miao, S.S.K. Ma, X. Wang, H. Su, S.H. Chan, Catalysis mechanisms of CO₂ and CO methanation, *Catal. Sci. Technol.* 6 (2016) 4048–4058.
- [28] S. Tada, T. Shimizu, H. Kameyama, T. Haneda, R. Kikuchi, Ni/CeO₂ catalysts with high CO₂ methanation activity and high CH₄ selectivity at low temperatures, *Int. J. Hydrogen Energy.* 37 (2012) 5527–5531.
- [29] D. Terribile, A. Trovarelli, J. Llorca, The preparation of high surface area CeO₂-ZrO₂ mixed oxides by a surfactant-assisted approach, *Catal. Today.* 43 (1998) 79–88.

- [30] Y. Zheng, M. Zhang, Preparation and electrochemical properties of nickel oxide by molten-salt synthesis, *Mater. Lett.* 61 (2007) 3967–3969.
- [31] M. Rudolph, M. Motylenko, D. Rafaja, Structure model of $\gamma\text{-Al}_2\text{O}_3$ based on planar defects, *Int. Union Crystallogr. J.* 6 (2014) 116–127.
- [32] C. Jiménez-González, Z. Boukha, B. de Rivas, J.J. Delgado, M.Á. Cauqui, J.R. González-Velasco, J.I. Gutiérrez-Ortiz, R. López-Fonseca, Structural characterisation of Ni/alumina reforming catalysts activated at high temperatures, *Appl. Catal. A Gen. Gen.* 466 (2013) 9–20.
- [33] F. Song, Q. Zhong, Y. Yu, M. Shi, Y. Wu, J. Hu, Y. Song, Obtaining well-dispersed Ni/ Al_2O_3 catalyst for CO_2 methanation with a microwave-assisted method, *Int. J. Hydrogen Energy.* 42 (2016) 4174–4183.
- [34] Z. Boukha, C. Jiménez-González, M. Gil-Calvo, B. de Rivas, J.R. González-Velasco, J.I. Gutiérrez-Ortiz, R. López-Fonseca, $\text{MgO}/\text{NiAl}_2\text{O}_4$ as a new formulation of reforming catalysts: Tuning the surface properties for the enhanced partial oxidation of methane, *Appl. Catal. B Environ. Environ.* 199 (2016) 372–383.
- [35] K. Ray, G. Deo, A potential descriptor for the CO_2 hydrogenation to CH_4 over Al_2O_3 supported Ni and Ni-based alloy catalysts, *Appl. Catal. B Environ.* 218 (2017) 525–537.
- [36] H. Li, H. Li, W.L. Dai, W. Wang, Z. Fang, J.F. Deng, XPS studies on surface electronic characteristics of Ni-B and Ni-P amorphous alloy and its correlation to their catalytic properties, *Appl. Surf. Sci.* 152 (1999) 25–34.
- [37] Z. Hou, O. Yokota, T. Tanaka, T. Yashima, Characterization of Ca-promoted Ni/ $\alpha\text{-Al}_2\text{O}_3$ catalyst for CH_4 reforming with CO_2 , *Appl. Catal. A Gen.* 253 (2003) 381–387.
- [38] E. Heracleous, A.F. Lee, K. Wilson, A.A. Lemonidou, Investigation of Ni-based alumina-supported catalysts for the oxidative dehydrogenation of ethane to ethylene: Structural characterization and reactivity studies, *J. Catal.* 231 (2005) 159–171.
- [39] J. Kugai, V. Subramani, C. Song, M.H. Engelhard, Y. Chin, Effects of nanocrystalline CeO_2 supports on the properties and performance of Ni – Rh bimetallic catalyst for oxidative steam reforming of ethanol, *J. Catal.* 238 (2006) 430–440.
- [40] X. Xu, L. Li, F. Yu, H. Peng, X. Fang, X. Wang, Mesoporous high surface area NiO synthesized with soft templates: Remarkable for catalytic CH_4 deep oxidation, *Mol. Catal.* 441 (2017) 81–91.
- [41] G.H. Yu, L.R. Zeng, F.W. Zhu, C.L. Chai, W.Y. Lai, Magnetic properties and

- x-ray photoelectron spectroscopy study of NiO/NiFe films prepared by magnetron sputtering, *J. Appl. Phys.* 90 (2001) 4039–4043.
- [42] A. Ahmed, T. Ali, M.N. Siddique, A. Ahmad, P. Tripathi, Enhanced room temperature ferromagnetism in Ni doped SnO₂ nanoparticles: a comprehensive study, *J. Appl. Phys.* 122 (2017) 083906.
 - [43] A.P. Grosvenor, M.C. Biesinger, R.S.C. Smart, N.S. McIntyre, New interpretations of XPS spectra of nickel metal and oxides, *Surf. Sci.* 600 (2006) 1771–1779.
 - [44] N. Weidler, J. Schuch, F. Knaus, P. Stenner, S. Hoch, A. Maljusch, R. Schäfer, B. Kaiser, W. Jaegermann, X-ray photoelectron spectroscopic investigation of plasma-enhanced chemical vapor deposited NiO_x, NiO_x(OH)_y, and CoNiO_x(OH)_y: influence of the chemical composition on the catalytic activity for the oxygen evolution reaction, *J. Phys. Chem. C.* 121 (2017) 6455–6463.
 - [45] A. Caballero, J.P. Holgado, V.M. Gonzalez de la Cruz, S.E. Habas, T. Herranz, M. Salmeron, In situ spectroscopic detection of SMSI effect in a Ni/CeO₂ system: hydrogen-induced burial and dig out of metallic nickel, *Chem. Commun.* 46 (2010) 1097–1099.
 - [46] P.A.U. Aldana, F. Ocampo, K. Kobl, B. Louis, F. Thibault-starzyk, M. Daturi, P. Bazin, S. Thomas, A.C. Roger, Catalytic CO₂ valorization into CH₄ on Ni-based ceria-zirconia. Reaction mechanism by operando IR spectroscopy, *Catal. Today.* 215 (2013) 201–207.
 - [47] V. Alcalde-Santiago, A. Davó-Quiñonero, D. Lozano-Castelló, A. Quindimil, U. De-La-Torre, B. Pereda-Ayo, J.A. González-Marcos, J.R. González-Velasco, A. Bueno-López, Ni/LnOx catalysts (Ln=La, Ce or Pr) for CO₂ methanation, *ChemCatChem.* 11 (2019) 810–819.
 - [48] N. Batra, J. Gope, Vandana, J. Panigrahi, R. Singh, P.K. Singh, Influence of deposition temperature of thermal ALD deposited Al₂O₃ films on silicon surface passivation, *AIP Adv.* 5 (2015) 067113.
 - [49] J.M. López, A.L. Gilbank, T. García, B. Solsona, S. Agouram, L. Torrente-Murciano, The prevalence of surface oxygen vacancies over the mobility of bulk oxygen in nanostructured ceria for the total toluene oxidation, *Appl. Catal. B Environ.* 174–175 (2015) 403–412.
 - [50] F. Liang, Y. Yu, W. Zhou, X. Xu, Z. Zhu, Highly defective CeO₂ as a promoter for efficient and stable water oxidation, *J. Mater. Chem. A.* 3 (2015) 634–640.
 - [51] J. Kim, S. Choi, J. Jo, S. Kyu, Y. Kim, Solution-processed lanthanum-doped Al₂O₃ gate dielectrics for high- mobility metal-oxide thin- film transistors, *Thin Solid Films.* 660 (2018) 814–818.

- [52] S. Lee, H. Choi, S. Shin, J. Park, G. Ham, H. Jung, H. Jeon, Permeation barrier properties of an Al₂O₃/ZrO₂ multilayer deposited by remote plasma atomic layer deposition, *Curr. Appl. Phys.* 14 (2014) 552–557.
- [53] D. Gamarra, G. Munuera, A.B. Hungría, M. Fernández-García, J.C. Conesa, P.A. Midgley, X.Q. Wang, J.C. Hanson, J.A. Rodríguez, A. Martínez-Arias, Structure-activity relationship in nanostructured copper-ceria-based preferential CO oxidation catalysts, *J. Phys. Chem. C* 111 (2007) 11026–11038.
- [54] D. Gamarra, A. Martínez-Arias, Preferential oxidation of CO in rich H₂ over CuO/CeO₂: Operando-DRIFTS analysis of deactivating effect of CO₂ and H₂O, *J. Catal.* 263 (2009) 189–195.
- [55] B.H. Solis, Y. Cui, X. Weng, J. Seifert, S. Schauermann, J. Sauer, S. Shaikhutdinov, H.J. Freund, Initial stages of CO₂ adsorption on CaO: a combined experimental and computational study, *Phys. Chem. Chem. Phys.* 19 (2017) 4231–4242.
- [56] H. Li, X. Jiao, L. Li, N. Zhao, F. Xiao, W. Wei, Y. Sun, B. Zhang, Synthesis of glycerol carbonate by direct carbonylation of glycerol with CO₂ over solid catalysts derived from Zn/Al/La and Zn/Al/La/M (M = Li, Mg and Zr) hydrotalcites, *Catal. Sci. Technol.* 5 (2015) 989–1005.
- [57] M.C. Raphulu, J. McPherson, E. Van der Lingen, J.A. Anderson, M.S. Scurrell, Investigation of the active site and the mode of Au/TiO₂ catalyst deactivation using Diffuse Reflectance Infrared Fourier transform Spectroscopy (DRIFTS), *Gold Bull.* 43 (2010) 21–28.
- [58] C.V. Miguel, A. Mendes, L.M. Madeira, Intrinsic kinetics of CO₂ methanation over an industrial nickel-based catalyst, *J. CO₂ Util.* 25 (2018) 128–136.

Universidad de Alicante

4

Design of active sites in NiO/CeO₂ catalysts for the CO₂ methanation: tailoring the NiO- CeO₂ contact

4.1. Introduction

4.2. Experimental section

- 4.2.1. Supports preparation
- 4.2.2. Catalysts preparation
- 4.2.3. Catalysts characterization
- 4.2.4. Catalytic tests
- 4.2.5. Mechanistic studies

4.3. Results and discussion

- 4.3.1. Catalysts characterization
- 4.3.2. CO₂ methanation tests
- 4.3.3. Fresh and used catalysts characterization by XPS
- 4.3.4. In-situ DRIFTS experiments
- 4.3.5. Pulse experiments with isotopic CO₂

4.4. Conclusions

4.5. References

4.1. Introduction

Currently, there is an increasing interest for alternative clean and sustainable energy sources that contribute to reduce, or mitigate, the global warming caused by the increase of the greenhouse gases influence and to reduce the fossil fuel dependence. In this sense, the capture and conversion of CO₂ to fuels seems to be a promising and attractive solution in a world with high energy demand [1,2]. The methanation of CO₂ is a sustainable solution since is a favourable reaction from the point of view of thermodynamics [3], it occurs faster than other reactions that form alcohols, proceeds at atmospheric pressure and moderately low temperatures and the methane produced can be directly injected into the existing network of natural gas pipelines and used as fuel of feedstock for the manufacture of other chemical products.

Nevertheless as explained in Chapter 1, the main problem in the CO₂ transformation into other products is the great stability of the molecule [4]: C=O bonds are highly stable and, therefore, a large amount of energy in the form of heat is required to allow their dissociation. Consequently, despite the reaction is thermodynamically favourable, it has strong kinetic limitations and thus, the use of a suitable catalyst is required to reach acceptable reaction rate and selectivity [5].

Metals such as Ni, Rh, Ru, Co or Pt, supported on different porous materials have been extensively studied since they allow to achieve considerable CO₂ methanation rates [6–8]. Noble metals, such as Pt or Ru, are much more active than Ni at low temperature (~200 °C). However, the scarce reserves and the prohibitive price of these noble metals along with the deactivation of metal sites by CO poisoning limits the commercialization and application of the prepared catalysts [9]. On the other hand, Ni has a good relationship between high catalytic activity and low price, and is usually the preferred option to accelerate the reaction, working at somewhat higher temperatures (>300 °C). Intense efforts have been made in order to design and improve Ni-based catalysts for the catalytic hydrogenations of CO₂. The catalytic behaviour of the Ni-based catalysts depends on several factors such as the type of support, Ni loading, addition of a second metal and preparation method [10].

It has already been proved the need for two distinct functional entities in an active catalyst, one for CO₂ activation and another one for the dissociation of H₂ [10]. Kwak et al. [11] have demonstrated that the reduction of CO₂ requires the presence of a catalyst capable of activating CO₂, such as a support oxide (Al₂O₃) itself or an oxide promoter (La₂O₃), and a metallic component (Pd) active in H₂ dissociation. This concept has been previously explored by our group for Ni-based catalysts supported on CeO₂, LaO_x and PrO_x oxides [12]. Summarizing, it was observed that Ni/CeO₂ is the most active catalyst among those compared because: i) Ni²⁺-ceria interaction provides a high number of

active sites for CO₂ dissociation; ii) the reduced Ni⁰ sites where H₂ dissociation occurs are the most electronegative; and iii) shows the lowest stability of surface CO₂ and H₂O species. Consequently, two type of active centres are required for the methanation of CO₂: NiO in intimate contact with ceria where CO₂ dissociation takes place and reduced Ni centres for the dissociation of H₂.

With that background, in this chapter the proportion of each active centre was varied by the modification of the Ni-CeO₂ interaction and the influence of this proportion in the CO₂ methanation was studied and deeply analysed. The goal of the study is to understand the role of the different active sites in the CO₂ methanation reaction and to optimize the proportion of each active site. This interaction has been modified by the Ni incorporation method and by controlling the surface of the ceria support. In this sense, three dimensionally ordered macroporous (3DOM) structures have been synthesized to improve Ni dispersion and contact. Ni has been introduced during the 3DOM synthesis by coimpregnation of successive impregnation of Ni and Ce precursors or after the CeO₂ 3DOM synthesis by Ni impregnation. Materials with uncontrolled structures (US) were also prepared by coprecipitation and Ni-impregnation.

4.2. Experimental section

4.2.1. Supports preparation

Supports were prepared with uncontrolled (US) and three dimensionally ordered macroporous (3DOM) structures. The synthesis of the macroporous catalyst (3DOM) was described elsewhere [13] and it is detailed in *Section 2.1.2* from *Chapter 2*. Briefly, polymethylmethacrylate (PMMA) colloidal crystals were synthesized by polymerization of divinylbenzene, methacrylic acid and methylmethacrylate in boiling aqueous solution. Then, a solution of cerium citrate in ethanol was infiltrated in the PMMA crystal template. Finally, the PMMA template was removed by calcination at 600 °C for 6 hours with a heating rate of 5 °C/min. The reference catalysts (US) were prepared by direct calcinations of the dried ethanolic solution of cerium citrate and the details of the synthesis are described in *Section 2.1.1*.

4.2.2. Catalysts preparation

Three catalysts with 3DOM structure and two catalysts with US structure have been prepared by different Ni incorporation methods: (i) impregnation of the previously

synthesized US and 3DOM CeO₂ supports with a ethanolic solution of nickel citrate. These catalysts were referenced as NiO/CeO₂-US (I) and NiO/CeO₂-3DOM (I), respectively. (ii) Successive impregnation of the PMMA crystal template with the ethanolic solution of nickel citrate and, subsequently with a ethanolic solution of cerium citrate. This catalyst was referenced as NiO/CeO₂-3DOM (SI). (iii) Coimpregnation of the PMMA crystal template with a ethanolic solution of cerium and nickel citrates. This sample was referred as NiO-CeO₂-3DOM (CI). The reference NiO-CeO₂-US (CI) catalyst was prepared by direct calcination of the dried ethanolic solution of nickel and cerium citrates. The target Ni content in all catalysts was 8.5% wt.%. Details of the different experimental conditions have been described in the Chapter 2 and the prepared materials are summarized in Table 4.1.

Table 4.1. Summary of synthesized samples.

Sample	Structure	Impregnation method	Target Ni content (%)
CeO ₂ -US	Undefined	-	0
CeO ₂ -3DOM	3DOM	-	0
NiO/CeO ₂ -US (I)	Undefined	Impregnation of CeO ₂ -US	8.5
NiO/CeO ₂ -3DOM (I)	3DOM	Impregnation of CeO ₂ -3DOM	8.5
NiO/CeO ₂ -3DOM (SI)	3DOM	Successive impregnation of PMMA	8.5
NiO-CeO ₂ -US (CI)	Undefined	-	8.5
NiO-CeO ₂ -3DOM (CI)	3DOM	Coimpregnation of PMMA	8.5

4.2.3. Catalysts characterization

The catalysts were characterized by means of complementary techniques. The nickel content was determined by ICP-OES. The catalysts morphology was studied by Field Emission Scanning Electron Microscopy (FESEM). The textural properties of the catalysts were characterized by N₂ adsorption-desorption isotherms at -196 °C and mercury porosimetry, after outgassing the catalysts under vacuum at 150 °C for 4 h and 50 °C for 12 h, respectively. The crystalline structure of the catalysts had been studied

by X-ray diffraction (XRD) and the average crystal size (D) was determined using the Scherrer equation [14,15]. The surface chemistry of the samples was analysed by X-ray photoelectron spectroscopy (XPS) and the reduction of the catalysts was studied by temperature programmed reduction with H₂ (H₂-TPR). Description of the techniques and of the experimental conditions and procedures has been detailed in *Chapter 2*.

4.2.4. Catalytic tests

Catalytic activity measurements were performed at the university of the Basque Country and the experimental conditions has been detailed in *Section 2.3.2*. Briefly, catalytic tests were performed using 400 mg of catalysts. The sample was pre-treated at 500 °C during 1 h under 20 % H₂/He. The reaction mixture (16 % CO₂ + 64 % H₂ and He balance) was fed with a total flow rate of 200 mL/min and the gas hourly space velocity was 12000 h⁻¹. The temperature was raised to 450 °C in steps of 25 °C, with a heating rate of 5 °C/min between steps, and the gas composition was measured in each step under steady state conditions. The gas composition was monitored with a gas chromatograph.

4.2.5. Mechanistic studies

Isotopic experiments were carried out at 350 °C with ¹³C¹⁸O₂ pulses, using 50 mg of the catalyst and a flowing mixture of 50 % H₂/He (20 mL/min). Three Ar pulses were first fed, and afterwards, three pulses of ¹²C¹⁶O₂ followed by three pulses of ¹³C¹⁸O₂. The exhaust gases were monitored with a mass spectrometer. The experimental procedures can be found in *Section 2.4.1*.

In-situ DRIFTS experiments were performed in an infrared spectrometer using a reaction cell with 70 mg of catalyst and the CO₂ methanation mixture (16 % CO₂ + 64 % H₂ and He balance). The temperature was raised up from 150 to 450 °C in steps of 100 °C. Spectra were recorded after 60 min in isothermal conditions at each temperature. All the experimental aspects are detailed in *Section 2.4.2*.

4.3. Results and discussion

4.3.1. Catalysts characterization

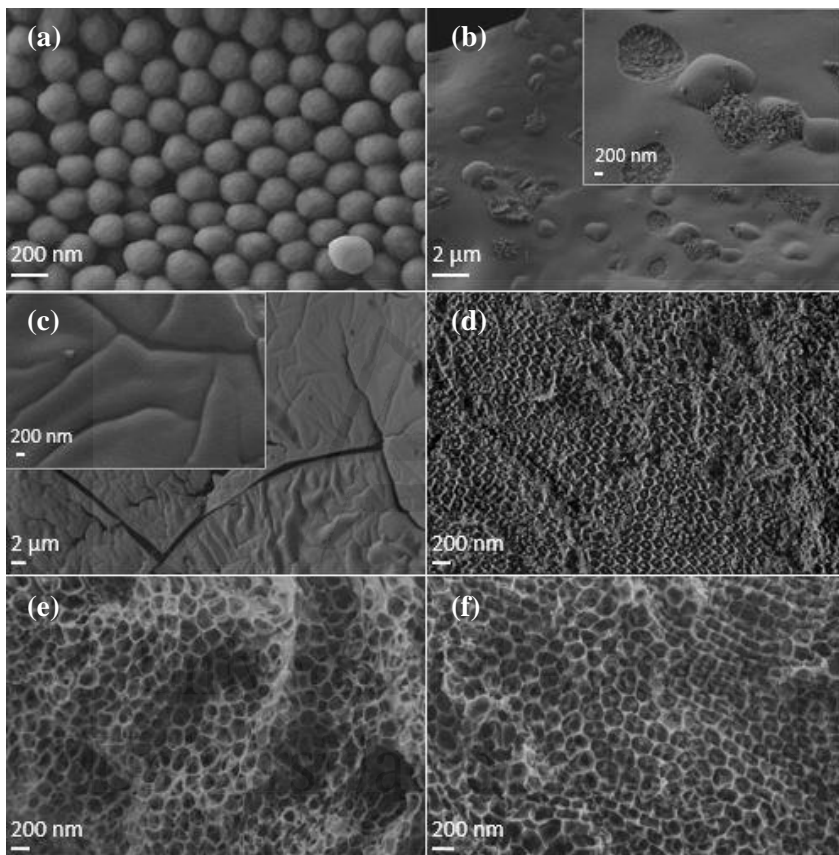


Figure 4.1. FESEM images of (a) PMMA spheres, (b) NiO/CeO₂-US (I), (c) NiO-CeO₂-US (CI), (d) NiO/CeO₂-3DOM (I), (e) NiO-CeO₂-3DOM (CI) and (f) NiO/CeO₂-3DOM (SI).

The morphology of the PMMA template and catalysts was analysed by FESEM and representative images are collected in Figure 4.1. It is observed that the PMMA template is composed by uniform and monodisperse spheres (Figure 4.1a.) with an average size of 220 ± 22 nm. Regarding catalysts, the direct calcination of the metal precursors (NiO/CeO₂-US (I) and NiO-CeO₂-US (CI), Figure 4.1b. and c., respectively) produces materials with closed and compact structure. However, surface differences are observed in reference catalysts depending on the Ni incorporation

method. A smooth surface formed by fused primary particles is obtained whether Ni is impregnated after the preparation of the CeO₂ support (NiO/CeO₂-US (I)), whereas a rough and cracked surface is observed if Ni is introduced by coprecipitation along with the cerium precursor (NiO-CeO₂-US (CI)). Conversely, catalysts with a well-defined three-dimensional structure (Figure 4.1d. – f.) formed by an ordered network of macropores (3DOM) were obtained by the PMMA-templating route. The pore size obtained in 3DOM structures (180 ± 22 nm) is smaller than the average size of PMMA spheres due to a partial collapse of the structure during the calcination. It is noteworthy that the presence of nickel during the formation of the 3DOM structure (NiO-CeO₂-3DOM (CI) and NiO/CeO₂-3DOM (SI)) (Figure 4.1e. and f., respectively), improves the quality and establishment of the macroporous structure. Note also that interstitial spaces, which are circled in Figure 4.2a. are generated between the PMMA spheres that have not been completely filled by the precursor solution during the infiltration and consequently, a bimodal pore size distribution is obtained in the 3DOM-catalysts (Figure 4.2b.), with sizes ranging between 60 – 80 nm and 160 – 180 nm for the interstitial spaces and macropores generated by the PMMA combustion, respectively.

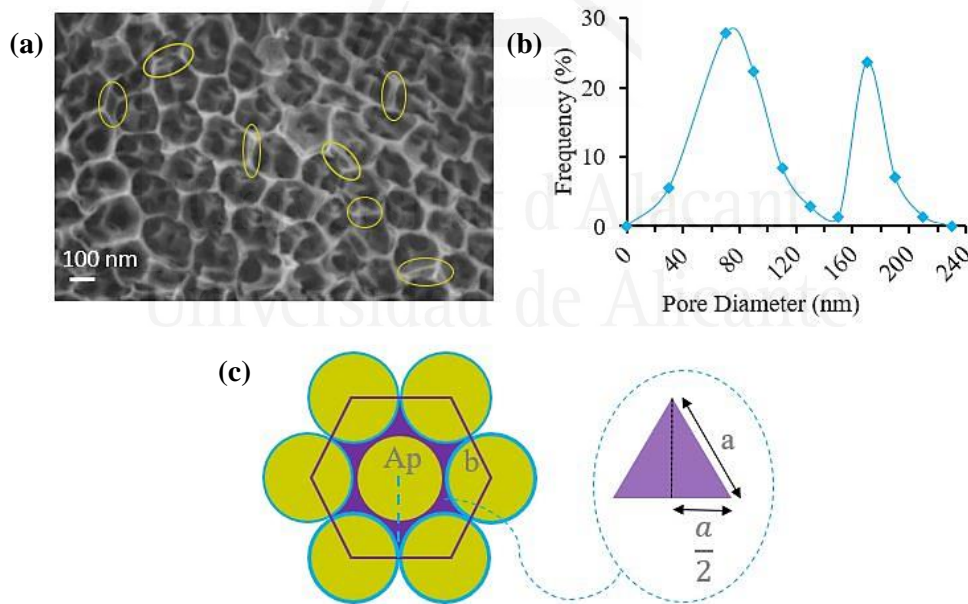


Figure 4.2. (a) detail of NiO/CeO₂-3DOM (SI), (b) pore size distribution of NiO/CeO₂-3DOM (SI) obtained from FESEM images and (c) hexagonal packing of PMMA spheres and interstitial holes obtained after infiltration (Ap: apothem and b: side length).

The PMMA spheres are packaged following a hexagonal pattern as shown in Figures 4.1a. and 4.2c. The theoretical size of the interstitial spaces has been estimated considering a PMMA sphere size of 220 nm, assuming triangular interstitial spaces and a CeO₂ thickness of 10 nm (see FESEM images) and taking into account the contraction observed after combustion of PMMA. The theoretical size of the interstitial spaces is 75 nm, which agrees with the value obtained by FESEM.

To obtain more information about the porous texture of the catalysts, N₂ adsorption-desorption isotherms were made at -196 °C and are shown in Figure 4.3a. All catalysts show a type II isotherm according to the IUPAC classification, characteristics of non-porous or macroporous adsorbents. All materials present a low adsorption of N₂ at low relative pressures denoting low microporosity, nonetheless clear differences are observed between 3DOM and US samples at higher relative pressures. In 3DOM samples, a well-defined hysteresis loop appears at high relative pressures, which is characterized by a rapid increase of the slope at relative pressures close to 1, suggesting the presence of macropores, whereas smaller hysteresis loop is observed at lower relative pressures in US samples, denoting the presence of lower amount and narrower pores (mesopores).

The morphological differences observed in US materials depending on the Ni incorporation method is also reflected in the N₂ uptake. Low N₂ adsorption is obtained for NiO/CeO₂-US (I) sample, denoting low porosity because of its smooth surface, whereas some mesoporosity is obtained in NiO-CeO₂-US (CI) as results of its rough and cracked surface. The Ni incorporation method also affects to the quality of the macroporous structure (3DOM), as was observed by FESEM, and consequently, higher adsorption uptakes are observed for samples in which Ni is incorporated prior to the formation of the 3DOM structures, NiO-CeO₂-3DOM (CI) and NiO/CeO₂-3DOM (SI), mainly by coimpregnation method (CI), whereas the addition of Ni after the formation of the 3DOM structure (NiO/CeO₂-3DOM (I)) does not affect the textural properties of the CeO₂ support (3DOM).

These observations were corroborated by Hg porosimetry (Figure 4.3b.). As expected, a bimodal pore size distribution is presented in 3DOM catalysts with two maxima centred at pore radii of 40 and 80 nm, corresponding to the interstitial spaces and to the porosity obtained by calcination of PMMA spheres, respectively, which agrees with the pore distribution obtained by analysing the FESEM images (Figure 4.2b.). Note also that, according to Hg porosimetry, the NiO-CeO₂-3DOM (CI) catalyst is the one with the most developed meso and macroporosity (V_2 and V_3 , Table 4.2.), while the rest have very similar pore volumes (Table 4.2.). These peaks are not observed in the case of US catalysts; however, it is observed that a small peak is obtained at radii

of 4 – 5 nm for NiO-CeO₂-US (CI) catalyst that is consistent with the hysteresis loop observed by N₂ adsorption-desorption isotherm.

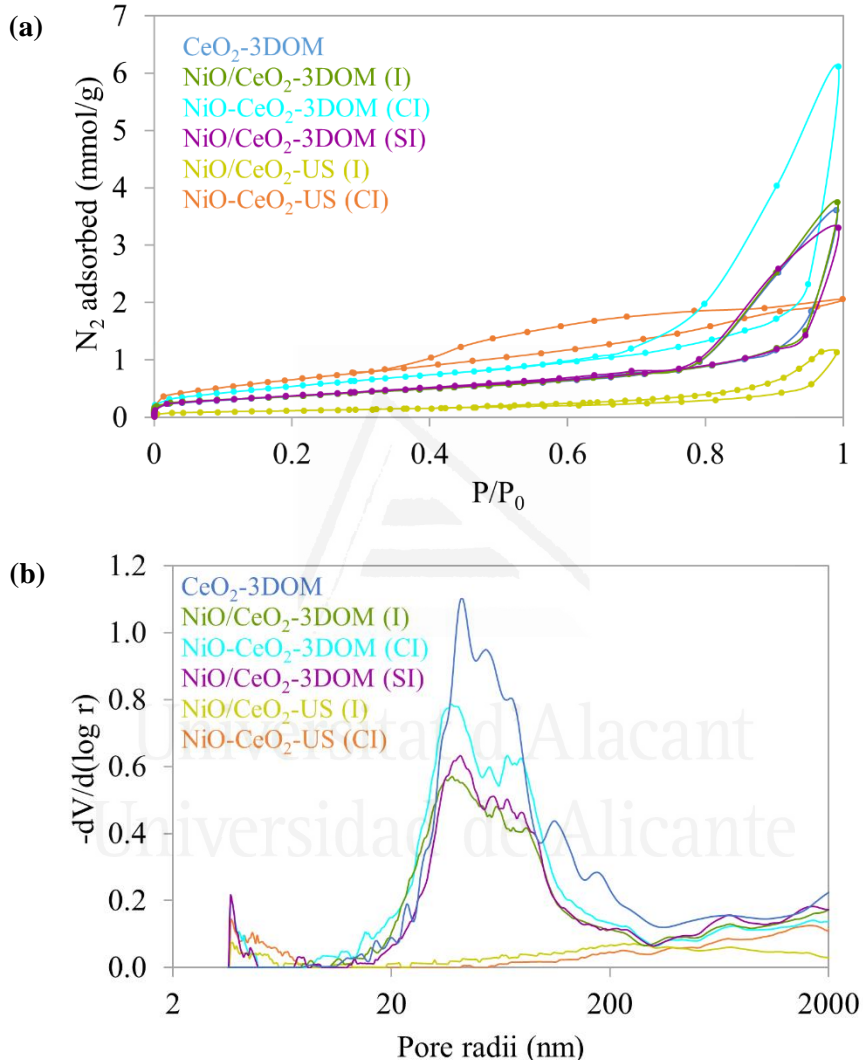


Figure 4.3. (a) N₂ adsorption-desorption isotherms at -196 °C for prepared catalysts and (b) Pore size distributions determined by mercury intrusion porosimetry.

The crystalline structure of the catalysts has been studied by X-ray diffraction (XRD). Figure 4.4. shows the diffractograms of all the synthesized catalysts together with the 3DOM CeO₂ support that was used as reference standard. In all cases, CeO₂

phase possesses a cubic fluorite type crystal structure (JCPDS 00-034-0394), and the lattice parameters (a , Table 4.2.) are very similar for all samples and are consistent with the value reported in the JCPDS database (0.5411 nm), indicating that there is no insertion of nickel cations in the CeO_2 lattice. Nickel cations are smaller (0.069 nm for Ni^{2+} and 0.056 nm for Ni^{3+}) [16] than Ce^{4+} (0.097 nm) [17], and their insertion would produce a deformation of the crystal lattice that would be reflected by the decrease of this parameter [18]. Characteristic peaks of NiO (JCPDS 01-075-0269) are also observed in the catalysts, and the intensity of those peaks depends on the Ni incorporation method employed. The worst dispersion is obtained by impregnation of Ni on the previously synthesized supports, NiO/CeO_2 -3DOM (I) and NiO/CeO_2 -US (I), while the incorporation of Ni prior to the formation of the ceria structure favors the Ni-dispersion, to a greater extent in the case of coimpregnation method (NiO-CeO_2 -3DOM (CI) and NiO-CeO_2 -US (CI)) as would be expected. Moreover, note that the incorporation of Ni prior to the formation of the CeO_2 structure affects the crystallinity of the CeO_2 phase; the diffraction peaks become wider and less intense indicating the stabilization of smaller crystals (see D values, Table 4.2.), which suggests a sintering prevention during the subsequent calcination step. However, the deposition of Ni after the formation of the CeO_2 structure (NiO/CeO_2 -3DOM (I) and NiO/CeO_2 -US (I)) does not affect the CeO_2 crystal size. This effect can be a consequence of the NiO-CeO_2 interaction, indicating a better and intimate contact in samples prepared by incorporation of Ni prior to the formation of the CeO_2 structure.

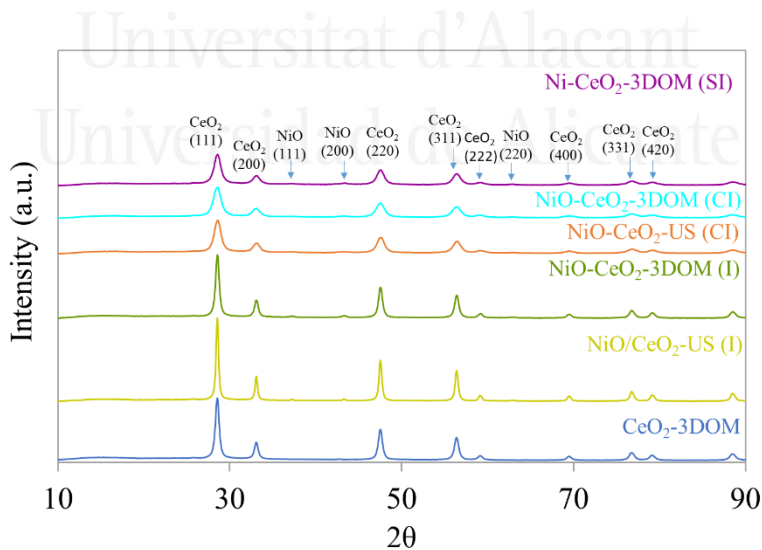


Figure 4.4. X-Ray diffractograms of the catalysts.

Table 4.2. Results of the catalysts characterization by N₂ adsorption, Hg porosimetry and XRD.

Sample	S _{B.E.T.} (m ² /g)	V ₂ (cm ³ /g) ^a	V ₃ (cm ³ /g) ^a	D (nm) CeO ₂	a (nm) CeO ₂
CeO ₂ -3DOM	31	0.03	0.30	14	0.5423
NiO/CeO ₂ -3DOM (I)	31	0.03	0.33	15	0.5415
NiO-CeO ₂ -3DOM (CI)	46	0.06	0.43	7	0.5415
NiO/CeO ₂ -3DOM (SI)	31	0.03	0.34	8	0.5415
CeO ₂ -US	13	0.01	0.01	21	0.5423
NiO/CeO ₂ -US (I)	10	0.01	0.01	22	0.5423
NiO-CeO ₂ -US (CI)	56	0.02	0.01	8	0.5415

^a V₂ and V₃ correspond to the mesopores and macropores volumes obtained by Hg porosimetry, respectively.

The surface of the catalysts was analysed by XPS. Ni_{2p} core level spectra of fresh and reduced catalysts are depicted in Figure 4.5a. and b., respectively, and the relative contribution of each peak is collected in Figure 4.5c. and d. The Ni_{2p} spectral region (Figure 4.5.) shows a main band in the 851 – 859 eV range together with a satellite structure at higher BE (859 – 866 eV). The assignment of Ni_{2p} peaks is still a matter of debate, however several authors have proposed that the nature of the nickel species can be deduced from the peaks of greater intensity [19,20]. According to literature, the main peaks centred at 852.3, 853.4 and 856.7 eV can be assigned to metallic Ni, NiO, and Ni₂O₃, respectively [19,21–23]. The peak at 856.0 eV can be also attributed to surface Ni³⁺ species associated to the presence of Ni²⁺ vacancies in NiO crystal lattices [21], which is close to the binding energy of Ni₂O₃ and Ni(OH)₂ [24].

Regarding fresh catalysts (Figure 4.5a.), three peaks are observed in the main region centred at around 853.2 and 857.2 eV, which can be assigned to surface Ni²⁺ species in NiO structure (surface NiO species), Ni²⁺ species in intimate contact with ceria surface (NiO-CeO₂ species) [24] and Ni³⁺ or Ni(OH)₂ species, respectively. In accordance with the observations of the previous chapter, this suggests that two NiO active centres of different nature are present in the prepared NiO/CeO₂ catalysts. The proportion of each active site depends on the Ni incorporation method. This proportion is shown in Figure 4.5c. It is observed that the proportion of Ni(OH)₂ or Ni³⁺ species is

constant in all 3DOM samples (around 35 %), while the proportion of surface NiO and Ni^{2+} species in intimate contact varies depending on the Ni incorporation method. The catalyst prepared by impregnation (NiO/CeO_2 -3DOM (I)) presents the highest proportion of surface NiO (25.4 %) and, therefore, the least amount of Ni^{2+} in intimate contact. This percentage of surface NiO decreases if Ni is incorporated prior to the 3DOM formation at the expense of an increase of the Ni^{2+} species in intimate contact (NiO-Ce), being the catalyst prepared by successive impregnations (NiO/CeO_2 -3DOM) (SI) the one that presents the greatest contact between ceria and Ni phases. Low amount of Ni(OH)_2 or Ni^{3+} species is observed in US samples as well as a less interaction between Ni and Ce phases regarding similar 3DOM materials (higher NiO proportions, peak at 853.2 eV Figure 4.5a.).

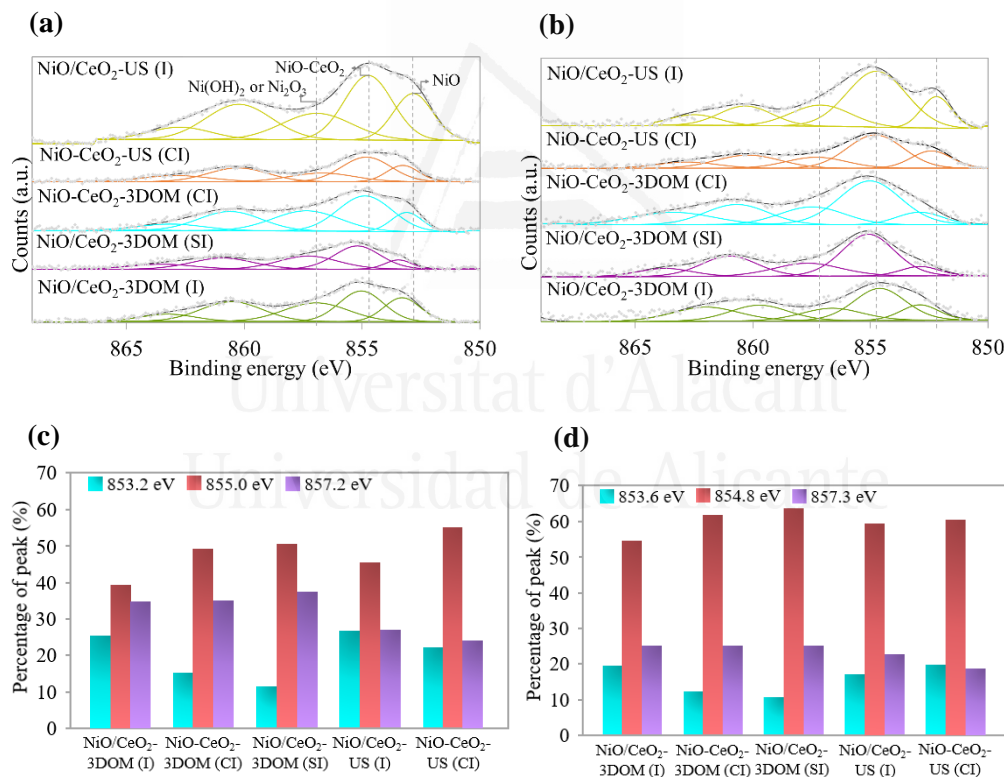


Figure 4.5. $\text{Ni}2\text{p}_{3/2}$ core level spectra percentage of each component used to fit the $\text{Ni}_{2\text{p}}_{3/2}$ spectral region for fresh **(a, c)** and reduced **(b, d)** catalysts.

The amount of Ni on the surface and the dispersion obtained also depend on the Ni-incorporation method (Table 4.3.). The real percentage of Ni incorporated in the catalysts (Ni % determined by ICP-OES, Ni_{ICP}) is very similar for all catalysts, and very closed to the theoretical value (around 8.5 %), which allows easy comparison of the catalytic results. Ni_{XPS} contents are close to real values (Ni_{ICP}) in catalysts prepared by successive impregnation and coimpregnation, which manifests a high dispersion of Ni particles along the ceria matrix, as was also confirmed by XRD. Nonetheless, Ni_{XPS} content is higher than the real value (Ni_{ICP}) for impregnated US sample, denoting accumulation of Ni particles on the external surface of ceria. Conversely, this Ni_{XPS} content is lower than the real value for impregnated 3DOM catalyst, indicating that some Ni-particles are located inside the porosity (macroporosity) of CeO₂ 3DOM support, being not detected by XPS.

Table 4.3. Surface composition (wt.%) of fresh and reduced catalysts determined by XPS and total Ni content determined by ICP-OES.

Catalyst	ICP						XPS					
	Fresh						Reduced					
	Ni	C	O	Ni	Ce	Ce ³⁺	C	O	Ni	Ce	Ce ³⁺	
CeO ₂ -3DOM	—	9.6	20.7	0.0	69.8	22.2	—	—	—	—	—	—
NiO/CeO ₂ -3DOM (I)	10.4	10.6	20.8	8.8	59.9	23.2	8.4	19.7	5.6	66.4	26.1	
NiO-CeO ₂ -3DOM (CI)	8.4	11.8	21.9	8.9	57.5	33.3	8.6	20.7	10.1	60.6	24.1	
NiO/CeO ₂ -3DOM (SI)	8.3	13.6	22.3	7.9	56.2	37.4	14.8	20.6	7.2	58.5	22.0	
NiO-CeO ₂ -US (I)	8.8	8.0	22.7	17.4	52.7	20.5	12.0	20.7	10.8	56.6	30.4	
NiO/CeO ₂ -US (CI)	8.2	13.1	19.7	9.0	58.2	24.3	8.8	18.3	10.8	62.1	23.8	

Analyzing the proportion of Ce³⁺ (Table 4.3), it is observed that the presence of Ni favors the reduction of ceria [25,26], increasing the amount of Ce³⁺ in surface in the catalysts against the support. It is also observed that there is a relationship between the amount of Ce³⁺ and the Ni incorporation method and therefore, with the contact between both phases. In this way, the NiO-CeO₂ (CI) catalysts (US and 3DOM) and NiO/CeO₂-3DOM (SI) presents higher Ce³⁺ content than catalysts prepared by impregnation. As mentioned throughout this chapter, the best contact is achieved by simultaneous incorporation of both phases during the synthesis. Moreover, note that the 3DOM structure favors the reduction of CeO₂ support; a higher percentage of Ce³⁺ is obtained in 3DOM catalysts regarding US ones, denoting a surface oxygen deficiency in the former. This higher surface oxygen vacancies proportion is attributed to the presence of PMMA template. During PMMA calcination, an O₂-poor environment is expected due to oxygen consumption by PMMA combustion and external O₂ diffusion restrictions inside the solid.

Regarding reduced catalyst, three peaks are also observed at 852.6, 854.8 and 857.3 eV (Figure 4.5b.). After reduction, peaks assigned to Ni²⁺ species in NiO structure and Ni²⁺ species in intimate contact shift to lower binding energy, denoting an electron-enrichment of Ni species caused by the reduction treatment. In this sense, surface NiO is reduced to Ni⁰. However, this peaks shift is more significant in conventional catalysts (NiO-CeO₂-US (I) and NiO-CeO₂-US (CI)) reflecting, again, less interaction between Ni and CeO₂ phases. The peaks distribution is also affected by the reduction treatment (Figure 4.5d.). A decrease of Ni³⁺ or Ni(OH)₂ species is observed together with an increase of Ni species in intimate contact. Ni(OH)₂ species can be decomposed to NiO after the reduction treatment, which occurs at around 300 °C [27]. With respect to Ni⁰ species (peak at 852.6 eV, Figure 4.5d.), differences are observed between samples in which Ni is incorporated by impregnation of the support (NiO/CeO₂-US (I) and NiO/CeO₂-3DOM (I)) and samples prepared by coimpregnation (NiO-CeO₂-US (CI) and NiO-CeO₂-3DOM (CI)) or successive impregnation (NiO/CeO₂-3DOM (SI)). The amount of Ni⁰ (Peak at 852.6 eV, Figure 4.5d.) decreased after the reduction treatment in samples prepared by direct impregnation of the supports whereas this peak is more or less constant in samples prepared by coimpregnation and successive impregnation. It seems that NiO-CeO₂ contact is improved after the thermal reduction in impregnated samples whereas no modification is obtained in the other catalysts. The strong metal-support interaction (SMSI) effect of ceria is well known [28,29]. It has been well established that through high temperature reduction, oxide moieties from the ceria support migrate over the metallic particles, blocking the surface and modifying its adsorption and catalytic properties [28,29]. The partial encapsulation of Ni particles by reduced ceria can explain the increase of the metal support interaction. As a result of

this partial encapsulation, lower Ni wt.% obtained by XPS could be expected. Surface composition of fresh and reduced catalysts determined by XPS is collected in Table 4.3. Surface Ni wt.% detected by XPS strongly decreases upon the reduction treatment in samples prepared by impregnation of the supports, denoting this partial encapsulation, whereas it remains constant in catalysts prepared by coimpregnation or successive impregnation. Note also that Ce³⁺ amount increases after the reduction treatment in impregnated samples, because of the easy reduction of ceria moieties in the surface. Consequently, the mobility of these reduced ceria moieties seems to be avoided by the intimate NiO-Ceria contact in samples prepared by coimpregnation or successive impregnation. This mobility impediment explains the sintering prevention during the subsequent calcination step observed by XRD (Figure 4.4.) in samples in which the incorporation of Ni was performed prior to the formation of the CeO₂ structure.

The reducibility of catalysts must be affected by the different NiO-ceria contact observed by XPS. Therefore, H₂-TPR were carried out to the fresh catalysts, and results are shown in Figure 4.6. The H₂-TPR profile of the CeO₂-3DOM support presents two peaks at 560 °C and 780 °C that can be attributed to the reduction of Ce⁴⁺ cations in the ceria surface and into the bulk, respectively. Conversely, CeO₂-US shows only the reduction of Ce⁴⁺ cations localized into the bulk ceria. The absence of surface reduction peak for CeO₂-US can be related with the lower surface area of this material with regard to CeO₂-3DOM. In addition, it has been reported that the oxygen-poor atmosphere during the template removal for 3DOM ceria synthesis affects the chemical features of the ceria surface and improves surface reducibility [13], in line with XPS results. This easily reduced surface of 3DOM samples is also pointed out in NiO/CeO₂ catalysts. TPR profiles of the corresponding NiO/CeO₂ catalysts show, in addition to the CeO₂ reduction peaks (shift to lower temperature), the peaks corresponding to the reduction of Ni species at 350 °C. In general, NiO reduction symmetrical peaks are obtained in US catalysts, while wider and non-symmetrical TPR peaks are observed in 3DOM ones at the same time that the peak at 560 °C almost disappears regarding CeO₂-US. The non-symmetrical peak observed in 3DOM samples could be assigned to the NiO reduction together with a Ni-catalyzed reduction of Ce⁴⁺ cations in the ceria surface, which is favoured by the easily reduced ceria surface in 3DOM samples with regard to US ceria. At this sense, in impregnated catalysts (NiO/CeO₂-US (I) and NiO/CeO₂-3DOM (I)) a peak at 350 °C is obtained ascribed to the reduction of Ni²⁺ species. However, a shoulder at higher temperature appears in the 3DOM sample, NiO/CeO₂-3DOM (I), along with a decrease of the reduction peak at 560 °C, ascribed to surface Ce⁴⁺ reduction. This shoulder observed only in 3DOM sample can be assigned to the Ni-catalyzed reduction of Ce⁴⁺ cations in the ceria surface favored by the easily reduced ceria surface in 3DOM samples with regard to US ceria. This Ni-catalyzed surface ceria reduction was already

observed by XPS, and could be indicative of the better NiO-Ceria contact observed for 3DOM samples, even in impregnated samples.

In the case of the catalysts obtained by the incorporation of Ni prior to the formation of the ceria structure, a widening and a shift of the Ni reduction peak at higher temperatures are observed, while the reduction peak of Ce⁴⁺ cations in the ceria surface almost disappears, which denotes a better contact between both phases in these catalysts.

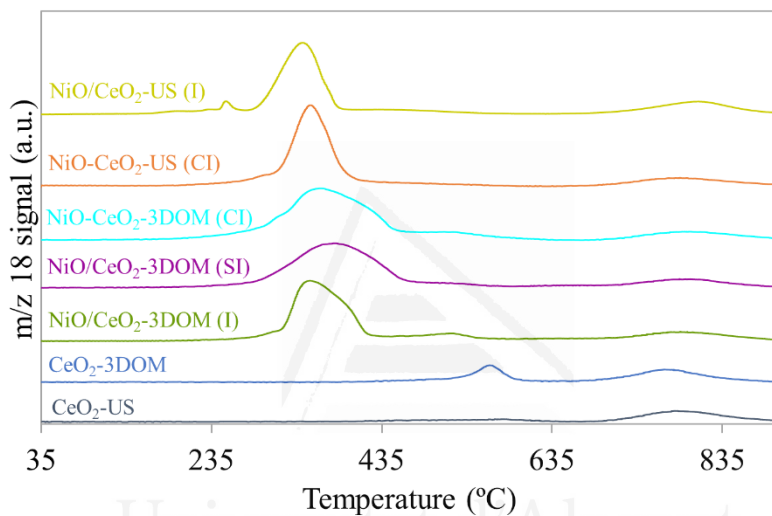


Figure 4.6. H₂-TPR characterization of the catalysts.

The percentage of nickel reduced during the H₂-TPR experiments was estimated taking into account the area under the reduction peaks and a reference CuO sample, and results are collected in Table 4.4. The consumption of H₂ obtained for NiO-CeO₂ US, coincides perfectly with the amount required for the total reduction of Ni²⁺ to Ni⁰. However, the consumption of H₂ is slightly higher than the amount required to reduce all Ni²⁺ on the catalyst for NiO/CeO₂-3DOM (I), which evidences that Ce⁴⁺ cations are also reduced in this wide double peak. This H₂ consumption increase is more significant in catalysts in which Ni is incorporated prior to the ceria formation, being more significant for 3DOM samples, corroborating the Ni-catalyzed reduction of surface ceria.

Table 4.4. Estimation of the percentage of nickel reduced from the amount of H₂ consumed during the H₂-TPR experiments. The presence of Ni²⁺ cations is assumed.

Sample	%Ni reduced
NiO/CeO ₂ -US (I)	100
NiO/CeO ₂ -3DOM (I)	113
NiO-CeO ₂ -US (CI)	121
NiO-CeO ₂ -3DOM (CI)	133
NiO/CeO ₂ -3DOM (SI)	143

4.3.2. CO₂ methanation tests

CO₂ conversion and CH₄ selectivity are depicted in Figure 4.7a. and b., respectively. The conversion curves of all catalysts are qualitatively similar; the conversion increases with temperature until a maximum value, which is limited by the thermodynamic equilibrium of the methanation reaction. The temperature required to achieve 50% of CO₂ conversion (T₅₀) follows the trend NiO/CeO₂-US (I) (294 °C) < NiO-CeO₂-US (CI) (324 °C) < NiO-CeO₂-3DOM (CI) (393 °C) < NiO/CeO₂-3DOM (SI) (>500 °C) < NiO/CeO₂-3DOM (I) (>> 500 °C). The selectivity to CH₄ decreases following the same trend, being NiO/CeO₂-US (I) the most and NiO/CeO₂-3DOM (I) the less productive catalyst. In all cases, selectivity to methane decreases from 400 °C since endothermic RWGS reaction (CO₂ + H₂ ↔ CO + H₂O) is favored and hence, CH₄ yield decreases at the expense of CO production.

This different catalytic behaviour seems to be, a priori, related to the NiO-Ceria contact, and consequently, the proportion of reduced Ni sites and NiO in intimate contact with ceria. Two mechanisms have been proposed for the CO₂ methanation reaction: dissociative and associative ones [30]. In the associative mechanism, CO₂ is chemisorbed without dissociation and subsequently, hydrogenated in two consecutive stages eliminating one oxygen per step. In contrast, in the dissociative method (the most common with ceria catalysts), CO₂ is dissociatively adsorbed followed by hydrogenation to methane. For ceria based catalysts it has been proposed that reduced cerium cations (Ce³⁺) are highly active sites for the chemisorption and dissociation of CO₂ [31]. The Ce³⁺ sites are oxidized to Ce⁴⁺ after the dissociation of CO₂ and, therefore, must be reduced again by the H₂ close to the active centres. Therefore, to analyze the catalytic results, two active centres should be taken into account: i) species of Ni in

close contact with ceria that are highly active for the dissociation of CO₂ and ii) reduced Ni⁰ where the dissociation of H₂ takes place.

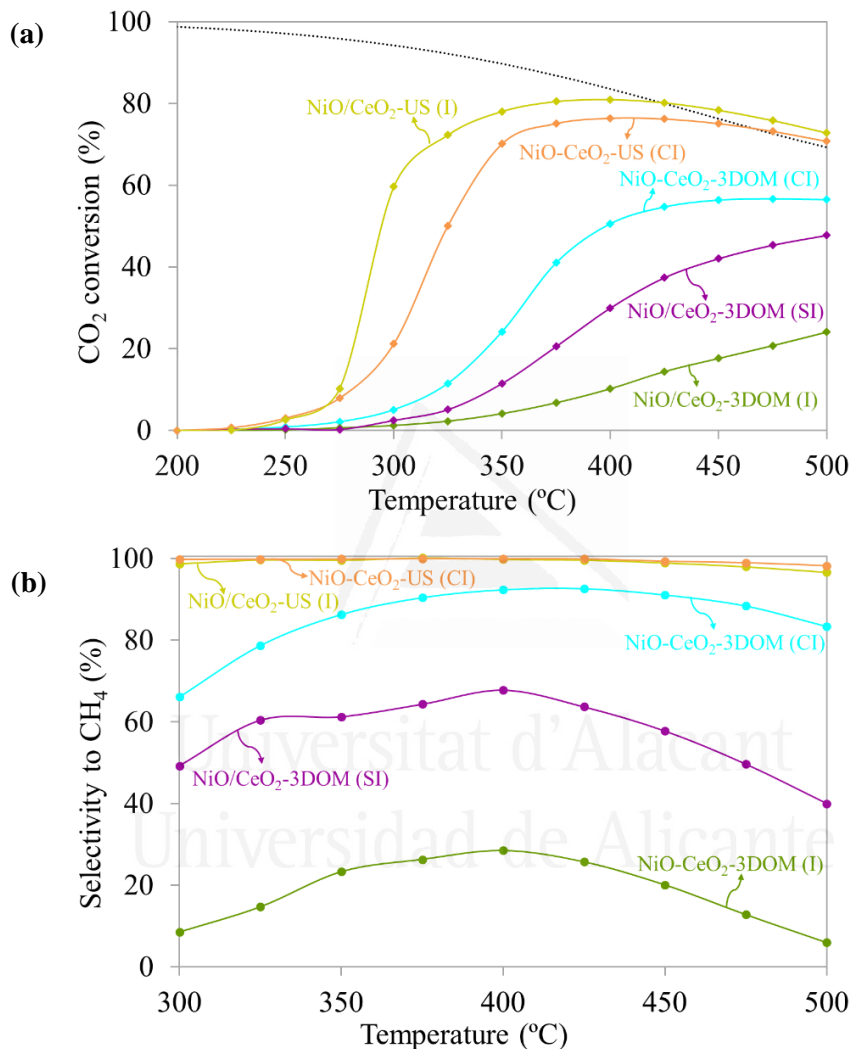


Figure 4.7. (a) CO₂ conversion and (b) CH₄ selectivity obtained during the catalytic methanation of CO₂.

As it was pointed out by XPS and H₂-TPR, the proportion of surface NiO and Ni²⁺ in intimate contact with ceria depends on the Ni-incorporation method and on the reducibility of ceria surface, which is affected by the 3DOM structure. The addition of Ni prior to the synthesis of CeO₂ structure generates a high proportion of Ni²⁺ in intimate

contact with ceria, which improves the reducibility of the ceria surface (Ce³⁺ sites) whereas less contact and lower Ni-catalyzed reducibility (Table 4.4.) is obtained for impregnated samples. Consequently, the former presents a high amount of active sites where CO₂ dissociation takes place, whereas the latter present high amount of active sites for H₂ dissociation. Thus, the NiO/CeO₂-3DOM (I) catalyst has a high number of centres for the dissociation and transfer of H₂, but not enough for the dissociation of CO₂, while the contrary occurs for NiO/CeO₂-3DOM (SI) catalyst. Figure 4.8. shows the mol of CO₂ converted per minute and atom on Ni⁰ (Ni atom determined by XPS). Hence, an optimal proportion of both sites is required to achieve the maximum conversion of CO₂: around 25% of Ni⁰ for H₂ dissociation and 75% of NiO in intimate contact with ceria for the CO₂ dissociation. When increasing NiO in intimate contact to higher level, the CO₂ dissociation is improved, but the dissociation and transfer of H₂ is hindered and, as consequence, part of this chemisorbed CO₂ is again desorbed as CO₂ or CO without hydrogenation taking place. Thus, CO₂ conversion decreases (Figure 4.7a.) and CH₄ selectivity decreases (Figure 4.7b.), e.g. as for Ni-CeO₂-3DOM (SI) catalyst. If surface Ni increases, the transfer of dissociated H atoms to the chemisorbed CO is favored, increasing the activity and selectivity to methane. Above 25% Ni⁰, the dissociation of CO₂ is restricted in a H-rich environment, and therefore, the activity is limited by the CO₂ dissociation, i.e. NiO-CeO₂-US (CI) and NiO/CeO₂-3DOM (I).

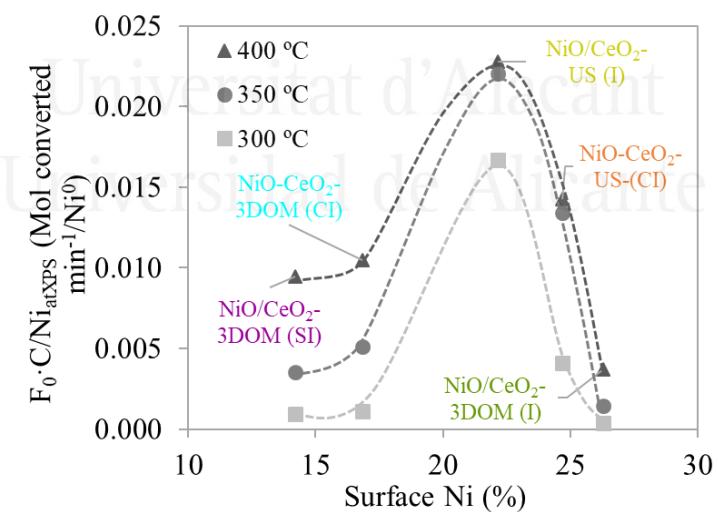


Figure 4.8. Relationship between the activity (mol converted, $F_0 \cdot C$) per Ni⁰ species (Ni atom determined by XPS, Ni_{at XPS}) at different temperatures. The proportion of surface Ni⁰ has been determined by XPS for reduced catalysts. This proportion has been calculated taking into account only Ni⁰ and NiO species. Where F₀ and C are the initial flow and the conversion of CO₂, respectively.

4.3.3. *In-situ DRIFTS experiments*

In situ DRIFTS experiments were carried out in order to obtain additional information about the reaction mechanism, and the most active catalysts, NiO/CeO₂-US (I) and NiO-CeO₂-US (CI), have been selected for these experiments. Figure 4.9. shows the spectra recorded at different temperatures after 60 min under reaction conditions, and a background spectrum recorded at room temperature in He has been subtracted in all cases. Several regions can be distinguished in all spectra. The intense band around 2400 cm⁻¹ belongs to gas phase CO₂, above 3500 cm⁻¹ are observed bands of O–H bonds in hydroxyls or bicarbonates, and below 1700 cm⁻¹ can be distinguished bands that can potentially be assigned to carbonate, bicarbonate or formate species [32–38].

The most active catalyst (NiO/CeO₂-US (I); Figure 4.9a.) shows bands at 150 °C that are consistent with the presence of monodentate and bidentate carbonates. These species are created by CO₂ chemisorption, and are detected in the spectrum at 150 °C because the reaction temperature is too low for taking place the methanation reaction (see catalytic test in Figure 4.7.). However, the bands disappear above 250 °C, and the negative bands observed indicate that carbonates present on the catalyst surface at room temperature in He (in the background spectra conditions) are removed during methanation. These in situ experiments allow concluding that the surface of this catalyst (NiO/CeO₂-US (I)), which combines the optimum proportion of active sites for CO₂ and H₂ dissociation, remains clean during the reaction.

However, this is not the case on the NiO-CeO₂-US (CI) catalyst, which is slightly less active. As deduced from XPS (Figure 4.5.), the NiO-CeO₂-US (CI) catalyst has a higher proportion of active sites for CO₂ chemisorption than sites for H₂ dissociation, and the consequence of this imbalance of active sites affects the surface carbon species observed under reaction conditions (Figure 4.9b.). At 150 °C is observed the presence of monodentate and bidentate carbonates, in agreement with NiO/CeO₂-US (I), and these species are depleted at higher temperatures. However, for the NiO/CeO₂-US (CI) catalyst the surface is not completely clean under reaction conditions, but bicarbonate bands are observed because the chemisorption of CO₂ is favored with regard to H₂ dissociation, which limits further hydrogenation.

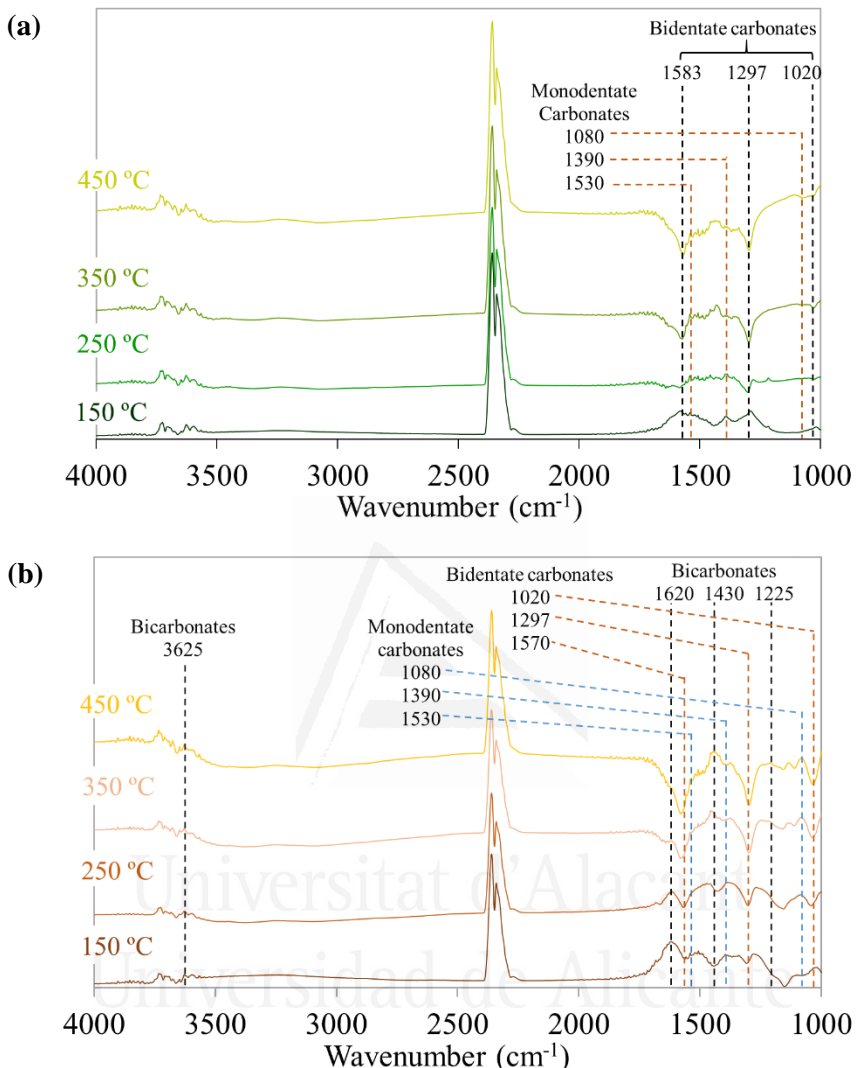


Figure 4.9. In situ DRIFTS experiments under H₂/CO₂/He at different temperatures. **(a)** NiO/CeO₂-US (I) and **(b)** NiO-CeO₂-US (CI). Spectra were recorder after 60 min under reaction conditions.

4.3.4. Pulse experiments with isotopic CO₂

Pulse experiments with isotopic ¹³C¹⁸O₂ were performed with NiO/CeO₂-US (I) and NiO-CeO₂-US (CI) at 350 °C, and the conclusions are consistent with the DRIFTS experiments. Figure 4.10. shows, as an example, the profiles of the signals detected during the first pulse of ¹³C¹⁸O₂ to each catalyst previously stabilized in a H₂/He flow at

the reaction temperature. The profile of Ar obtained in a previous pulse of this gas is also included to have a reference of the peak shape for a gas without chemical interaction with the catalysts.

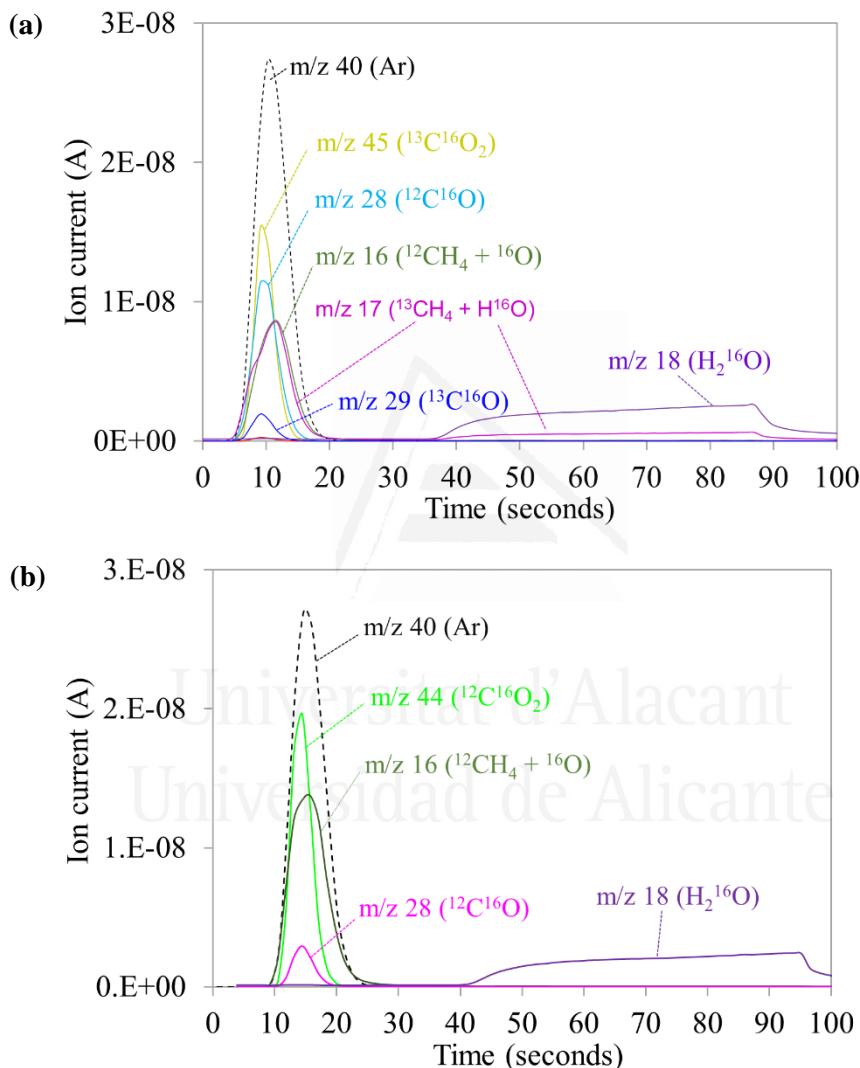


Figure 4.10. First pulse of Ar and ¹³C¹⁸O₂ at 350 °C, over (a) NiO/CeO₂-US (I) and (b) NiO-CeO₂-US (CI).

Different peaks of CO₂, CO and CH₄ species are observed in the same position than the Ar peak. The area of these peaks depends on the reaction conversion and

selectivity, and their position evidences that the reaction steps involved in their creation are fast. However, a broad H₂¹⁶O band appears delayed with regard to the other peaks, indicating that water desorption is much slower than the other steps.

Note that all oxygen-containing species detected in Figure 4.10. come with ¹⁶O, which belongs to catalyst oxygen, while ¹⁸O from the pulsed ¹³C¹⁸O₂ is retained on the catalysts. This evidences that the chemisorption of ¹³C¹⁸O₂ leads to a fast dissociation of the oxygen, and the carbon species left are either hydrogenated to CH₄ or reoxidized with catalyst oxygen.

On the contrary, carbon species with ¹³C and ¹²C are detected, and this means that not only carbon of the pulsed ¹³C¹⁸O₂ reacts but also the surface carbon species previously present on the catalysts. This is consistent with the DRIFTS spectra that provided evidences of the removal of carbon surface species present on the catalysts before the catalytic experiments.

For quantitative analysis of the pulse experiments, the area under the peaks was integrated and the amount of each specie was calculated. Figure 4.11. shows results of these calculations, expressed as mass balance of carbon, for three consecutive pulses of ¹³C¹⁸O₂.

The most active catalyst (NiO/CeO₂-US (I)) shows the same behaviour during the three pulses (Figure 4.11a.). The ¹³C¹⁸O₂ pulsed is consumed and CH₄ is released as reaction product, as expected. Both ¹²CH₄ and ¹³CH₄ are detected, confirming that hydrogenation not only occurs on carbon species created upon ¹³C¹⁸O₂ chemisorption but also on previously chemisorbed species. In addition, an important proportion of ¹³C¹⁶O₂ is observed, and this evidences the exchange of oxygen atoms between the gas molecules and the catalyst. Note that the proportion of species with ¹⁸O is negligible, evidencing that the catalyst oxygen is highly involved in the reaction. This is also observed in the H₂O molecules (Figure 4.12.), all of them coming with catalyst oxygen. Controversially, CO species are also observed in Figure 4.11a., while the catalytic tests were 100 % selective towards CH₄ formation, and this apparent disagreement is due to the different experimental conditions of the catalytic tests and pulse experiments. In the catalytic tests, CO₂ and H₂ concentrations are in stoichiometric proportion while a large excess of H₂ is used in the pulse experiments.

The behaviour of the catalyst NiO-CeO₂-US (CI) (Figure 4.11b.) is not stable in consecutive pulses. The first pulse yields a high proportion of ¹²CH₄ and ¹²CO₂, that is, the carbon species present on the catalyst before the ¹³C¹⁸O₂ pulse react first, and ¹³C-containing species are observed in further cycles. This difference between NiO/CeO₂-US (I) and NiO-CeO₂-US (CI) confirms once more that the most active catalyst (NiO/CeO₂-US (I)) is more effective hydrogenating the surface carbon species, and that

is very important to optimize the proportion of active sites for CO_2 and H_2 dissociation in order to optimize the methanation activity.

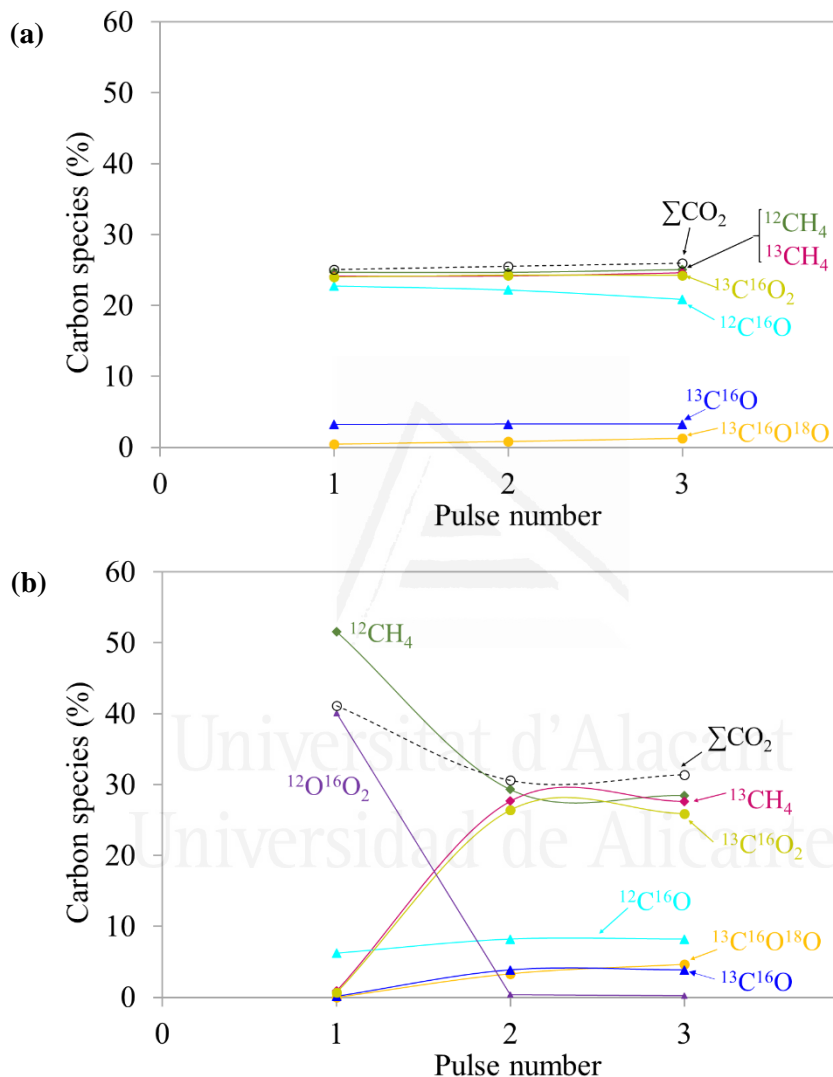


Figure 4.11. Percentage of carbon species in three consecutive pulses of $^{13}\text{C}^{18}\text{O}_2$ at 350°C , over (a) NiO/CeO₂-US (I) y (b) NiO-CeO₂-US (CI).

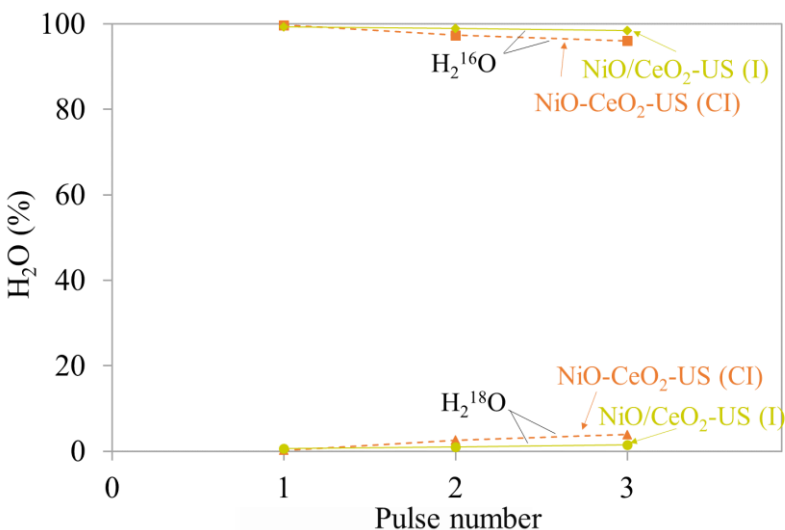


Figure 4.12. Percentage of H₂O species in three consecutive pulses of ¹³C¹⁸O₂ at 350 °C, over NiO/CeO₂-US (I) and NiO-CeO₂-US (CI).

4.4. Conclusions

In this work NiO/CeO₂ catalysts have been prepared and optimized in order to obtain an optimum performance in the CO₂ methanation reaction. To achieve this goal, the Ni incorporation method and the surface of the ceria support was varied in order to modify Ni-Ce interaction. In this sense, three dimensionally ordered macroporous (3DOM) structures have been synthesized and Ni introduced during the 3DOM synthesis by i) coimpregnation; ii) successive impregnation of Ni and Ce precursors or iii) Ni impregnation after CeO₂ 3DOM synthesis. Materials with uncontrolled structures (named US) were also prepared by coprecipitation and Ni impregnation. From all the above results and discussion, the following conclusions can be drawn:

- ❖ The introduction of nickel during the formation of the 3DOM structure, NiO-CeO₂-3DOM (CI) and NiO/CeO₂-3DOM (SI), favors the Ni-dispersion and improves the definition of the macroporous structure.
- ❖ XRD results indicate that Ni is not incorporated into the ceria lattice in any case but the incorporation of Ni prior to the formation of the CeO₂ structure affects the crystallinity of the CeO₂ phase; stabilizing smaller crystals suggests a sintering prevention during the subsequent calcination step. However, the deposition of Ni after the formation of the CeO₂ structure does not affect the CeO₂ crystal size.

❖ XPS pointed out that NiO/CeO₂ catalyst combines two types of active sites: NiO-Ceria interface and reduced Ni⁰ particles efficient for CO₂ and H₂ dissociation, respectively. The proportion of surface Ni⁰ and NiO-Ceria varies depending on the Ni incorporation method and surface area of the support. The catalysts prepared by impregnation (NiO/CeO₂-3DOM (I) and NiO/CeO₂-US (I)) present higher proportion of surface Ni⁰ and, therefore, the least amount of NiO in intimate contact. This percentage of surface NiO decreases if Ni is incorporated before to the formation of the CeO₂ structure at the expense of an increase of the NiO-Ceria interface, being the catalyst prepared by successive impregnations (NiO/CeO₂-3DOM (SI)) the one that presents the greatest contact between ceria and Ni phases.

❖ The reducibility of catalysts is also affected by the different NiO-Ceria contact observed by XPS. Ni-catalyzed reduction of Ce⁴⁺ cations in the ceria surface is observed in samples with high NiO-Ceria interface. This Ni-catalyzed ceria reduction was already observed by XPS and could be indicative of the better NiO-Ceria contact observed.

❖ The catalytic behaviour is related to the NiO-Ceria contact, and consequently, the proportion of reduced Ni⁰ sites and NiO intimate contact with ceria. The addition of Ni prior to the synthesis of CeO₂ structure generates a high proportion of NiO in intimate contact with ceria, and thus, a high number of active sites where CO₂ dissociation takes place, whereas the incorporation by impregnation generates high number of active sites for H₂ dissociation. Both cases lead to a low CO₂ conversion. An optimal proportion of both sites is required to achieve the maximum conversion of CO₂: around 25 % of surface Ni⁰ for H₂ dissociation and 75 % of NiO-Ceria interface for the CO₂ dissociation.

❖ In situ DRIFTS experiments allow concluding that the surface of the catalyst (NiO/CeO₂-US (I)), which combines the optimum proportion of active sites for CO₂ and H₂ dissociation remains clean during the reaction. However, this is not the case on the NiO-CeO₂-US (CI) catalyst, which has a higher proportion of active sites for CO₂ chemisorption than sites for H₂ dissociation. This imbalance of active sites has consequences in the surface carbon species observed under reaction conditions and thus, in the catalytic activity.

❖ Pulse experiments with isotopic CO₂ confirmed once more that the most active catalyst (NiO/CeO₂-US (I)) is more effective hydrogenating the surface carbon species, and that is very important to optimize the proportion of active sites for CO₂ and H₂ dissociation in order to optimize the methanation activity.

4.5. References

- [1] Z. Jiang, T. Xiao, V.L.K. Kuznetsov, P.P. Edwards, Turning carbon dioxide into fuel, *Philos. Trans. R. Soc. A.* 368 (2010) 3343–3364.
- [2] O.S. Bushuyev, P. De Luna, C.T. Dinh, L. Tao, G. Saur, J. van de Lagemaat, S.O. Kelley, E.H. Sargent, What should we make with CO₂ and how can We make it?, *Joule.* 2 (2018) 1–8.
- [3] N.M. Martín, P. Velin, M. Skoglundh, M. Bauer, P.-A. Carlsson, Catalytic hydrogenation of CO₂ to methane over supported Pd, Rh and Ni catalysts, *Catal. Sci. Technol.* 7 (2017) 1086-1094.
- [4] C. Creutz, E. Fujita, Carbon dioxide as a feedstock, in: *Carbon Manag. Implic. R&D Chem. Sci. Technol.*, National Academy Press, Washington DC, 2001: p. 83.
- [5] W. Wei, G. Jinlong, Methanation of carbon dioxide: An overview, *Front. Chem. Sci. Eng.* 5 (2011) 2–10.
- [6] P. Frontera, A. Macario, M. Ferraro, P. Antonucci, Supported catalysts for CO₂ methanation: A Review, *Catalysts.* 7 (2017) 59.
- [7] W. Wang, S. Wang, X. Ma, J. Gong, Recent advances in catalytic hydrogenation of carbon dioxide, *Chem. Soc. Rev.* 40 (2011) 3703–3727.
- [8] E. Alper, O.Y. Orhan, CO₂ utilization: Developments in conversion processes, *Petroleum.* 3 (2017) 109–126.
- [9] W.A. Wan Abu Bakar, R. Ali, N.S. Mohammad, The effect of noble metals on catalytic methanation reaction over supported Mn/Ni oxide based catalysts, *Arab. J. Chem.* 8 (2015) 632–643.
- [10] M.A.A. Aziz, A.A. Jalil, S. Triwahyono, A. Ahmad, CO₂ methanation over heterogeneous catalysts: Recent progress and future prospects, *Green Chem.* 17 (2015) 2647–2663.
- [11] J.H. Kwak, L. Kovarik, J. Szanyi, Heterogeneous catalysis on atomically dispersed supported metals: CO₂ reduction on multifunctional Pd catalysts, *ACS Catal.* 3 (2013) 2094–2100.
- [12] M. Florea, G. Postole, F. Matei-Rutkovska, A. Urda, F. Neatur, L. Massin, P. Gelin, Influence of Gd and Pr doping on the properties of ceria: texture, structure, redox behaviour and reactivity in CH₄/H₂O reactions in the presence of H₂S, *Catal. Sci. Technol.* 8 (2018) 1333–1348.
- [13] V. Alcalde-Santiago, A. Davó-Quiñonero, D. Lozano-Castelló, A. Bueno-López, On the soot combustion mechanism using 3DOM ceria catalysts, *Appl. Catal. B Environ.* 234 (2018) 187–197.
- [14] A.W. Burton, K. Ong, T. Rea, I.Y. Chan, On the estimation of average crystallite

- size of zeolites from the Scherrer equation: A critical evaluation of its application to zeolites with one-dimensional pore systems, *Microporous Mesoporous Mater.* 117 (2009) 75–90.
- [15] S.. Misturea, R.. Snyderb, X-ray diffraction, in: *Encycl. Mater. Sci. Technol.* (Second Ed., 2001: pp. 9799–9808.
 - [16] H.N. Luitel, S. Mizuno, T. Tani, Y. Takeda, Broadband-sensitive Ni^{2+} – Er^{3+} based upconverters for crystalline silicon solar cells, *RSC Adv.* 6 (2016) 55499–55506.
 - [17] W.F. Lim, K.Y. Cheong, Oxygen vacancy formation and annihilation in lanthanum cerium oxide as a metal reactive oxide on 4H-silicon carbide, *Phys. Chem. Chem. Phys.* 16 (214AD) 7015–7022.
 - [18] F. Ocampo, B. Louis, L. Kiwi-Minsker, A.C. Roger, Effect of Ce/Zr composition and noble metal promotion on nickel based $\text{Ce}_x\text{Zr}_{1-x}\text{O}_2$ catalysts for carbon dioxide methanation, *Appl. Catal. A Gen.* 392 (2011) 36–44.
 - [19] A.P. Grosvenor, M.C. Biesinger, R.S.C. Smart, N.S. McIntyre, New interpretations of XPS spectra of nickel metal and oxides, *Surf. Sci.* 600 (2006) 1771–1779.
 - [20] A.G. Marrani, V. Novelli, S. Sheehan, D.P. Dowling, D. Dini, Probing the redox states at the surface of electroactive nanoporous NiO thin films, *ACS Appl. Mater. Interfaces.* 6 (2014) 143–152.
 - [21] X. Xu, L. Li, F. Yu, H. Peng, X. Fang, X. Wang, Mesoporous high surface area NiO synthesized with soft templates: Remarkable for catalytic CH_4 deep oxidation, *Mol. Catal.* 441 (2017) 81–91.
 - [22] G.H. Yu, L.R. Zeng, Magnetic properties and X-ray photoelectron spectroscopy study of NiO/NiFe films prepared by magnetron sputtering, *J. Appl. Phys.* 90 (2001) 4039–4043.
 - [23] A. Ahmed, T. Ali, M.N. Siddique, A. Ahmad, P. Tripathi, Enhanced room temperature ferromagnetism in Ni doped SnO_2 nanoparticles: a comprehensive study, *J. Appl. Phys.* 122 (2017) 083906.
 - [24] N. Weidler, J. Schuch, F. Knaus, P. Stenner, S. Hoch, A. Maljusch, R. Schäfer, B. Kaiser, W. Jaegermann, X-ray photoelectron spectroscopic investigation of plasma-enhanced chemical vapor deposited NiO_x , $\text{NiO}_x(\text{OH})_y$, and $\text{CoNiO}_x(\text{OH})_y$: influence of the chemical composition on the catalytic activity for the oxygen evolution reaction, *J. Phys. Chem. C.* 121 (2017) 6455–6463.
 - [25] L. Pastor-Pérez, T. Ramírez-Reina, S. Ivanova, M.Á. Centeno, A. Sepúlveda-Escribano, Ni- CeO_2 /C Catalysts with Enhanced OSC for the WGS Reaction, *Catalysts.* 5 (2015) 298–309.
 - [26] L. Pastor-Pérez, R. Buitrago-Sierra, A. Sepúlveda-Escribano, CeO_2 -promoted Ni/activated carbon catalysts for the water e gas shift (WGS) reaction, *Int. J.*

- Hydrogen Energy. 39 (2014) 17589–17599.
- [27] S. Ni, X. Lv, T. Li, X. Yang, L. Zhang, The investigation of Ni(OH)₂/Ni as anodes for high performance Li-ion batteries, *J. Mater. Chem. A*. 1 (2013) 1544–1547.
 - [28] H.P. Sun, X.P. Pan, G.W. Graham, H.-W. Jen, R.W. McCabe, S. Thevuthasan, C.H.F. Peden, Partial encapsulation of Pd particles by reduced ceria-zirconia, *Appl. Phys. Lett.* 87 (2005) 1–3.
 - [29] A. Caballero, J.P. Holgado, V.M. Gonzalez de la Cruz, S.E. Habas, T. Herranz, M. Salmeron, In situ spectroscopic detection of SMSI effect in a Ni/CeO₂ system: hydrogen-induced burial and dig out of metallic nickel, *Chem. Commun.* 46 (2010) 1097–1099.
 - [30] B. Miao, S.S.K. Ma, X. Wang, H. Su, S.H. Chan, Catalysis mechanisms of CO₂ and CO methanation, *Catal. Sci. Technol.* 6 (2016) 4048–4058.
 - [31] V. Alcalde-Santiago, A. Davó-Quiñonero, D. Lozano-Castelló, A. Quindimil, U. De-La-Torre, B. Pereda-Ayo, J.A. González-Marcos, J.R. González-Velasco, A. Bueno-López, Ni/LnO_x catalysts (Ln=La, Ce or Pr) for CO₂ methanation, *ChemCatChem.* 11 (2019) 810–819.
 - [32] M.C. Raphulu, J. McPherson, E. Van der Lingen, J.A. Anderson, M.S. Scurrell, Investigation of the active site and the mode of Au/TiO₂ catalyst deactivation using Diffuse Reflectance Infrared Fourier transform Spectroscopy (DRIFTS), *Gold Bull.* 43 (2010) 21–28.
 - [33] H. Li, X. Jiao, L. Li, N. Zhao, F. Xiao, W. Wei, Y. Sun, B. Zhang, Synthesis of glycerol carbonate by direct carbonylation of glycerol with CO₂ over solid catalysts derived from Zn/Al/La and Zn/Al/La/M (M = Li, Mg and Zr) hydrotalcites, *Catal. Sci. Technol.* 5 (2015) 989–1005.
 - [34] A. Karelovic, P. Ruiz, Improving the hydrogenation function of Pd/γ-Al₂O₃ catalyst by Rh/γ-Al₂O₃ Addition in CO₂ methanation at low temperature, *ACS Catal.* 3 (2013) 2799–2812.
 - [35] B.H. Solis, Y. Cui, X. Weng, J. Seifert, S. Schauermann, J. Sauer, S. Shaikhutdinov, H.J. Freund, Initial stages of CO₂ adsorption on CaO: a combined experimental and computational study, *Phys. Chem. Chem. Phys.* 19 (2017) 4231–4242.
 - [36] D. Gamarra, A. Martínez-Arias, Preferential oxidation of CO in rich H₂ over CuO/CeO₂: Operando-DRIFTS analysis of deactivating effect of CO₂ and H₂O, *J. Catal.* 263 (2009) 189–195.
 - [37] D. Gamarra, G. Munuera, A.B. Hungría, M. Fernández-García, J.C. Conesa, P.A. Midgley, X.Q. Wang, J.C. Hanson, J.A. Rodríguez, A. Martínez-Arias, Structure-activity relationship in nanostructured copper-ceria-based preferential CO oxidation catalysts, *J. Phys. Chem. C*. 111 (2007) 11026–11038.

- [38] P.A.U. Aldana, F. Ocampo, K. Kobl, B. Louis, F. Thibault-starzyk, M. Daturi, P. Bazin, S. Thomas, A.C. Roger, Catalytic CO₂ valorization into CH₄ on Ni-based ceria-zirconia. Reaction mechanism by operando IR spectroscopy, *Catal. Today.* 215 (2013) 201–207.



Universitat d'Alacant
Universidad de Alicante

5

Highly active, selective and stable NiO-CeO_2 nanoparticles for CO_2 methanation

5.1. Introduction

5.2. Experimental details

- 5.2.1. Catalysts preparation
- 5.2.2. CO_2 methanation tests
- 5.2.3. Catalysts characterization

5.3. Results and discussion

- 5.3.1. CO_2 methanation tests
- 5.3.2. Catalysts characterization

5.4. Conclusions

5.5. References

Universitat d'Alacant
Universidad de Alicante

5.1. Introduction

Nanoparticles are receiving significant attention in research dealing with materials science and technology, and they are of special interest for catalysis applications [1–4]. Catalysts applied to heterogeneous catalytic reactions usually consist of metal or metal oxide nanoparticles dispersed on a high surface area support. The size of these nanoparticles affects the performance of the catalyst because the surface structure and electronic properties can change in this size range, and therefore reactions can be sensitive to particles size.

Cerium oxide is a relevant material in many catalysts formulation, usually working in combination with other metal or metal oxides. The role of cerium oxide depends on the catalyst and on the reaction, and as example, it is known that cerium oxide improves dispersion of supported metals and involves ceria oxygen in the redox processes occurring during the catalysed reactions [5–7]. Usually, ceria promotes or cooperates with nanoparticles of other elements, but some examples have been also reported about the positive properties of ceria nanoparticles in heterogeneous catalysts. For instance, it has been reported that gold supported on ceria nanoparticles is much more active as CO oxidation catalyst than counterpart catalysts with bulk ceria [8]. The same conclusion has been reported for Cu/CeO₂ catalysts [9], and inverse catalysts consisting of ceria nanoparticles dispersed on bulk CuO are more selective for CO oxidation in H₂-rich gas mixtures than conventional CuO/CeO₂ catalysts prepared without particle size control [10]. It was also demonstrated in our group that ceria-praseodymia nanoparticles are very active catalysts for diesel soot combustion [11], even outperforming the activity of Pt-based catalysts.

This previous success of ceria nanoparticles in certain catalytic applications lead us to think in the potential application of this type of material to other catalyzed reaction of current relevance, like CO₂ methanation. This reaction is known since 1910 [12–16], but more attention is receiving in the recent years because it has been proposed as a potential route to diminish CO₂ emissions producing a valuable fuel [17–26]. This process would be of special interest once H₂ is massively obtained from renewable sources [27–30]. For practical application of the CO₂ methanation process, a catalyst is required to overcome the kinetic barrier of the reaction, and the most promising catalysts are based on ruthenium [31–38], palladium [39–41], rhodium [42–45] and nickel [46–52]. Nickel is the cheapest metal of the list, becoming a good option for mild temperature (200 – 400 °C), and the promoting effect of ceria has been previously reported [21,22,49]. NiO-CeO₂ catalysts are among the most active noble metal-free catalysts for CO₂ methanation [21,22] and it is accepted that the cooperation between the NiO and CeO₂ plays a critical role in the catalyst behaviour. It is known that two

type of active sites are required for CO₂ methanation. Reduced nickel particles are efficient sites for H₂ dissociation while CO₂ dissociation takes preferentially place on oxygen vacancies located at the NiO-CeO₂ interface, and a proper ratio between both types of sites is necessary to obtain high catalytic activity [53].

Considering this background, the goal of this chapter is to prepare, characterize and test NiO-CeO₂ mixed oxide nanoparticles for CO₂ methanation. The behaviour of this novel material has been compared with other reference NiO-CeO₂ catalysts, including a mixed oxide with the same composition but prepared without control of the size, a counterpart NiO-CeO₂ mixed oxide with three dimensionally ordered macroporous (3DOM) structure and an inverse catalyst consisting of bulk NiO-supported CeO₂ nanoparticles among others.

5.2. Experimental details

5.2.1. Catalysts preparation

Five catalysts have been compared in this chapter, which are referred as NiO-CeO₂-np, NiO-CeO₂-3DOM (CI), NiO-CeO₂-US (CI), NiO-CeO₂-np/NiO-CeO₂-3DOM (CI) and CeO₂-np/NiO, and the synthesis procedure of all catalysts is described in *Chapter 2*. The metal precursors used were Ce(NO₃)₃·6H₂O and Ni(NO₃)₂·6H₂O, and the amount used were in all cases those required to obtain a target 8.5 wt. % of Ni, except for CeO₂-np/NiO that was 36 wt. % because NiO is used as support.

Briefly, (i) NiO-CeO₂-np catalyst was prepared by the reversed microemulsion method using n-heptane, Triton X-100 as surfactant, hexanol as co-surfactant and the required amount of Ni and Ce precursors, (ii) NiO-CeO₂-3DOM (CI) catalyst was prepared by the wetness impregnation procedure of the colloidal crystal template of polymethylmethacrylate (PMMA) with an ethanol solution of the Ni and Ce precursors, adding citric acid in stoichiometric ratio. The synthesis of the macroporous support (3DOM) was described elsewhere [54,55]. (iii) NiO-CeO₂-US (CI) was prepared in a similar way than NiO-CeO₂-3DOM (CI), but without hard template, (iv) to synthesize the NiO-CeO₂-np/NiO-CeO₂-3DOM (CI) catalyst, the NiO-CeO₂ mixed oxide nanoparticles were dispersed in ethanol applying ultrasounds. Then, NiO-CeO₂-3DOM (CI) was added to the suspension in 1:1 weight radio, and (v) CeO₂-np/NiO was prepared by impregnation of the NiO bulk with an ethanol suspension of CeO₂-np. Bulk NiO was synthetized by calcination of the Ni precursor and CeO₂ nanoparticles was prepared in a similar way than NiO-CeO₂-np, but without Ni precursor.

5.2.2. *CO₂ methanation tests*

Catalytic activity measurements were performed using the experimental system available at the University of Alicante and the experimental conditions have been detailed in *Section 2.3.1* from *Chapter 2*. Briefly, catalytic tests were performed using 200 mg of catalyst mixed with SiC particles. The sample was pre-treated at 500 °C during 1 h under 50% H₂/N₂ (200 mL/min). The reaction mixture (16% CO₂ + 64% H₂ and He balance) was fed with a total flow rate of 200 mL/min and the gas hourly space velocity was 12000 h⁻¹. The temperature was increased in steps of 50 °C between 100 and 500 °C and the gas composition was monitored at steady state with specific gas analysers (AwiteFLEX COOL).

The stability under reaction conditions of the NiO-CeO₂-np and NiO-CeO₂-US (CI) catalysts was studied. Three consecutive catalytic cycles were performed with the same parcel of catalyst following the described protocol, and the same CO₂ conversion and selectivity was obtained during the three cycles. After the third cycle, the temperature was kept at 300 °C and the reaction was conducted for 25 hours.

5.2.3. *Catalysts characterization*

The catalysts were characterized by means of complementary techniques. Textural properties have been determined by N₂ adsorption-desorption isotherms at -196 °C, after outgassing the catalysts under vacuum at 150 °C for 4 hours. Pore size distribution was determined by Hg intrusion porosimetry, after outgassed at 50 °C under vacuum for 12 hours. Crystalline properties of the catalysts were studied by XRD. The Ni content was measured by ICP-OES and the catalysts morphology was observed by FESEM. The reduction of the catalysts was studied by temperature programmed reduction experiments (H₂-TPR) and the consumption of H₂ was quantified using a reference CuO sample.

5.3. Results and discussion

5.3.1. *CO₂ methanation tests*

Figure 5.1. shows the CO₂ conversion curves obtained in methanation experiments together with the CH₄ selectivity profiles.

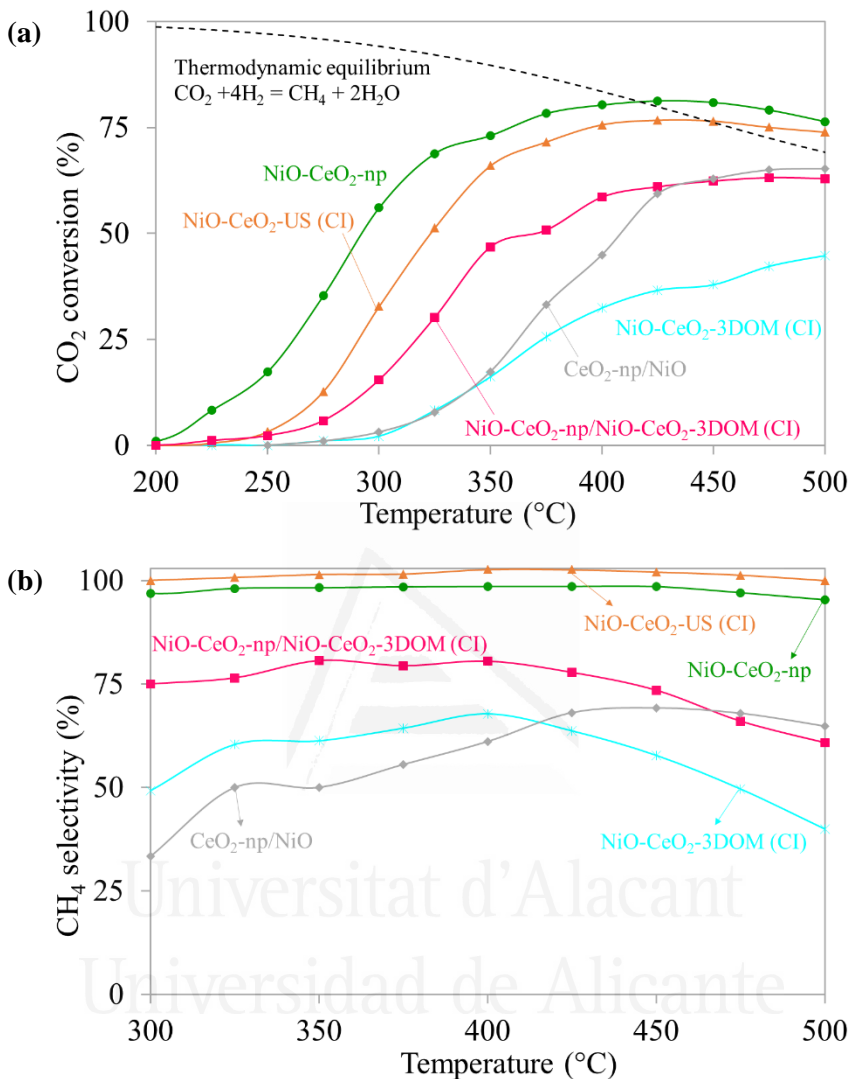


Figure 5.1. (a) CO₂ conversion and (b) CH₄ selectivity obtained during the CO₂ methanation catalytic experiments (200 mg of catalyst; 200 mL/min; CO₂, H₂ and N₂ in 16:64:20 %v proportion; Pre-treatment in 50 %H₂/N₂ at 500 °C).

The reaction of CO₂ hydrogenation to CH₄ is exothermic ($\Delta H_{25^\circ\text{C}} = -165 \text{ kJ/mol}$), but the activation energy is high due to the stability of CO₂ and H₂. For this reason, CO₂ consumption only starts once the temperature is high enough to overcome the energy barrier. The onset temperature depends on the catalyst, being 200 °C for the most active one (NiO-CeO₂-np). As expected, CO₂ conversion increases with temperature until the thermodynamic equilibrium of the reaction is achieved. The NiO-CeO₂ nanoparticles

(NiO-CeO₂-np) show the highest activity at temperatures with kinetic control of the reaction, being more active than the counterpart catalyst prepared without control of the particle size (NiO-CeO₂-US (CI)). For instance, at 275 °C the CO₂ methanation rate achieved with the novel NiO-CeO₂-np catalyst is near 3 times higher to that achieved with the reference catalyst (NiO-CeO₂-US (CI)). All other catalysts showed lower activity, and the CO₂ conversion curves are delayed to higher temperature. It was demonstrated in a previous study [53] that the Ni-CeO₂ interaction is a critical feature for the catalytic activity. Two type of active sites are necessary for proper methanation of CO₂, one of them being reduced Ni sites where H₂ is dissociated and other sites where CO₂ is chemisorbed and dissociated, which seem to be related with vacant sites created at the NiO-CeO₂ interface. This complex catalytic system requires a proper cooperation between both types of active sites, and it was previously demonstrated [53] that this cooperation is much more effective, for instance, in NiO-CeO₂-US (CI) than in NiO-CeO₂-3DOM (CI). Current results give a step forward, and show that the NiO-CeO₂-np nanoparticles outperform the behaviour of conventional counterpart catalysts.

The selectivity towards CH₄ formation of the novel catalyst (NiO-CeO₂-np) is near 100% in the whole range of temperatures screened, and the reference counterpart material (NiO-CeO₂-US (CI)) is also highly selective to CH₄ while the remaining catalysts yield a mixture of CO + CH₄ in different proportions, as deduced from Figure 5.1b. Since the carbon balances are properly closed, no other carbon products but CO and CH₄ are expected to be yielded.

A long-term catalytic test was performed at 300 °C with the catalysts NiO-CeO₂-np and NiO-CeO₂-US (CI) in order to evaluate the stability of the material, and the results obtained are included in Figure 5.2. This experiment evidences that the NiO-CeO₂ nanoparticles keep the same activity and stability for 25 hours, without deactivation evidences. This indicates that these nanoparticles are not only very active and selective for CO₂ hydrogenation to CH₄, but they also are highly stable under reaction conditions. The reference catalyst shows a small deactivation at the beginning of the experiment, but after that, also maintained the same activity and selectivity for a long period of time.

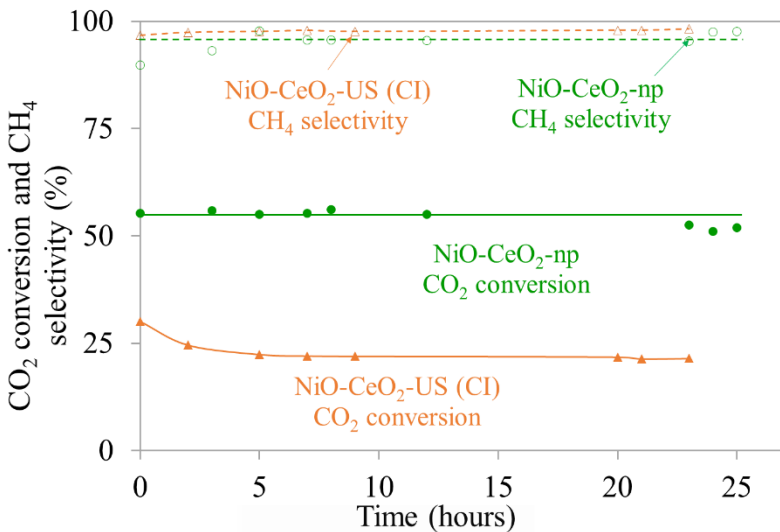


Figure 5.2. CO₂ methanation stability tests performed with NiO-CeO₂-np and NiO-CeO₂-US (CI) at 300 °C (200 mg of catalyst; 200 mL/min; CO₂, H₂ and N₂ in 16:64:20 %v proportion; pretreatment in 50 % H₂/N₂ at 500 °C).

5.3.2. Catalysts characterization

In order to understand the high performance of the NiO-CeO₂-np material, the catalysts have been characterized by different techniques. Table 5.1. compiles the Ni loading, determined by ICP-OES, and the specific surface area, measured by N₂ adsorption-desorption isotherms at -196 °C.

The Ni content is around the target 8.5 wt. % for all catalysts, except for the inverse CeO₂-np/NiO catalyst whose target was 36 % because NiO is used as support. Therefore, these similar values rule out that differences in the catalytic behaviour are related with differences in the Ni content. On the contrary, very relevant differences are noticed in the specific surface area of the catalysts.

Among the nickel catalysts, the highest surface area and micropore volume is achieved by the NiO-CeO₂ nanoparticles (NiO-CeO₂-np), only being slightly lower than that of the nickel-free ceria nanoparticles (CeO₂-np; 133 m²/g)). The specific surface area and micropore volumes of the 3DOM catalyst (NiO-CeO₂-3DOM (CI); 46 m²/g) and of the counterpart reference material obtained without hard template (NiO-CeO₂-US (CI); 56 m²/g) are lower to that of NiO-CeO₂ nanoparticles, as expected, and all the obtained values are in agreement with those previously reported for similar ceria-based materials prepared by reversed microemulsion method [56–58] and for ceria materials with 3DOM structure [59,60]. The highest surface area of the NiO-CeO₂-np catalyst

could be one of the arguments to explain the highest catalytic activity of this material (see Figure 5.1.).

Finally, the specific areas of catalysts consisting of supported nanoparticles ($\text{NiO-CeO}_2\text{-np}/\text{NiO-CeO}_2\text{-3DOM (CI)}$) $60 \text{ m}^2/\text{g}$; $\text{CeO}_2\text{-np}/\text{NiO}$ $66 \text{ m}^2/\text{g}$) are lower to values obtained with pure nanoparticles due to the diluting effect of the supports.

Table 5.1. Ni content determined by ICP-OES and BET specific surface area and pore volume determined from N_2 adsorption-desorption isotherms at -196°C .

Catalyst	Ni (wt.%)	B.E.T. specific surface area (m^2/g)	Pore volume (D.R.) (cm^3/g)
$\text{CeO}_2\text{-np}$	-	131	0.053
$\text{NiO-CeO}_2\text{-np}$	8.7	122	0.044
$\text{NiO-CeO}_2\text{-US (CI)}$	8.2	56	0.020
$\text{NiO-CeO}_2\text{-np}/\text{NiO-CeO}_2\text{-3DOM (CI)}$	8.5	60	0.021
$\text{CeO}_2\text{-np}/\text{NiO}$	36.6	66	0.025
$\text{NiO-CeO}_2\text{-3DOM (CI)}$	8.4	46	0.018

Additional information about the porosity of the catalysts is obtained from the shape of the N_2 adsorption-desorption isotherms shown in Figure 5.3.

Ceria nanoparticles ($\text{CeO}_2\text{-np}$ and $\text{NiO-CeO}_2\text{-np}$) show the highest adsorption at low partial pressure, which can be attributed to N_2 adsorption on the surface of the nanometric particles. In addition, the hysteresis loop above 0.7 P/P_0 in the $\text{CeO}_2\text{-np}$ isotherm evidences the presence of mesopores, and part of this porosity is depleted and becomes narrower in the $\text{NiO-CeO}_2\text{-np}$ mixed oxide.

The isotherm of the reference material $\text{NiO-CeO}_2\text{-US (CI)}$ prepared without control of the structure is quite flat, as expected due to the bulk nature of this material, and in accordance with its lower surface area in comparison to nanoparticles. The isotherm of the 3DOM mixed oxide ($\text{NiO-CeO}_2\text{-3DOM (CI)}$) shows no adsorption at low partial pressure, due to the null microporosity of this material, while shows a well-defined hysteresis loop above 0.7 P/P_0 with a typical shape of macroporous materials.

Finally, the isotherms of the supported nanoparticles (NiO-CeO₂-np/NiO-CeO₂-3DOM (CI)) and CeO₂-np/NiO) are consistent with the presence of mixed phases, combining certain adsorption at low partial pressure, due to the presence of micropores, together with certain hysteresis loop at high pressures consistent with the presence of larger pores.

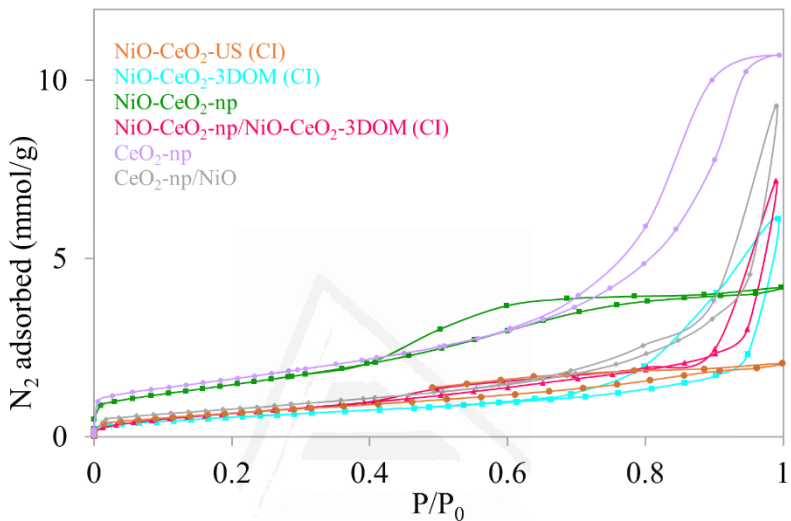


Figure 5.3. N₂ adsorption-desorption isotherms at -196 °C.

The characterization of the porous structure was completed by mercury intrusion porosimetry, and the pore size distributions obtained by this technique are included in Figure 5.4. In agreement with the N₂ adsorption conclusions, CeO₂-np presents pores in the mesoporous range, with radii smaller than 20 nm, and this porosity disappears in the NiO-CeO₂ mixed oxide (NiO-CeO₂-np). The reference material (NiO-CeO₂-US (CI)) shows few porosity, with a wide band above 200 nm due to the large interparticles space, and the macroporous mixed oxide (NiO-CeO₂-3DOM (CI)) shows a pore size distribution with most pores in the 20-200 nm range left upon the hard template removal.

The catalysts with a mixture of phases show pores that can be assigned to each phase in the mixture. NiO-CeO₂-np/NiO-CeO₂-3DOM (CI) shows pores with radii smaller than 20 nm, due to the NiO-CeO₂ nanoparticles, and wider pores with a maximum in the pore size distribution at 50 nm. A bimodal pore size distribution was obtained CeO₂-np/NiO, with nanoparticle pores below 20 nm and large pores with maximum at 60 nm.

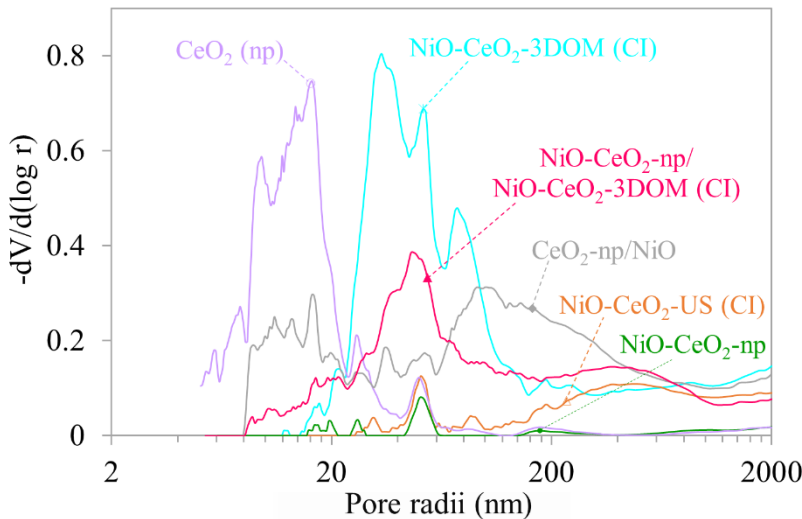


Figure 5.4. Pore size distribution determined by Hg intrusion porosimetry.

In conclusion, the porosity characterization confirms formation of high surface area materials by the reversed microemulsion method and meso/macroporous materials using the PMMA hard template. The highest catalytic activity of the $\text{NiO-CeO}_2\text{-np}$ could be attributed to its highest surface area, ruling out differences due to the nickel content.

The conclusions of the porosity characterization are supported by the microscopy analysis of the catalysts. Figure 5.5. shows TEM images of the different materials, where it is confirmed that particles of $\text{CeO}_2\text{-np}$ and $\text{NiO-CeO}_2\text{-np}$ (Figures 5.5a. and 5.5b., respectively) are smaller than particles of the catalyst prepared without control of the size ($\text{NiO-CeO}_2\text{-US (CI)}$; Figure 5.5c.). Considering the BET surface area of the nanoparticles (122 and $131\text{ m}^2/\text{g}$; Table 5.1), and assuming spherical shape, it is predicted that the average size of the $\text{CeO}_2\text{-np}$ and $\text{NiO-CeO}_2\text{-np}$ nanoparticles must be around $6\text{-}7\text{ nm}$, which is consistent with the size observed in Figures 5.5a. and 5.5b. The particles of $\text{NiO-CeO}_2\text{-US (CI)}$ are larger than those of $\text{CeO}_2\text{-np}$ and $\text{NiO-CeO}_2\text{-np}$, and the picture in Figure 5.5c. suggests that the size is more heterogeneous. TEM images of $\text{NiO-CeO}_2\text{-np}/\text{NiO-CeO}_2\text{-3DOM (CI)}$ (Figure 5.5d.) and $\text{CeO}_2\text{-np/NiO}$ (Figure 5.5f.) evidence mixture of particles of different size, with small nanoparticles mixed with large particles of $\text{NiO-CeO}_2\text{-3DOM (CI)}$ and NiO respectively. Large particles with heterogeneous size are also observed in $\text{NiO-CeO}_2\text{-3DOM (CI)}$ (Figure 5.5e.), but the 3DOM structure is hardly observed by TEM.

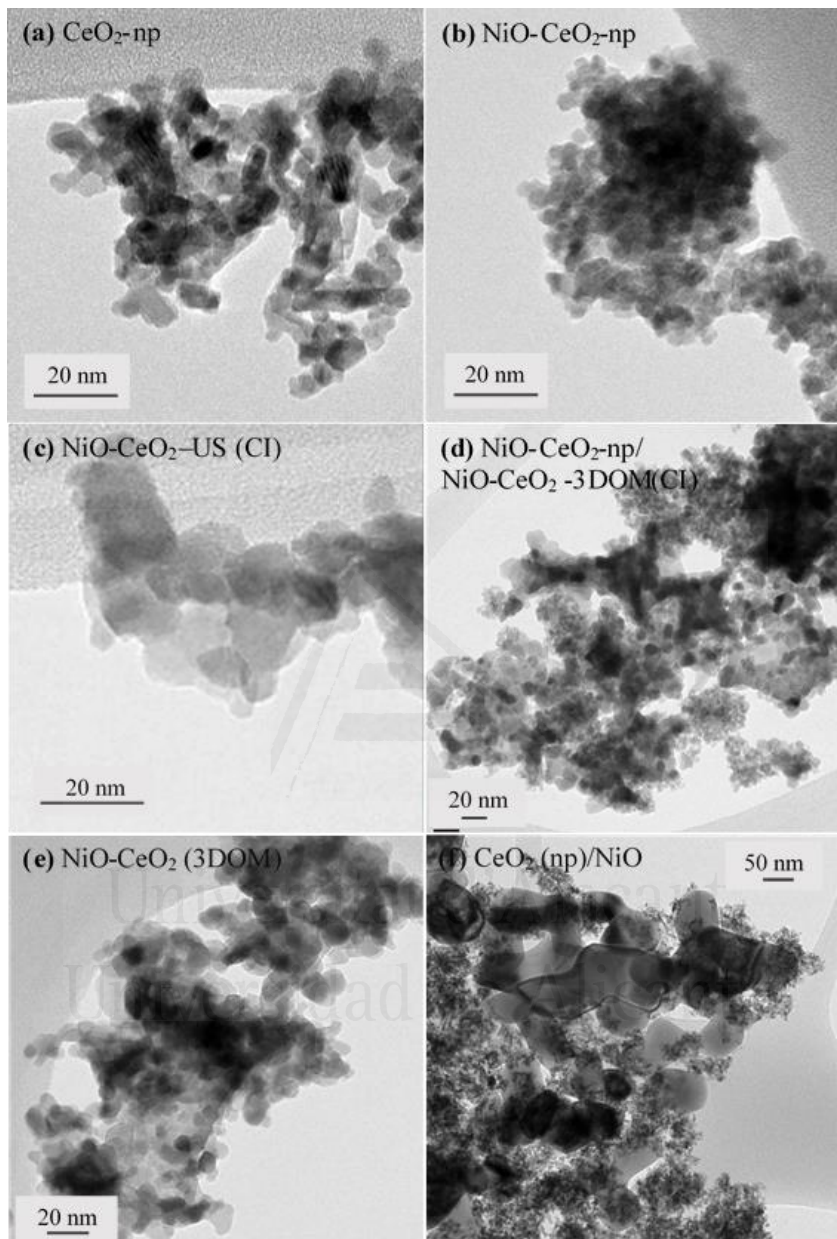


Figure 5.5. TEM images of the catalysts. (a) CeO₂-np, (b) NiO-CeO₂-np, (c) NiO-CeO₂-US (CI), (d) NiO-CeO₂-np/NiO-CeO₂-3DOM (CI), (e) NiO-CeO₂-3DOM and (f) CeO₂-np/NiO.

The macroporous structure is much better observed by SEM microscopy, and Figure 5.6. shows a representative image of the NiO-CeO₂-3DOM (CI) catalyst (Figure 5.6a.) together with an image of the NiO-CeO₂-US (CI) catalyst for comparison (Figure

5.6b.). The catalyst prepared using PMMA hard template shows spherical voids created upon the colloidal crystal template removal, and the macroporous nature of the catalyst is nicely observed in Figure 5.6a., while a flat surface is observed in the catalysts prepared by direct calcination of the metal precursors without control of the size (Figure 5.6b.).

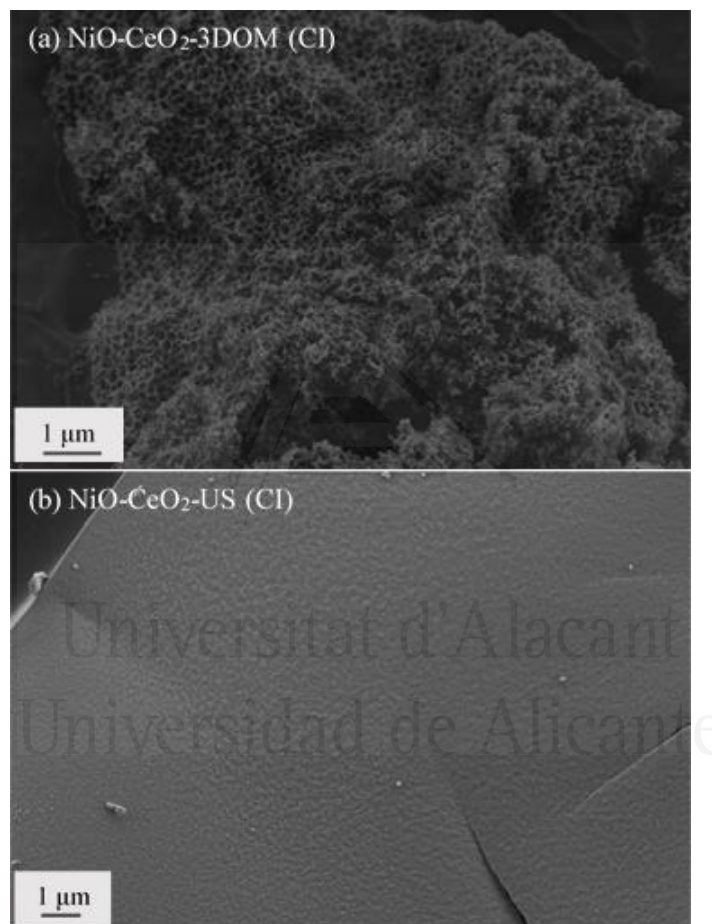


Figure 5.6. SEM images of the catalysts. **(a)** NiO-CeO₂-3DOM (CI) and **(b)** NiO-CeO₂-US (CI).

The crystallinity of the catalysts was characterized by XRD, and Figure 5.7. compiles the diffractograms obtained. For proper interpretation of the diffractograms, it must be taken into account that ceria-based materials usually consist of primary single crystals packed in larger structures. The porosity of these materials comes from the

surface of the crystals and from the space left among crystals, but there is not porosity inside a single crystal. N₂ adsorption and Hg porosimetry techniques provided information about the porosity of the catalysts, while XRD is useful to identify the nature of the crystalline phases and to obtain information about the size of the primary crystallites.

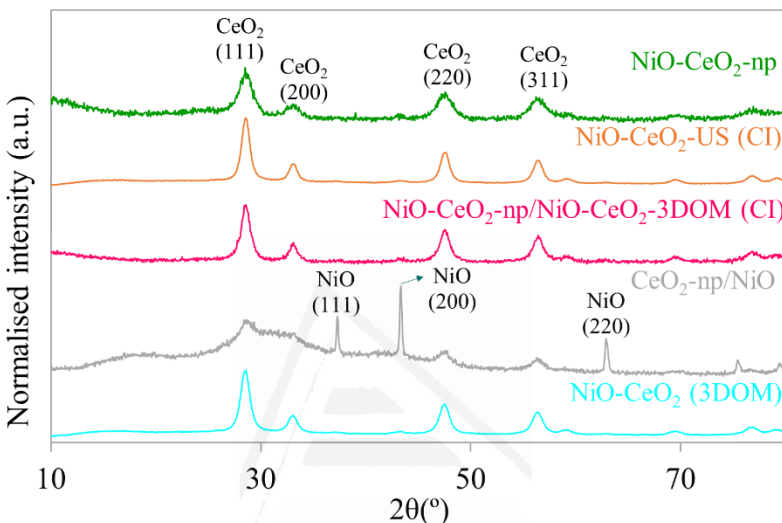


Figure 5.7. X-Ray diffractograms of the catalysts. Normalisation of the intensity has been carried out dividing each diffractogram by the maximum of the CeO₂ (111) peak.

All catalysts present the typical peaks of the fluorite structure of ceria, and peaks attributed to NiO are also evidenced in the diffractogram of CeO₂-np/NiO, as expected. Tiny peaks of NiO are also observed in other catalysts, mainly in NiO-CeO₂-3DOM (CI) and NiO-CeO₂-US (CI).

It is important to pay attention to the shape of the peaks, because provides information about the size of the primary crystallites. The intensity of the diffractograms has been normalized by dividing each diffractogram by the maximum of the CeO₂ (111) peak, to facilitate comparison of peaks broadening from a qualitative point of view. NiO-CeO₂-3DOM (CI) and NiO-CeO₂-US (CI) peaks of ceria are the narrowest, while peaks of nanoparticle-containing catalysts are broader. This is in agreement with the presence of smaller crystals in nanoparticle catalysts and larger crystals in NiO-CeO₂-3DOM (CI) and NiO-CeO₂-US (CI), in accordance with the BET specific surface areas (Table 5.1.) and with the TEM images (Figure 5.5.) of these materials.

Finally, the reducibility of the catalysts was characterized by H₂-TPR, and the reduction profiles are included in Figure 5.8. The curve obtained with CeO₂-np presents two peaks with maxima at 500 and 800 °C, attributed to surface and bulk reduction, respectively. The area under the peaks has been quantified, and the amount of H₂ consumed in each event has been related with the reduction of the oxide (data in Table 5.2.). The surface reduction of ceria (0.09 H₂ mole/CeO₂ mole) is almost twice bulk reduction (0.05 H₂ mole/CeO₂ mole), which is expected for high surface area ceria.

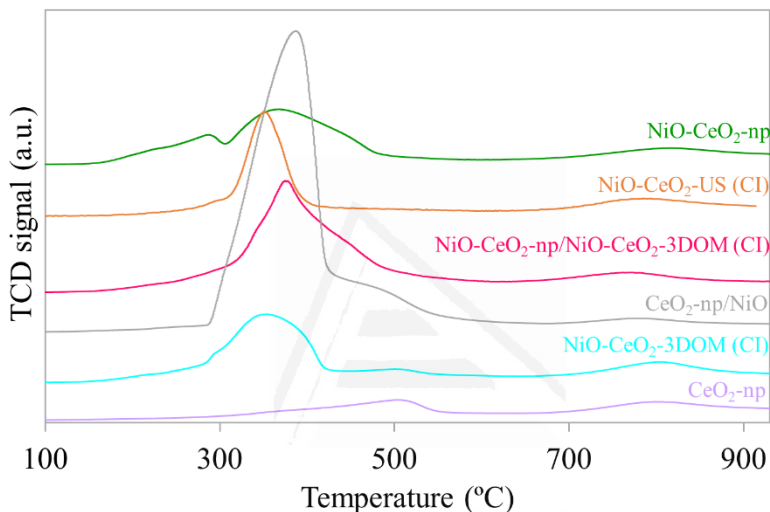


Figure 5.8. Temperature programmed reduction experiments with H₂.

The surface reduction peak is shifted to lower temperature for nickel-containing catalysts with regard to CeO₂-np, and the area under the surface reduction peak increases. This is due to the reduction of NiO together with surface ceria, and to the catalytic effect of nickel in ceria reduction. The shape of the surface reduction peak evidences that several events are taking place below 600 °C, since shoulders and/or double peaks are observed in the H₂-TPR profiles of all Ni-containing catalysts. These events include NiO and surface CeO₂ reduction, and it cannot be ruled out the presence of different Ni-O-Ce species with different interaction and reducibility.

The onset reduction temperature is also different for each catalyst, and the lowest onset reduction is attained by the NiO-CeO₂-np catalyst (160 °C), this catalyst also being the most active one in the CO₂ methanation reaction (Figure 5.1.). The reduction profile of this catalyst below 600 °C presents a main peak with maximum at 365 °C and a

smaller one at lower temperature. The amount of H₂ consumed in this double peak (Table 5.2.) is enough to reduce all NiO to Ni (1.47 H₂ mole/NiO mole), and there is additional H₂ left for surface ceria reduction (0.13 H₂ mole/CeO₂ mole). These results evidence the presence of, at least, two types of surface species of different reducibility on NiO-CeO₂-np. Comparing the surface reduction profile of NiO-CeO₂-np with that of the reference catalyst NiO-CeO₂-US (CI), for instance, it is observed that the reduction of the reference material starts at higher temperature (250 °C), and the amount of H₂ consumed in surface reduction is lower. This comparison evidences that the NiO-CeO₂ interaction is much more efficient in NiO-CeO₂ nanoparticles than in the reference material with the same composition but prepared without control of the size, leading to the formation of highly reducible Ni-O-Ce entities at the surface of the NiO-CeO₂ nanoparticles.

Table 5.2. H₂ consumed in Temperature Programmed Reduction experiments.

Catalyst	H ₂ mole/NiO mole 100-600 °C	H ₂ mole/CeO ₂ mole* 100-600 °C	H ₂ mole/CeO ₂ mole 600-950 °C
NiO-CeO ₂ -np	1.47	0.13	0.06
NiO-CeO ₂ -US (CI)	1.21	0.06	0.08
NiO-CeO ₂ -np/NiO-CeO ₂ -3DOM (CI)	2.29	0.36	0.10
CeO ₂ -np/NiO	1.12	0.25	0.05
NiO-CeO ₂ -3DOM (CI)	1.43	0.12	0.09
CeO ₂ -np	-	0.09	0.05

*For this calculation, the amount of H₂ required for 100 % NiO reduction to Ni has been subtracted from the total consumed in the 100 – 600 °C range.

In conclusion, the highest activity of the novel NiO-CeO₂-np catalyst for CO₂ methanation could be related, in the one hand, with the high specific surface area and small crystal size, and on the other hand, to the presence of highly-reducible Ni-O-Ce species on the nanoparticles surface.

5.4. Conclusions

A catalyst consisting of NiO-CeO₂ mixed oxide nanoparticles has been prepared, characterized and tested for CO₂ methanation. The behaviour of this material has been compared with other reference NiO-CeO₂ catalysts, including a mixed oxide with the same composition but prepared without control of the size, a counterpart NiO-CeO₂ mixed oxide with three dimensionally ordered macroporous (3DOM) structure and an inverse catalyst consisting of CeO₂ nanoparticles supported on bulk NiO among others.

The NiO-CeO₂-np catalyst is the most active for CO₂ methanation among those compared, being much more active than the reference catalyst with the same composition but prepared without control of the size. For instance, at 275 °C the CO₂ methanation rate achieved with the novel NiO-CeO₂-np catalyst is near 3 times higher to that achieved with the reference catalyst (NiO-CeO₂-US (CI)).

The selectivity towards CH₄ formation of the NiO-CeO₂-np catalyst is ~100 % in the whole range of temperature studied, and is also highly stable, keeping the same activity during 25 hours of catalytic experiment.

The high activity of this NiO-CeO₂-np catalyst is related with its high specific surface area (122 m²/g) and with the presence of highly-reducible Ni-O-Ce species on the nanoparticles surface.

5.5. References

- [1] A.T. Bell, The impact of nanoscience on heterogeneous catalysis, *Science* 299 (2003) 1688–1691.
- [2] D. Astruc, F. Lu, J.. Aranzaes, Nanoparticles as recyclable catalysts: the frontier between homogeneous and heterogeneous catalysis, *Angew. Chem. Int. Ed. Engl.* 44 (2005) 7852–7872.
- [3] A. Corma, H. Garcia, Supported gold nanoparticles as catalysts for organic reactions, *Chem. Soc. Rev.* 37 (2008) 2096–2126.
- [4] Y. Liang, Y. Li, H. Wang, J. Zhou, J. Wang, T. Regier, H. Dai, Co₃O₄ nanocrystals on graphene as a synergistic catalyst for oxygen reduction reaction, *Nat. Mater.* 10 (2011) 780–786.
- [5] A. Trovarelli, Catalytic properties of ceria and CeO₂-containing materials, *Catal. Rev.* 38 (1996) 439–520.
- [6] A. Trovarelli, C. De Leitenburg, M. Boaro, G. Dolcetti, The utilization of ceria in industrial catalysis, *Catal. Today*. 50 (1999) 353–367.

- [7] T. Montini, M. Melchionna, M. Monai, P. Fornasiero, Fundamentals and catalytic applications of CeO₂-based materials, *Chem. Rev.* 116 (2016) 5987–6041.
- [8] S. Carrettin, P. Concepción, A. Corma, J.M. Lopez Nieto, V.. Puntes, Nanocrystalline CeO₂ increases the activity of Au for CO oxidation by two orders of magnitude, *Angew. Chemie Int. Ed.* 43 (2004) 2538–2540.
- [9] T.. Nguyen, C.. Dinh, D. Mrabet, M.. Tran-Thi, T.. Do, Controlled synthesis of ceria nanoparticles for the design of nanohybrids, *J. Colloid Interface Sci.* 394 (2012) 100–107.
- [10] A. Hornés, A.B. Hungría, A. López Cámara, M. Fernández García, A. Martínez Arias, L. Barrio, M. Estrella, G. Zhou, J.J. Fonseca, J.C. Hanson, J.A. Rodriguez, Inverse CeO₂/CuO catalyst as an alternative to classical direct configurations for preferential oxidation of CO in hydrogen-rich stream, *J. Am. Chem. Soc.* 132 (2010) 34–35.
- [11] N. Guillén-Hurtado, A. García-García, A. Bueno-López, Active oxygen by Ce-Pr mixed oxide nanoparticles outperform diesel soot combustion Pt catalysts, *Appl. Catal. B Environ.* 174–175 (2015) 60–66.
- [12] T. Van Herwijnen, H. Van Doesburg, W.A. De Jong, Kinetics of the methanation of CO and CO₂ on a nickel catalyst, *J. Catal.* 28 (1973) 391–402.
- [13] B.. Sexton, G.. Somorjai, The hydrogenation of CO and CO₂ over polycrystalline rhodium: Correlation of surface composition, kinetics and product distributions, *J. Catal.* 46 (1977) 167–189.
- [14] R. Maatman, A kinetic study of the methanation of CO₂ over nickel-alumina, *J. Catal.* 62 (1980) 349–356.
- [15] F. Solymosi, A. Erdöhelyi, M. Kocsis, Methanation of CO₂ on supported Ru catalysts, *J. Chem. Soc. Faraday Trans. 1 Phys. Chem. Condens. Phases.* 77 (1981) 1003–1012.
- [16] T. Yoshida, K. Nishizawa, M. Tabata, H. Abe, T. Kodama, M. Tsuji, Y. Tamaura, Methanation of CO₂ with H₂-reduced magnetite, *J. Mater. Sci.* 28 (1993) 1220–1226.
- [17] J.Y. Park, T. Krauthammer, Development of an LEFM dynamic crack criterion for correlated size and rate effects in concrete beams, *Int. J. Impact Eng.* 36 (2009) 92–97.
- [18] T. Abe, M. Tanizawa, K. Watanabe, A. Taguchi, CO₂ methanation property of Ru nanoparticle-loaded TiO₂ prepared by a polygonal barrel-sputtering method, *Energy Environ. Sci.* 2 (2009) 315–321.
- [19] S.K. Hoekman, A. Broch, C. Robbins, R. Purcell, CO₂ recycling by reaction with

- renewably-generated hydrogen, *Int. J. Greenh. Gas Control.* 4 (2010) 44–50.
- [20] S. Sharma, Z. Hu, P. Zhang, E.W. Mcfarland, H. Metiu, CO₂ methanation on Ru-doped ceria, *J. Catal.* 278 (2011) 297–309.
- [21] S. Tada, T. Shimizu, H. Kameyama, T. Haneda, R. Kikuchi, Ni/CeO₂ catalysts with high CO₂ methanation activity and high CH₄ selectivity at low temperatures, *Int. J. Hydrogen Energy.* 37 (2012) 5527–5531.
- [22] P.A.U. Aldana, F. Ocampo, K. Kobl, B. Louis, F. Thibault-starzyk, M. Daturi, P. Bazin, S. Thomas, A.C. Roger, Catalytic CO₂ valorization into CH₄ on Ni-based ceria-zirconia. Reaction mechanism by operando IR spectroscopy, *Catal. Today.* 215 (2013) 201–207.
- [23] M.A.A. Aziz, A.A. Jalil, S. Triwahyono, R.R. Mukti, Y.H. Taufiq-yap, M.R. Sazegar, Highly active Ni-promoted mesostructured silica nanoparticles for CO₂ methanation, *Appl. Catal. B Environ.* 147 (2014) 359–368.
- [24] J.C. Matsubu, V.N. Yang, P. Christopher, Isolated metal active site concentration and stability controls catalytic CO₂ reduction selectivity Isolated metal active site concentration and stability controls catalytic CO₂ reduction selectivity, *J. Am. Chem. Soc.* 137 (2015) 3076–3084.
- [25] F. Wang, S. He, H. Chen, B. Wang, L. Zheng, M. Wei, D.G. Evans, Active site dependent reaction mechanism over Ru/CeO₂ catalyst toward CO₂ methanation, *J. Am. Chem. Soc.* 138 (2016) 6298–6305.
- [26] K. Ray, G. Deo, A potential descriptor for the CO₂ hydrogenation to CH₄ over Al₂O₃ supported Ni and Ni-based alloy catalysts, *Appl. Catal. B Environ.* 218 (2017) 525–537.
- [27] J.D. Holladay, J. Hu, D.L. King, Y. Wang, An overview of hydrogen production technologies, *Catal. Today.* 139 (2009) 244–260.
- [28] G. Gahleitner, Hydrogen from renewable electricity: An international review of power-to-gas pilot plants for stationary applications, *Int. J. Hydrogen Energy.* 38 (2012) 2039–2061.
- [29] H. Ahmad, S.K. Kamarudin, L.J. Minggu, M. Kassim, Hydrogen from photocatalytic water splitting process: A review, *Renew. Sustain. Energy Rev.* 43 (2015) 599–610.
- [30] T. He, P. Pachfule, H. Wu, Q. Xu, P. Chen, Hydrogen carriers, *Nat. Rev. Mater.* 1 (2016) 16059–16079.
- [31] N.M. Gupta, V.S. Kamble, A. Rao, R.M. Iyer, On the mechanism of CO and CO₂ methanation over Ru/molecular-sieve catalyst, *J. Catal.* 60 (1979) 57–67.
- [32] F. Solymosi, A. Erdöhelyi, T. Bánsági, Infrared study of the surface interaction

- between H₂ and CO₂ over rhodium on various supports, *Phys. Chem. Condens. Phases.* 77 (1981) 2645–2657.
- [33] S. Scirè, C. Crisafulli, R. Maggiore, S. Minicò, S. Galvagno, Influence of the support on CO₂ methanation over Ru catalysts: an FT-IR study, *Catal. L.* 51 (1998) 41–45.
 - [34] T. Abe, M. Tanizawa, K. Watanabe, T. Akira, CO₂ methanation property of Ru nanoparticle-loaded TiO₂ prepared by a polygonal barrel-sputtering method, *Energy Environ. Sci.* 2 (2009) 315–321.
 - [35] Q. Lin, X.Y. Liu, Y. Jiang, Y. Wang, Y. Huang, T. Zhang, Crystal phase effects on the structure and performance of ruthenium nanoparticles for CO₂ hydrogenation, *Catal. Sci. Technol.* 4 (2014) 2058–2063.
 - [36] C. Janke, M.S. Duyar, M. Hoskins, R. Farrauto, Catalytic and adsorption studies for the hydrogenation of CO₂ to methane, *Appl. Catal. B, Environ.* 152–153 (2014) 184–191.
 - [37] D.C. Upham, A.R. Derk, S. Sharma, H. Metiu, E.W. McFarland, CO₂ methanation by Ru-doped ceria: the role of the oxidation state of the surface, *Catal. Sci. Technol.* 5 (2015) 1783–1791.
 - [38] J.A.H. Dreyer, P. Li, L. Zhang, G.K. Beh, R. Zhang, P.H. Sit, W.Y. Teoh, Influence of the oxide support reducibility on the CO₂ methanation over Ru-based catalysts, *Appl. Catal. B Environ.* 219 (2017) 715–726.
 - [39] A. Erdöhelyi, M. Pásztor, F. Solymosi, Catalytic hydrogenation of CO₂ over supported palladium, *J. Catal.* 98 (1986) 166–177.
 - [40] A. Karelovic, P. Ruiz, Improving the hydrogenation function of Pd/γ-Al₂O₃ catalyst by Rh/γ-Al₂O₃ Addition in CO₂ methanation at low temperature, *ACS Catal.* 3 (2013) 2799–2812.
 - [41] X. Wang, H. Shi, J.H. Kwak, J. Szanyi, Mechanism of CO₂ hydrogenation on Pd/Al₂O₃ catalysts: kinetics and transient DRIFTS-MS studies, *ACS Catal.* 5 (2015) 63337–6349.
 - [42] Z. Zhang, A. Kladi, X.E. Verykios, Effects of carrier doping on kinetic parameters of CO₂ hydrogenation on supported rhodium catalysts, *J. Catal.* 148 (1994) 737–747.
 - [43] C. De Leitenburg, A. Trovarelli, J. Kaspar, A temperature-programmed and transient kinetic study of CO₂ activation and methanation over CeO₂ supported noble metals, *J. Catal.* 166 (1997) 98–107.
 - [44] M. Jacquemin, A. Beuls, P. Ruiz, Catalytic production of methane from CO₂ and H₂ at low temperature: Insight on the reaction mechanism, *Catal. Today.* 157 (2010) 462–466.

- [45] A. Karelovic, P. Ruiz, Mechanistic study of low temperature CO₂ methanation over Rh/TiO₂ catalysts, *J. Catal.* 301 (2013) 141–153.
- [46] S. Fujita, H. Terunuma, M. Nakamura, N. Takezawa, Mechanisms of Methanation of CO and CO₂ over Ni, *Ind. Eng. Chem. Res.* 30 (1991) 1146–1151.
- [47] A.E. Aksoylu, A.N. Akin, Z.I. Önsan, D.L. Trimm, Structure/activity relationships in coprecipitated nickel-alumina catalysts using CO₂ adsorption and methanation, *Appl. Catal. A Gen.* 145 (1996) 185–193.
- [48] M. Yamasaki, H. Habazaki, T. Yoshida, E. Akiyama, A. Kawashima, K. Asami, K. Hashimoto, M. Komori, K. Shimamura, Compositional dependence of the CO₂ methanation activity of Ni/ZrO₂ catalysts prepared from amorphous Ni-Zr alloy precursors, *Appl. Catal. A Gen.* 163 (1997) 187–197.
- [49] Q. Pan, J. Peng, T. Sun, S. Wang, S. Wang, Insight into the reaction route of CO₂ methanation: Promotion effect of medium basic sites, *Catal. Commun.* 45 (2014) 74–78.
- [50] R.A. Hubble, J.Y. Lim, J.S. Dennis, Kinetic studies of CO₂ methanation over a Ni/γ-Al₂O₃ catalyst, *Faraday Discuss.* 192 (2016) 529–544.
- [51] L. Xu, F. Wang, M. Chen, J. Zhang, K. Yuan, L. Wang, K. Wu, G. Xu, W. Chen, CO₂ methanation over a Ni based ordered mesoporous catalyst for the production of synthetic natural gas, *Roya Soc. Chem. Adv.* 6 (2016) 28489–28499.
- [52] L. Xu, F. Wang, M. Chen, D. Nie, X. Lian, Z. Lu, H. Chen, K. Zhang, P. Ge, CO₂ methanation over rare earth doped Ni based mesoporous catalysts with intensified low-temperature activity, *Int. J. Hydrogen Energy.* 42 (2017) 15523–15539.
- [53] A. Cárdenas-Arenas, A. Quindimil, A. Davó-Quiñonero, E. Bailón-García, D. Lozano-Castelló, U. De-La-Torre, B. Pereda-Ayo, J.A. González-Marcos, J.R. González-Velasco, A. Bueno-López, Design of active sites in Ni/CeO₂ catalysts for the methanation of CO₂: tailoring, *Appl. Mater. Today.* 19 (2020) 100591.
- [54] V. Alcalde-Santiago, A. Davó-Quiñonero, I. Such-Basáñez, D. Lozano-Castelló, A. Bueno-López, Macroporous carrier-free Sr-Ti catalyst for NO_x storage and reduction, *Appl. Catal. B Environ.* 220 (2018) 524–532.
- [55] A. Davó-Quiñonero, J. González-Mira, I. Such-Basáñez, J. Juan-Juan, A. Bueno-López, D. Lozano-Castelló, Improved CO Oxidation Activity of 3DOM Pr-Doped Ceria Catalysts: Something Other Than an Ordered, *Catalysts.* 7 (2017) 67.
- [56] D. Terribile, A. Trovarelli, J. Llorca, C. De Leitenburg, G. Dolcetti, The synthesis and characterization of mesoporous high-surface area ceria prepared

- using a hybrid organic/inorganic route, *J. Catal.* 178 (1998) 299–308.
- [57] D. Terribile, A. Trovarelli, J. Llorca, C. de Leitenburg, G. Dolcetti, The preparation of high surface area CeO₂-ZrO₂ mixed oxides by a surfactant-assisted approach, *Catal. Today.* 43 (1998) 79–88.
- [58] A. Martínez-Arias, M. Fernández-García, V. Ballesteros, L.. Salamanca, J.. Conesa, C. Otero, J. Soria, Characterization of high surface area Zr-Ce (1:1) mixed oxide prepared by a microemulsion method, *Langmuir*. 15 (1999) 4796–4802.
- [59] G. Zhang, Z. Zhao, J. Xu, J. Zheng, J. Liu, G. Jiang, A. Duan, H. He, Comparative study on the preparation, characterization and catalytic performances of 3DOM Ce-based materials for the combustion of diesel soot, *Appl. Catal. B Environ.* 107 (2011) 302–315.
- [60] G.I.N. Waterhouse, J.B. Metson, H. Idriss, D. Sun-waterhouse, Physical and optical properties of inverse opal CeO₂ photonic crystals, *Chem. Mater.* 20 (2008) 1183–1190.

6

Effect of carbon content in the NiO/CeO_2 catalysts for the CO_2 methanation

6.1. Introduction

6.2. Experimental details

6.2.1. Catalysts preparation

6.2.2. Catalysts characterization

6.2.3. CO_2 methanation tests

6.3. Results and discussion

6.3.1. Catalysts characterization

6.3.2. CO_2 methanation tests

6.4. Conclusions

6.5. References

Universitat d'Alacant
Universidad de Alicante

6.1. Introduction

The problem of climate change must be approached from two perspectives, an adaptation to existing climate change and the implementation of mitigation processes that reduce emissions, in order to stabilize the levels of greenhouse gases in the atmosphere [1,2]. In this sense, science has a very important role that consists of renewing and optimizing polluting industrial processes, transforming them into environmentally friendly processes. Among the proposals to mitigate CO₂ emissions, CO₂ capture, storage and utilization technologies are a medium-term solution to mitigate environmental impacts while allowing the continued use of fossil fuels until the technologies of renewable energy are ready for implementation [3].

The catalytic conversion of CO₂ into methane has increased the interest of the scientific community [4–6], as it is presented as a potential route to produce a valuable fuel from a contaminant using excess electricity from renewable sources (in the process known as Power-to-Gas) [7,8]. Although the CO₂ methanation reaction is exothermic [5], it has some kinetic limitations generated by the high stability of the reactive gases, which requires a catalyst to accelerate the reaction to values with practical relevance for industrial application [6,9]. As described in detail in Chapter 1, usually, the active phases of the catalysts used to accelerate the CO₂ methanation reaction are prepared by impregnating the Ni or Ru precursors. Ru is more active than Ni at low temperatures [10–13], but Ni has a good relationship between high catalytic activity and low price [9,14–16]. For this reason, Ni is usually the preferred option to accelerate the reaction, working at somewhat higher temperatures (> 300 °C).

Various supports have been studied to deposit the active phase [10,17–21]. Cerium oxide is widely used as support in many catalysts [14,22–26]. Ceria is well known for its redox properties, where Ce⁴⁺/Ce³⁺ species coexist and for its ability to store oxygen, which can improve catalytic activity [24,25]. Also, the interaction between Ni and CeO₂-based oxides can inhibit Ni growth [27]. The focus on the development of optimal catalysts for the CO₂ methanation reaction is oriented towards the modification of the support, the addition of promoters and the use of new materials. In this sense, optimizing the use of ceria, for example, mixing it with another support with a higher surface area and a lower price than ceria, can be interesting.

Carbon xerogels are excellent catalytic supports and they are used in various catalytic reactions [28–30], since they offer certain advantages, such as their low cost, high mechanical resistance, high surface area that allows a good dispersion of the active phase, the possibility of modifying the pore size distribution, good reductive properties, easy recovery of the active metal from the spent catalyst by burning off the support and the possibility of modifying easily their surface chemistry [31].

Intensive efforts have been made to design and improve Ni-based catalysts for CO₂ methanation. Previous studies have shown the need for two different types of active sites in a catalyst for CO₂ methanation: one responsible for CO₂ activation and the other for H₂ dissociation and transfer and its proportion depends, to a large extent, on the metal-support interaction [9,32]. Considering this background, the goal of this study is to prepare, characterize and test NiO/CeO₂-NiO/C catalysts for CO₂ methanation in order to analyse the effect of carbon both in the nature of the Nickel active sites and in the behaviour of the NiO/CeO₂ phases.

6.2. Experimental details

6.2.1. Catalysts preparation

Catalysts based on physical mixture of NiO/CeO₂ and NiO/C were prepared and the details of the synthesis are described in the *Section 2.1.4* from *Chapter 2*. Briefly, CeO₂ support was prepared by calcination of the cerium nitrate and carbon support was prepared using resorcinol formaldehyde resin as carbon precursor. Nickel (10 wt. %) was loaded by incipient wetness impregnation on the support. Finally, NiO/CeO₂ and NiO/C were physically mixed in 0, 25, 50, 75% and 100% NiO/C proportion. The catalysts have been referred as 100%NiO/CeO₂, 75%NiO/CeO₂-25%NiO/C, 50%NiO/CeO₂-50%NiO/C, 25%NiO/CeO₂-75%NiO/C and 100%NiO/C.

6.2.2. Catalysts characterization

The catalysts were characterized by means of complementary techniques. The nickel content was determined by ICP-OES and the carbon content was determined by combustion in a thermobalance. Textural properties have been characterized by N₂ adsorption-desorption at -196 °C and CO₂ adsorption at 0 °C, after outgassing the catalysts under vacuum at 150 °C for 8 hours. The redox properties were studied by H₂-TPR and the surface groups were determined by He-TPD. XPS spectra were obtained to study the electronic state of the added metal species, after a reduction treatment at 500 °C for 1 h (heating ramp 10 °C/min) under of 50% H₂/He (80 mL/min). Description of the techniques and of the experimental conditions and procedures has been detailed in *Chapter 2*.

6.2.3. *CO₂ methanation tests*

Catalytic activity measurements were performed at the University of Alicante and the experimental conditions has been detailed in *Section 2.3.1*. Briefly, catalytic tests were performed using 200 mg of catalyst mixed with SiC particles. The sample was pre-treated at 500 °C during 1 h under 50% H₂/N₂ (200 mL/min). After cooling to room temperature, the reaction mixture (16% CO₂ + 64% H₂ and He balance) was fed with a total flow rate of 200 mL/min and the gas hourly space velocity was 12000 h⁻¹. The temperature was increased in steps and the gas composition was monitored with a gas chromatograph.

6.3. Results and discussion

6.3.1. *Catalysts characterization*

In order to understand the influence of the carbon presence in the catalytic properties of the NiO₂-CeO₂ catalysts, materials have been characterized by different techniques. To obtain information about the porous texture of the catalyst, N₂ adsorption-desorption isotherms at -196 °C and CO₂ adsorption isotherms at 0 °C were made and are shown in Figure 6.1a and 6.1b, respectively.

N₂ adsorption-desorption isotherms show that all materials have type IV isotherms, according to the IUPAC classification, with the presence of a hysteresis loop typical of the presence of mesopores, whose filling is produced by capillary condensation [33]. N₂ uptake is low for 100% NiO/CeO₂ catalyst with regard to NiO/CeO₂-NiO/C catalysts. The isotherms shape of catalysts with carbon combines rapid N₂ uptake at very low relative pressures, attributed to the presence of microporosity, with uptake at intermediate pressures and a hysteresis loop that evidences the presence of mesopores. As expected, the adsorption capacity of these materials increases when increasing the carbon content present in the catalyst.

In the CO₂ adsorption isotherms shown in Figure 6.1b, clear differences about the microporosity are observed between the carbon-free catalyst (100%NiO/CeO₂) and the catalysts with carbon. The isotherm of the 100% NiO/CeO₂ catalyst shows no CO₂ adsorption, denoting a null narrow microporosity, while the isotherms of the catalysts with carbon show an increase in CO₂ adsorption according to the amount of carbon present in the mixture. This agrees with the N₂ adsorption isotherms at -196 °C results and is associated with the higher surface area of carbon with regard to metal oxides.

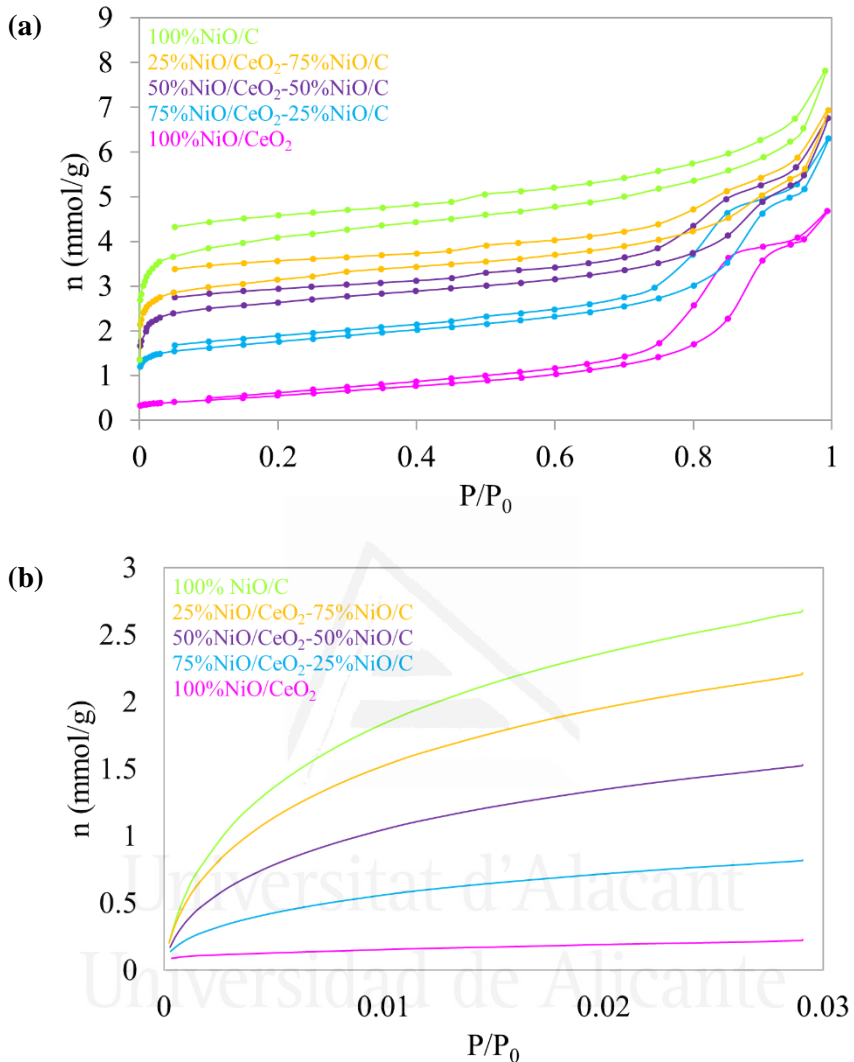


Figure 6.1. isotherms (a) N₂ adsorption-desorption at -196 °C and (b) CO₂ adsorption at 0 °C.

Table 6.1. summarizes the textural properties obtained from the N₂ and CO₂ adsorption isotherms. In general, the samples with carbon exhibit higher specific surface areas and micropore volumes than the 100% NiO/CeO₂ catalyst, and the higher the carbon content, the higher the BET specific surface area. The BET area increases from 48 m²/g for the carbon-free catalyst (100% NiO/CeO₂) to 267 m²/g for the ceria-free one, and the micropore volume increases from 0.01 to 0.20 cm³/g.

Table 6.1. Results of the catalysts characterization by ICP-OES, TG, N₂ adsorption-desorption isotherms at 196 °C and CO₂ adsorption at 0 °C.

Catalyst	Ni (wt.%)	C (wt.%)	S _{B.E.T.^a} (m ² /g)	V _{D.R. (CO₂)} (cm ³ /g)
100% NiO-C	11.0	84.3	267	0.20
25% NiO/CeO ₂ -75% NiO/C	10.4	64.5	209	0.16
50% NiO/CeO ₂ -50% NiO/C	10.3	43.9	174	0.11
75% NiO/CeO ₂ -25% NiO/C	8.9	22.7	131	0.06
100% NiO/CeO ₂	10.2	-	48	0.01

^aS_{B.E.T.}: BET surface area calculated from N₂ adsorption-desorption isotherms data.

^bV_{D.R. (CO₂)}: micropore volume calculated by the Dubinin-Radushkevich equation to the CO₂ adsorption data.

Regarding the elemental composition, the actual Ni and C content of the catalysts were determined by ICP-OES and combustion in a thermobalance, respectively, and they are showed in Table 6.1. The measured percentage of Ni incorporated in the catalysts is very similar in all samples and is near the target value (10 %), and the obtained carbon values are also close to the target ones.

Figure 6.2. shows the gas profiles of the xerogel carbon support obtained in the He-TPD experiment. CO and H₂O were not emitted during the thermal treatment, and only CO₂ was evolved. Two CO₂ peaks are observed, a first peak at low temperatures (from 150 to 450 °C) with a maximum at 370 °C and a second peak at higher temperatures (from 450 to 730 °C) with a maximum of 640 °C. The He-TPD peaks have been tentatively assigned to the different functional groups by comparison with the data available in the literature [34]. The first CO₂ peak can be attributed to carboxylic acid functions, while the higher temperature CO₂ peak can be tentatively assigned to lactones decomposition.

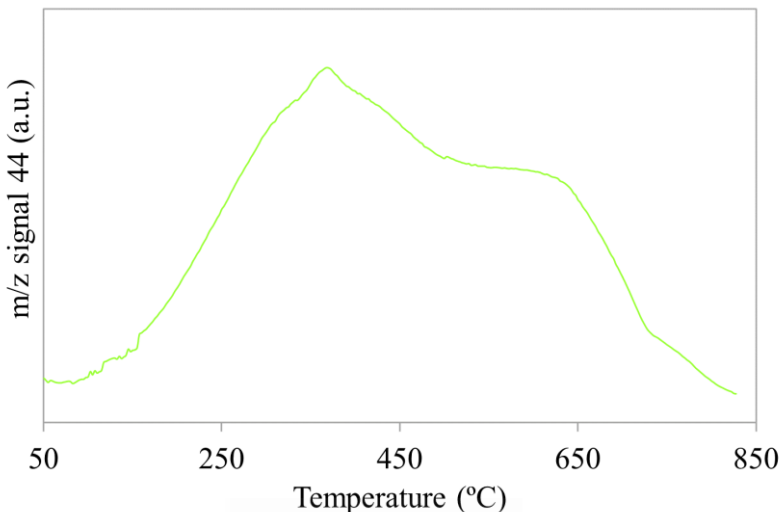


Figure 6.2. He-TPD profiles of the xerogel carbon support.

The redox properties of the catalysts and the interaction between the nickel species and supports have been studied by H₂-TPR. Figure 6.3. shows the reduction profiles, where several reduction events can be observed. The area under the peaks between 230 and 470 °C has been quantified, and the amount of H₂ consumed has been related with the amount required for the total reduction of Ni²⁺ to Ni⁰ (Table 6.2.). In 100%NiO/CeO₂ catalyst, the H₂ consumption is higher than the amount required to reduce all Ni²⁺ to Ni⁰, which evidences that Ce⁴⁺ cations are also reduced in this wide double peak. This H₂ consumption is significantly increased in carbon-containing catalysts, being more significant for 100%NiO/C catalyst. The high consumption of H₂ in carbon-containing catalysts can be attributed to the Ni-catalyzed reduction of surface ceria and to the decomposition of the surface groups on the carbon, since the CO₂ evolved can be reduced by H₂ yielding CH₄ and H₂O (CO₂ methanation reaction).

The carbon-free catalyst shows a main peak at 340 °C with a shoulder at 380 °C, and a small peak at 250 °C. The main peak at 340 °C can be assigned to the simultaneous NiO and surface ceria reduction, and the shoulder at 380 °C to the Ni-catalysed surface ceria reduction. The small peak at 250 °C suggests the presence of a small amount of highly reducible NiO, probably highly dispersed NiO nanoparticles. Finally, the high temperature peak at 785 °C can be assigned to ceria bulk reduction.

The curve obtained for ceria-free catalyst presents two peaks at 310 and 670 °C. The peak at 310 °C can be assigned to NiO species reduction and, probably to CO₂ emissions produced by the decomposition of the surface carbon groups. The peak at 670

°C can be attributed to CO₂ emissions produced by the decomposition of surface carbon species, according with He-TPD results.

The profiles of the carbon/ceria-containing catalysts present a shift of the reduction peaks to lower temperature. All NiO/CeO₂-NiO/C catalysts present NiO reduction events at 305 and 345 °C, which can be attributed to reduction of the surface NiO species and NiO species in intimate contact with ceria surface, respectively. In addition, in this event, the CO₂ emissions produced by the decomposition of the surface carbon groups and CO₂ methanation reaction must be considered. The reduction temperature of the surface NiO species decreases and the area under the peak increases when increasing the carbon content of the catalyst, while the area under the peak of the NiO species in intimate contact with ceria decreases.

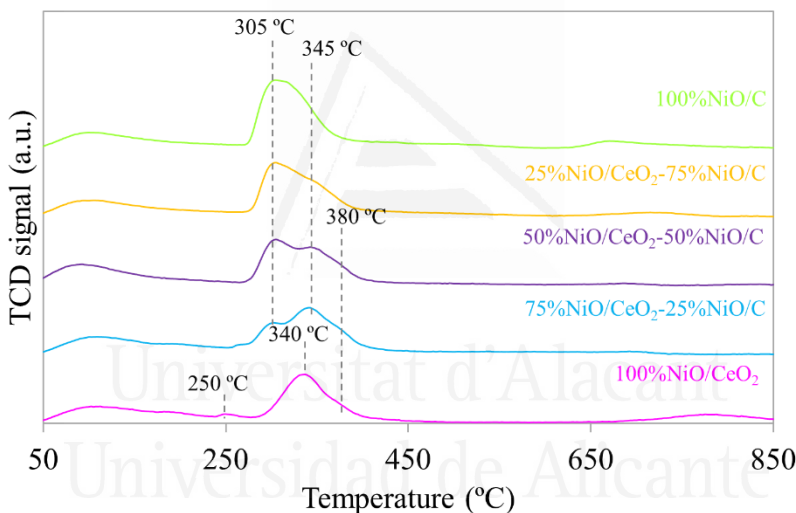


Figure 6.3. Temperature programmed reduction experiments with H₂.

In conclusion, the reducibility of the NiO species is better in the carbon-containing catalysts than in carbon-free one. This can be attributed to the high surface area of the carbon support, which favours the dispersion of the nickel particles, and/or to the chemical effect of carbon in the NiO-CeO₂ interaction.

Table 6.2. H₂ consumed in Temperature Programmed Reduction experiments.

Catalyst	H ₂ mole/NiO mole
100%NiO-C	5.0
25%NiO/CeO ₂ -75%NiO/C	4.5
50%NiO/CeO ₂ -50%NiO/C	4.0
75%NiO/CeO ₂ -25%NiO/C	4.9
100%NiO/CeO ₂	3.5

The surface of the catalysts has been analyzed by XPS. Ni_{2p} core level spectra of the reduced catalysts and the percentages of each component are shown in Figure 6.4a. and 6.4b, respectively. In the Ni_{2p} spectral region a principal band is observed in the 851-861 eV range together with satellite peaks at higher binding energy. There is no consensus about the assignation of the peaks of the Ni_{2p} spectral region, however several authors have proposed that the nature of the nickel species can be deduced from the position and deconvolution of the highest intensity peak [35–37]. In general, peaks that appear below 852 eV can be attributed to metallic nickel, and above this energy peaks can be assigned to NiO, Ni₂O₃ and Ni(OH)₂ [35,38–40].

Analyzing the Ni_{2p} energy region of 100%NiO/CeO₂ catalyst after reduction (Figure 6.3a.), three main peaks are observed at 853.4, 855.2 and 857.4, which can be assigned to surface Ni²⁺ species, Ni²⁺ species in intimate contact with the support and Ni³⁺ or Ni(OH)₂, respectively. With respect to the position of these species, differences are observed between carbon free one and carbon-containing catalysts. Peaks corresponding to surface Ni²⁺ and Ni²⁺ species in intimate contact with the support present a shift to higher binding energy with regards to 100%NiO/CeO₂ catalyst.

Also, differences in the proportion of the Ni species are observed between the carbon-containing catalysts and carbon-free one, and these are shown in Figure 6.4b. and Table 6.3. NiO species in intimate contact with the support (peak at 855 eV) predominate in carbon-free catalyst, and this specie can be related to the reduction peak at 340 °C observed in the H₂-TPR profile. The band that appears at the lowest binding energy (853 eV), attributed to surface NiO species, can be related with easily reduced species observed in the H₂-TPR profile at 250 °C. Conversely, in carbon-containing catalysts, surface NiO species are predominated. In line with H₂-TPR profiles, the presence of carbon favors the reducibility of the NiO-CeO₂ species therefore, the proportion of the peak that appears at a lower energy level is higher in carbon-containing

catalysts than in carbon-free one. In a previous work was determined that the proportion and coexistence of these two species is very important for the CO₂ methanation reaction, because Ni⁰ species are necessary for H₂ dissociation and NiO species in close contact with ceria are responsible of the CO₂ chemisorption and dissociation [32].

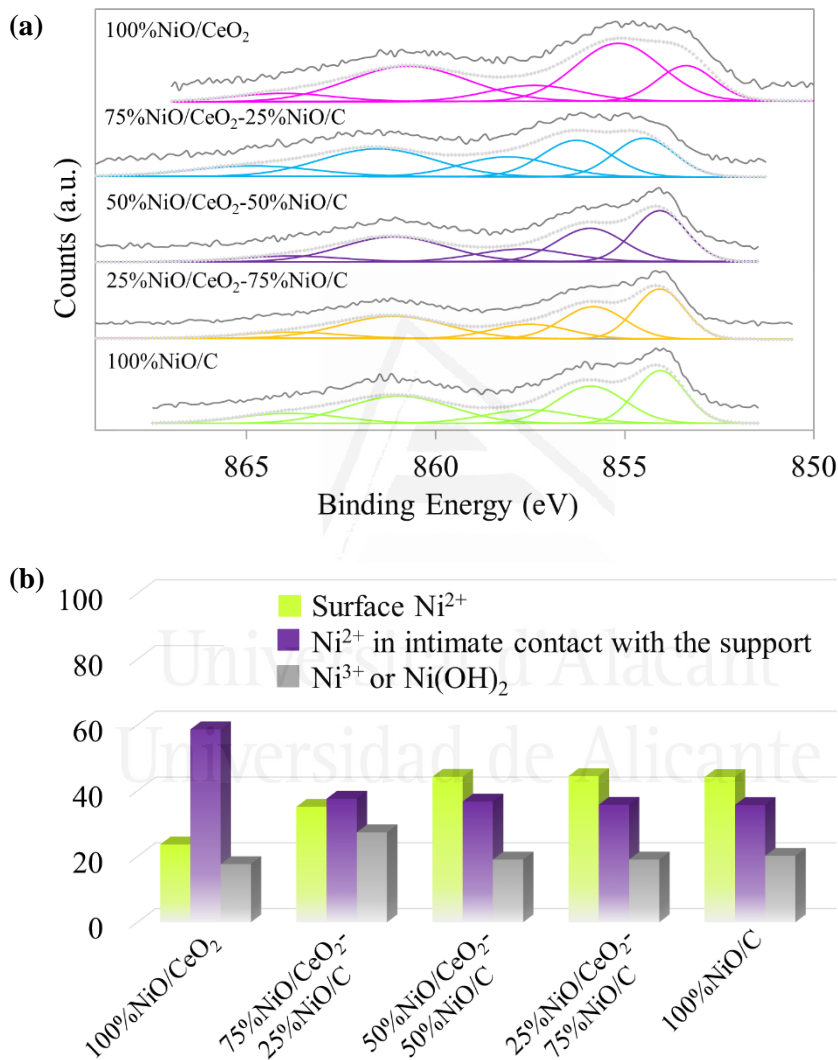


Figure 6.4. (a) Ni_{2p} core level spectra and (b) percentage of each component for reduced catalysts (pretreatment in 50% H₂/He at 500 °C).

Table 6.3. Surface composition (wt.%) of the reduced catalysts obtained by XPS.

Catalyst	C	O	Ni	Ni ⁰	Ce	Ce ³⁺
100%NiO/CeO ₂	11.3	18.5	11.7	23.6	58.4	22.1
75%NiO/CeO ₂ -25%NiO/C	33.5	15.5	12.7	35.1	38.4	27.4
50%NiO/CeO ₂ -50%NiO/C	65.7	9.3	13.5	44.2	11.5	21.1
25%NiO/CeO ₂ -75%NiO/C	75.7	9.5	13.0	44.5	1.8	21.9
100%NiO/C	77.5	10.7	11.8	44.2	—	—

Ce_{3d}, C_{1s} and O_{1s} regions were also analysed and they are shown in Figure 6.5a.-c., respectively. XPS spectrum of Ce_{3d} gives five spin-orbit doublets from 3d_{5/2} and 3d_{3/2}. The 3d_{5/2} level consists of three compounds for Ce⁴⁺ (v, v'' and v''') and two compounds for Ce³⁺ (v₀ and v') [41]. The proportion of Ce³⁺ and Ce⁴⁺ cations on the surface of the samples are calculated by integrated areas of the respective peaks and the information is collected in Table 6.3. Analysing the proportion of Ce³⁺, it is observed that there are no significant differences between 100%NiO/CeO₂ sample and carbon-containing catalysts, except to 75%NiO/CeO₂-25%NiO/C catalyst. This can indicate that the presence of carbon does not influence the reduction of the ceria.

O_{1s} spectra (Figure 6.5c.) shows also different contributions and its information is collected in Table 6.4. O_{1s} spectra of NiO/CeO₂ materials could be fitted using two Gaussian peaks centred at around 529 and 531 eV, which are designated as O_{LBE} and O_{HBE}, respectively. The peak O_{LBE} can be attributed to the presence of O²⁻ ions in the lattice from O-Ce⁴⁺ bond. The assignation of O_{HBE} peak is controversial in context of the O_{1s} spectra of CeO₂. According to various reports, the O_{HBE} peaks corresponds to the presence of oxygen in the form of adsorbed species such as -OH group or CO₂, oxygen present in the form of O-Ce³⁺ bond, and can be attributed to the presence of oxygen vacancies in the sample [42]. Three peaks were required to fit this region for carbon-containing catalysts, which are centered at around 529.6, 531 and 355 eV. The peak 529.6 eV is generally attributed to metal oxide oxygen (NiO and CeO₂). The peaks centered at 531 and 533 eV correspond to oxygenated groups on the carbon surface, O-C and O=C bonds [43]. In this sense, in the samples with a high content of CeO₂, the contribution of the oxygen bonded to metal species is dominant whereas the oxygenated groups increase as the carbon content present in the support increases.

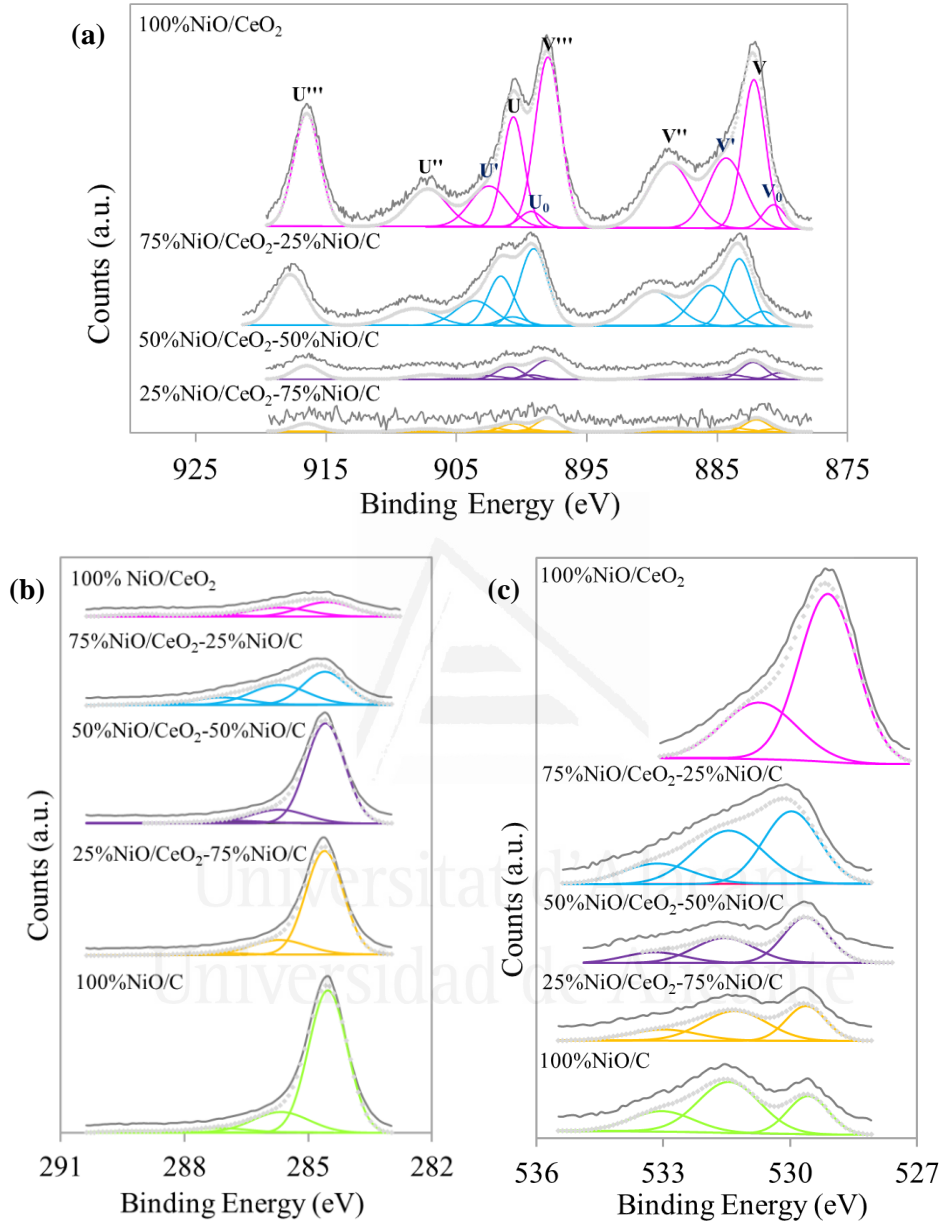


Figure 6.5. (a) Ce3d, (b) C1s and (c) O1s spectra of the catalysts after reduction treatment.

Table 6.4. Deconvolution of C1s and O1s spectral regions of the reduced catalysts.

Sample	C _{1s} eV	Assig.	Peak %	O _{1s} eV	Assig.	Peak %	O _{xps} %
100%NiO/CeO ₂	284.5	C-C	50.1	529.1	O _{LBE}	69.7	18.5
	285.7	C-O	36.0	530.7	O _{HBE}	30.3	
	287.3	C=O	6.4				
	289.0	C-OOH	7.5				
75%NiO/CeO ₂ -25%NiO/C	284.6	C-C	46.8	530.0	O-M	44.0	15.5
	285.7	C-O	37.3	531.5	O-C	40.8	
	287.1	C=O	13.6	533.1	O=C	15.2	
	288.7	C-OOH	2.3				
50%NiO/CeO ₂ -50%NiO/C	284.6	C-C	81.6	529.6	O-M	48.3	9.3
	285.7	C-O	16.0	531.6	O-C	35.8	
	286.8	C-O/C=O	2.4	533.2	O=C	15.9	
25%NiO/CeO ₂ -75%NiO/C	284.6	C-C	80.4	529.6	O-M	34.2	9.5
	285.7	C-O	17.2	531.3	O-C	47.2	
	287.2	C=O	2.4	533.0	O=C	18.6	
100%NiO/C	284.5	C-C	78.6	529.6	O-M	26.3	10.7
	285.7	C-O	16.5	531.4	O-C	52.6	
	287.2	C=O	3.6	533.0	O=C	21.1	
	289.1	C-OOH	1.3				

6.3.2. CO₂ methanation tests

The CO₂ methanation has been studied, and the conversion curves are plotted in Figure 6.6a. together with the CH₄ selectivity profile in Figure 6.6b.

The CO₂ conversion curve is similar in all catalysts and, as expected, CO₂ conversion increases with increasing temperature until the thermodynamic equilibrium of the reaction is reached. Due the stability of CO₂ and H₂ molecules, the activation energy is high and depends on the catalysts, being 200 °C for 100%NiO/CeO₂, 25%NiO/CeO₂-75%NiO/C and 50%NiO/CeO₂-50%NiO/C catalysts, 225 °C for 75%NiO/CeO₂-25%NiO/C catalyst and 275 °C for 100%NiO/C catalyst. There are differences in the slopes of the catalytic curves, and the temperature required to achieve 50 % of CO₂ conversion follows the trend 100%NiO/CeO₂ (275 °C) < 25%NiO/CeO₂-75%NiO/C (300 °C) < 50%NiO/CeO₂-50%NiO/C (325 °C) < 75%NiO/CeO₂-25%NiO/C. The carbon-containing catalysts showed lower activity. In all cases, the CH₄ selectivity is very high, around 98% at 300 °C, and this decreases from 400 °C since at high temperatures the RWGS reaction (CO₂ + H₂ ↔ CO + H₂O) is favored and, therefore, the production of CO increases and decreases the production of CH₄. The

catalytic behavior shows a relationship between the CO₂ conversion and the carbon content present in the sample, except for the 100% NiO/CeO₂ sample.

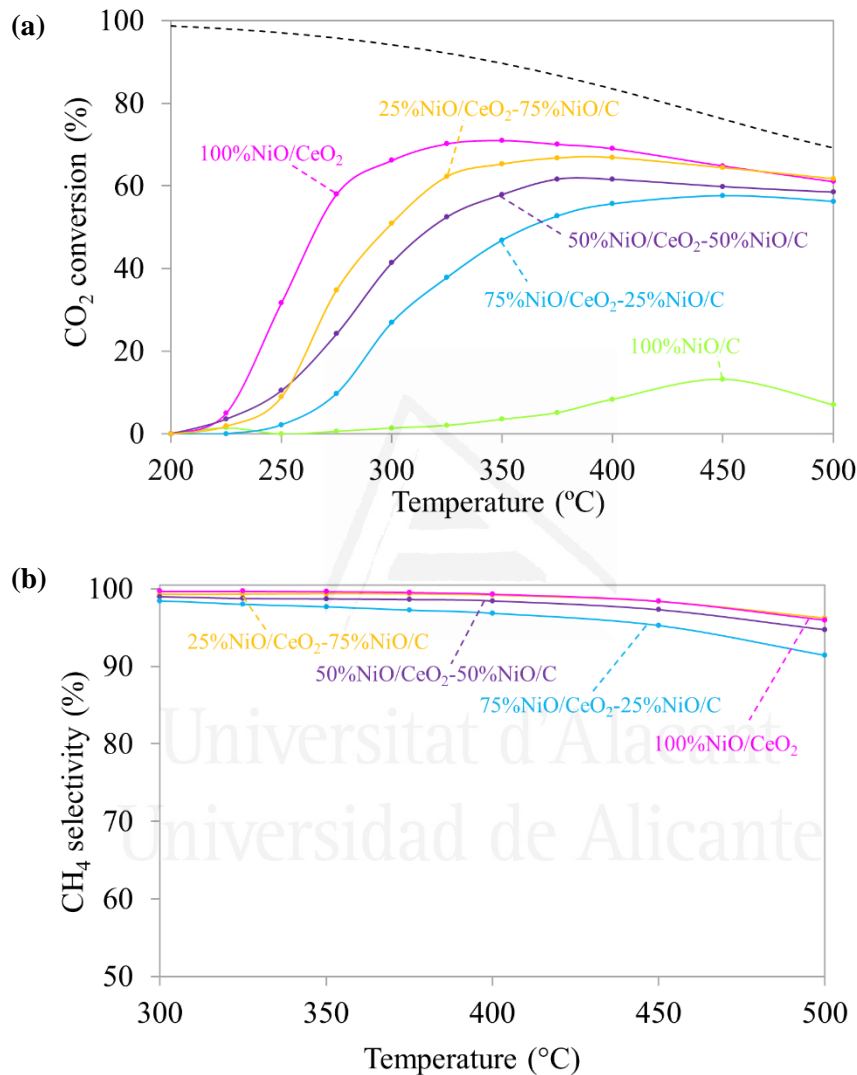


Figure 6.6. CO₂ methanation catalytic test. (a) CO₂ conversion and (b) CH₄ selectivity.

In order to study the influence of replacing part of the ceria support with carbon on the catalytic properties, the Figure 6.7. shows the normalized CO₂ conversion curves by percentage of CeO₂. At 300 °C the most active one was 25%NiO/CeO₂-75%NiO/C and all other catalysts showed less than half the catalytic conversion of this material.

This behaviour seems to be related to the high surface area and good reducibility of the catalysts with carbon. 25%NiO/CeO₂-75%NiO/C catalyst is the catalyst with carbon and ceria with the highest surface area, which favours the dispersion of the nickel particles, and, as it was pointed out by H₂-TPR and XPS, the chemical effect of carbon in the NiO-CeO₂ interaction favours the reducibility of the NiO species. In this sense, the presence of carbon as a support allow obtaining a catalyst with a high catalytic performance in the CO₂ methanation reaction using only ~25% of ceria.

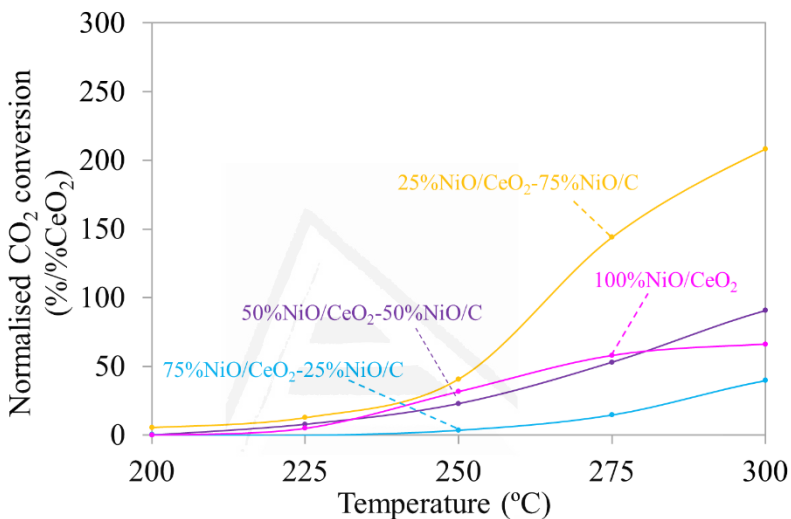


Figure 6.7. CO₂ conversion curves normalised by percentage of CeO₂ for CO₂ methanation reaction.

6.4. Conclusions

This work has been oriented to prepare, characterize and test catalysts for the CO₂ methanation reaction by modifying the conventional NiO/CeO₂ catalyst with carbon, in order to optimize the use of ceria. In this sense, catalysts have been prepared by mixing the NiO/CeO₂ and NiO/C phases in different proportions (0, 25, 50, 75% and 100% NiO/C). From the results obtained in the catalytic tests and the characterization of the catalysts, the following conclusions can be drawn:

- ❖ A catalyst with a high catalytic performance for the CO₂ methanation reaction has been obtained incorporating carbon as part of the support and using only 25% of the NiO/CeO₂ component.

- ❖ The incorporation of the carbon support increases the specific surface area and micropores volumes in comparison with the carbon-free catalyst (100% NiO/CeO₂) from 48 m²/g for the 100% NiO/CeO₂ catalyst to 267 m²/g for the ceria-free one, and the micropore volume increases from 0.01 to 0.20 cm³/g.
- ❖ The presence of carbon favours the reducibility of the NiO/CeO₂ catalyst. The reduction profiles of the carbon-containing catalysts exhibit a reduction peak shift at a lower temperature compared with the carbon-free catalyst. The XPS spectra show that the proportion of the peak that appears at a lower energy level (surface NiO species) is higher in carbon-containing catalysts than in carbon-free one content.
- ❖ 100% NiO/CeO₂ and 25% NiO/CeO₂-75% NiO/C catalysts are the most active for CO₂ methanation (65 and 60% CO₂ conversion at 350 °C, respectively), being the 25% NiO/CeO₂-75% NiO/C catalyst a viable option in order to reduce and optimize the use of ceria support. The high activity of the 25% NiO/CeO₂-75% NiO/C catalyst is related with the high specific surface area of the carbon support, which favours the dispersion of the nickel particles, and/or to the chemical effect of carbon in the NiO-CeO₂ interaction. The presence of carbon does not affect the selectivity towards CH₄ and all tested catalyst show high selectivity, around 98% in the whole range of temperature studied.

6.5. References

- [1] P. Nema, S. Nema, P. Roy, An overview of global climate changing in current scenario and mitigation action, *Renew. Sust. Energ. Rev.* 16 (2012) 2329–2336.
- [2] S. Planton, M. Déqué, F. Chauvin, L. Terray, Expected impacts of climate change on extreme climate events, *C. R. Geosci.* 340 (2008) 564–574.
- [3] C. Hepburn, E. Adlen, J. Beddington, E.A. Carter, S. Fuss, N. Mac Dowell, J.C. Minx, P. Smith, C.K. Williams, The technological and economic prospects for CO₂ utilization and removal, *Nature*. 575 (2019) 87–97.
- [4] K. Stangeland, D. Kalai, H. Li, Z. Yu, CO₂ Methanation: The Effect of Catalysts and Reaction Conditions, *Energy Procedia*. 105 (2017) 2022–2027.
- [5] C. Mebrahtu, F. Krebs, S. Abate, S. Perathoner, G. Centi, R. Palkovits, CO₂ Methanation: Principles and Challenges, in: *Stud. Surf. Sci. Catal.*, 1st ed., Elsevier B.V., 2019: pp. 85–103.
- [6] P. Frontera, A. Macario, M. Ferraro, P. Antonucci, Supported Catalysts for CO₂ Methanation: A Review, *Catalysts*. 7 (2017) 59.
- [7] M. Götz, J. Lefebvre, F. Mörs, A. McDaniel Koch, F. Graf, S. Bajohr, R. Reimert, T. Kolb, Renewable Power-to-Gas: A technological and economic

- review, *Renew. Energ.* 85 (2016) 1371–1390.
- [8] J. Guilera, T. Andreu, N. Basset, T. Boeltken, F. Timm, I. Mallol, J.R. Morante, Synthetic natural gas production from biogas in a waste water treatment plant, *Renew. Energ.* 146 (2020) 1301–1308.
 - [9] M. V. Konishcheva, D.I. Potemkin, S.D. Badmaev, P. V. Snytnikov, E.A. Paukshtis, V.A. Sobyanin, V.N. Parmon, On the mechanism of CO and CO₂ methanation over Ni/CeO₂ catalysts, *Top. Catal.* 59 (2016) 1424–1430.
 - [10] S. Scirè, C. Crisafulli, R. Maggiore, S. Minicò, S. Galvagno, Influence of the support on CO₂ methanation over Ru catalysts: an FT-IR study, *Catal. Letters.* 51 (1998) 41–45.
 - [11] N.M. Gupta, V.S. Kamble, A. Rao, R.M. Iyer, On the mechanism of CO and CO₂ methanation over Ru/molecular-sieve catalyst, *J. Catal.* 60 (1979) 57–67.
 - [12] P. Panagiotopoulou, Hydrogenation of CO₂ over supported noble metal catalysts, *Appl. Catal. A Gen.* 542 (2017) 63–70.
 - [13] L. Falbo, C.G. Visconti, L. Lietti, J. Szanyi, The effect of CO on CO₂ methanation over Ru/Al₂O₃ catalysts: a combined steady-state reactivity and transient DRIFT spectroscopy study, *Appl. Catal. B Environ.* 256 (2019) 117791.
 - [14] S. Tada, T. Shimizu, H. Kameyama, T. Haneda, R. Kikuchi, Ni/CeO₂ catalysts with high CO₂ methanation activity and high CH₄ selectivity at low temperatures, *Int. J. Hydrog. Energy.* 37 (2012) 5527–5531.
 - [15] S. Rahmani, M. Rezaei, F. Meshkani, Preparation of highly active nickel catalysts supported on mesoporous nanocrystalline γ-Al₂O₃ for CO₂ methanation, *J. Ind. Eng. Chem.* 20 (2014) 1346–1352.
 - [16] S.M. Lee, Y.H. Lee, D.H. Moon, J.Y. Ahn, D.D. Nguyen, S.W. Chang, S.S. Kim, Reaction mechanism and catalytic impact of Ni/CeO_{2-x} catalyst for low-temperature CO₂ methanation, *Ind. Eng. Chem. Res.* 58 (2019) 8656–8662.
 - [17] N.M. Martín, P. Velin, M. Skoglundh, M. Bauer, P.-A. Carlsson, Catalytic hydrogenation of CO₂ to methane over supported Pd, Rh and Ni catalysts, *Catal. Sci. Technol.* 7 (2017) 1086.
 - [18] J.H. Kwak, L. Kovarik, J. Szanyi, Heterogeneous catalysis on atomically dispersed supported Metals: CO₂ reduction on multifunctional Pd catalysts, *ACS Catal.* 3 (2013) 2094–2100.
 - [19] M. Li, H. Amari, A.C. Van Veen, Metal-oxide interaction enhanced CO₂ activation in methanation over ceria supported nickel nanocrystallites, *Appl. Catal. B Environ.* 239 (2018) 27–35.
 - [20] R.A. Hubble, J.Y. Lim, J.S. Dennis, Kinetic studies of CO₂ methanation over a Ni/γ-Al₂O₃ catalyst, *Faraday Discuss.* 192 (2016) 529–544.

- [21] M. Cai, J. Wen, W. Chu, X. Cheng, Z. Li, Methanation of carbon dioxide on Ni/ZrO₂-Al₂O₃ catalysts: Effects of ZrO₂ promoter and preparation method of novel ZrO₂-Al₂O₃ carrier, *J. Nat. Gas Chem.* 20 (2011) 318–324.
- [22] D. Gamarra, A. Martínez-Arias, Preferential oxidation of CO in rich H₂ over CuO/CeO₂: Operando-DRIFTS analysis of deactivating effect of CO₂ and H₂O, *J. Catal.* 263 (2009) 189–195.
- [23] D.G. Araiza, D.G. Arcos, A. Gómez-cortés, G. Díaz, Dry reforming of methane over Pt-Ni/CeO₂ catalysts: Effect of the metal composition on the stability, *Catal. Today.* (2019).
- [24] A. Davó-Quiñonero, J. González-Mira, I. Such-Basañez, J. Juan-Juan, A. Bueno-López, D. Lozano-Castelló, Improved CO oxidation activity of 3DOM Pr-doped ceria catalysts: Something other than an ordered, *Catalysts.* 7 (2017) 67.
- [25] V. Alcalde-santiago, A. Davó-quijonero, D. Lozano-castelló, On the soot combustion mechanism using 3DOM ceria catalysts, *Appl. Catal. B Environ.* 234 (2018) 187–197.
- [26] A. Trovarelli, C. De Leitenburg, M. Boaro, G. Dolcetti, The utilization of ceria in industrial catalysis, *Catal. Today.* 50 (1999) 353–367.
- [27] R.P. Ye, Q. Li, W. Gong, T. Wang, J.J. Razink, L. Lin, Y.Y. Qin, Z. Zhou, H. Adidharma, J. Tang, A.G. Russell, M. Fan, Y.G. Yao, High-performance of nanostructured Ni/CeO₂ catalyst on CO₂ methanation, *Appl. Catal. B Environ.* 268 (2020) 118474 .
- [28] L. Ning, S. Liao, H. Li, R. Tong, C. Dong, M. Zhang, W. Gu, X. Liu, Carbon-based materials with tunable morphology confined Ni (0) and Ni-N_x active sites: Highly efficient selective hydrogenation catalysts, *Carbon.* 154 (2019) 48–57.
- [29] S. Cattaneo, F.J.S. Trujillo, N. Dimitratos, A. Villa, The effect of carbon nanofibers surface properties in hydrogenation and dehydrogenation reactions, *Appl. Sci.* 9 (2019) 5061.
- [30] N.A.M. Barakat, M.T. Amen, F.S. Al-Mubaddel, M.R. Karim, M. Alrashed, NiSn nanoparticle-incorporated carbon nanofibers as efficient electrocatalysts for urea oxidation and working anodes in direct urea fuel cells, *J. Adv. Res.* 16 (2019) 43–53.
- [31] I.C. Gerber, P. Serp, A theory/experience description of support effects in carbon-supported catalysts, *Chem. Rev.* 120 (2019) 1250–1349.
- [32] A. Cárdenas-Arenas, A. Quindimil, A. Davó-Quiñonero, E. Bailón-García, D. Lozano-Castelló, U. De-La-Torre, B. Pereda-Ayo, J.A. González-Marcos, J.R. González-Velasco, A. Bueno-López, Design of active sites in Ni/CeO₂ catalysts for the methanation of CO₂: tailoring, *Appl. Mater. Today.* 19 (2020) 100591.
- [33] M. Thommes, K. Kaneko, A. V. Neimark, J.P. Olivier, F. Rodriguez-Reinoso, J.

- Rouquerol, K.S.W. Sing, Physisorption of gases, with special reference to the evaluation of surface area and pore size distribution (IUPAC Technical Report), Pure Appl. Chem. 87 (2015) 1051–1069.
- [34] J.L. Figueiredo, M.F.R. Pereira, M.M.A. Freitas, J.J.M. Órfão, Modification of the surface chemistry of activated carbons, Carbon. 37 (1999) 1379–1389.
 - [35] A.P. Grosvenor, M.C. Biesinger, R.S.C. Smart, N.S. McIntyre, New interpretations of XPS spectra of nickel metal and oxides, Surf. Sci. 600 (2006) 1771–1779.
 - [36] G.H. Yu, L.R. Zeng, Magnetic properties and x-ray photoelectron spectroscopy study of NiO/NiFe films prepared by magnetron sputtering, J. Appl. Phys. 90 (2001) 4039–4043.
 - [37] X. Xu, L. Li, F. Yu, H. Peng, X. Fang, X. Wang, Mesoporous high surface area NiO synthesized with soft templates: Remarkable for catalytic CH₄ deep oxidation, Mol. Catal. 441 (2017) 81–91.
 - [38] G.H. Yu, L.R. Zeng, F.W. Zhu, C.L. Chai, W.Y. Lai, Magnetic properties and x-ray photoelectron spectroscopy study of NiO/NiFe films prepared by magnetron sputtering, J. Appl. Phys. 90 (2001) 4039–4043.
 - [39] N. Weidler, J. Schuch, F. Knaus, P. Stenner, S. Hoch, A. Maljusch, R. Schäfer, B. Kaiser, W. Jaegermann, X-ray photoelectron spectroscopic investigation of plasma-enhanced chemical vapor deposited NiO_x, NiO_x(OH)_y, and CoNiO_x(OH)_y: influence of the chemical composition on the catalytic activity for the oxygen evolution reaction, J. Phys. Chem. C. 121 (2017) 6455–6463.
 - [40] G.H. Yu, L.R. Zeng, F.W. Zhu, C.L. Chai, W.Y. Lai, Magnetic properties and X-ray photoelectron spectroscopy study of NiO/NiFe films prepared by magnetron sputtering, J. Appl. Phys. 90 (2001) 4039–4043.
 - [41] M. Romeo, K. Bak, J. El Fallah, F. Le Normand, L. Hilaire, C.C. Levels, XPS study of the reduction of cerium dioxide, Surf. Interface Anal. 20 (1993) 508–512.
 - [42] I. Singh, K. Landfester, R. Muñoz-Espi, A. Chandra, Evolution of hollow nanostructures in hybrid Ce_{1-x}Cu_xO₂ under droplet confinement leading to synergetic effects on the physical properties, Nanotechnology. 28 (2017) 075601.
 - [43] A. Elmouwahidi, E. Bailón-García, A.F. Pérez-Cadenas, F. Carrasco-Marín, J. Castelo-Quibén, Carbon-vanadium composites as non-precious catalysts for electro-reduction of oxygen, Carbon. 144 (2019) 289–300.



Stable NiO-CeO₂ nanoparticles with improved carbon resistance for methane dry reforming. The size matters

7.1. Introduction

7.2. Experimental details

7.2.1. Catalysts preparation

7.2.2. Catalytic tests

7.2.3. Catalysts characterization

7.3. Results and discussion

7.3.1. Catalysts characterization

7.3.2. Catalytic tests

7.3.3. XPS analysis of the catalysts before and after the DRM tests

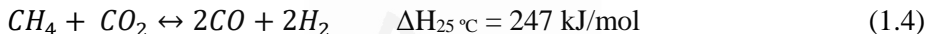
7.4. Conclusions

7.5. References

7.1. Introduction

Dry Reforming of methane (DRM) has been proposed to diminish emission of greenhouse gases to the atmosphere, catalyzing the reaction between CH₄ and CO₂ to yield a mixture of H₂ and CO (syngas) [1–5]. DRM is an environmental friendly pathway alternative to conventional syngas production by steam reforming. The syngas obtained by DRM can be used for Fischer-Tropsch synthesis of hydrocarbons of different nature, therefore contributing to decrease greenhouse gases emissions producing products with practical interest. DRM has been proposed to valorise waste emissions using biogas as feedstock, as a chemical way to store solar energy, and it has been also proposed to be applied to natural gas with high concentration of CO₂, among other applications [6,7].

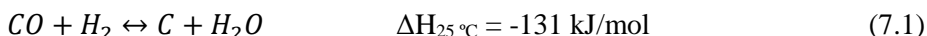
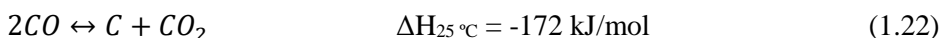
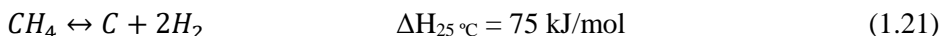
DRM is endothermic,



and also presents high activation energy due to the stability of the reactant gases. For this reason, the use of a catalyst is necessary to activate the reaction together with temperatures in the 650–850 °C range.

The most efficient DRM catalysts are supported noble metals (Ru, Rh, and Pt) and certain supported transition metals (Ni and Co) [8]. Noble metal catalysts are more active and better carbon resistant than Co and Ni catalysts, but the high price of noble metals limits their practical application. Among suitable catalysts, Ni-based catalysts are the most interesting at industrial level because combine a lower price than noble metals with a suitable catalytic activity [7,9–11].

The main problem of Ni catalysts is that suffer severe deactivation due to carbon formation under DRM conditions due to side reactions [12–15]. Carbon is a by-product that inhibits the catalyst due to encapsulation of the metal particles and/or blockage of the catalyst porosity [9]. In addition, carbon accumulation on the catalyst could not only lead to deactivation, but can also cause reactor plugging. Carbon is mainly formed by CH₄ decomposition (Equation 1.21.), but hydrogenation of CO and CO₂ (Equation 1.22.), and disproportionation of CO can also contribute (Equation 7.1.) [9].



The nature of the Ni support strongly affects the activity of the catalysts and the carbon resistance, and different supports have been studied, such as ZrO₂, CeO₂, ZrO₂-CeO₂, Al₂O₃, MgO, TiO₂, SiO₂, MgAl₂O₄ and ZSM5 among others [16]. Ceria-based supports are among the most efficient, because they promote nickel dispersion and prevent sintering due to the strong metal–support interaction [17]. It is known that DRM requires two type of actives sites on a Ni catalyst, including reduced Ni sites for CH₄ dissociation and basic sites for CO₂ chemisorption and dissociation. It has been also reported that basic supports, like those of ceria, provide efficient sites for such dissociation of CO₂ [9] and that the reaction between adsorbed CH₄ and CO with ceria oxygen prevents the formation of carbon on the nickel phase.

It is also well-known that the shape of a catalyst plays a critical role in the catalytic behavior, and ceria nanoparticles have shown high catalytic activity in different reactions, such as water gas shift [18,19], photocatalytic water splitting [20] and soot combustion [21,22] among others. NiO-CeO₂ nanoparticles were successfully prepared and tested for CO₂ methanation in Chapter 5, showing high activity, selectivity and stability.

Taking into account the promising behavior of nickel-ceria catalysts for DRM, and the critical issue of deactivation by carbon formation as undesired by-product, the goal of this chapter was to improve the carbon resistance of nickel-ceria DRM catalysts. A NiO-CeO₂ DRM catalyst is presented, which consist of mixed oxide nanoparticles. It is demonstrated that these nanoparticles present enough stability under the severe temperatures of DRM, and improved carbon resistance with regard to a counterpart NiO-CeO₂ mixed oxide prepared without control of the size.

7.2. Experimental details

7.2.1. Catalysts preparation

Two catalysts have been tested in this study, which are referred as NiO-CeO₂-np and NiO-CeO₂-US (CI), and the synthesis procedure is described in *Chapter 2*. Briefly, the novel catalyst, NiO-CeO₂-np (mixed nanoparticles), has been prepared by the reversed microemulsion method using the amount of Ni and Ce precursors required to obtain 8.5 wt. % of Ni in the final catalyst dissolved in water, and a microemulsion was prepared adding n-heptane, Triton X-100 and hexanol. The precipitation of the oxides was forced adding a similar microemulsion with a base (tetramethylammonium hydroxide) instead of the metal precursors. The reference catalyst (NiO-CeO₂-US (CI))

was prepared with the same composition, but without control of the structure dissolving Ni and Ce precursors in water and citric acid in stoichiometric proportions.

7.2.2. Catalytic tests

Catalytic activity tests were performed at the Sorbonne University and the experimental conditions have been detailed in *Chapter 2, Section 2.3.3*. Briefly, DRM tests were carried out in a fixed-bed reactor coupled to a gas chromatograph. The catalysts were reduced in situ before the experiments at 500 °C for 1 hour under 100 mL/min of 5% H₂/Ar. DRM experiments were performed afterwards at 700 °C under 100 mL/min of 10% CH₄ + 10% CO₂ with Ar balance. The mass of catalyst was 300 mg (GHSV 24000 h⁻¹).

7.2.3. Catalysts characterization

The catalysts were characterized by different complementary techniques. The nickel loading was determined by ICP-OES. The catalysts morphology was studied by Transmission Electron Microscopy (TEM). The textural properties of the catalysts were characterized by N₂ adsorption-desorption isotherms at -196 °C, after outgassing the catalysts under vacuum at 150 °C for 4 h. The reduction of the catalysts was studied by temperature programmed reduction with H₂ (H₂-TPR), and the amount of carbon accumulated on the catalysts during the DRM tests was determined by combustion in a thermobalance. The catalysts were characterized before and after the DRM tests by XRD and XPS, for study the crystalline structure and the surface of the catalysts, respectively.

7.3. Results and discussion

7.3.1. Catalysts characterization

The catalysts NiO-CeO₂-np and NiO-CeO₂-US (CI) were characterized by different techniques. Part of this characterization was already presented in *Chapter 5* together with characterization of other materials. However, the relevant characterization for proper interpretation of the current chapter is included in this section, paying special attention to differences between the properties of the two materials compared.

The amount of Ni is near the target (8.5 wt. %) in both materials (NiO-CeO₂-np 8.7 wt. % and NiO-CeO₂-US (CI) 8.2 wt. %), and ceria fluorite is the main crystalline phase in the diffractograms of both fresh catalysts (Figure 7.1.), suggesting formation of NiO-CeO₂ mixed oxides, as expected. Tiny peaks of NiO were observed in the diffractogram of fresh NiO-CeO₂-US (CI), evidencing few segregation of phases. The peaks broadening of the fresh catalysts indicate that crystallite size of NiO-CeO₂-np is smaller to that of NiO-CeO₂-US (CI), as expected (data in Table 7.1.).

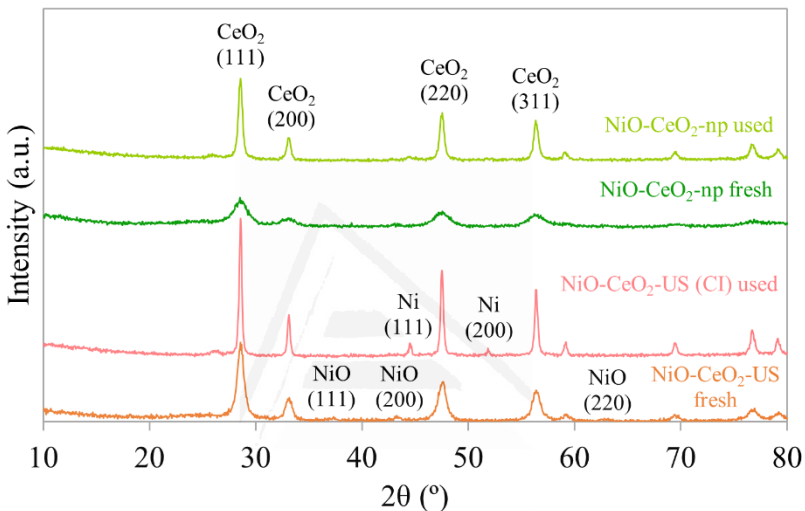


Figure 7.1. X-Ray diffractograms of the fresh and used catalysts.

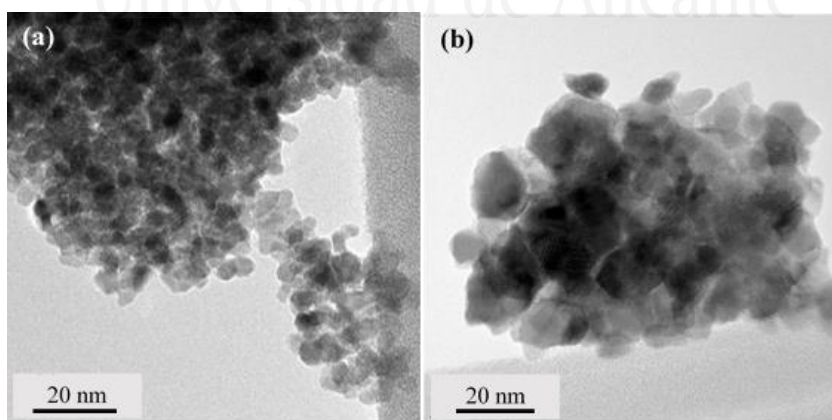
The intensity of the XRD peaks increased after the DRM reaction, obtaining much more intense peaks with the reference catalyst NiO-CeO₂-US (CI) than with NiO-CeO₂-np. The reference catalyst additionally shows peaks of metal nickel, confirming the presence of segregated nickel species. The crystallite sizes of ceria have been calculated with the Scherrer's equation using the (111) CeO₂ peak of the diffractograms and values have been compiled in Table 7.1. confirming the smaller crystallite size of NiO-CeO₂-np with regard to NiO-CeO₂-US (CI) both for fresh and used catalysts.

The smaller crystallite size of fresh NiO-CeO₂-np, predicted by XRD, is consistent with the results of N₂ adsorption. As expected, the specific surface area of NiO-CeO₂-np (122 m²/g) is higher to that of NiO-CeO₂-US (CI) (56 m²/g) due to the smaller size of the primary particles (see TEM images in Figure 7.2.).

Table 7.1. Ni content and specific surface area of the catalysts.

Catalyst	Ni (wt. %)	B.E.T. specific surface area (m ² /g)	CeO ₂ crystallite size (nm)
NiO-CeO ₂ -np fresh	8.7	122	7
NiO-CeO ₂ -np used	-	-	19
NiO-CeO ₂ -US (CI) fresh	8.2	56	13
NiO-CeO ₂ -US (CI) used	-	-	32

In this type of materials, the surface area comes from the external area of the primary particles together with the space left among particles, and can be assumed that primary particles are single crystals. For this reason, the smaller the primary particles/crystals the higher the specific surface area. Assuming spherical shape of the primary crystals, it is estimated from surface area values that the primary crystals size is 6-7 nm for NiO-CeO₂-np, which is consistent with the crystallite size obtained by XRD. This estimation increases to 15 nm for NiO-CeO₂-US (CI), but in this case the size of primary crystals is heterogeneous and must be considered as an average value. This is clearly observed in the TEM images of Figure 7.2. NiO-CeO₂-np image shows smaller crystals with homogeneous size, being consistent with the estimated size (6-7 nm), while the size of the crystals in the NiO-CeO₂-US (CI) image is non homogeneous, and larger crystals can be distinguished.

**Figure 7.2.** TEM images of the catalysts. (a) NiO-CeO₂-np and (b) NiO-CeO₂-US (CI).

The formation of nanoparticles also affects the reducibility of the catalyst, as observed in Figure 7.3. Both catalysts present H₂ consumption above 700 °C due to the reduction of bulk ceria, and the amount consumed is similar for both catalysts (0.06–0.08 H₂ mole/CeO₂ mole). On the contrary, important differences are noticed in the reduction profiles below 500 °C, where surface reduction events take place. Surface reduction of NiO-CeO₂-US (CI) shows a well-defined peak with a small shoulder at low temperature. This is consistent with the formation of a NiO-CeO₂ mixed oxide where Ni²⁺ and Ce⁴⁺ cations are reduced simultaneously, and the small shoulder is probably due to the low amount of segregated NiO, as deduced from XRD NiO tiny peaks. The surface reduction of NiO-CeO₂-np is quite different, with two well defined peaks that evidence the presence of two types of surface species with different reducibility. The maxima of the largest peak at 365 °C is quite similar to that of the surface reduction of NiO-CeO₂-US (CI) (350 °C), and the low temperature peak, with onset temperature at 160 °C and maximum at 288 °C, evidences the presence of highly reducible species in the nanoparticles catalyst. In addition, the amount of H₂ consumed for surface reduction of the catalysts is higher for NiO-CeO₂-np (147 H₂ mole/ NiO mole) than for NiO-CeO₂-US (CI) (121 H₂ mole/ NiO mole). The amounts of H₂ consumed are larger in both cases than the amounts required for NiO reduction to Ni, evidencing simultaneous reduction of ceria.

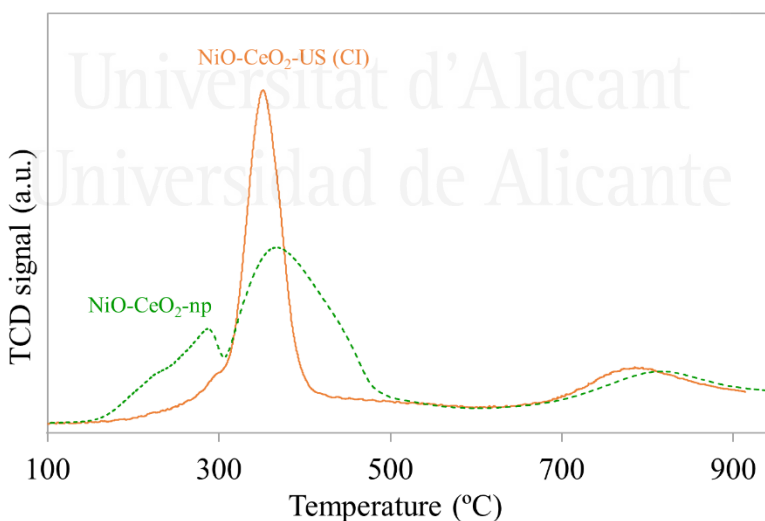


Figure 7.3. Temperature programmed reduction experiments with H₂.

In summary, characterization has showed that the novel NiO-CeO₂-np catalyst consists of homogeneously dispersed NiO-CeO₂ mixed oxide nanoparticles (6-7 nm) with higher surface area and improved surface reducibility with regard to the conventional NiO-CeO₂-US (CI) prepared without control of the structure.

7.3.2. Catalytic tests

The catalyst was tested for DRM at 700 °C for 5 hours under stoichiometric CH₄/CO₂ conditions, and the conversion curves are plotted in Figure 7.4. and compared with those obtained with the reference mixed oxide. Both catalysts reached high conversion values for CO₂ and CH₄ (above 80%), but the nanoparticles catalyst was slightly more active. The CH₄ conversion predicted by thermodynamics for the experimental conditions of these experiments is ~90 % [3,23], and the values obtained with both catalysts are only slightly lower. The conversion values shown in Figure 7.4. are high in comparison with those reported in literature for other Ni/CeO₂-based catalysts tested in comparable conditions. For instance, 30% CH₄ conversion was reported for a 12 wt.%Ni/CeO₂ catalyst prepared by incipient impregnation and tested at 700 °C with a stoichiometric CO₂/CH₄ mixture, and the catalyst suffered strong deactivation during reaction due to carbon formation [24]. In this case, the performance was significantly improved by optimizing the loading of the active phase on SBA15. In another example, Ni-Co/CeO₂-ZrO₂ catalysts were tested for DRM, and the CH₄ conversion at 700 °C dropped from 35 to 25 % approximately after 3 hours under reaction conditions due to carbon accumulation [25]. Higher conversion was achieved with a 26 wt. % Ni-ceria system prepared by combustion synthesis, reaching 65 % CH₄ conversion at 750 °C [26].

The H₂/CO ratio yielded by the catalysts tested in the current study (Figure 7.4c.) is slightly lower to 1, which is the predicted thermodynamic ratio for DRM. Values lower to 1 are obtained due to certain side reactions (CO_x methanation, reversed water gas shift and CH₄ decomposition) taking place together with DRM.

In summary, the catalytic tests confirmed that both the nanoparticle catalyst and the reference mixed oxide prepared for comparison are efficient catalysts for DRM, with few room for improvement in catalytic activity and selectivity because both catalysts approached the conversion and selectivity values predicted by thermodynamics. Nevertheless, resistance to carbon accumulation is required for this application, and nanoparticles improved carbon resistance with regard to the reference counterpart catalyst, as deduced from Figure 7.5. where thermograms obtained in air with both catalysts after the DRM catalytic tests have been plotted.

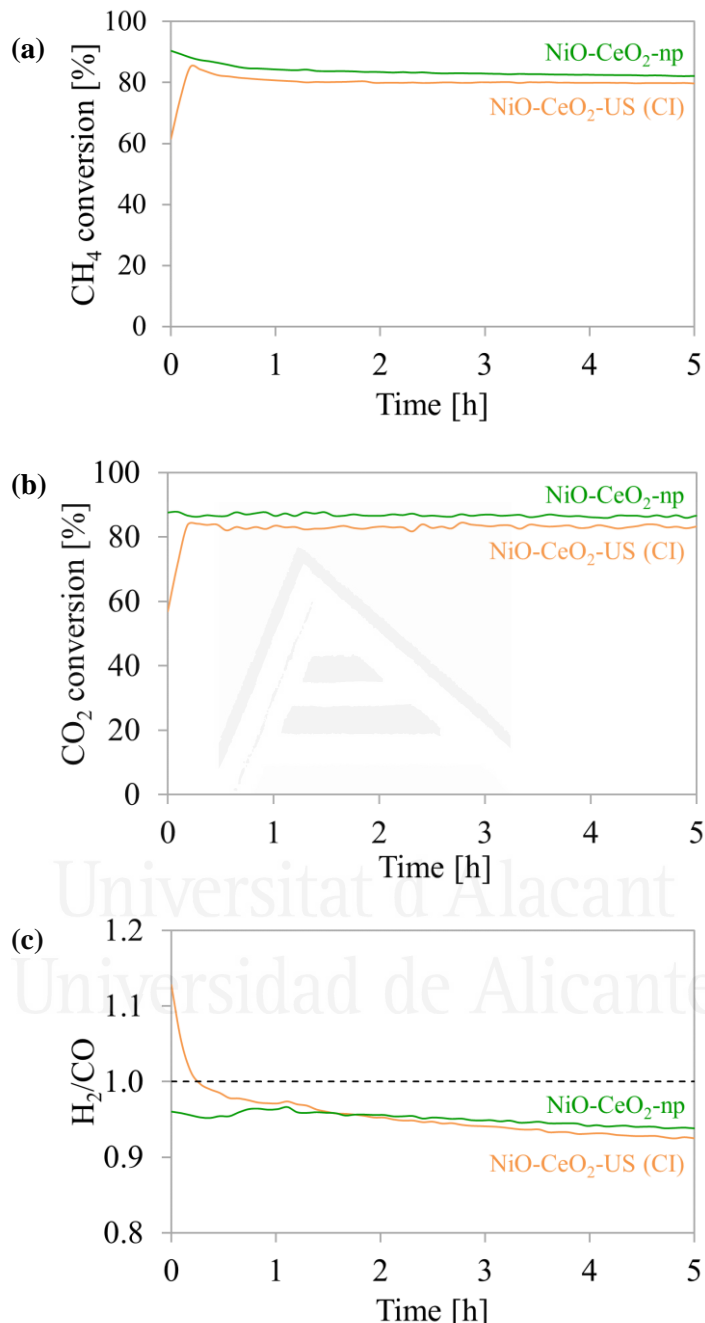


Figure 7.4. Methane dry reforming experiments: **(a)** CO₂ conversion, **(b)** CH₄ conversion and **(c)** H₂/CO yield. (700 °C; 100 mL/min; 10% CH₄ + 10% CO₂ with Ar balance; 300 mg of catalyst; pretreatment in situ at 500 °C, 1 hour, 100 mL/min of 5% H₂/Ar).

The amount of carbon accumulated on the catalysts during DRM was quantified measuring the weight dropped above 450 °C due to the combustion of such carbon. These results reveal that the amount of carbon on the novel NiO-CeO₂-np catalyst is 2.7 times lower to that on the counterpart reference NiO-CeO₂-US (CI) catalyst, that is, the novel catalyst reduced by 63% the accumulation of carbon during DRM. The average carbon accumulation rate during the catalytic tests is 17 µg_{carbon}·h⁻¹·gcatalyst⁻¹ for NiO-CeO₂-np and 45 µg_{carbon}·h⁻¹·gcatalyst⁻¹ for NiO-CeO₂-US (CI).

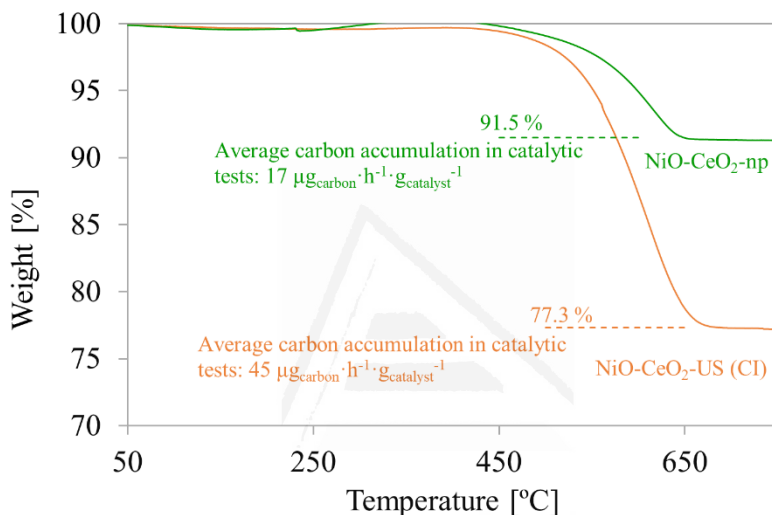


Figure 7.5. Combustion in air in a thermobalance of carbon accumulated on the catalysts during DRM experiments.

It has been reported that, for NiO/CeO₂-based catalysts, two conditions are relevant to diminish carbon formation [25]. One of them is the strong interaction between the Ni phase and the ceria support and the other one is to ensure high oxygen mobility within the ceria lattice. The NiO-CO₂ contact is expected to be good in mixed oxides, as those prepared in the current study, but certain differences were noticed in XRD and H₂-TPR characterization. These techniques provided evidences about the improved NiO-CeO₂ contact in the catalyst with the best carbon resistance (NiO-CeO₂-np) with regard to that in the reference mixed oxide (NiO-CeO₂-US (CI)). It has been also proposed that decreasing the particle size of nickel hinders carbon formation if the size is too small for carbon nucleation and growth [25], and therefore, the better formation of the NiO-CeO₂ mixed oxide in the NiO-CeO₂-np catalyst and the smaller crystallite size would explain the improved carbon resistance.

7.3.3. XPS analysis of the catalysts before and after the DRM tests

The as-prepared catalysts were characterised by XPS, and also after the DRM experiments. The spectra obtained in the Ni_{2p} energy region are included in Figure 7.6., showing the most intense band at 851–859 eV with their satellites at 859–866 eV.

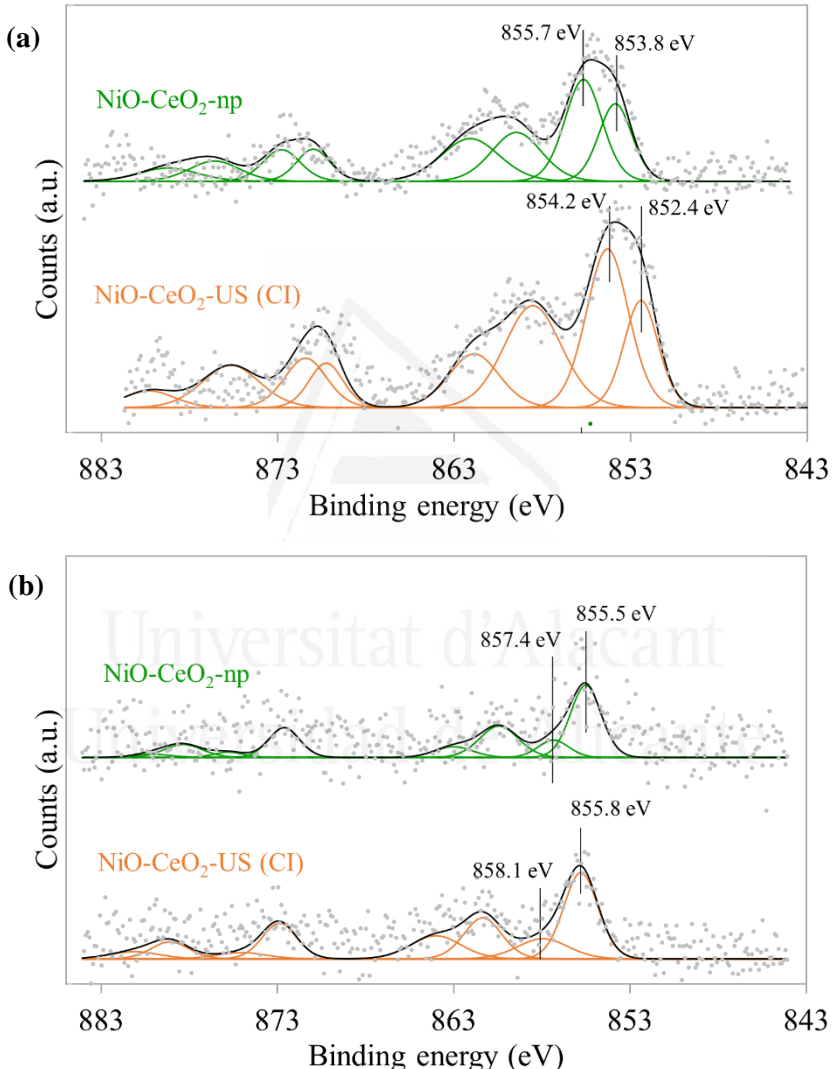


Figure 7.6. XPS spectra recorded in the Ni_{2p} energy region. **(a)** Fresh catalysts and **(b)** after the DRM experiments.

There is not general consensus about the assignment of Ni_{2p} peaks, but it has been proposed that the nature of the nickel species can be deduced from the position and deconvolution of the highest intensity peak [27,28]. Peaks of metallic nickel are expected to appear below 852 eV, and above this energy peaks can be assigned to NiO, Ni₂O₃ and Ni(OH)₂ [27,29–32]. According to this assignment, cationic species of nickel are present on the surface of both fresh catalysts, as expected considering that catalysts were calcined. The ratio of the areas (or intensities) of the main peaks in the spectra is similar for both fresh catalysts, but the binding energies of the maxima are higher for NiO-CeO₂-np than for NiO-CeO₂-US (CI). This could be related to the better NiO-CeO₂ interaction achieved in the nanoparticles, as deduced from XRD and H₂-TPR. The higher binding energies of nickel cations in NiO-CeO₂-np suggest higher interaction between these cations and ceria, that is, this interaction leads to the transfer of negative charge density from NiO to CeO₂.

The intensity of the Ni_{2p} spectra decreased for the used catalysts, and much noisier spectra were obtained due to the accumulation of carbon on the surface. The position of the most intense Ni_{2p} peak shifts towards higher binding energy after the DRM experiments, indicating changes in the surface of both catalysts that stabilize the oxidized species of nickel. The shift in the position of the Ni_{2p} peaks affects to NiO-CeO₂-US (CI) in a much higher extent than to NiO-CeO₂-np, that is, the shift for nanoparticles is 1.7 eV while it is higher than 3 eV for the reference catalyst. This is consistent with the important changes detected by XRD for NiO-CeO₂-US (CI) after the catalytic tests, but XRD predicts the presence of reduced nickel while XPS evidences the formation of nickel cations with high positive charge density. This suggests the segregation of metal nickel during the reaction, but the surface of these segregated nickel particles seems to be highly oxidised.

Changes in the oxidation state of the cerium cations are also detected by XPS before and after the catalytic tests, as deduced from Figure 7.7. XPS spectra of cerium combines peaks assigned to Ce³⁺ and Ce⁴⁺, as it has been labelled in the figure, and the proportion of Ce³⁺ cations with regard to Ce³⁺ + Ce⁴⁺ can be estimated as the ratio between the area under the Ce³⁺ peaks and the total area under the spectrum. The estimated Ce³⁺ percentages, compiled in Table 7.2., predict that the amount of Ce³⁺ in the fresh catalysts is not very different to each other (18 vs 23 %). However, the behaviour under reaction conditions is very different for each catalyst. While the average oxidation state of cerium cations in NiO-CeO₂-US (CI) does not change during the DRM tests (18 % before and after the tests), the Ce³⁺ percentage in NiO-CeO₂-np drops from 23 to 11 %. This suggests that ceria in this catalyst is getting significantly involved in the redox processes taken place under reaction conditions, and probably this participation of ceria explains the higher stability of the nickel species. That is, Ni_{2p} and

Ce_{3d} XPS characterization suggests that cooperation between nickel and cerium oxides during DRM is much more efficient in the NiO-CeO₂-np catalyst than in the reference material prepared without control of the structure.

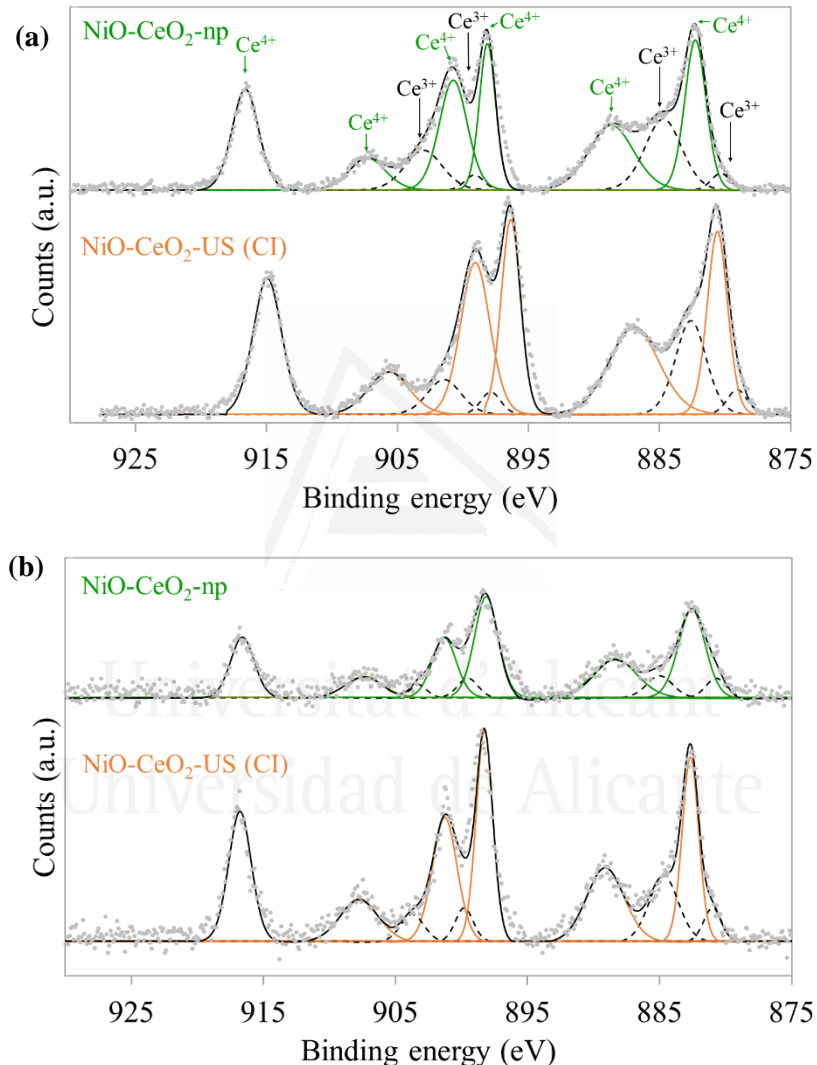


Figure 7.7. XPS spectra recorded in the Ce_{3d} energy region. **(a)** Fresh catalysts and **(b)** after the DRM experiments.

Table 7.2. Ce³⁺ percentage determined from XPS analysis.

Catalyst	Ce ³⁺ (%)
NiO-CeO ₂ -np fresh	23
NiO-CeO ₂ -np used	11
NiO-CeO ₂ -US (CI) fresh	18
NiO-CeO ₂ -US (CI) used	18

In summary, XPS suggests that the improved carbon resistance of the NiO-CeO₂-np catalyst prepared in nanoparticle shape with regard to the counterpart mixed oxide prepared without control of the size is related to the better interaction and cooperation between nickel and cerium cations. The participation of cerium cations in the redox processes taking place during DRM seems to stabilize cationic species of nickel. In a wider outlook of the reaction pathway, it is known that nickel active sites are responsible for CH₄ dissociation, leading to CO + H₂ formation throughout the desired DRM reaction mechanism, or catalyzing carbon deposits formation throughout an undesired pathway. The success of the DRM pathway depends on the high interaction between nickel and ceria phases, avoiding segregation of nickel crystals with high enough size to catalyse carbon formation.

7.4. Conclusions

A NiO-CeO₂ DRM catalyst has been presented (8.7 wt. % Ni), which consist of mixed oxide nanoparticles (122 m²/g; 6-7 nm). These nanoparticles showed catalytic stability during 5 hours under the severe conditions of DRM (700 °C), and improved carbon resistance with regard to a counterpart NiO-CeO₂ mixed oxide (56 m²/g; average 15 nm) prepared without control of the size.

Both the nanoparticles and the reference catalyst present high activity and selectivity for DRM, almost reaching the conversion and ratio of products predicted by thermodynamics for the experimental conditions used. Nevertheless, nanoparticles reduced by 63% the accumulation of carbon.

XPS and H₂-TPR suggest that the improved carbon resistance of the nanoparticles is related to the better interaction and cooperation between NiO and CeO₂ mixed phases. In nanoparticles, participation of cerium cations in the redox processes taking place during DRM seems to stabilize cationic species of nickel. On the contrary,

the catalyst prepared without control of the structure suffered certain segregation of Ni during DRM reaction (while not the nanoparticles), and the presence of segregated Ni would be responsible of the catalytic formation of carbon.

7.5. References

- [1] M. Usman, W.M.A. Wan Daud, H.F. Abbas, Dry reforming of methane: Influence of process parameters. A review, *Renew. Sustain. Energy Rev.* 45 (2015) 710–744.
- [2] N. Abdel, K. Aramouni, J.G. Touma, B.A. Tarboush, J. Zeaiter, M.N. Ahmad, Catalyst design for dry reforming of methane: Analysis review, *Renew. Sustain. Energy Rev.* 82 (2018) 2570–2585.
- [3] Y. Wang, L. Yao, S. Wang, D. Mao, C. Hu, Low-temperature catalytic CO₂ dry reforming of methane on Ni-based catalysts: A review, *Fuel Process. Technol.* 169 (2018) 199–206.
- [4] A. Abdulrasheed, A. Abdul, Y. Gambo, M. Ibrahim, H. Umar, M. Yusuf, S. Hamid, A review on catalyst development for dry reforming of methane to syngas: Recent advances, *Renew. Sustain. Energy Rev.* 108 (2019) 175–193.
- [5] W. Jang, J. Shim, H. Kim, S. Yoo, H. Roh, A review on dry reforming of methane in aspect of catalytic properties, *Catal. Today.* 324 (2019) 15–26.
- [6] M. Fan, A.Z. Abdullah, S. Bhatia, Catalytic technology for carbon dioxide reforming of methane to synthesis gas, *ChemCatChem.* 1 (2009) 192–208.
- [7] D. Pakhare, J. Spivey, A review of dry (CO₂) reforming of methane over noble metal catalysts, *Chem. Soc. Rev.* 43 (2014) 7813–7837.
- [8] X.E. Verykios, Catalytic dry reforming of natural gas for the production of chemicals and hydrogen, *Int. J. Hydrogen Energy.* 28 (2003) 1045–1063.
- [9] B. Abdullah, N. Azeanni, A. Ghani, D.N. Vo, Recent advances in dry reforming of methane over Ni-based catalysts, *J. Clean. Prod.* 162 (2017) 170–185.
- [10] Z. Boukha, M. Kacimi, M.F. R. Pereira, J.L. Faria, J.L. Figueiredo, M. Ziyad, Methane dry reforming on Ni loaded hydroxyapatite and fluoroapatite, *Appl. Catal. A Gen.* 317 (2007) 299–309.
- [11] G. Valderrama, A. Kiennemann, M.R. Goldwasser, Dry reforming of CH₄ over solid solutions of LaNi_{1-x}Co_xO₃, *Catal. Today.* 133–135 (2008) 142–148.
- [12] S.P. Padi, L. Shelly, E.P. Komarala, D. Schweke, S. Hayun, B.A. Rosen, Coke-free methane dry reforming over nano-sized NiO-CeO₂ solid solution after exsolution, *Catal. Commun.* 138 (2020) 105951.
- [13] J. Juan-Juan, M.C. Román-Martínez, M.J. Illán-Gómez, Effect of potassium

- content in the activity of K-promoted Ni/Al₂O₃ catalysts for the dry reforming of methane, *Appl. Catal. A Gen.* 301 (2006) 9–15.
- [14] M. García-Diéguéz, I.S. Pieta, M.C. Herrera, M.A. Larrubia, L.J. Alemany, Nanostructured Pt- and Ni-based catalysts for CO₂-reforming of methane, *J. Catal.* 270 (2010) 136–145.
 - [15] Y. Wang, L. Li, Y. Wang, P. Da Costa, C. Hu, Highly carbon-resistant Y doped NiO–ZrO_m catalysts for dry reforming of methane, *Catalysts.* 9 (2019) 1–13.
 - [16] M.M. Barroso-Quiroga, A.E. Castro-Luna, Catalytic activity and effect of modifiers on Ni-based catalysts for the dry reforming of methane, *Int. J. Hydrogen Energy.* 35 (2010) 6052–6056.
 - [17] N. Laosiripojana, W. Sutthisripok, S. Assabumrungrat, Synthesis gas production from dry reforming of methane over CeO₂ doped Ni/Al₂O₃: Influence of the doping ceria on the resistance toward carbon formation, *Chem. Eng. J.* 112 (2005) 13–22.
 - [18] Q. Fu, A. Weber, M. Flytzani-Stephanopoulos, Nanostructured Au-CeO₂ catalysts for low-temperature water-gas shift, *Catal. Letters.* 77 (2001) 87–95.
 - [19] P. Franco, M. Martino, V. Palma, A. Scarpellini, I. De Marco, Pt on SAS-CeO₂ nanopowder as catalyst for the CO-WGS reaction, *Int. J. Hydrogen Energy.* 43 (2018) 19965–19975.
 - [20] A. Primo, T. Marino, A. Corma, R. Molinari, H. García, Efficient visible-light photocatalytic water splitting by minute amounts of gold supported on nanoparticulate CeO₂ obtained by a biopolymer templating method, *J. Am. Chem. Soc.* 133 (2011) 6930–6933.
 - [21] J. Liu, Z. Zhao, J. Wang, C. Xu, A. Duan, G. Jiang, Q. Yang, The highly active catalysts of nanometric CeO₂-supported cobalt oxides for soot combustion, *Appl. Catal. B Environ.* 84 (2008) 185–195.
 - [22] N. Guillén-Hurtado, A. García-García, A. Bueno-López, Active oxygen by Ce-Pr mixed oxide nanoparticles outperform diesel soot combustion Pt catalysts, *Appl. Catal. B Environ.* 174 (2015) 60–66.
 - [23] Y. Cui, H. Zhang, H. Xu, W. Li, Kinetic study of the catalytic reforming of CH₄ with CO₂ to syngas over Ni/α-Al₂O₃ catalyst: The effect of temperature on the reforming mechanism, *Appl. Catal. A Gen.* 318 (2007) 79–88.
 - [24] N. Wang, W. Chu, T. Zhang, X.S. Zhao, Synthesis, characterization and catalytic performances of Ce-SBA-15 supported nickel catalysts for methane dry reforming to hydrogen and syngas, *Int. J. Hydrogen Energy.* 37 (2011) 19–30.
 - [25] P. Djinovic, I.G.O. Crnivec, B. Erjavec, A. Pintar, Influence of active metal loading and oxygen mobility on coke-free dry reforming of Ni-Co bimetallic catalysts, *Appl. Catal. B Environ.* 125 (2012) 259–270.

- [26] V.M. Gonzalez-DelaCruz, J.P. Holgado, R. Pereñíguez, A. Caballero, Morphology changes induced by strong metal-support interaction on a Ni-ceria catalytic system, *J. Catal.* 257 (2008) 307–314.
- [27] A.P. Grosvenor, M.C. Biesinger, R.S.C. Smart, N.S. McIntyre, New interpretations of XPS spectra of nickel metal and oxides, *Surf. Sci.* 600 (2006) 1771–1779.
- [28] A.G. Marrani, V. Novelli, S. Sheehan, D.P. Dowling, D. Dini, Probing the redox states at the surface of electroactive nanoporous NiO thin films, *ACS Appl. Mater. Interfaces.* 6 (2014) 143–152.
- [29] X. Xu, L. Li, F. Yu, H. Peng, X. Fang, X. Wang, Mesoporous high surface area NiO synthesized with soft templates: Remarkable for catalytic CH₄ deep oxidation, *Mol. Catal.* 441 (2017) 81–91.
- [30] G.H. Yu, L.R. Zeng, F.W. Zhu, C.L. Chai, W.Y. Lai, Magnetic properties and X-ray photoelectron spectroscopy study of NiO/NiFe films prepared by magnetron sputtering, *J. Appl. Phys.* 90 (2001) 4039–4043.
- [31] A. Ahmed, T. Ali, M.N. Siddique, A. Ahmad, P. Tripathi, Enhanced room temperature ferromagnetism in Ni doped SnO₂ nanoparticles: A comprehensive study, *J. Appl. Phys.* 122 (2017) 083906.
- [32] N. Weidler, J. Schuch, F. Knaus, P. Stenner, S. Hoch, A. Maljusch, R. Schäfer, B. Kaiser, W. Jaegermann, X-ray photoelectron spectroscopic investigation of plasma-enhanced chemical vapor deposited NiO_x, NiO_x(OH)_y, and CoNiO_x(OH)_y: influence of the chemical composition on the catalytic activity for the oxygen evolution reaction, *J. Phys. Chem. C.* 121 (2017) 6455–6463.

8

General conclusions/ Conclusiones generales

- 8.1. General conclusions**
- 8.2. Conclusiones generales**



Universitat d'Alacant
Universidad de Alicante

8.1. General Conclusions

From the study of the CO₂ methanation mechanism on NiO/CeO₂ and NiO/Al₂O₃ catalysts the following conclusions have been obtained:

- ❖ The higher methanation activity and selectivity of NiO/CeO₂ catalyst is attributed to: i) this combines two different active sites for the CO₂ dissociation at NiO-ceria interface and for H₂ dissociation on reduced Ni⁰ particles; ii) water desorption is the slowest step, and due to the high oxygen mobility throughout the ceria lattice, water is not necessarily formed on the same active sites that chemisorb CO₂, i.e., the CO₂ chemisorption on sites are not blocked by water molecules; iii) the NiO/CeO₂ surface does not accumulate carbon-containing species under reaction conditions, which allows faster chemisorption and dissociation of CO₂.
- ❖ The mechanism study on NiO/Al₂O₃ showed that: i) all the steps of the mechanism take place on the same active sites, there is not specific active sites for H₂ dissociation, and molecular H₂ must reduce surface species; ii) the slow release of water and the accumulation of surface formates on these sites delay the chemisorption of further CO₂ molecules; iii) the CO release as undesired by-product is result of the formation of formates as reaction intermediates.

From the study about the role and optimization of active sites in NiO/CeO₂ catalysts for the CO₂ methanation, the most important conclusions are summarised below:

- ❖ Three dimensionally ordered macroporous (3DOM) structures have been synthesized and Ni introduced during the 3DOM structure synthesis by the methods i) co-impregnation; ii) successive impregnation of Ni and Ce precursors and iii) Ni impregnation after CeO₂ 3DOM synthesis. Materials with uncontrolled structures were also prepared by co-impregnation and Ni impregnation methods. Materials with uncontrolled structures (named US) were also prepared by co-precipitation and Ni impregnation of the CeO₂-US support.
- ❖ The catalytic behaviour is related to the NiO-Ceria contact, and consequently, the proportion of reduced Ni⁰ sites and NiO intimate contact with ceria. The proportion of the active sites varies depending of the Ni incorporation method and surface area of the support. The addition of Ni prior to the synthesis of CeO₂ structure generates a high proportion of NiO in intimate contact with ceria and, consequently, the former presents a high amount of active sites where CO₂ dissociation takes place. This percentage of NiO in intimate contact decreases if Ni is incorporated by impregnation method and generates high number of active sites for H₂ dissociation. The reducibility of ceria is also affected by the different NiO-Ceria contact. Ni-catalyzed reduction of Ce⁴⁺ cations

in the ceria surface is observed in samples with high NiO-Ceria interface, which could be indicative of the better NiO-Ceria contact observed.

- ❖ An optimal proportion of both sites is required to achieve the maximum conversion of CO₂: around 25% of surface Ni for H₂ dissociation and 75% of NiO in intimate contact with ceria for the CO₂ dissociation. When increasing NiO in intimate contact to higher level, the CO₂ dissociation is improved, but the dissociation and transfer of H₂ is hindered and, as consequence, CO₂ conversion and CH₄ selectivity decreases, as NiO/CeO₂-3DOM (SI) and NiO-CeO₂-3DOM (CI) catalysts. Above 25% of surface Ni, the dissociation of CO₂ is restricted in a H-rich environment, and therefore, the activity is limited by the CO₂ dissociation, i.e. NiO-CeO₂-US (CI) and NiO-CeO₂-3DOM (I).

- ❖ Is very important to optimize the proportion of active sites for CO₂ and H₂ dissociation in order to optimize the methanation activity. An imbalance of active sites has consequences in the surface carbon species observed under reaction conditions and thus, in the catalytic activity.

From the study of the NiO-CeO₂ mixed oxide nanoparticles, which were prepared, characterized and tested for CO₂ methanation reaction, and compared with other reference NiO-CeO₂ catalysts, it has been possible to conclude the following:

- ❖ A catalyst consisting of NiO-CeO₂ mixed oxide nanoparticles has been prepared, characterized and tested for CO₂ methanation. The behaviour of this material has been compared with other reference NiO-CeO₂ catalysts, including a mixed oxide with the same composition but prepared without control of the size, a counterpart NiO-CeO₂ mixed oxide with three dimensionally ordered macroporous (3DOM) structure and an inverse catalyst consisting of CeO₂ nanoparticles supported on bulk NiO among others.

- ❖ The NiO-CeO₂-np catalyst is the most active for CO₂ methanation among those compared, being much more active than the reference catalyst with the same composition but prepared without control of the size. The high activity of this NiO-CeO₂-np catalyst is related with its high specific surface area (122 m²/g) and with the presence of highly-reducible Ni-O-Ce species on the nanoparticles surface. Additionally, the selectivity towards CH₄ formation of this material is ~100 % in the whole range of temperature studied, and is also highly stable, keeping the same activity during 25 hours of catalytic experiment.

From the study about the effect of carbon content in the NiO/CeO₂ catalysts for the CO₂ methanation, it has been possible obtained the following conclusions:

❖ Catalysts consisting of NiO/CeO₂ and NiO/C physical mixture (0, 25, 50, 75 and 100 % of NiO/C content) have been prepared, characterized and tested for the CO₂ methanation reaction. The carbon-free and 25%NiO/CeO₂-75%NiO/C catalysts are the most actives for CO₂ methanation (65 and 60% of CO₂ conversion at 350 °C), being the 25%NiO/CeO₂-75%NiO/C catalyst a viable option in order to reduce and optimize the use of ceria.

❖ The presence of carbon increases the specific surface area, and favours the reducibility of the NiO/CeO₂ phases. The reduction profiles of the carbon-containing catalysts exhibit a reduction peak shift at a lower temperature and an increase in the surface NiO species compared to the carbon-free catalyst. The good catalytic behavior of the 25%NiO/CeO₂-75%NiO/C catalyst is related with the high specific area of the carbon support, which favours the dispersion of the nickel particles, and/or to the chemical effect of carbon in the NiO/CeO₂ interaction.

The study of stable NiO-CeO₂ nanoparticles with improved carbon resistance for methane dry reforming reaction (DRM) has led to the conclusions summarized below:

❖ A catalyst consists of NiO-CeO₂ mixed oxide nanoparticles has been prepared, characterized and tested to DRM. The behaviour catalytic of this material has been compared with other reference NiO-CeO₂ catalyst, consisting a mixed oxide with the same composition but prepared without control of the size. Both catalysts present high activity, selectivity and stability during 5 hours under the severe conditions of DRM reaction (700 °C). Nevertheless, nanoparticles reduced by 63% the accumulation of carbon with regard to a counterpart reference catalyst without control of the size.

❖ The carbon resistance of the nanoparticles can be related to the better interaction and cooperation between NiO and CeO₂ mixed phases. In nanoparticles, participation of cerium cations in the redox processes taking place during DRM seems to stabilize cationic species of nickel. On the contrary, the catalyst prepared without control of the structure suffered certain segregation of Ni during DRM reaction (while not the nanoparticles), and the presence of segregated Ni would be responsible of the catalytic formation of carbon.

8.2. Conclusiones generales

Del estudio del mecanismo de reacción de metanación de CO₂ sobre catalizadores NiO/CeO₂ y NiO/Al₂O₃ se han obtenido las siguientes conclusiones:

❖ La alta actividad catalítica y selectividad del catalizador NiO/CeO₂ es atribuida a: i) este catalizador combina dos sitios activos diferentes, la disociación de CO₂ se lleva

a cabo en la interfase NiO-ceria y la disociación de H₂ se da sobre partículas de Ni⁰ reducidas; ii) La desorción de agua es el paso más lento, y debido a la alta movilidad del oxígeno a lo largo de la red de la ceria, el agua no se forma necesariamente en los mismos sitios activos donde se quimisorbe el CO₂, es decir, la quimisorción de CO₂ en los sitios no está bloqueada por las moléculas de agua; iii) la superficie de NiO/CeO₂ no acumula especies de carbono bajo condiciones de reacción, lo cual permite una quimisorción y disociación de CO₂ más rápida.

❖ El estudio del mecanismo sobre el catalizador NiO/Al₂O₃ mostró que: i) todos los pasos del mecanismo tienen lugar sobre los mismos sitios activos, no hay sitios activos específicos para la disociación de H₂, y el H₂ molecular debe reducir las especies superficiales; ii) la liberación lenta de agua y la acumulación de formiato superficial en estos sitios retrasan la quimisorción de más moléculas de CO₂; iii) el CO como subproducto no deseado es el resultado de la formación de formiato como intermediarios de reacción.

Las conclusiones del estudio sobre el papel y optimización de sitios activos en catalizadores NiO/CeO₂ para la reacción de metanación de CO₂ se resumen a continuación:

❖ Se han sintetizado sólidos macroporosos con orden tridimensional y se ha introducido Ni durante la síntesis mediante los métodos i) coimpregnación; ii) impregnación sucesiva de los precursores de Ni y Ce y iii) impregnación del Ni después de la síntesis del soporte de CeO₂ 3DOM. Además, se prepararon materiales sin control de la estructura (denominados US) mediante los métodos de coimpregnación e impregnación del Ni sobre el soporte de CeO₂ US.

❖ El comportamiento catalítico está relacionado con el contacto NiO-Ceria, y consecuentemente, con la proporción de sitios activos de Ni⁰ reducido y NiO en íntimo contacto con la ceria. La proporción de sitios activos varía según el método de incorporación del níquel. La adición de Ni previo a la síntesis de la estructura de CeO₂ genera una alta proporción de especies de NiO en íntimo contacto con la ceria y, consecuentemente, una alta cantidad de sitios activos donde se produce la disociación de CO₂. Este porcentaje de NiO en íntimo contacto decrece cuando el Ni es incorporado por el método de impregnación, lo cual genera una gran cantidad de sitios activos para la disociación de H₂. La reducibilidad de la ceria también se ve afectada por el contacto NiO-ceria. En muestras con una alta interfase NiO-ceria se ha observado la reducción catalizada por Ni de los cationes Ce⁴⁺, lo cual podría ser indicativo del mejor contacto observado entre NiO-ceria.

❖ Se requiere una proporción óptima de ambos sitios para lograr la máxima conversión de CO₂: alrededor del 25% de Ni superficial para la disociación de H₂ y el 75% de NiO en contacto íntimo con la ceria para la disociación de CO₂. Al aumentar el NiO en contacto íntimo a un nivel superior, se mejora la disociación del CO₂, pero se afecta la disociación y transferencia de H₂ y, como consecuencia, la conversión de CO₂ y la selectividad de CH₄ disminuye, como sucede en los catalizadores NiO/CeO₂-3DOM (SI) y NiO-CeO₂-3DOM (CI). Por encima del 25% del Ni superficial, la disociación del CO₂ está restringida en un entorno rico en H y, por lo tanto, la actividad está limitada por la disociación del CO₂, como pasa en los catalizadores NiO-CeO₂-US (CI) y NiO-CeO₂-3DOM (I).

❖ Es muy importante optimizar la proporción de sitios activos para la disociación de CO₂ e H₂ con el fin de optimizar la actividad de la metanación de CO₂. Un desequilibrio de sitios activos tiene consecuencias sobre las especies de carbono generadas en condiciones de reacción y, por tanto, en la actividad catalítica.

A partir del estudio de las nanopartículas de óxido mixto NiO-CeO₂, las cuales fueron preparadas, caracterizadas y probadas en la reacción de metanación de CO₂, y comparadas con otros catalizadores NiO-CeO₂ de referencia, ha sido posible concluir lo siguiente:

❖ Se ha preparado, caracterizado y probado un catalizador basado en nanopartículas de óxido mixto de NiO-CeO₂, para su uso en la reacción de metanación de CO₂. El comportamiento de este material se ha comparado con otros catalizadores NiO-CeO₂ de referencia, incluyendo un óxido mixto con la misma composición, pero preparado sin control del tamaño, un óxido mixto NiO-CeO₂ con estructura macroporosa con orden tridimensional (3DOM) y un catalizador inverso compuesto por nanopartículas de CeO₂ soportadas sobre un bulk de NiO, entre otros.

❖ Entre los catalizadores comparados, el catalizador NiO-CeO₂-np es el más activo para la metanación de CO₂, siendo mucho más activo que el catalizador de referencia con la misma composición, pero preparado sin control del tamaño. La alta actividad de este catalizador está relacionada con su alta superficie específica (122 m²/g) y con la presencia de especies de Ni-O-Ce altamente reducibles en la superficie de las nanopartículas. Adicionalmente, la selectividad hacia la formación de CH₄ de este material es ~100% en todo el rango de temperatura estudiado, y además es altamente estable, manteniendo la misma actividad durante 25 horas de experimento catalítico.

A partir del estudio sobre el efecto del contenido de carbón en catalizadores NiO/CeO₂ para la metanación de CO₂, se han obtenido las siguientes conclusiones:

- ❖ Se prepararon y caracterizaron catalizadores compuestos por una mezcla física de NiO/CeO₂ y NiO/C (0, 25, 50, 75 y 100% de contenido de NiO/C), y se probaron en la reacción de metanación de CO₂. El catalizador sin carbón y el catalizador 25%NiO/CeO₂-75%NiO/C son los más activos para la reacción de metanación de CO₂, (60 y 65% de conversión de CO₂, respectivamente a 350 °C), siendo el catalizador 25%NiO/CeO₂-75%NiO/C una opción viable en miras a optimizar y reducir el uso de ceria.
- ❖ La presencia de carbón aumenta la superficie específica y favorece la reducibilidad del catalizador NiO/CeO₂. Los perfiles de reducción de los catalizadores que contienen carbón presentan un desplazamiento del pico de reducción hacia valores de temperatura más bajos y un aumento en las especies de NiO superficial en comparación con el catalizador libre de carbono. El buen comportamiento catalítico del catalizador 25%NiO/CeO₂-75%NiO/C está relacionada con la alta área específica del soporte de carbón, el cual favorece la dispersión de las partículas de níquel, y/o al efecto químico del carbón en la interacción NiO/CeO₂.

El estudio de nanopartículas de NiO-CeO₂ estables y con resistencia mejorada a la acumulación de carbón para su uso en la reacción de reformado en seco de metano (DRM) ha permitido extraer las siguientes conclusiones:

- ❖ Se ha preparado, caracterizado y probado un catalizador de nanopartículas de óxido mixto de NiO-CeO₂ para la reacción DRM. El comportamiento catalítico de este material se ha comparado con otro catalizador NiO-CeO₂ de referencia, que consiste en un óxido mixto con la misma composición, pero preparado sin control del tamaño. Ambos catalizadores presentan alta actividad, selectividad y estabilidad durante 5 horas bajo las severas condiciones de reacción DRM (700 °C). Sin embargo, las nanopartículas redujeron en un 63% la acumulación de carbón con respecto al catalizador de referencia sin control del tamaño.
- ❖ La resistencia a la acumulación de carbón de las nanopartículas puede estar relacionada con una mejor interacción y cooperación entre las fases mixtas NiO y CeO₂. En las nanopartículas, la participación de cationes de cerio en los procesos redox, que tienen lugar durante la DRM, parece estabilizar las especies catiónicas de níquel. Por el contrario, el catalizador preparado sin control de la estructura sufrió cierta segregación de Ni durante la reacción de DRM (mientras que las nanopartículas no), y la presencia de Ni segregado sería la responsable de la formación catalítica de carbón.

Curriculum Vitae

Andrea Cárdenas Arenas was born on the 17th December of 1991 in Charalá, Colombia. She graduated in Metallurgical Engineering from the Industrial University of Santander (UIS) in 2017. After that, she won a SANTIAGO GRISOLIA grant from the government of the Generalitat Valenciana to develop the Doctoral Thesis at the Department of Inorganic Chemistry of the University of Alicante. Simultaneously, during her first year as PhD student, she obtained a Master's degree in Materials Science. As reflected in this Doctoral Thesis, she has focused her research on the design and synthesis of NiO-CeO₂ catalysts for two very important reactions in the CO₂ valorisation field, such as the CO₂ methanation and dry reforming of methane reactions.

Publications

A. Cárdenas-Arenas, E. Bailón-García, D. Lozano-Castelló, P. Da Costa, A. Bueno-López, Stable NiO-CeO₂ nanoparticles with improved carbon resistance for methane dry reforming, *Journal of Rare Earths* (in press).

A. Cárdenas-Arenas, H.S. Cortés, E. Bailón-García, A. Davó-Quiñonero, D. Lozano-Castelló, A. Bueno-López, **2021**, Active, selective and stable NiO-CeO₂ nanoparticles for CO₂ methanation, *Fuel Processing Technology*. Vol 212: 106637. Citations: 0 Impact factor: 4.982 Rank: 11/216 Percentile: 95th Source Scopus.

A. Cárdenas-Arenas, A. Quindimil, A. Davó-Quiñonero, E. Bailón-García, D. Lozano-Castelló, U. De-La-Torre, B. Pereda-Ayo, J.A. González-Marcos, J.R. González-Velasco, A. Bueno-López, **2020**, Design of active sites in Ni/CeO₂ catalysts for the methanation of CO₂: tailoring the Ni-CeO₂ contact. *Applied Materials Today*. Vol 19: 100591. Citations: 3 Impact factor: 16.683 Rank: 1/210 Percentile: 99th Source Scopus.

A. Cárdenas-Arenas, A. Quindimil, A. Davó-Quiñonero, E. Bailón-García, D. Lozano-Castelló, U. De-La-Torre, B. Pereda-Ayo, J.A. González-Marcos, J.R. González-Velasco, A. Bueno-López, **2020**, Isotopic and in situ DRIFT study of the CO₂ methanation mechanism using Ni/CeO₂ and Ni/Al₂O₃ catalysts. *Applied Catalysis B: Environmental*. Vol 265: 118538. Citations: 13 Impact factor: 8.352 Rank: 32/460 Percentile: 93rd Source Scopus.

B. Sellers-Anton, E. Bailón-García, **A. Cárdenas-Arenas**, A. Davó-Quiñonero, D. Lozano-Castelló, A. Bueno-López, **2020**, Enhancement of the generation and transfer of active oxygen in Ni/CeO₂ catalysts for soot combustion by controlling the Ni-ceria contact and the three-dimensional structure. *Environmental Science and Technology*. Vol 54: 2439-2447. Citations: 1 Impact factor: 7.864 Rank: 7/115 Percentile: 94th Source Scopus.

A.F. Gualdrón-Reyes, **A. Cárdenas-Arenas**, C.A. Martínez, V.V. Kouznetsov, A.M. Meléndez, **2017**, Fabrication of transparent TiO₂ nanotube-based photoanodes for CdS/CdTe quantum co-sensitized solar cells, *Journal of Physics: Conference Series*. Vol 786: 012044. Citations: 4 Impact factor: 0.54 Rank: 186/224 Percentile: 17th Source Scopus.

Stays, scientific congresses and courses with international impact.

Title: Catalizador de nanopartículas de NiO-CeO₂ altamente activo, selectivo y estable para el reformado seco de metano; Congress: IV Encuentro de Jóvenes Investigadores SECAT (IV JJII SECAT 2020); Type of participation: Poster; City: Bilbao (Spain); Date: 21/09/2020.

International stay in the Sorbonne Université: Campus Pierre and Marie Curie, Saint Cyr L'Ecole (Francia). From 10/09/2019 to 10/12/2019. Main purpose: Test NiO-CeO₂ catalysts with different structure for methane dry reforming, including NiO-CeO₂ mixed oxide nanoparticles, catalysts without control of the size and catalysts with three dimensionally ordered macroporous structure (3DOM). Center director: Patrick Da Costa (Institut Jean le Rond d'Alembert).

Title: Design of active sites in Ni/CeO₂ catalysts for the methanation of CO₂: tailoring the Ni-CeO₂ contact; Congress: 14th European Congress on Catalysis (EuropaCat 2019); Type of participation: Poster; City: Aachen (Germany); Date: 18/08/2019.

Title: Diseño de sitios activos en catalizadores de Ni-CeO₂ para la reacción de metanación de CO₂; Congress: Reunión Bienal de la Sociedad Española de Catálisis (SECAT'19); Type of participation: Oral; City: Cordoba (Spain); Date: 24/06/2019.

Title: Estudio mediante gases isotópicos y espectroscopía DRIFT in-situ del mecanismo de metanación de CO₂ en catalizadores Ni/CeO₂ y Ni/Al₂O₃; Congress: Reunión Bienal de la Sociedad Española de Catálisis (SECAT'19); Type of participation: Oral; City: Cordoba (Spain); Date: 24/06/2019.

Specialization course: Escuela de Verano: Avances en Catálisis Orgánica. Organizing entities: Sociedad Española de Catálisis (SECAT)/Universidad de Córdoba. City: Cordoba (Spain). Date: 27-06-2019. Hours: 12

Title: Fabricación de fotoánodos basados en nanotubos de TiO₂ cosensibilizados con puntos cuánticos de CdS/CdTe para su uso en celdas solares; Congress: II Congreso Colombiano de Electróquímica (II CCEQ), 2º Simposio en Nanociencia y Nanotecnología (2º SNN); Type of participation: Poster; City: Bucaramanga (Colombia); Date: 4/10/2016

Title: Fabrication of oriented TiO₂ nanotubes membranes on ITO glass as photoanodes for solar cells; Congress: 4th Latin-American Congress of Photocatalysis, Photoelectrochemistry and Photobiology (4th LACP3 2016); Type of participation: Poster; City: Bucaramanga (Colombia); Date: 25/04/2016.

Research projects and grants

Reference: UACOVID19-04; Title: Diseño de mascarillas avanzadas y fabricación mediante impresión 3D; Funding body: Vicerrectorado de Investigación y Transferencia de Conocimiento de la Universidad de Alicante; Call: 2020; Principal investigator: Agustín Bueno López (Universidad de Alicante); Date: 01/05/2020-31/12/2020; Amount: 10750 €; Type: Researcher.

Reference: BEFPI/2019/036; Title: Estancia en el centro Institut Jean le Rond d'Alembert; Funding body: Consellería de Innovación, Universidades, Ciencia y Sociedad Digital de la Generalitat Valenciana; Call: 2019; Principal investigator: Andrea Cárdenas Arenas (Universidad de Alicante); Date: 01/09/2019-30/11/2019; Amount: 4090 €; Type: Scientific coordinator.

Reference: GRE18-01; Title: Diseño de soportes específicos mediante impresión 3D para su aplicación en catálisis y adsorción; Funding body: Vicerrectorado de Investigación y Transferencia de Conocimiento de la Universidad de Alicante; Call: 2018; Principal investigator: Ester Bailón García; Date: 01/07/2019-31/12/2020; Amount: 10625 €; Type: Researcher.

Reference: GRISOLIAP/2017/185; Title: Diseño de catalizadores con orden tridimensional para la metanación de CO₂; Funding body: Consellería de Innovación, Universidades, Ciencia y Sociedad Digital de la Generalitat Valenciana; Call: 2017; Principal investigator: Dolores Lozano Castelló (Universidad de Alicante); Date: 01/12/2017-08/01/2021; Amount: 72743 €; Type: Scientific coordinator.

Universitat d'Alacant
Universidad de Alicante

